MODELING OF LIQUEFACTION USING COUPLED FINITE ELEMENT ANALYSIS

Ph.D. THESIS

by

SUNITA KUMARI

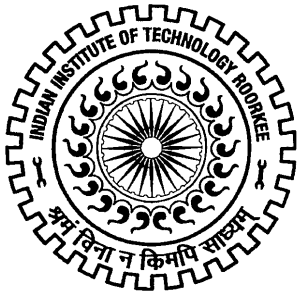

DEPARTMENT OF CIVIL ENGINEERING
INDIAN INSTITUTE OF TECHNOLOGY ROORKEE
ROORKEE-247667, UTTARAKHAND, INDIA

JULY, 2014

MODELING OF LIQUEFACTION USING COUPLED FINITE ELEMENT ANALYSIS

A THESIS

Submitted in partial fulfilment of the requirements for the award of the degree

of

DOCTOR OF PHILOSOPHY

in

CIVIL ENGINEERING

by

SUNITA KUMARI

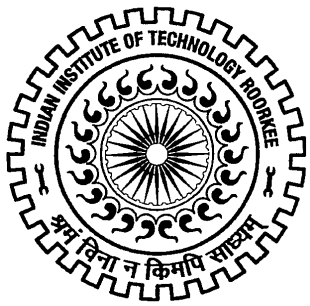

DEPARTMENT OF CIVIL ENGINEERING
INDIAN INSTITUTE OF TECHNOLOGY ROORKEE
ROORKEE-247667, UTTARAKHAND, INDIA

JULY, 2014

INDIAN INSTITUTE OF TECHNOLOGY ROORKEE
ROORKEE

CANDIDATE'S DECLARATION

I hereby certify that the work which is being presented in this thesis entitled **"Modeling of Liquefaction using Coupled Finite Element Analysis"** in partial fulfilment of the requirements for the award of the Degree of Doctor of Philosophy and submitted in the Department of Civil Engineering of the Indian Institute of Technology Roorkee, Roorkee is an authentic record of my own work carried out at Department of Civil Engineering during the period from July, 2011 to July, 2014 under the supervision of **Dr. V. A. Sawant**, Associate Professor, Department of Civil Engineering, Indian Institute of Technology Roorkee, Roorkee, India.

The matter presented in this thesis has not been submitted by me for the award of any other degree of this or any other Institute.

(Sunita Kumari)

This is to certify that the above statement made by the candidate is correct to the best of my knowledge.

(V. A. Sawant)
Supervisor

Date: /07/2014

The Ph.D. Viva-Voce Examination of **Mrs. Sunita Kumari**, Research Scholar, has been held on _____.

Signature of Supervisor Chairman, SRC External Examiner

Head of the Department/Chairman,ODC

Appendix-A
(*To be used in initial submission***)**

INDIAN INSTITUTE OF TECHNOLOGY ROORKEE
ROORKEE

CANDIDATE'S DECLARATION

I hereby certify that the work which is being presented in this thesis entitled **Modeling of Liquefaction using Coupled Finite Element Analysis** in partial fulfilment of the requirements for the award of the Degree of Doctor of Philosophy and submitted in the Department of **Civil Engineering** of the Indian Institute of Technology Roorkee, Roorkee is an authentic record of my own work carried out during a period from **July, 2011** to **July, 2014** under the supervision of **Dr. V. A. Sawant**, Department of **Civil Engineering**, Indian Institute of Technology Roorkee.

The matter presented in this thesis has not been submitted by me for the award of any other degree of this or any other Institute.

(Sunita Kumari)

This is to certify that the above statement made by the candidate is correct to the best of our knowledge.

(V. A. Sawant)
Supervisor

Date: 15 /07/2014

ABSTRACT

Soils are made of an assemblage of particles having different shapes and sizes in form of a skeleton whose voids are made up of water and air. The interaction of pore pressure with soil skeleton during earthquake results in the 'weakening' of soil-fluid composite which reduces the effective stress in soil mass, causing liquefaction. Liquefaction takes place often in saturated loose sands under earthquake and impact loadings. The pioneering experimental work associated with liquefaction phenomenon and cyclic mobility was proposed by Seed and Lee (1966), Seed and Idriss (1971), Castro and Poulos (1977), Seed 1979, Seed et al. (1985). The physical phenomenon is well defined whereas; the analytical modeling of soil liquefaction and computer simulation remains a challenge. Therefore, soil behaviour has been analysed by considering the effects of transient flow of the pore-fluid through voids. Hence, it requires a two-phase continuum formulation for saturated porous media.

Based on a detailed review of literature, the present study has been directed towards the establishment of an adequate mathematical framework to describe the liquefaction phenomenon. In the proposed study, a fully coupled formulation is developed to predict the liquefaction phenomenon of a finite and semi-infinite saturated sandy layer assuming plane strain condition. The saturated soil mass is considered as a saturated porous media using Biot's theory with *u–p* formulation. The variational principle is applied to the field equations of fluid flow in a fully saturated porous elastic continuum, and the finite element method is used to numerically solve the resulting continuity equation and equilibrium equation. The soil behaviour is defined using Pastor–Zienkiewicz Mark III model which describe the inelastic behaviours under dynamic loadings. This formulation is used to evaluate the responses of respective pore fluid and soil mass. A transmitting boundary is introduced to differentiate between near field and far field. Kelvin elements have been incorporated at transmitting boundary to absorb the wave energy and prevent back propagation of wave into the domain. In the far field, infinite elements are incorporated in the solution algorithms to simulate the infinite extent of the domain in 2-D plane strain finite element analyses. Newmark-Beta method is used for integration in time domain. In-situ stresses are computed from static analysis prior to dynamic analysis. Cyclic and Seismic analysis are performed considering finite and infinite domain. A parametric study is conducted to highlight the significance of

permeability, shear modulus and frequency on the response of liquefaction phenomenon. A significant reduction in displacement and EPP is observed with increase in shear modulus. Displacements are affected marginally with change in permeability whereas EPP is affected significantly. With decrease in permeability, considerable increase in EPP is observed. Effect of cyclic frequency is drastic for the range of frequencies considered in the analysis. It is noticed that the liquefaction occurs throughout all the depth of sand layer at frequency 1 Hz and 2 Hz of the cyclic loading, whereas no liquefaction is observed at 0.5 Hz. Similar trends of displacements and EPP are observed for variation in shear modulus and permeability for El-Centro earthquake input motion. For the case of Bhuj earthquake ground motion, only soil domains with shear modulus more than 50000 kPa are sustainable. For smaller values of shear modulus, soil domain is liquefying at early stage of earthquake ground motion.

PLAXIS 3D software based on UBC3D-PLM model has been used to analyze 3-D modeling of liquefaction and mitigation. The present study was directed to examine the effectiveness of remedial measures for liquefaction. The models with and without remedial countermeasures were analyzed. A comparative study was performed to highlight the effect of countermeasure on liquefaction. The stone column resulted in the smaller strains and cyclic mobility of the soil stratum. Maximum lateral strains and highest EPP in soil domain were observed in the no-remediation case with surcharge. Smaller values of displacements are predicted in comparison with the benchmark Model 1, but the variation is marginal. In lack of surcharge at surface, stone-columns are apparently ineffective in controlling settlements. As compared to Model 1, a reduction of around 40% in EPP is visible in Model 2. Predicted values for Model 4 are less than those evaluated for the benchmark Model 3 and the variation is noteworthy. Due to presence of a surcharge, stone columns are very effective in settlement reduction. The values obtained in Model 4 are about 50% less than those in Model 3, signifying the competency of the Model 4 in controlling the displacement produced during seismic shaking showing stiffer composite-material behavior. A significant reduction value of maximum EPP is visible in Model 4 as compared to maximum EPP in Model 3. Study presented effectiveness of mitigation measures in controlling liquefaction.

ACKNOWLEDGEMENTS

It gives me great pleasure in expressing my deep regards and sense of gratitude to my supervisor Dr. V. A. Sawant, Associate Professor, Department of Civil Engineering, Indian Institute of Technology, Roorkee for his inspiration, expert guidance, moral support, encouragement, and timely help throughout this work.

I also wish to express my sincere thanks to Head, Civil Engineering Department, I. I. T. Roorkee for extending me the facilities and cooperation for the successful completion of this work. Thanks are due to Q.I.P. Centre, I. I. T. Roorkee for offering me admission to PhD program and supporting me in every possible way.

My sincere thanks to Prof. Mahendra Singh and Dr. R. S. Jakka for their kind support and timely suggestions throughout this work. Suggestions and motivation provided by Prof. M. N. Viladkar and Prof. N. K. Samadhiya are duly acknowledged. Thanks are also due to other faculty members of the department who have directly or indirectly extended their helps. I would also like to express my thanks to Mrs. Chitra and Mr. Gupta for kind help in office works.

I am thankful to family of Dr. V. A. Sawant for helping me and my children during all good and odd times at Roorkee.

It is my great pleasure to acknowledge the support provided by my colleague Dr. N S Maurya for looking after my personal works at my parent institute in my absence. Thanks are also due to all my friends, co-research scholars Kiran, Haider, Pradeep, Gulshan, Rupali, Siddharth, Vinay and M. Tech Student Pragyan, Shashank, Mandeep, Mahesh for their generous support.

I sincerely and gratefully acknowledge the blessings of my parents and mother-in-law who was always a source of inspiration to me for pursuing higher studies. I am especially indebted to my husband Sunil Kumar for his innumerable sacrifices, tremendous patience and strong motivation through all the good and adverse times. Cheerfulness and tolerance capacity, amidst all odds, of my daughter Srishti and son Srijan are admirable.

Last but not the least; I want to express my sincere thanks to all those who directly or indirectly helped me at various stages of this work.

July 2014 (Sunita Kumari)

TABLE OF CONTENTS

LIST OF TABLES

LIST OF FIGURES

NOTATIONS

Notation	Description
u	Displacement of solid phase
p	Pressure of fluid phase
σ'_{ij}	Effective stress tensor
σ_{ij}	Total stress tensor
ρ	Average density of the soil-pore fluid mixture
ρ_s	Soil particle and water density
ρ_f	Density of the pore fluid
n	Porosity
γ	Unit weight
z	Depth from surface
$[k]$	Permeability tensor
$[M]_e$	Mass matrix of an element
$[K]_e$	Stiffness matrix of an element
$[Q]_e$	Coupling matrix of an element
$\{f\}_u$	Force vector for solid phase
K_b	Averaged bulk modulus
K_s	Bulk modulus of the soil grains
K_f	Bulk modulus of the pore fluid
$[G]_e$	Dynamic coupling matrix of an element
$[S]_e$	Compressibility matrix of an element
$[H]_e$	Permeability matrices of an element
$\{f\}_p$	Force vector for fluid phase

Δu_i , $\Delta \dot{u}_i$, $\Delta \ddot{u}_i$	Vectors of incremental displacement, velocity and acceleration, respectively
α and β	Newmark's integration constants
Δt	Time increment
g	Gravitational acceleration
N_i	Shape function associated with displacement node i
N_i^p	Shape function associated with pore pressure node i
u, w	Displacements at any point within the element
u_i, w_i	Displacements at the element node i
ξ, η	Natural co-ordinates
ξ_i, η_i	Natural co-ordinates of node i
$[J]$	Jacobian matrix
Γ_{ij}	Term in the i^{th} row and j^{th} column of inverse of the Jacobean matrix $[J]$
$\{\varepsilon\}$	Strain vector
E	Modulus of Elasticity
$[B]$	Strain-displacement transformation matrix
$[B^p]$	Pore pressure transformation matrix
$\{\delta\}$	Vector of unknown displacements
ε_x, ε_z, γ_{xz}	Cartesian strain components
σ_x, σ_z, τ_{xz}	Cartesian stress components
$[D]$	Elasticity constitutive matrix
μ	Possion's ratio
$\Delta\varepsilon^e$	Plastic strain

$\Delta\varepsilon^{p}$	Modulus of elasticity of third layer
$\Delta\sigma$	Stress increment
$\Delta\varepsilon$	Strain increment
$[D^{ep}]$	Elasto-plasto constitutive matrix
n	Normal vector in loading direction
$n_{gL/U}$	Flow direction vector during loading or unloading condition
$H_{L/U}$	Loading or unloading plastic modulus
$\Delta u', \Delta w'$	Relative displacements in ξ, η directions
G_0	Initial shear modulus of soil mass
K_0	Initial bulk modulus of soil mass
G	Shear modulus
K	Bulk modulus
p	Mean effective stress
q	Deviatoric stress
p_a	Atmospheric pressure
η	Stress ratio
d_g	Dilatancy of sand
d_f	Dilatancy at yield
$d\varepsilon_v^p$	Plastic volumetric increments
$d\varepsilon_s^p$	Deviatoric strains increments
ϕ	Angle of friction
g	Dimensionless parameter
f	Plastic potential surface

M_g	Slope of the critical state line
α and M_f	Constants
p_g and p_c	Size parameters
H_0	Initial loading plastic modulus
ε_q^p	Plastic shear strain
H_{DM}	Discrete memory factor
γ_{DM}	Parameter for considering reloading discrete memory factor
ζ	Mobilized stress function
η_u	Unloading stress ratio
ΔF	Incremental load vector
Δu	Incremental displacement vector
u_i	Displacement for i th increment
m_e	Number of yielded elements
m_p	Number of yielded points within the given element
$\Delta\delta^e$	Incremental displacement vector for element
$\Delta\sigma^e$	incremental stress vector for element
σ_{Ti}^e	Total stress vector for i^{th} increment for element
$\{\Delta\sigma\}_{ext}$	extra stress over yield stress
γ_s	Density of soil
G	Shear modulus of soil
k_r^*	Complex stiffness in horizontal direction
S_1 and S_2	Dimensionless parameters in horizontal direction

J_0, J_1, and J_2	First kind of Bessel functions of order zero, one and two, respectively
Y_0, Y_1 and Y_2	Second kind of Bessel functions of order zero, one and two, respectively
S_{v1} and S_{v2}	Dimensionless parameters in vertical direction
Z_r	Distance of the horizontal transmitting boundary from the base
ΔF_i	Dynamic load increment vector at current time step
$[C]$	Damping matrix
$[C_r]$	Radiation damping
$[C_m]$	Material damping
α_1 and α_2	Mass and stiffness proportional scalar constants
ξ_r	Damping ratio
ω_i	Frequency corresponding to *i* th mode of system
c' and ϕ'_p	cohesion and peak effective friction angle
σ'_{max} *and* σ'_{min}	Maximum and minimum principal effective stress
ϕ'_{mob}	Mobilized friction angle during hardening
K^e	Elastic bulk modulus
G^e	Elastic shear modulus
K_B^e *and* K_G^e	Bulk and shear moduli at reference stress condition
n_k and n_g	Parameter for rate of stress dependency of stiffness
ψ_{mob}	Mobilized dilation angle
K_G^p	Plastic shear modulus
n_p	Model parameter for stress dependency of the plastic shear modulus

	Plastic strain increment multiplier
ϕ'_{ult}	Ultimate mobilized friction angle
R_f	Failure ratio
n_{ev}	Number of shear stress reversals in loading to unloading
f_{dens}	Parameter to calibrate densification rule
k_{dens}	Factor used to correct densification rule for loose and cohesionless soil
$K^{p}_{G,Primary}$	Initial value of K_G^p for primary yield surface
ϕ'_{cv}	Constant
ε_{dil}	Accumulated plastic deviatoric strain
f_{post}	Parameter to limit the exponential multiplier term
dp_w	Increment of the pore pressure
and K'	Undrained and drained bulk moduli of the soil
μ_u	Poisson ratio in undrained condition

CHAPTER - 1

INTRODUCTION

1.1 GENERAL

Liquefaction is one of the most important, complex and controversial topics in earthquake geotechnical engineering. It's devastating effects drew the attention of geotechnical experts when the Alaska earthquake (M_w = 9.2) was followed by the Niigata earthquake (M_w = 7.5) in the span of three-month in year 1964. Both earthquakes produced spectacular examples of liquefaction damages. Failures of slope, foundations of buildings and bridges were noticed. Some of the buried structures were observed floating at ground level after earthquake. There onwards, the liquefaction phenomenon has been studied extensively by numerous researchers in the last five decades. Researchers have proposed different terminologies and methods of analysis. Various aspects of liquefaction and relevant mechanism were learnt from case histories and experimental model studies. In the recent years numerical simulations were attempted to understand the process of liquefaction. In spite of these studies, numerous questions are still to be answered on basic mechanism of liquefaction. Understanding these mechanisms and evaluating the capabilities of emerging analysis methods against physical data (case histories and model studies) are essential steps toward developing safe and efficient design methods.

1.2 MECHANISMS OF LIQUEFACTION

The response of a saturated sand deposit seismic motion is a very significant and challenging problem of soil dynamics and a completely satisfactory generalized solution does not yet exist. For loose to medium sands, the dynamic response is governed by the effects of progressive pore pressure increase that develops during an earthquake. The earthquake motion generates dynamic shear stresses and strains resulting slip at interface between granular materials. This inter-granular slip results in volumetric compaction at the developed shear strain levels during earthquakes (Silver and Seed, 1971). Due to inability of water to drain rapidly in saturated sand particles, volumetric compaction takes place slowly. Subsequently, the relaxing sand skeleton transfers part of its inter-granular stresses to the pore-water resulting rise in pore pressure. This reduction in effective stress causes a structural rebound in the sand skeleton to absorb the difference in volume between the compaction due to granular slippage and the reduction in pore-water volume

due to increased pore pressure and drainage. In the severe earthquake condition, the pore pressures generated may increase such that effective stresses are reduced to zero. As a result, the sand has negligible shearing strength and deforms like a liquid temporarily which is defined as zero effective stress state in the soil indicating occurrence of liquefaction (Seed and Idriss, 1967). On the contrary in denser sand, the zero effective stress state may never develop and cycles of alternative contraction and dilation may result. This is defined as 'cyclic mobility'. If the saturated sand layer can drain during earthquake motion there will be simultaneous generation and dissipation of pore pressure. Thus the rate of increase of pore pressure will be less than for completely undrained sand. In an undrained layer of sand the pore pressures generated at various locations by an earthquake will not be in instantaneous equilibrium with each other and a continuous redistribution takes place under the current gradients established by the earthquake motions. The pore pressure established at any time reveals the net effects of simultaneous generation and redistribution.

1.3 APPROACHES OF ANALYSIS

During last five decades considerable advancement has been made in defining the liquefaction phenomena. There are three main approaches: (1) field observations before, during and/or after earthquakes, (2) laboratory experiments, and (3) numerical simulations. In the theoretical studies, three different methods have been developed: (1) total stress approaches, (2) quasi-effective stress approaches, and (3) effective stress – based techniques, which are also referred to as fully coupled methods.

Although some geotechnical engineering problems may be idealized as quasi-static analysis or dynamic analysis in one-phase media, due to the coupled effects of the solid and the fluid, it is difficult to predict the dynamic soil behavior by using total stress approaches. In reality, saturated soil behaves as a two-phase medium. A realistic approach should incorporate the soil-fluid interaction. The mixture theory, characterized by the concept of volume fractions, perhaps yields the most consistently developed framework for the treatment of liquid-saturated porous solids.

The response of fluid-saturated porous media has been investigated through experimental and numerical studies. But, soils in particular have attracted significant interest due to the crucial factor it plays in design of pavements, foundations, hydraulic structures and earth retaining structures. It is clear from the literature (Seed et al. 1988) that liquefaction phenomenon is involved with the interaction of pore pressure and soil skeleton. This

interaction results in weakening of the soil-fluid composite during the periodic motion such as earthquake. Due to this feature, failure/damage takes place rather than the overall acceleration forces. It appears that, during the motion, the interstitial pore pressure increased, reducing the inter-particle forces in solid phase of the soil and causing a loss of strength.

For very slow phenomena with adequate drainage, drained static behaviour can be assumed for the behaviour of the two phases as, soil skeleton (the deformable porous solid) and water (the incompressible pore fluid) phase. These two phases can be decoupled and solutions can be found separately for the soil skeleton and pore fluid via usual mechanics and effective stress principles even for nonlinear problems. On the other hand, if the loading is applied very rapidly and drainage is prevented, an assumption of undrained conditions can be made, and the pore pressure can be calculated via the bulk modulus of the fluid, and again a single set of field equations need to be solved. However, under transient consolidation and dynamic conditions, such decoupling does not occur.

A qualitative and quantitative prediction of the phenomena leading to permanent deformation or unacceptably high build up of pore pressure is therefore essential to guarantee the safe behaviour of engineering structures under transient consolidation and dynamic conditions. There are various approaches to model the behavior of a two-phase porous medium. Usually, they are categorized as uncoupled and coupled approaches. In the uncoupled analysis, the response of saturated soil is modeled without incorporating the interaction between soil and fluid, and then the pore pressure is accounted separately through a pore pressure generation model. In the coupled analysis, a mathematical framework is developed for computation of displacements and pore pressures at each time step. It resembles closely with the liquefaction phenomena as compared to uncoupled approach. Hence, the usual decoupled and factor of safety approach may not be considered as most appropriate in the analysis of such dynamic behaviour.

The first finite element formulation of the two-phase (quasi-static) consolidation problem was proposed by Sandhu (1968) and by Sandhu and Wilson (1969). Other researchers have approximated Biot's equation with varying degree of accuracy and sophistication (Ghaboussi and Wilson, 1972). They considered the fully saturated case and proposed an approach based on two sets of non-homogeneous nodal variables, namely, the displacements in soil media and pore pressure. This *u-p* approach was generally used for the finite element analysis of consolidation, but later on Ghaboussi and Wilson (1973)

extended it to partially saturated case. This formulation was also applicable to the solution of undrained (static) problems.

Unlike most engineering materials, the constitutive relationships of soils are highly nonlinear from the initial phase of loading. Deformation and strength characteristics of soils are very much affected by different factors such as soil structure, loading rate, stress history, strain level and current stress state. In practice, it is necessary to idealize the soil behavior in order to develop suitable constitutive models. Soil behaviour under seismic loading is complex. Even if liquefaction does not occur, the development of excess pore pressures may lead to excessive soil softening, weakening or to partial loss of stability and even to bearing capacity failures. Rational analysis for the prediction of earthquake generated pore pressures involves a fundamental description of the soil constitutive behaviour. Also, the constitutive model should be able to predict permanent volume changes during seismic analysis. Zienkiewicz et al. (1978) extended *u-p* formulation to the non-linear range and Zienkiewicz and Shiomi (1984) proposed various solution strategies suited for specific cases, such as undrained conditions, consolidation, compressible/incompressible fluid phase, etc.

For successful prediction of liquefaction, the development of the accurate numerical tool is necessary and the need becomes more and more intense. For problems which involve the deformation of a soil mass, numerical methods are generally well suited for modeling the significant mechanics and boundary conditions. The finite element method (FEM) is a powerful and versatile numerical technique in modeling geotechnical engineering problems. However, domain of every finite element model has to be restricted at some finite boundary. For wave propagation related studies, the usual finite boundary of the domain may cause the seismic waves to be reflect back and superimpose with the outward waves. Therefore, the boundary conditions involved in simulating the dynamic behavior of semi-infinite soil media are a major challenge in FEM. The preferred boundary of the domain should ideally be radiating to outgoing waves and transparent to incoming waves. One way is to increase the size of the domain and consequent number of elements. But it will increase the computational effort to a great extent. To reduce the computational effort, the attempts must be directed towards reducing number of elements and at the same time boundary should be located away from the source. This can be achieved with introduction of infinite elements at the boundary. The infinite element is a recently developed technique to deal with the infinite media in the finite element analysis. The

basic idea is to place elements with a special shape function for the geometry at the infinite boundary.

A very sophisticated numerical model would be required to meticulously model all the above mentioned aspects of liquefaction and lateral spreading. A advance constitutive relation is required to simulate seismic excitation, soil softening behaviour, large distortions, the accumulation of excess pore pressures with subsequent loss of shear strength, redistribution of pore pressure and possible progressive failure. The model also should be able to predict the deformations continuing even after the end of seismic loading and consolidation with dissipation of excess pore pressure. The resulting numerical formulation would be highly non-linear and would need to consider inertial loads also. In the present study, such computational tools have been used to reproduce the above mentioned mechanisms of liquefaction and predict the soil response.

The present research is based on the modern version of porous media theories comprising of: (1) to implement the developed porous media models into numerical procedures and to validate the numerical solutions; (2) to impart the material constitutive models into the numerical algorithms; (3) to study special phenomena related to saturated porous media considering finite and semi-infinite domain.

1.4 OBJECTIVES OF PRESENT STUDY

Objective of the present study is to develop a methodology for obtaining behaviour of saturated soils subjected to earthquake motions using numerical modelling. Based on the finite element method, three types of analysis are proposed as 2D plane strain nonlinear analysis considering finite domain, 2D plane strain nonlinear analysis considering semi-finite domain using FORTRAN and 3D nonlinear analysis for liquefaction modeling and mitigation using PLAXIS 3D. It is aimed to study the effect of some key parameters of the soil system on the response of liquefaction phenomena. It is also aimed to study the effect of stone column on mitigation of liquefaction.

1.5 SCOPE OF PRESENT STUDY

Based on a detailed review of literature pertaining to the above aspects, the present study has been directed towards to model liquefaction behavior and mitigation in a saturated soil system during cyclic and seismic excitation, the proposed research work has been divided in following parts:

1. A numerical model is to be developed for a robust Biot's formulation, in which the governing equations of motion of the soil mixture are coupled with the global mass balance equations, to describe the realistic behaviour of saturated soil under earthquake loading.
2. Once this is accomplished the model can be incorporated into a finite element code, where it would govern the response of each soil element within a larger soil structure.
3. The establishment of an adequate constitutive relationship to employ elasto-plastic nonlinear constitutive models for material behavior and obtain reliable solutions of displacements and pore pressures.
4. To incorporate the transmitting boundary in the nonlinear analysis.
5. To conduct the parametric study, highlighting the significance of some key parameters such as frequency, permeability and shear modulus on the response of liquefaction phenomena.
6. To incorporate the infinite elements in the solution algorithms to simulate the infinite extent of the domain in the proposed 2-D plane strain finite element analyses.
7. To conduct 3D numerical analysis using PLAXIS 3D in a series of four separate models.
8. To consider the effect of mitigation measures by considering model with stone columns, and with a surface foundation surcharge.

Though most of the above aspects have been addressed separately by various researchers, a comprehensive analysis method incorporating all of these together has not been attempted. This makes the present work unique and original.

1.6 LAYOUT OF THESIS

The thesis is divided in seven chapters. The contents of each chapter are briefly described below:

The various aspects of the identified problem for the present investigation are briefly discussed and the objectives of the present study are defined in **Chapter 1**.

Chapter 2 highlights the literature review pertaining to different approaches for simulation of liquefaction phenomenon. A critical appraisal of the available literature is presented and the gaps are identified for consideration in the present study.

Chapter 3 is devoted to the dynamics of porous media with finite element implementation. The theoretical formulation of the problem is discussed in detail. A

detailed finite element formulation to perform the linear analysis is presented including Newmark Beta Integration method.

Chapter 4 presents nonlinear analysis of the problem in 2-D plane strain finite element analyses. The theoretical formulation pertaining to nonlinear technique and implementation of the transmitting boundary in the finite element program is presented in detail. The solution algorithm to incorporate soil nonlinearity is also discussed. The results of the parametric study for finite domain subjected to cyclic and seismic loading are discussed.

Chapter 5 includes the boundary conditions involved in simulating the dynamic behavior of semi-infinite soil media. The 2D finite element formulation for infinite element is also discussed. The results obtained from the parametric study are illustrated.

Chapter 6 discusses a 3D numerical analysis in a series of four separate models using PLAXIS 3D. The material constitutive behaviour of UBC3D-PLM model is also discussed. This model is studied first without, then with stone columns, and with a surface foundation surcharge with and without stone column. The results obtained from the parametric study are illustrated.

Chapter 7 summarizes the emerging trends, major conclusions, limitations and future scope of the present study.

CHAPTER - 2

LITERATURE REVIEW

2.1 INTRODUCTION

The failure of the civil engineering structures occurs during earthquake due to various reasons amongst which liquefaction of sandy soils is one of the most significant, interesting, complex and challenging phenomena in geotechnical engineering. Dewaikar and Halkude (2002), Shukla et al. (2011) and Shukla (2013) have extended static earth pressure theories to incorporate seismic effect to find earth pressure on retaining wall. Some of the major earthquakes such as the Niigata and Alaska 1964, Loma-Prieta 1989, Kobe 1995, Bhuj 2001 and many others, have marked the destructive behavior of liquefaction phenomenon. For the last few decades, it has received a lot of interest among researchers and academicians. They have proposed different methodologies for understanding the liquefaction phenomenon and estimation of its consequences on the performance of geotechnical systems and structures. The basic mechanism of liquefaction phenomenon and its different assessment method are presented in the following sections.

2.2 SOIL LIQUEFACTION

The appropriate definition for soil liquefaction has been the subject of a continuing discussion within the geotechnical professionals. Castro and Poulos (1977) defined soil liquefaction as a phenomenon when saturated soil mass subjected to monotonic or cyclic loading, loses its partial or full shear strength due to generation of excess pore pressure (EPP). Briefly, the change of a granular material from solid to liquefied state due to rise in pore pressure is defined as liquefaction (Marcuson, 1978).

Liquefaction frequently occurs in saturated loose sand under dynamic and seismic loadings. The structures resting on liquefiable soil, are most prone to damage and destruction. Loose sands are prone to compact under vibration, induced by seismic or cyclic loading. This results in decrease in volume which is often prevented by lack of drainage, long drainage path, having relatively low permeability or high frequency of cyclic load, during the period of vibration. This results in nearly undrained conditions which cause build up in high pore pressures to neutralize this contractive behavior and consequent decrease of the effective

stress. A state of zero effective stress in the soil mass may occur, lead to a failure known as 'initial liquefaction'. However, for dense sand, initial liquefaction state may never be attained. But cycles of alternative contraction and dilation may be possible resulting in 'cyclic mobility' (Youd and Idriss 2001; Popescu et al., 2006).

The most common feature of liquefaction is related with the tendency for soil grains to rearrange when sheared. Consequently, anything (such as particle cementation, soil fabric etc.) that prevents the rearrangement of soil grains will decrease the liquefaction susceptibility. Natural soil deposits, prior to the Holocene age (more than 10,000 years old) are generally not prone to liquefaction (Youd and Perkins, 1978). Several methods and numerical models have been developed in the last five decades for assessing and evaluating the soil liquefaction. Earlier studies were directed in the assessment of liquefaction potential based on the evaluation of soil strength parameters. With the advent of computer era, attempts were directed in numerical prediction of liquefaction behaviour. Accordingly, the available literature is discussed separately in these two major approaches in the subsequent sections. They are further divided into sub-groups on the basis of adopted methodology.

2.3 ASSESSMENT OF SOIL LIQUEFACTION POTENTIAL

The basic methods used for evaluation of liquefaction potential can be mainly categorized into two groups:

a) Empirical methods based on in-situ test data

b) Methods based on laboratory tests

2.3.1 Empirical Methods Based on Field Test Data

After the earthquakes in Alaska (1964) and Niigata (1964), Seed and Idriss (1971) developed a methodology known as the 'simplified procedure' for assessing liquefaction potential of various soil types during an earthquake which makes use of laboratory data of cyclic triaxial loading tests. It requires ground response analysis and the testing of representative soil samples under cyclic loading conditions assuming, shear stresses developed at any location in a soil deposit during an earthquake are due to the upward propagation of shear waves in the soil mass. This method takes into consideration of soil type, relative density, initial confining pressure, intensity and duration of ground shaking. This simplified procedure has been modified and updated by the different academician and researchers.

Seed (1979) made an attempt to develop correlations between liquefaction potential and standard penetration resistance. SPT values (*N*) obtained in the field for sand need to be corrected for accounting the effect of overburden pressure. The possible effects of pore pressure dissipation in different layers of a deposit during and following earthquake shaking was also reported.

Seed et al. (1983) established a criterion for assessing the liquefaction potential of sandy soils from interpretation of field data for different sites with their known status as liquefied or not liquefied in respective earthquakes in the different countries. The results of this study are then extended to other magnitude earthquakes incorporating the magnitude scaling factor in the calculation for cyclic stress ratio (*CSR*) induced by an earthquake at a given depth in horizontal soil deposit.

Later several researchers proposed different empirical methods based on field tests such as Standard Penetration Test (SPT), Cone Penetration Test (CPT), Becker Penetration Test (BPT), Shear wave velocity results. The flow chart for the basic steps of these methods is tabulated in Fig. 2.1. For all these methods, *CSR* has been calculated for a given earthquake amplitude at a definite depth in the soil deposit using the following relation:

$$CSR = \left(\frac{\tau_{av}}{\sigma'_{vo}\, MSF} \right) = 0.65 \left(\frac{a_{\max}}{g} \right) \left(\frac{\sigma_{vo}}{\sigma'_{vo}} \right) R_d \,/\, MSF \tag{2.1}$$

In which, *MSF* is a magnitude scaling factor, σ'_{vo} is the effective overburden pressure, σ_{vo} is the total overburden pressure, and $a_{\max}$ is the peak ground acceleration.

The R_d is a factor that depends upon depth and stiffness of soil mass that can be evaluated by given equations (Liao and Whitman, 1986).

$R_d = 1.0 - 0.00765H$ for $H \leq 9.15$m (2.2a)

$R_d = 1.174 - 0.0267H$ for $9.15\text{m} < H \leq 23\text{m}$ (2.2b)

In which, *H* is the depth below the ground in meters.

The SPT values are affected by several factors. Correction should be applied to the values before use. Equation given below incorporates these corrections.

$$(N_1) = N_m C_N C_E C_B C_R C_S \tag{2.3}$$

In which, N_m is Measured standard penetration resistance, C_N is correction factor to normalize N_m for a common reference effective overburden pressure, C_E is hammer energy ratio (ER) correction factor, C_B is borehole diameter correction factor, C_R is rod length correction factor, C_S is for samplers with or without liners correction factor. Youd and Idriss (2001) discussed these factors elaborately.

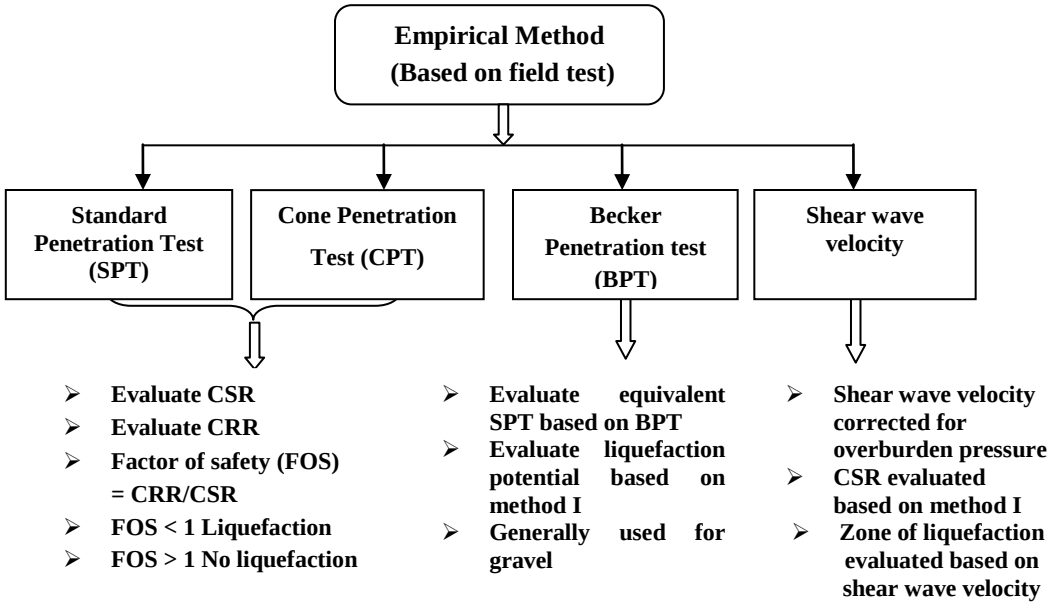

Fig.2.1 Empirical methods based on field test data

The cyclic resistance ratio (*CRR*) can be evaluated using Fig.2.2 after determination of $(N_1)_{60}$. *CRR* is first explained by Seed et al. (1983) and later on, it is modified by others (Youd and Idriss 2001). A factor of safety for liquefaction potential can be evaluated by comparing this value with cyclic stress ratio (*CSR*) using Eq. (2.1). If this factor of safety is less than unity at a particular depth, liquefaction is likely to occur at that particular location.

Another commonly used empirical method is based on cone penetration resistance value. This method is presented by Robertson and Companella (1985) and Seed and De-Alba (1986) which is basically similar to the earlier one, but it uses in-situ recorded cone tip resistance and friction ratio. Robertson and Wride (1998) have extensively documented CPT method for evaluation of liquefaction potential. This method has became more popular in recent year as CPT gives more reliable results than SPT along with availability of more and more CPT data from sites affected by earthquakes.

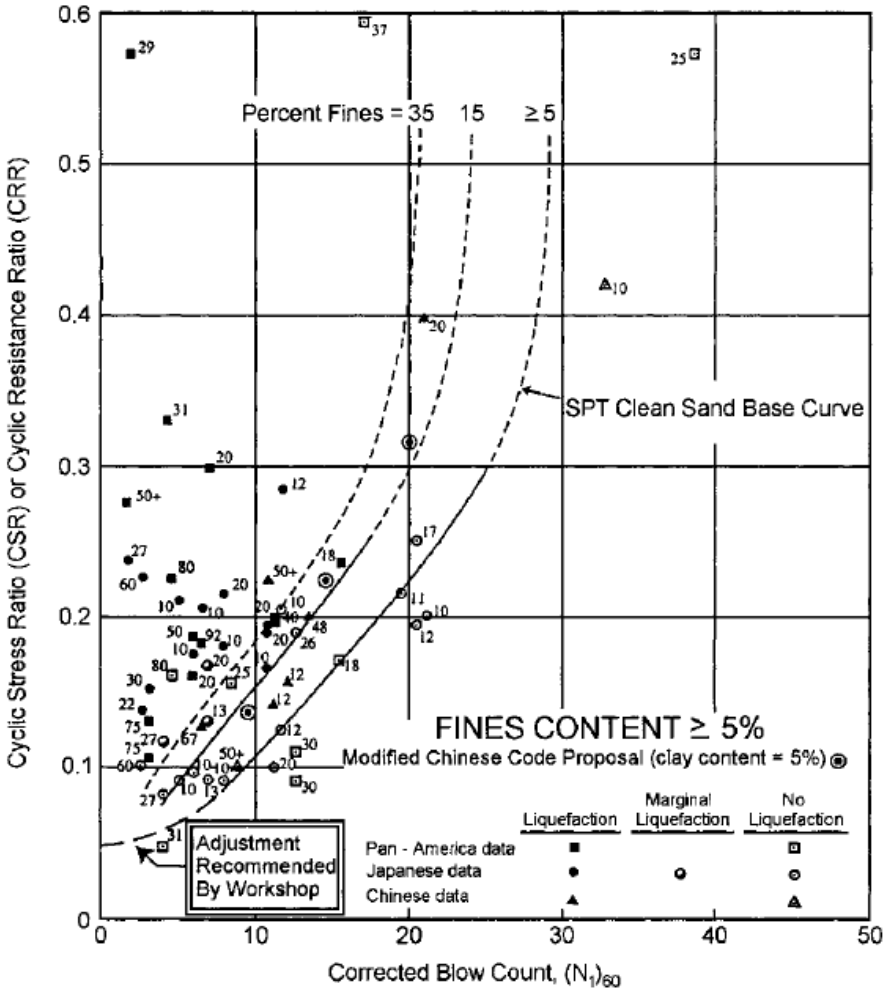

Fig.2.2: Graph used to evaluate the CRR for clean and silty sands for earthquakes having magnitude 7.5 (after Youd and Idriss 2001).

Robertson and Wride (1998) had recommended the curve for calculating CRR from normalised cone tip resistance as shown in Fig.2.3. The corrected cone tip resistance (q_{cN}) can be calculated from the following equation:

$$q_{cN} = C_Q \frac{q_c}{P_a} \tag{2.4}$$

In which q_c is the measured cone tip resistance and P_a is l00 kPa or approximately one atmosphere of pressure in the same units used for σ'_{v0}. σ'_{v0} is the vertical effective stress, C_Q is used as a normalizing factor for cone penetration resistance; $C_Q = \left(P_a / \sigma'_{v0}\right)^n$, and n is an exponent which varies with type of soil (0.5 to 1.0).

Generally, soils with considerable gravel contents cannot be reliably evaluated using CPT or SPT because the gravel particles are larger in relation to the effective size of the penetrometers. Becker penetration test (BPT) results are used for finding equivalent SPT values for these types of soils. These equivalent SPT data are used for the evaluation of liquefaction resistance of the soil (Harder and Seed, 1986).

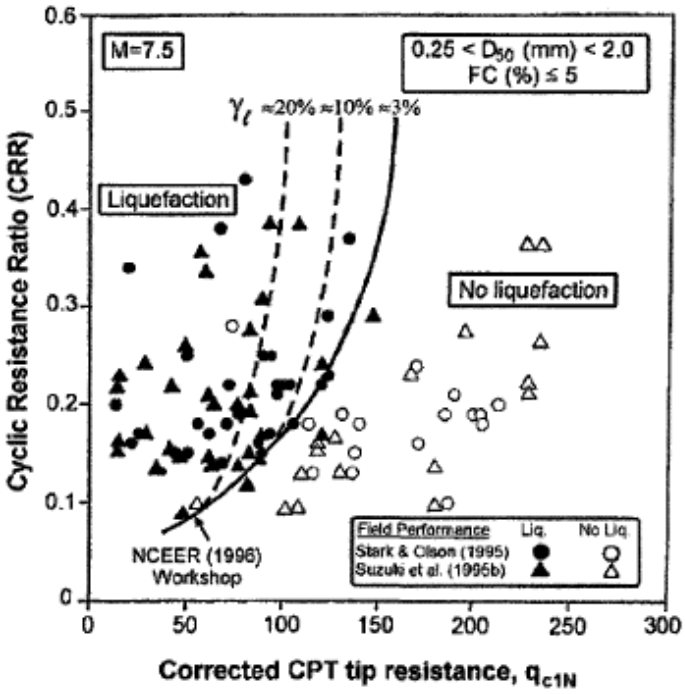

Fig 2.3: Recommended CRR verses CPT value along with empirical liquefaction data (after Robertson and Wride, 1998)

Andrus and Stokoe (1997, 2000) presented another empirical method commonly used for susceptibility of soil liquefaction based on shear wave velocity. This method is used for calculating liquefaction potential in loose soil using shear wave velocity (V_s). It is more effective as shear wave velocity and the liquefaction resistance is affected by the similar type of soil parameters (e.g., void ratio, permeability, soil type etc.). Youd and Idriss (2001) discussed that measurements of shear wave velocity are possible in soils where borings or soundings may not be allowable. It is quite difficult to extract undisturbed samples using CPT and SPT in gravelly soil. In situ seismic wave velocity measurements are done at small strains, whereas pore pressure buildup and the initiation of liquefaction are medium to high strain phenomena. Jakka et al. (2011) employed SASW method for field dynamic site characterization of the ash pond from measured shear wave velocity. Youd and Idriss (2001),

Andrus and Stokoe (1997, 2000) recommended criteria for measuring the liquefaction resistance using V_{s1} as shown in Fig. 2.4. Firstly, overburden stress correction is applied to the shear wave velocity (V_{s1}) given by following equation:

$$V_{s1} = V_s \sqrt[4]{P_a / \sigma'_{v0}} \tag{2.5}$$

In which, $P_{a \text{ and }} \sigma'_{v0}$ are atmosphere pressure and initial effective vertical stress in kPa respectively. Then *CSR* can be evaluated from chart (Fig.2.4) presented by Andrus and Stokoe, (2000).

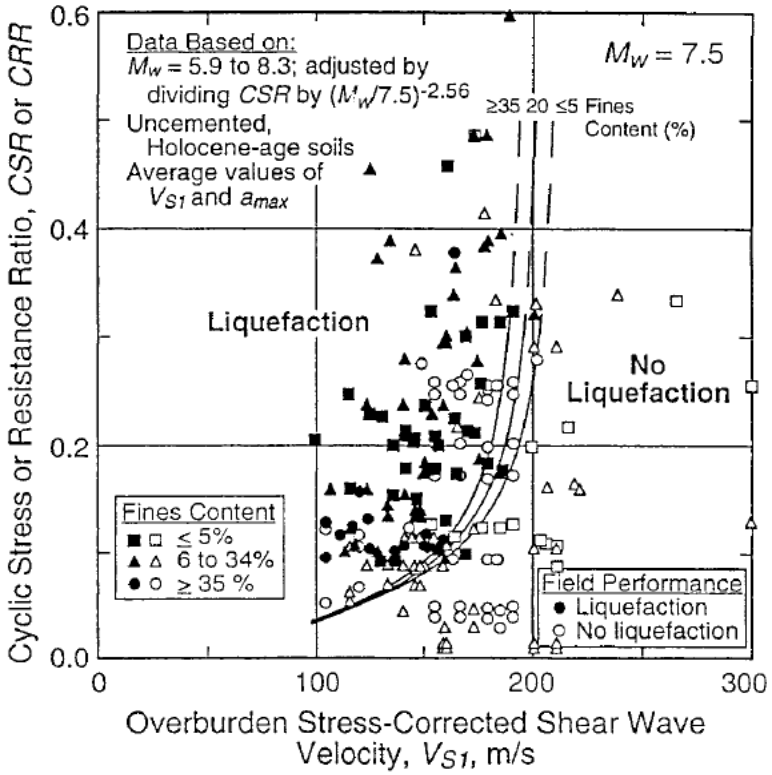

Fig.2.4: Recommended CRR verses V_{s_1} data along with empirical liquefaction data (after Andrus and Stokoe, 2000)

Iwasaki et al. (1984) projected two simplified methods for assessment of liquefaction potential of saturated sand. It is based on a liquefaction resistance factor F_L and a liquefaction potential index I_L. The excessive pore pressure generated in the saturated sands and the effects of soil liquefaction on the resistivity of grounds surrounding structures were expressed using factor F_L.

Kramer and Seed (1988) performed an experimental investigation to estimate the stress conditions necessary to trigger liquefaction. The influence of various parameters on these stress condition was also evaluated. Initiation of liquefaction was observed at high initial shear stress levels, due to increases in shear stress under undrained conditions of only a few percent of the initial shear stress. The author proposed a relationship to compute factor of safety against the initiation of liquefaction. The distinction between the initiation stage and the effects of liquefaction had been also illustrated.

Popescu et al. (1997) performed numerical analysis for four different types of input motion (generated based on four different response spectra) for a stochastically variable soil. These results were compared with the liquefaction susceptibility of a soil deposit predicted by the simplified methods using empirical correlations between normalized penetration resistance and cyclic resistance ratio for level ground conditions. It was found that stochastic model predictions were in good agreement with the results of the liquefaction assessment based on those empirical correlations. It was concluded that the simplified method, which is based on field measurement results, unconditionally accounts for natural soil variability. The simplified method is designed for horizontal soil deposits and provides a good estimation of the liquefaction susceptibility at the given site, but cannot account for seismic effects on structures (e.g. total and differential settlements) and effects of seismic loading rate.

Hwang et al. (2004) presented a reliability analysis method using Seed et al. (1985) liquefaction analysis concept. The empirical acceleration attenuation law has been used to derive the probability density distribution function (*PDF*) and the statistics for the earthquake generated *CSR*. From the regression of the liquefaction and non-liquefaction data from different earthquakes around the world, with minor modifications using logistic model proposed by Liao et al. (1988) charts has been presented. Based on the proposed method, the liquefaction probability related to a safety factor can be easily evaluated. The effect of some key parameters on the liquefaction probability was also discussed.

Idriss sand Boulanger (2006) recommended revised semi-empirical procedures for accessing the liquefaction potential of saturated sands. Revised SPT and CPT based liquefaction correlations were recommended for use in practice after re-evaluations of key parameters such as the stress reduction factor (r_d), earthquake magnitude scaling factor for cyclic stress ratios, overburden correction factor for cyclic stress ratios (K_s), and the overburden correction

factor for penetration resistances (C_N). In addition, shear wave velocity based procedure was briefly discussed.

Tsai et al. (2009) presented a simplified dilatometer test (DMT)-based methods to access liquefaction resistance of soils in terms of cyclic resistance ratio (*CRR*). Horizontal stress index (K_D) and dilatometer modulus (E_D) have been used as an index for evaluating liquefaction resistance of soils. The correlations between these parameters are derived from regression analysis of test results obtained from SPT, CPT, and DMT. The developed *CRR*–K_D and *CRR*–E_D curves for evaluating liquefaction resistance are validated with available case histories.

Chang et al. (2011) adopted SPT based methods for liquefaction and non liquefaction incidents observed during Chi-chi earthquake of 1999. The study shows that the SPT value and peak ground acceleration are most crucial in evaluating liquefaction potential. The authors compared the error in predicting liquefaction and non-liquefaction occurrences, and concluded that Tokimatsu and Yoshimi's method is more precise than the other methods.

Dixit et al. (2012 a, b) reported the susceptibility of soil liquefaction using simplified empirical procedure based on number of SPT blow counts (*N* values) of the soil layers for Mumbai city. The factors of safety against liquefaction (FS) along the depths of soil profiles for different earthquakes were evaluated with 2 % probability of exceeding in 50 years.

Boulanger et al. (2012) re-examined and re-evaluated liquefaction case history database for liquefaction triggering criteria based on SPT value replacing earlier estimates of earthquake magnitudes with current estimates of their moment magnitudes and using improved estimates of peak ground accelerations. The author has also included a re-examination of the selection and computation of representative SPT $(N_1)_{60}$ values for the majority of case histories. Dixit et al. (2012c) predicted free field surface motion at 142 locations in Mumbai. Seismic site response analysis was performed to predict surface motion from propagation of earthquake ground motions from the bedrock.

2.3.2 Methods Based on Laboratory Tests

Laboratory tests are one of the effective means of evaluating soil liquefaction. The cyclic triaxial test and the cyclic simple shear test in undrained condition are most commonly used laboratory tests for evaluation of cyclic strength ratio CSR.

a) Undrained Cyclic Triaxial Test

The soil is undergone through a series of cyclic shear strains which reverse directions several times during an earthquake. Casagrande (1936) performed drained, strain-controlled triaxial tests on initially loose and dense sand specimens. By performing test at different effective confining pressures, critical void ratio has been related to the effective confining pressure, and called the locus as critical void ratio, (CVR) line. CVR line could be used to mark the boundary between loose (contractive) and dense (dilative) states which was considered to mark the boundary between soils susceptible to liquefaction (Fig.2.5).

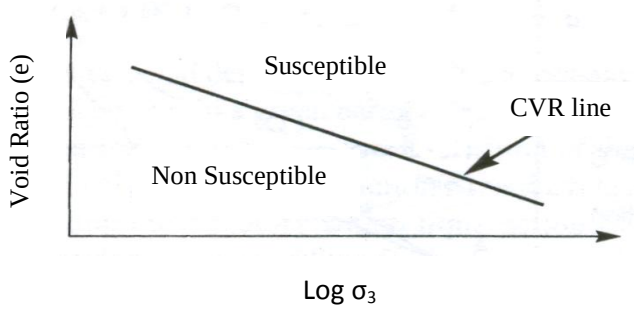

Fig. 2.5 CVR line as a boundary between Susceptibility and non-susceptibility to liquefaction

In the 1960s, comprehensive laboratory investigation programs on liquefaction of sands were initiated at the University of California, Berkeley. Seed and Lee (1966) reported the first set of comprehensive triaxial test data on sand. After that, undrained cyclic triaxial tests have been widely used for evaluating the liquefaction phenomena in sandy soil. In cyclic triaxial tests, the 45° inclined plane in the specimen represents the shear plane (usually the horizontal plane) in the ground and the cyclic shear stress (i.e., the half of the deviator stress) on that plane simulates the cyclic loading during an earthquake. Seed and Idriss (1971) have proposed a general method for predicting liquefaction potential during an earthquake using laboratory data of cyclic triaxial loading tests. By compiling the results of liquefaction test on various sandy soils, average standard curves for initial liquefaction for a given number of cyclic load application was developed (Fig. 2.6). These curves can be used for evaluation of liquefaction potential in the field.

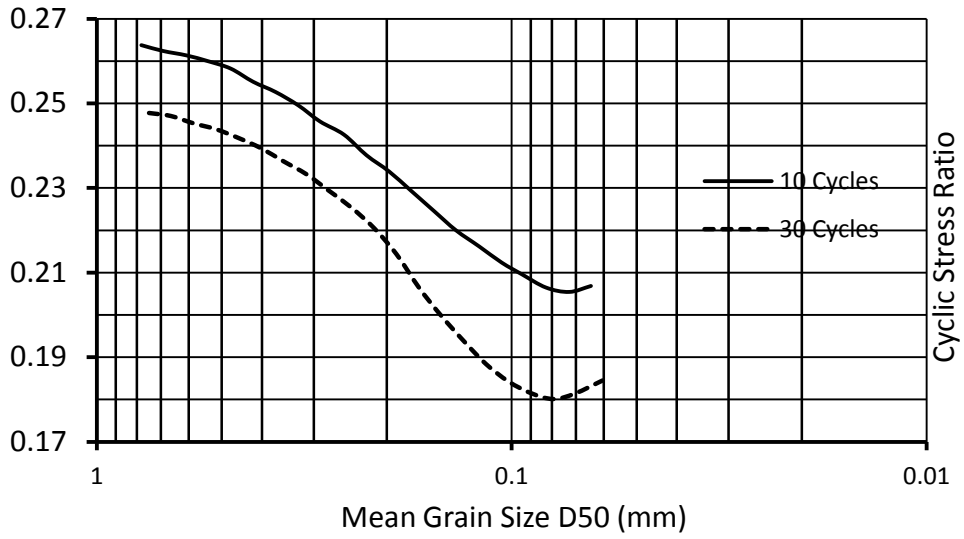

Fig. 2.6 Stress ratio causing liquefaction of sands in 10 and 30 cycles (after Das and Ramana, 2011)

Sitharam et al. (2012) performed cyclic strain controlled laboratory triaxial undrained tests on sand samples collected at Ahmedabad City of Gujarat (India) to study the factors controlling the liquefaction potential and pore pressure generation. Base sand, clean sand and sand with non-plastic fines were tested using cyclic strain controlled triaxial undrained tests for different combination of shear strain amplitudes, initial effective confining pressure and relative density (R_D).

Vaid and Sivathayalan (2000) presented a detail study on Fraser River sand using different sample preparation methods. The sample preparation method at a given initial void ratio and stress state has a considerable effect on the strength of the sample. It was also concluded that moist-tamping samples resulted in a very strain softening response; the strength ultimately reached the steady state. The air-pluviated specimen demonstrated a quasi steady state type response due to lesser extent of strain softening. However, for the range of relative densities and soil types investigated, water-pluviated sample behaved in a strain-hardening (dilative) manner, having no sign of strain softening. Therefore, the sample preparation method has considerable influence on the cyclic resistance of soils. Wijewickreme et al. (2005) found that specimens reconstituted by the water-pluviation had higher cyclic strength as compared to the specimen prepared by air-pluviation for Fraser River sand. Jafari-Mehrabadi (2006)

also documented the details about the effect of sample preparation method on liquefaction strength of soil.

Liyanapathirana and Poulos (2004) investigated the influence of nature of the earthquake on the evaluation of liquefaction potential of a granular deposit during seismic loading. The pseudo-velocity (V) is used as a parameter for defining the nature of earthquake which is defined as the gross area under the acceleration record of the earthquake at a given depth below the ground surface. A simplified method has been proposed to evaluate the liquefaction potential of a soil deposit based on the pseudo-velocity after analyzing a different type of earthquake records from different locations of the world. Jakka et al. (2010 a, b) reported the liquefaction behaviour of pond ash by conduction cyclic triaxial tests. The authors observed that the developed correlation between SPT (N) and shear velocity is significantly different than the correlation reported for the soils. Kamatchi et al. (2010) proposed a methodology which enables the calculation of realistic values of inelastic base shear and corresponding displacement of a building for site-specific earthquakes by considering the actual characteristics of soil stratum.

b) Cyclic Simple Shear Test

Peacock and Seed (1968) was the first who performed liquefaction analyses of clean uniform Monterey, California, sand using cyclic simple shear apparatus. It was observed that the cyclic stress required to cause initial liquefaction under triaxial conditions was considerably higher than the cyclic stress required to cause initial liquefaction under simple shear conditions. Prakash, (1981) conducted a simple shear test under cyclic conditions to reproduce this type of deformation conditions in the laboratory. However, it may also be approximately reproduced by the cyclic triaxial compression tests. Vaid and Sivathayalan (1996) and Riemer and Seed (1997) discussed some relationship between the liquefaction resistance of sands evaluated from triaxial tests and simple shear tests. Vaid and Sivathayalan (1996) reported that the ratio (C_r) between cyclic resistance in simple shear and that in cyclic triaxial test depends on the soil relative density and the confining stress level. For a given confining pressure and specific relative density, the *CSR* required to cause liquefaction was reported smaller under simple shear than that under triaxial condition. It was found that at a relative density of 40%, C_r was about 0.78 irrespective of the confining stress level.

However, at the dense soil (R_D = 72%) it varies between 0.62 and 0.7 when the confining pressure increases from 50 to 400 kPa.

Yoshimine et al. (1999) measured the undrained shear strengths in the laboratory for clean Toyoura (Japan) sand. Later, these results were compared with field performance data. Tatsouka et al. (1990) had given a correlation which was used for converting the soil relative density to equivalent cone resistance (q_{cN}). It was observed that the behaviour of clean Toyoura sand in simple shear was consistent with the field performance observations. The undrained shear strength is overestimated in triaxial compression tests and underestimated in triaxial extension tests.

Ishihara and Yoshimine (1992) established a family of curve using direct Shear test results in which the volumetric strain resulting from dissipation of pore pressure was correlated with density of sand and normally used to estimate factor of safety against liquefaction.

The other laboratory test used for studying the undrained behaviour of sand is the hollow cylinder torsional shear test. Prevost and Popescu (1996) discussed that the laboratory soil samples exhibits a large scatter due to errors associated with the disturbance of sample (during sample collection, transportation and preparation), spatial variability of soil properties in natural deposits, testing errors, results in affecting its reliability. In spite of all these facts, laboratory tests are still very useful tools for assessing soil liquefaction potential.

2.4 PREDICTION OF SOIL LIQUEFACTION

All the empirical methods described above, such as 'simplified procedure' are useful for assessing the soil liquefaction. But, neither of these methods (based on field test data) is able to consider the effect of EPP redistribution due to dissipation, nor they are able to evaluate the amount of deformation for a soil deposit. The deformation can be calculated by performing some type of dynamic analysis. There are several methods are available which predicts soil liquefaction and deformation, considering EPP redistribution. These methods for predicting liquefaction can be roughly divided into two groups:

a) Physical modeling

b) Numerical modeling (Finite Element Methods)

2.4.1 Physical Modeling

The most commonly used physical modelling methods used for predicting soil liquefaction are the shake table test and centrifuge test. These methods are discussed in more details in following section.

Shake Table Test

This method also known as 1-g shake table test. Soil is placed in a tank resting upon a shake table. Seismic motion is applied to the base of the table. Liquefaction susceptibility of the soil is observed for certain level of acceleration using this method (Prakash and Gupta 1970, Finn et al. 1971, Arya et al. 1978, Krishna and Latha 2007, Maheshwari et al. 2012).

Prakash and Gupta (1970) concluded that in case of coarse sands pore pressure start dissipating immediately on attaining a maximum value which shows that chances of large movements are less, but in case of fine sand possibility of large movement is more because pore pressure developed remains constant for some time and then dissipates slowly whereas liquefaction potential reduces with increase in relative density. Fine sands get liquefied at small acceleration.

Krishna and Latha (2007) performed shake table study on geotextile-reinforced wrap-faced soil-retaining walls. It was observed that the response of the wrap-faced soil-retaining walls is highly influenced by the base acceleration levels, frequency of shaking, and quantity of reinforcement and magnitude of surcharge pressure on the crest. The effects of these different parameters on acceleration response at different elevations of the retaining wall, horizontal soil pressures and face deformations were also presented.

Maheshwari et al. (2012) performed shake table test on sand samples having R_D = 25%, with and without reinforcements. The main parameters like maximum pore pressure (U_{max}), time required to built-up U_{max} and dissipation time were measured at different levels of accelerations ranging from 0.1–0.4 g. It was noted that the liquefaction resistance of sand reinforced with synthetic and coir fibers has been increased.

Centrifuge Testing

Centrifuge modeling has been considered among the best experimental methods for modeling and observing soil liquefaction phenomena. It creates stress conditions in the model which closely simulate those in the full-scale prototype (Alam 2005, Alam et al. 2005, Dewoolkar et

al. 2007). During last three decades, centrifuge modelling has been gaining popularity in liquefaction response analysis. One of the major research project VELACS (Verification of Liquefaction Analysis by Centrifuge Studies) was funded by National Science Foundation. Researchers from various universities and industries were actively involved on that project. The VELACS project showed the effectiveness of centrifuge tests for studying the effects of earthquake loading in cohesionless soil (Arulanandan and Scott, 1993). Jafari- Meharabadi (2006) presented a study on mitigation measures of liquefaction, based on eight centrifuge tests and subsequent numerical modeling. Madabhushi and Schofield (1993) remarked that for the characteristic frequency of the system higher than the predominant frequency of input seismic motion, characteristic frequency reduced during vibration to a value close to the predominant input seismic frequency due to subsequent degradation of soil stiffness and build up of excess pore pressure.

The response of 4 model cantilever retaining walls supporting granular liquefiable backfill in centrifuge experiments were presented by Dewoolkar et al. (2000, 2001). Experimental study highlighted contribution of EPP to seismic earth pressure. Dynamic increment in lateral thrust was well interrelated to EPP but independent of wall stiffness. The dynamic lateral thrust was observed to act between 0.6 and 0.8 of the wall height.

Hausler (2002) discussed the numerous advantages and disadvantages of using centrifuge as a tool in geotechnical earthquake engineering. It was reported that a small scale model which actually represents a large soil deposit in a prototype scale can be easily monitored in earthquake motion. So, it is efficient, cost effective and less laborious as compared to full scale testing. Direct observation is also possible for modes of failure and deformation. It is also much easier to identify new failure modes and mechanisms using centrifuge tests. A series of unnecessary seismic waves might be generated by the reflection of seismic waves at each end wall of the prototype box which reflected back by the opposite side wall. This may stimulate different behaviour in the model irrespective of the field condition. It could be reduced by placing softer material like Duxseal at boundary wall of the box to behave like viscous boundaries.

2.4.2 Numerical Modeling

Physical modeling and centrifuge modeling for liquefaction predictions are time consuming and expansive. Attempts were made to develop different numerical procedures to simulate

and predict soil liquefaction utilising the advanced computation facility available nowadays. For a highly nonlinear behaviour, like in the case of saturated soil under earthquake loading, these numerical simulations are very useful and cost-effective. Based on the type of mathematical formulation and the techniques of solving, they are broadly classified as coupled, partially-coupled and uncoupled analyses.

To calculate the responses more accurately, these numerical models should be calibrated and validated first, based on centrifuge tests. One of the largest studies for finding the effectiveness of these numerical models was the VELACS, sponsored by the NSF between 1991 and 1993. Some of the numerical models used in the VELACS project were: Dynaflow (multi yield plasticity model), DIANA-SWAN, SWANDYNE (Generalised plasticity model), DYSAC2, LINOS, SUMDES (bounding surface model), LIQCA (classical plasticity) and QUAD4 (total stress) (Arulanandan and Scott, 1993). Ganesalingam et al. (2013) analyzed the influence of initial pore pressure distribution on the consolidation response of a cylindrical soil layer analytically using a simple series solution method and by finite-element analysis using PLAXIS.

Uncoupled Analysis

Numerical simulation using uncoupled analysis is done to evaluate displacements and volumetric strains. Then these results are utilized further to compute excess pore pressure. The effectiveness of this type of analysis depends on the strong interdependence between phenomena so that they considerably influence each other during dynamic loading. If the strong interdependence does not exist in between them, then an uncoupled analysis may present sensible predictions of behaviour of soil mass during cyclic loading.

Newmark's method is one of the common methods used for time history analysis. SHAKE (one dimensional) or QUAD4 (for two-dimensional case) are two main programs used widely for simulating liquefaction phenomenon in uncoupled way. The yield criterion is based on limit equilibrium analyses potential sliding surface with degraded soil properties of the soil mass.

The part of the average acceleration record greater than the yield value is double integrated to evaluate lateral displacement of the surface with minimum yield acceleration (Cooke, 2000).

Martin et al. (1975) proposed a densification model for liquefaction. In saturated sand, if drainage is not allowed to occur during the loading stage, the tendency for contraction during

cycles of loading leads to a progressive increase in excess pore pressure. This model is based on the assumption that the permanent volumetric strain occurs during one cycle of uniform shear strain in an undrained simple shear test and the total volumetric strain in a drained simple shear test are equal.

Finn et al. (1977) emphasised to consider the different parameters while computing the behaviour of saturated sand layers subjected to a seismic loading. These key parameters were initial in-situ shear modulus, the variation of shear modulus with shear strain, simultaneous build-up and dissipation of pore pressures, changes in effective mean normal stress, hardening and damping.

Chern and chang (1995) developed a mathematical model for accessing liquefaction characteristics of soil subjected to earthquake induced cyclic loading based on cyclic triaxial results. This model was able to predict cyclic shear strength, number of cycle require for causing liquefaction and generation of excess pore pressure. White and Zaman (1998) and Li et at. (2000) derived a porous media model describing the accumulation and flow of fluid within a domain which consists of a differential expression determining the saturated fluid sub domain and a relation describing the pressure distribution within that domain.

Liyanapathirana and Poulos (2002) proposed numerical model based on effective stress. This model can be used to get excess pore pressure and reduction in shear strength due to seismic loading. The pore pressure generation is evaluated using the equivalent cycle pore pressure model proposed by Seed et al. 1976. One of the main advantages of the proposed model is that it requires few model parameters in comparison with other ground response analyses.

Jaya et al. (2008, 2012) presented the seismic response analysis of deeply embedded ventilation stack incorporating the effects of SSI (soil–structure interaction). Site-specific design ground motion was applied to the finite element domain. Specific charts were developed from laboratory tests for site-specific modulus reduction and damping ratio. These charts were employed to simulate nonlinear behaviour. Results highlighted strong correlation of site relative stiffness and the soil layer depth. Similar study was extended to study the effects of SSI on seismic response of a deeply embedded Nuclear Island Building.

Zheng and Luna (2011) presented a nonlinear soil model to examine the effect of the deep soil deposit and liquefaction on ground response. This soil model is based on input ground motion and soil properties from laboratory test as input parameters. These parameters have been obtained from usual in-situ and laboratory tests. The author implemented the model to

examine the ground response analysis for a typical Missouri highway bridge site. The effect of liquefaction and the deep soil deposit on the ground response analyses was reported.

Partially-Coupled Analysis

The partially-coupled analysis considers the partial interactions between the solid and fluid media in a simplified way. The equations of stress equilibrium are solved for unknown displacements. Then plastic components of volumetric strains are obtained from shear strains which are used to derive the generated excess pore pressure. These steps are performed at every time step. The partially coupled analyses tend to use less complex soil models and easily obtainable soil properties. But, sometime these assumptions may result in inaccuracies in expected behaviour (Cooke, 2000). The literature reported variable success ratio using the partially coupled approach for evaluating the behaviour of liquefiable soil. Puebla et al. (1997) successfully implemented the UBCSAND constitutive model in FLAC to predict the generated excess pore pressure and deformations in liquefiable sand below an embankment. Finn (1988, 1991) also successfully validated the results obtained by TARA-3 with centrifuge studies results.

Lo'Pez-Querol and Bla´ zquez (2007) presented a unified liquefaction constitutive model considering endochronic theory. The constitutive model considers contractive and dilative behaviors' along with soil collapse. A 2-D coupled finite element code CMLIQ (Cyclic Mobility and Liquefaction) was developed. The predictions from the numerical model were checked with centrifuge tests experimental results for successful validation.

Andrianopoulos et al. (2010) developed a new plasticity model for the simulation of monotonic and cyclic loading of cohesionless soils. This model is implemented in FLAC using its User-Defined-Model (UDM). It incorporates bounding surface plasticity model assuming Critical State Soil behaviour with a vanishing elastic region to incorporate the non-linear soil response. A number of parametric analyses were performed to evaluate the earthquake-induced liquefaction. The accuracy and computational cost is noted with the successful prediction of centrifuge test prediction in the VELACS project.

Oka et al. (2012) presented numerical study on evaluation of liquefaction potential of granular soils below embankment using QUAKE/W program. Based on the computed normal and shear stresses, a methodology is suggested to account for the additional stresses (generated due to presence of embankment) in the application of cyclic stress method. Dashti

and Bray (2013) incorporated UBCSAND model in FLAC-2D to validate the results obtained from centrifuge experiments of structures with shallow foundations on liquefiable sand. The soil model was able to capture the impact of deviatoric displacements and volumetric strains under partially drained condition. One limitation was noticed for the case of slower rates of earthquake energy application. The extent of soil softening and accumulated displacement was overestimated four times.

The results obtained from numerical simulation either by partially-coupled or uncoupled solution is not completely in order with the results of VELACS project. This shows that some other numerical tool based on finite element scheme or coupling methology of porous media can perform better. Different types of available finite element analysis techniques are briefly discussed here.

Coupled Analysis

In coupled numerical analysis the analysis domain, such as a liquefiable soil deposit, is expressed by coupled field equations. These equations are solved by considering coupling between solid and fluid phase under dynamic loading (inertial coupling is an added advantage). A fully-coupled effective stress analysis accounts for the dynamic interaction between the solid and fluid phase. Resulting dynamic equilibrium equation and flow continuity equation are solved simultaneously. Various researchers have studied the effectiveness of different fully coupled finite element codes for predicting the response of saturated soil under dynamic loading.

Finite Element Method is a sound numerical procedure. Thus, it is possible to transform the mixture theory in the regime of elastoplastic nonlinear constitutive models for evaluating the consistent solutions of displacements and pore pressure.

First of all, Sandhu and Wilson (1969) started finite element method to study flow through saturated porous media. A variational principles approach has been incorporated into the dynamic stress equilibrium and continuity equation for a fully saturated soil. Resulting coupled equations are solved numerically using finite element approximations.

Ghaboussi and Wilson (1972) applied variational approach to the Biot's dynamic field equations for saturated porous elastic media in the regime of finite element formulation. This formulation has considered the compressible nature of solid and fluid phases to simulate dynamic soil-structure interaction and wave propagation studies in saturated soils.

Prevost (1980, 1982) discussed the multiphase formulation of porous media. The extended Biot's theory with nonlinear elastic model was integrated to investigate the transient response of soil deposits. The two-phase saturated porous medium is defined by the stress, acceleration, velocity and displacement fields within each phase. Finite element method is used to solve numerically the coupled equation of mixture's theories. Accuracy and adaptability of the proposed procedure is verified by comparing responses of various initial value problems, pseudo-static and dynamic studies.

Zienkiewicz et al. (1984, 1999) summarized different analysing methods on numerical simulation of the Biot-type formulation. Later, the numerical solution has been applied to study the undrained, drained and dynamic behavior of saturated porous media.

Popescu and Prevost (1993) presented a validation of a numerical model based on multiyield plasticity theory by using results of centrifuge model soil tests (VELACS). The model parameters were estimated from the results of conventional laboratory tests with numerical correlation formulae. A unique set of constitutive parameters were suggested to be used in the numerical simulation.

Oka et al. (1994) formulated an easy and realistic numerical approach for prediction of liquefaction response using *u*-*p* formulation (*u*-displacement of the solid phase and *p*-pore pressure). Finite element method is applied for stress equilibrium equation over the domain represented by number of elements. The finite difference method is employed for the spatial discretization of the continuity equation to define the pore pressure at the center of the each element. An elasto-plastic constitutive model which incorporate non-linear kinematic hardening rule is developed to illustrate the stress-strain behavior of loose sand subjected to cyclic loading. The validation of the proposed model is done by comparing the numerical response with analytical solutions for the transient response of saturated porous solids.

Madabhushi and Zeng (1998) simulated the response of gravity quay walls subjected to seismic load using coupled finite element code SWANDYNE. A new numerical technique is used to model the absorbing boundaries, used for simulation of the free field condition in the centrifuge experiments. The initial displacement and velocity induced in centrifuge model were properly considered in the numerical analysis. The results obtained from numerical study were in good agreement with centrifuge results in dry as well as saturated condition.

Cooke (2000) presented the fully-coupled analyses for considering the fluid-solid interaction and highlighted importance of some key parameters. These parameters along with the overall soil mass behaviour might be difficult to evaluate in the analysis.

Oka et al. (2002) incorporated finite deformation theory considering a cyclic elasto-plastic model for prediction of liquefaction response. Both *u-p* formulation and *u-w-p* formulation (displacement - relative fluid displacement – pore pressure) were assumed with efficient Lagrangian FEM method to study efficiency of *u-w-p* formulation. It was observed that the *u-w-p* formulation is essential for highly permeable soils during earthquake with comparatively high frequency.

Zhang (2003) proposed an advanced nonlinear computational model and implemented with OpenSees software to analyze the soil-structure-foundation domain of Middle Channel Bridge. The model demonstrated a simplified and better explanation of the seismic excitation along the boundaries of the soil domain. The computational procedure was applied to simulate the seismic response to examine the effects of soil nonlinearity with lateral spreading.

Byrne et al. (2004) presented a numerical model which is based on effective stress approach. This model is used to validate the centrifuge test results. A lack of full saturation and densification at any depth due to the application of the high-acceleration level in centrifuge study were mostly responsible for the apparent limitation on liquefaction at that particular depth.

Snieder and Beukel (2004) introduced liquefaction cycle as a framework to define the coupled phenomena usually takes place in fluid-saturated granular soil, result to liquefaction. The numerical implementation of the liquefaction cycle evaluated that the scale analysis is unreliable in case of the presence of strong spatial variations in the permeability which restrain fluid migration. The numerical model was applied to enumerate the effect of a relatively low-permeability layer on the liquefaction behaviour of soil deposit.

Jafari-Meharabadi (2006) used DYNAFLOW for the successful simulation of eight centrifuge tests for finding the seismic liquefaction countermeasures of waterfront slopes. Popescu et al. (2006) provided a finite element implementation of the extension of Biot's theory of porous media for dynamic behavior of saturated loose sand considering nonlinear behaviour. Two numerical applications involving the seismic behaviour of saturated soil

deposits were discussed. The dynamic interaction between structure and liquefying soil was examined in the first application, whereas the second numerical application considered the liquefaction of stochastically spatially variable soils. The dependency of the characteristic frequency of the domain on was highlighted.

Taiebat et al. (2007) developed a fully coupled dynamic algorithm based on *u–P* formulation to evaluate the liquefaction potential of saturated sandy deposits. Coupled equations were integrated in time domain using generalized Newmark method. A critical state two-surface plasticity model and a densification model were considered to characterize soil behaviour. The generation of pore pressure was in agreement with centrifuge test observations in case of the critical state two-surface plasticity model.

Jeremic et al. (2008), Taiebat et al. (2010) presented simulation of pore fluid and soil skeleton responses using fully coupled dynamic field equations with $u- p-U$ formulation. This model also takes in to account water accelerations (U) in the analysis. This model is functional in modeling dynamic interaction between media of different stiffnesses such as in soil–foundation–structure interaction. The verification and validation issues corresponding to fully coupled modeling of saturated porous media were also explored to predict the response of horizontal and sloping grounds under earthquake excitations.

Dewoolkar et al. (2009) simulated the two centrifuge experiments on the similar type of cantilever retaining wall model having liquefiable backfill with using DIANA–SWANDYNE II program. Code is based on Biot's formulation. The parameters of the Pastor–Zienkiewicz mark III constitutive model used in the dynamic simulations of the soil were obtained from the back-analysis of centrifuge test on horizontal-ground model. Predictions for total earth pressure and its point of application, excess pore pressure, deflection and bending strains of the wall, were in reasonable agreement. On the other hand estimated values of backfill displacements and accelerations were less reasonable.

Shahir and Pak (2010) presented a three-dimensional coupled dynamic analysis to discuss the dynamic behaviour of shallow foundations on liquefied soils. Simulation of the proposed numerical model is verified and validated with the results of centrifuge experimental measurements. A sensible relationship was proposed for assessment of liquefaction-derived displacement of a rigid footings resting on homogeneous loose to medium fine sand. A comprehensive parametric study was also carried out for some key parameters.

Bao and Sture (2011) proposed a fuzzy set plasticity theory based cyclic constitutive model, which can model dilatancy effect during seismic loading. A numerical study was carried out and the results were compared with centrifuge experimental data of liquefied sand. The suggested model efficiently captures the features of rise in pore pressure and consequent reduction in strength during cyclic loading. A good match in between numerical study and the centrifuge results illustrated that the fuzzy set model is an efficient tool for evaluating liquefaction potential.

Shan et al. (2012) developed the exact solutions to one dimensional transient analysis of incompressible saturated single layer porous media under four types of boundary conditions based on the Biot's theory of porous media. A relation between the solid displacement *u* and the relative displacement *w* was derived, and the well-posed initial conditions and boundary conditions were proposed.

Taiyab et al. (2010) presented numerical simulation of granular soil under cyclic loading using finite element code based on coupled analysis. A comparison between of numerical study using finite element code and shake-table study was discussed with respect to the mitigation of quay wall damage during earthquake (Taiyab 2011, Taiyab et al. 2014). Densifying the loose sand near toe is one of the ways to prevent damage. It was concluded that the displacement of a quay wall took mainly due to shear strain in the foundation and the densification of soil at the toe was effective in mitigation of the quay wall damage significantly.

Based on the available literature it has been observed that partially or fully coupled finite element computer codes have been able to predict the measured behaviour of liquefiable soils successfully. The percentage of success seems to be dependent on the type of problem analyzed in some particular cases. Therefore, a numerical code should be critically selected after examining its ability to predict the liquefaction behaviour for the range of applied conditions.

2.5 CRITICAL APPRAISAL

Based on the above review of literature, following observations are made.

1. To understand the phenomena of liquefaction, mainly two types of approaches have been studied in the past: empirical approach based on in-situ and experimental test

data of soil samples and modeling of field conditions where liquefaction is known to have occurred in past.

2. In the earlier study, undrained cyclic laboratory tests had been mainly used to access the liquefaction potential of a soil mass but due to difficulties in collecting undisturbed samples of loose sandy soils, whereas most of the researchers have preferred to use in situ tests such as SPT, CPT, BPT and shear velocity results.
3. Empirical field-based methods for determining liquefaction potential have two critical constituents: i) The analytical framework to systematize past experiences, and ii) An appropriate in-situ index which could be able to represent the soil liquefaction characteristics. The original simplified procedure proposed by Seed and Idriss 1971 for estimating earthquake-induced cyclic shear stresses is still to be necessary component of the empirical and semi-empirical analysis framework. The various parameters of this framework are redefined to include improvements in the in-situ index tests (e.g., SPT, CPT, BPT, V_s) and the liquefaction/no-liquefaction cases are complied accordingly.
4. In a semi-empirical approach, experimental results and the theoretical approach combined together to provide the more confidence in the response analysis of liquefaction phenomenon. It is used to interpolate or extrapolate to areas with inadequate field data to restrain a solely empirical solution.
5. Due to errors associated with the disturbance of sample during sample collection, transportation and preparation, the laboratory soil samples results in affecting its reliability. Despite this, laboratory tests are still very useful method for evaluating soil liquefaction potential.
6. A fully coupled dynamic approach to model the liquefaction phenomena occur in loose sand, has been discussed by many researchers. They have generally used Coupled dynamic field equations and continuity equation of extended Biot's theory to conclude the responses of pore fluid and soil skeleton.
7. Liquefaction and spreading problems is frequently related with semi – infinite soil domain. However, in general the finite element modelling only satisfies the boundary displacement conditions of finite domains.

8. A number of terminologies, methods and procedures to study the response of liquefaction phenomena have been proposed, and a reliable approach has been slow to come out.

2.6 CONCLUDING REMARKS

1. Before 1975, dynamic analysis of geotechnical engineering problems was based on mainly total stresses approach because of unavailability of the practical models which can predict pore pressures.
2. Most of the researchers have presented the analysis of liquefaction based on empirical approach (generally Seed's Cyclic Stress Approach), whereas very few researchers have presented the numerical analysis with uncoupled approach.
3. Methods based on empirical relation are not able to evaluate the amount of soil deformation and the effect of EPP redistribution due to dissipation.
4. The results obtained from numerical simulation either by partially-coupled or uncoupled solution is not completely in order with the results of VELACS project. This shows that some other numerical tool based on finite element scheme or coupling methodology of porous media can perform better.
5. The uncoupled approach is not able to take into account the progressive stiffness degradation caused by the increase in pore pressures in the soil mass. Only coupled approach model is able to consider the gradual loss of soil strength due to build-up of pore pressures.
6. For spatially unbounded seismic problems, the finite outer boundaries are problematic because undesired spurious reflections are usually generated; especially when the medium is elastic or little material damping takes place in nonlinear constitutive model formulations.
7. Undesired reflections affect the numerical simulation results and should be omitted from the calculations. The desired boundary should ideally be radiating to outgoing waves and transparent to incoming waves. Hence the boundary should be properly modelled using coupled kelvin element and finite-infinite element coupled element.

The liquefaction problems involve a different type of complexity in its solution algorithm due to several issues. The solution algorithm has to consider the various aspects like, soil-fluid interaction, sudden phase transition from solid to liquid behaviour, nonlinearity of responses,

material instability, and limitations in experimental and numerical investigations. Due to this reason, development of reliable and accurate predictive methods for analysing the occurrence and simulation of the liquefaction phenomena has been still a great challenge for the researchers and academicians. Based on the above aspects, the present study has been directed towards to model liquefaction behavior and mitigation in a saturated soil system during cyclic and seismic excitation. A detailed study is presented in subsequent sections.

CHAPTER - 3

FINITE ELEMENT IMPLEMENTATION

3.1 DYNAMICS OF POROUS MEDIA

Saturated soils and other two phase media has been the subject of investigation, both experimentally and numerically over last five decades. The interaction between soil and fluid under cyclic loading may lead to rise in pore pressure, which may result in softening of material and reduction in shear strength. Pore pressure build-up and its dissipation have significant impact on the response of geotechnical engineering problems. Attempts are made to predict development and dissipation of pore pressure. Pore pressure associated with pile driving results in lower initial pile capacity. However pile-setup mechanism gets developed with dissipation of pore pressure resulting increase in pile capacity (Sawant et al. 2013). Ganesalingam et al. (2013) analyzed the influence of initial pore pressure distribution on the consolidation response of a cylindrical soil layer analytically using a simple series solution method and by finite-element analysis using PLAXIS. Similarly, Sivakugan et al. (2014) predicted post-construction settlements by assuming a sinusoidal initial pore water pressure distribution at the end of the construction period applied instantaneously. Pore pressure rise during blasting and earthquake may develop in saturated soils causing reduction in effective stress. In the extreme situation, the shearing resistance of soil may reduce to zero and behaves like a viscous fluid. This phenomenon is known as ‘liquefaction’. Liquefaction takes place often in saturated loose sands under earthquake and impact loadings. Loose sands are vulnerable to compaction under dynamic loading. The potential consequences of liquefaction can be illustrated by the near collapse of the Lower San Fernando dam near Los Angeles during the 1971 earthquake.

The example quoted above involved the interaction of pore pressure and the soil skeleton which results in the ‘weakening’ of soil-fluid composite during earthquake. During the motion, the interstitial pore pressure increased, thus reducing the inter-particle forces in solid phase of the soil and causing a loss of strength (Pastor et al. 2000). A quantitative prediction of the phenomena leading to permanent deformation or unacceptably high build-up of pore pressures is therefore essential to guarantee the safe behaviour of structures. In the analysis of

such dynamic behaviour, the usual decoupled and factor of safety approach may not be most appropriate.

A general theory of three-dimensional deformation of porous fluid-saturated media was first proposed by Biot (1941). Later, Biot (1956) extended this quasi-static theory to wave propagation in saturated geological media. For an isotropic saturated porous medium, Biot (1956) proposed the kinetic energy of the soil-fluid mixture to be quadratic in velocities of the solid and fluid and included a coupling term. The dissipative function was postulated to be quadratic in relative velocity. For constitutive equations, Biot (1941, 1956) stated that there exists an energy function quadratic in solid strain and change of water content (fluid strain). The work of Biot received great attention and has been widely used (Deresiewicz 1960, Deresiewicz and Rice (1962), Paul 1976, Derski 1978, Zienkiewicz and Shiomi (1984), Simon et al. 1986, Halpern and Christiano (1986), Chan et al. 1988). Eventually, this coupled formulation was extended to implement different developed constitutive models in a 2-D finite element program (Abifadel 1991, Ragheb 1994, Parra 1996, Ardino et al. 2001, Yang 2000, Nair et al. 2005).

Mixture theories based on the principles of mechanics were developed by Green and Naghdi (1965). These theories were applied to model the dynamics of fluid-saturated solids (Garg 1971, Morland 1972, Garg et al. 1974). Morland (1972) first used the concept of volume fraction in modern mixture theories to explain the behavior of porous media. Bowen (1982) summarized all findings of the mixture theory and applied the concept of the volume fractions for saturated porous media.

In the present study, a fully coupled formulation is proposed for modelling liquefaction phenomena using Biot's theory (Biot, 1941), which can predict displacement as well as generation and dissipation of excess pore pressure.

3.2 FINITE ELEMENT FORMULATION

The Biot formulation provides a mathematical description of physical behavior which can adequately describe the transient behaviour of saturated soil for most geomechanics applications, except notably fast pile driving and explosive events. The basic equations for the Biot formulation are:

i) The equilibrium equation of the soil-pore fluid mixture.

ii) The equilibrium equation for the pore fluid which is a generalization of the Darcy's equation to include the acceleration of the soil skeleton.
iii) The conservation of mass for the pore fluid.
iv) The concept of effective stress.
v) The constitutive equation.

In dynamic analysis, a fully drained calculation assumes no change in pore pressure occurred, usually on the basis that permeability is high. However, a high permeability may lead to a high fluid velocity which, in turn, would be accompanied with a high fluid acceleration. The high level of fluid velocity and acceleration would introduce substantial changes in pore pressure and invalidate the original assumption of the calculation.

On the other hand, a fully undrained calculation during earthquake shaking could be justified for soils with relatively low permeability such as silt and clay, but not in the case of sand, where drainage can be substantial during the short duration of seismic activity. Furthermore, this assumption of no drainage breaks down during the consolidation stage. To obtain a correct spatial distribution of permanent settlement, the build-up, the redistribution and drainage of the pore pressure has to be as accurate as possible.

In a completely coupled formulation, three conditions of equilibrium or momentum balance must be satisfied. These include momentum balance for the soil–fluid mixture, momentum balance for the fluid phase alone, and finally mass balance for the soil-fluid system. As a consequence, the pore pressure of fluid (p) will be treated as an additional unknown other than displacements of solid and fluid phase (u, u_f). It is observed that the relative velocity of fluid has negligible impact on the system for dynamic problems in which high-frequency vibrations are not significant (Zienkiewicz et al. 1999). So these can be eliminated. Eventually, the equations for fluid momentum balance and mass balance can be combined together resulting two governing equations with solid displacement (u) and fluid pressure (p) as the primary variables. This form is known as u–p formulation. The presence of the solid acceleration in the fluid momentum balance equation will affect the non-symmetric equations and may result unstable solutions in some situations (Park, 1983).

3.2.1 *u–p* formulation

The theory of effective stress of the saturated soil mass is described by the relationship between effective stress, total stress and pore pressure. Zienkiewicz et al. (1999) postulated the relationship as $[\sigma'] = [\sigma] - \alpha [\delta] p$, where $[\sigma']$ and $[\sigma]$ are effective and total stress tensors, respectively. $[\delta]$ represents Kronecker delta and α is Biot constant depending on the geometry of the voids. In most of the cases, value of α can be approximated to unity and this leads to the classical effective stress definition (Terzaghi, 1943) as $[\sigma'] = [\sigma] - \alpha [\delta] p$.

The final momentum balance equation for the soil-fluid system can be expressed in two dimensional Cartesian co-ordinates as:

$$\begin{aligned} \frac{\partial \sigma_{xx}}{\partial x} + \frac{\partial \tau_{xz}}{\partial z} + \rho g_x - \rho \ddot{u}_x - \rho_f \ddot{w}_x = 0 \\ \frac{\partial \tau_{xz}}{\partial x} + \frac{\partial \sigma_{zz}}{\partial z} + \rho g_z - \rho \ddot{u}_z - \rho_f \ddot{w}_z = 0 \end{aligned} \tag{3.1}$$

In which, σ_{xx} and σ_{zz} are normal effective stresses (tensile positive) acting on the soil and pore pressure p (compression negative) for the fluid in the pores, g_x and g_z are the body acceleration, ρ is the average density of the soil-fluid system, ρ_f is the fluid density, u_x and u_z are the displacement of the soil, and $\ddot{w}_x$, $\ddot{w}_z$ are the averaged relative fluid acceleration. For saturated soil, average density is related to density of soil-solids ρ_s and density of water ρ_f as $\rho = \eta \rho_f + (1-\eta)\rho_s$.

Equation (3.1) can be written in matrix form as:

$$\begin{bmatrix} \frac{\partial}{\partial x} & \frac{\partial}{\partial z} \end{bmatrix} \begin{bmatrix} \sigma_{xx} & \tau_{xz} \\ \tau_{xz} & \sigma_{zz} \end{bmatrix} + \rho \begin{Bmatrix} g_x \\ g_z \end{Bmatrix} - \rho \begin{Bmatrix} \ddot{u}_x \\ \ddot{u}_z \end{Bmatrix} - \rho_f \begin{Bmatrix} \ddot{w}_x \\ \ddot{w}_z \end{Bmatrix} = 0 \tag{3.2}$$

The *u-p* formulation neglects average fluid acceleration.

$$\nabla \sigma + \rho \begin{Bmatrix} g_x \\ g_z \end{Bmatrix} - \rho \begin{Bmatrix} \ddot{u}_x \\ \ddot{u}_z \end{Bmatrix} = 0$$

Applying variational approach,

$$\int \left(u^T \nabla \sigma + u^T \rho \begin{Bmatrix} g_x \\ g_z \end{Bmatrix} - u^T \rho \frac{\partial^2 u}{\partial t^2} \right) dA = 0$$

$$u^T\sigma - \int \nabla u^T \sigma dA + \int u^T \rho \begin{Bmatrix} g_x \\ g_z \end{Bmatrix} dA - \int u^T \rho \frac{\partial^2 u}{\partial t^2} dA = 0$$

Since, $\sigma = D\varepsilon - p = DB\{u_e\} - N^P\{p_e\}$

[*D*] is defined as constitutive relation matrix. [*B*] is strain-displacement transformation matrix. {ε} is strain vector. [B^{P}] is pore pressure transformation matrix. *N* and N^{p} are defined as shape function of displacement and pore pressure respectively. The detail descriptions of these terms in the present pretext are presented in subsequent section.

$$\int u_e{}^T B^T \left(DBu_e - N^P p_e\right) dA + \rho \int u_e{}^T N^T \begin{Bmatrix} g_x \\ g_z \end{Bmatrix} dA - \rho \int u_e{}^T N^T \frac{\partial^2 u_e}{\partial t^2} dA = 0$$

$$\int B^T DB\, dA\{u_e\} + \int B^T N^p dA\{p_e\} - \rho \int N^T \begin{Bmatrix} g_x \\ g_z \end{Bmatrix} dA - \rho \int N^T N \{\ddot{u}_e\} dA = 0$$

$$\int \rho N^T N dA \{\ddot{u}_e\} + \int B^T DB dA \{u_e\} - \int B^T N^p dA \{p_e\} = \rho \int N^T \begin{Bmatrix} g_x \\ g_z \end{Bmatrix} dA$$

$$[M]\{\ddot{u}_e\} + [K]\{u_e\} - [Q]\{p_e\} = \{f_u\} \tag{3.3}$$

In which, { u_e } is the solid displacement vector and { p_e } is the pore pressure vector. {f }$_{\mathrm{u}}$ is the force vector.[*M*], [*K*] and [*Q*] are mass, stiffness and coupling matrices of an element, respectively. These matrices and force vector for an element are given by following expressions:

$$[M] = \int \rho [N]^T [N]\, dA \;\; ; \;\; [K] = \int [B]^T [D][B]\, dA$$
$$[Q] = \int [B]^T \left[N^P\right] dA \;\; ; \;\; \{f_u\} = \int \rho [N]^T \begin{Bmatrix} g_x \\ g_z \end{Bmatrix} dA \tag{3.4}$$

Continuity Equation of the fluid phase

The continuity equation for the fluid phase can be expressed as

$$\frac{\dot{p}}{K_b} + \frac{\partial \dot{u}_x}{\partial x} + \frac{\partial \dot{u}_z}{\partial z} + \frac{d\dot{w}_x}{\partial x} + \frac{\partial \dot{w}_z}{\partial z} = 0 \tag{3.5}$$

In which, K_{b} is the averaged bulk modulus of soil-fluid system, whereas K_{s} and K_{f} are bulk modulus of the soil-solids and fluid defined by the relationship:

$$\frac{1}{K_b} = \frac{1-n}{K_s} + \frac{n}{K_f}$$

The generalized Darcy equation gives relation between fluid velocity and pore pressure as:

$$\begin{Bmatrix} \dot{w}_x \\ \dot{w}_z \end{Bmatrix} = \frac{\upsilon_k}{\upsilon_f \rho_k g_k} \begin{bmatrix} k_{xx} & k_{xz} \\ k_{zx} & k_{zz} \end{bmatrix} \begin{Bmatrix} \frac{\partial p}{\partial x} + \rho_f g_x - \rho_f \ddot{u}_x - \frac{\rho_f \ddot{w}_x}{n} \\ \frac{\partial p}{\partial z} + \rho_f g_z - \rho_f \ddot{u}_z - \frac{\rho_f \ddot{w}_z}{n} \end{Bmatrix} \tag{3.6}$$

where, g_k is gravitational acceleration. Furthermore, υ_k, ρ_k are the viscosity and density of the fluid, at which the permeability is measured, and υ_f is the actual viscosity of the fluid. The permeability tensor consists of k_{xx}, k_{xz}, k_{zx}, k_{zz}. For material with isotropic permeability k (unit = length/time) $k_{xx} = k_{zz} = k \quad and \quad k_{xz} = k_{zx} = 0$:

Eq. (3.5) can be written as:

$$\frac{\partial}{\partial t}\left(\frac{p}{K_b} + \frac{\partial u_x}{\partial x} + \frac{\partial u_z}{\partial z} \right) + \nabla \begin{Bmatrix} \dot{w}_x \\ \dot{w}_z \end{Bmatrix} = 0$$

Applying variational approach,

$$\frac{\partial}{\partial t}\int \left(\frac{p^T p}{K_b} + p^T \varepsilon \right) dA + \int p^T \nabla \begin{Bmatrix} \dot{w}_x \\ \dot{w}_z \end{Bmatrix} dA = 0 \tag{3.7}$$

Substituting the values from Eqs. (3.6) and (3.7), the following equation is derived:

$$\frac{\partial}{\partial t}\int \left(\frac{1}{K_b} p_e{}^T N^{pT} N^p p_e + p_e{}^T N^{pT} B\, u_e \right) dA + \int p_e{}^T N^{pT} \nabla \left[\frac{[K]}{\gamma_w} \begin{Bmatrix} -\frac{\partial P}{\partial x} + \rho_f g_x - \rho_f \ddot{u}_x \\ -\frac{\partial P}{\partial z} + \rho_f g_z - \rho_f \ddot{u}_z \end{Bmatrix} \right] dA = 0 \tag{3.8}$$

$$\frac{\partial}{\partial t}\left(\int p_e{}^T \frac{N^{pT}}{K_b} N^p p_e dA \right) = p_e^T \frac{\partial}{\partial t}\left(\int \frac{N^{pT}}{K_b} N^p p_e dA \right)$$

$$= p_e^T \int \frac{1}{K_b} N^{pT} N^p dA\, \dot{p}_e$$

$$\frac{\partial}{\partial t}\left(\int p_e{}^T N^{pT} B u_e dA \right) = p_e^T \int N^{pT} B\, dA \dot{u}_e$$

$$\int {p_e}^T {N^p}^T \nabla \left[\frac{[k]}{\gamma_w} \begin{Bmatrix} -\frac{\partial P}{\partial x} + \rho_f g_x - \rho_f \ddot{u}_x \\ -\frac{\partial P}{\partial y} + \rho_f g_z - \rho_f \ddot{u}_z \end{Bmatrix} \right] dA = \frac{1}{\gamma_w} {p_e}^T \int {N^p}^T [k] \nabla \begin{Bmatrix} -\frac{\partial P}{\partial x} + \rho_f g_x - \rho_f \ddot{u}_x \\ -\frac{\partial P}{\partial z} + \rho_f g_z - \rho_f \ddot{u}_z \end{Bmatrix} dA$$

$$= \frac{1}{\gamma_w} {p_e}^T \begin{bmatrix} -{N^p}^T [k] \begin{Bmatrix} \frac{\partial P}{\partial x} \\ \frac{\partial P}{\partial z} \end{Bmatrix} + \int \nabla {N^p}^T [k] \nabla N^p p_e dA \\ + \int {N^p}^T [k] \rho_f \nabla \begin{Bmatrix} g_x \\ g_z \end{Bmatrix} dA - \rho_f \int {N^p}^T [k] B \, dA \, \ddot{u}_e \end{bmatrix}$$

Substituting the above terms in Eq. (3.8), the following equation is derived:

$$[G]\{\ddot{u}_e\} + [Q]^T \{\dot{u}_e\} + [S]\{\dot{p}_e\} + [H]\{p_e\} = [f_p] \tag{3.9}$$

In which, $\{f\}_p$ is the force vector for fluid phase, and [*G*], [*S*], and [*H*] are dynamic coupling, compressibility and permeability matrices of an element. These matrices and force vector are evaluated by following expressions.

$$[G]_e = \frac{1}{g} \int [N^p]^T [k][B] dA \quad ; \quad [S]_e = \frac{1}{K_b} \int [N^p]^T [N^p] dA$$

$$[H]_e = \frac{1}{\gamma_w} \int [B^p]^T [k][B^p] dA \quad ; \quad \{f_p\} = \int \rho [N]^T \begin{Bmatrix} g_x \\ g_y \end{Bmatrix} dA \tag{3.10}$$

3.3 TIME INTEGRATION SCHEME

The implementation of dynamic finite element formulation requires an integration procedure for time marching. The procedure is referred to as time integration scheme. If the solution is based on the use of the governing equations at the last time step (known values), the integration procedure is called an explicit time integration scheme. Central difference method is an extensively used explicit method for time marching. Explicit integration method can work without factorization of the stiffness matrix. However, this method is conditionally stable and requires that the time step be smaller than a critical value. The other category of time integration procedure is called implicit time integration scheme, in which the solution is based on the use of the governing equations at the current time step. The effectiveness of the implicit time integration scheme lies in that it is unconditionally stable. Houbolt method, Wilson method, Newmark method and Alpha method are examples of the implicit method.

Selection of proper time integration scheme depends on the range of operating frequencies of the system. The lower frequencies are major concern in most dynamic geotechnical engineering problems, because these modes contribute most to the overall dynamic behaviours. Moreover, at higher frequencies discretization may cause ill effect rather than represent real physical behaviour of the system. Hence, adapted time marching method must have some form of numerical dissipation able to damp out the higher frequencies. At the same time, it should accurately predict the behaviour at low frequency without attenuation. Thus, requirements for a suitable time integration scheme are (1) The scheme should be unconditionally stable (2) The scheme should have the capacity of numerical dissipation which can be controlled by a parameter without altering time step (3) The numerical dissipation should not affect the lower frequency modes considerably. Newmark's method (1959) has been widely used in dynamic analyses of geotechnical engineering problems.

3.3.1 Newmark Beta Method

To evaluate displacements at each time step by solving the incremental dynamic force equilibrium equation, the implicit time stepping method proposed by Newmark (1959) is used. The Newmark-beta method extensively has been used in time-history analysis for prediction of the dynamic response. In 1959, N. M. Newmark developed a family of time stepping methods. Velocity and displacement at current time step are related to displacement, velocity, and acceleration at current and previous time steps using following relationships.

$$\begin{aligned} \dot{u}_{i+1} &= \dot{u}_i + \Delta t \left\{ (1-\alpha)\, \ddot{u}_i + \alpha\, \ddot{u}_{i+1} \right\} \\ u_{i+1} &= u_i + \dot{u}_i \Delta t + 0.5 \Delta t^2 \left\{ (1-\alpha)\, \ddot{u}_i + \alpha\, \ddot{u}_{i+1} \right\} \end{aligned} \tag{3.11}$$

On rearranging and substituting, $\beta = \alpha/2$,

$$u_{i+1} = u_i + \dot{u}_i \Delta t + \Delta t^2 \left\{ (0.5-\beta)\, \ddot{u}_i + \beta\, \ddot{u}_{i+1} \right\} \tag{3.12}$$

Incremental velocity, (from Eq. 3.11)

$$\Delta \dot{u}_i = \dot{u}_{i+1} - \dot{u}_i = \left\{ (1-\alpha)\, \ddot{u}_i + \alpha\, \ddot{u}_{i+1} \right\} \Delta t = \ddot{u}_i\, \Delta t + \left(\ddot{u}_{i+1} - \ddot{u}_i \right) \alpha\, \Delta t$$

$$\Delta \dot{u}_i = \ddot{u}_i\, \Delta t + \Delta \ddot{u}_i\, \alpha\, \Delta t \tag{3.13a}$$

Similarly, $\Delta u_i = u_{i+1} - u_i = \dot{u}_i \Delta t + 0.5 \Delta t^2 \ddot{u}_i + \left(\ddot{u}_{i+1} - \ddot{u}_i \right) \beta\, \Delta t^2$

$$\Delta u_i = \dot{u}_i \Delta t + 0.5 \Delta t^2 \ddot{u}_i + \Delta \ddot{u}_i \, \beta \, \Delta t^2 \tag{3.13b}$$

Multiplying Eq. (3.13a) by $\Delta t/2$ and subtracting from Eq. (3.13b),

$$\Delta \dot{u}_i \, \frac{\Delta t}{2} = \ddot{u}_i \, \frac{\Delta t^2}{2} + \Delta \ddot{u}_i \, \alpha \, \frac{\Delta t^2}{2}$$

$$\Delta u_i - \Delta \dot{u}_i \, \frac{\Delta t}{2} = \dot{u}_i \Delta t + \Delta \ddot{u}_i \left(\beta - \frac{\alpha}{2} \right) \Delta t^2$$

$$\Delta u_i - \Delta \dot{u}_i \, \frac{\Delta t}{2} - \dot{u}_i \Delta t = \Delta \ddot{u}_i \left(1 - \frac{\alpha}{2\beta} \right) \beta \, \Delta t^2 \tag{3.14}$$

From Eq. (3.13a),

$$\Delta \dot{u}_i = \ddot{u}_i \, \Delta t + \frac{\alpha}{\beta \, \Delta t} \left(\Delta u_i - \Delta \dot{u}_i \, \frac{\Delta t}{2} - \dot{u}_i \Delta t \right) \Big/ \left(1 - \frac{\alpha}{2\beta} \right)$$

$$\Delta \dot{u}_i \left(1 - \frac{\alpha}{2\beta} \right) \Delta t = \ddot{u}_i \left(1 - \frac{\alpha}{2\beta} \right) \Delta t^2 + \frac{\alpha}{\beta} \left(\Delta u_i - \Delta \dot{u}_i \, \frac{\Delta t}{2} - \dot{u}_i \Delta t \right)$$

$$\Delta \dot{u}_i \left(1 - \frac{\alpha}{2\beta} \right) \Delta t = \ddot{u}_i \left(1 - \frac{\alpha}{2\beta} \right) \Delta t^2 + \frac{\alpha}{\beta} \Delta u_i - \frac{\alpha}{2\beta} \Delta \dot{u}_i \, \Delta t - \frac{\alpha}{\beta} \dot{u}_i \Delta t$$

$$\Delta \dot{u}_i \, \Delta t = \ddot{u}_i \left(1 - \frac{\alpha}{2\beta} \right) \Delta t^2 + \frac{\alpha}{\beta} \Delta u_i - \frac{\alpha}{\beta} \dot{u}_i \Delta t$$

$$\Delta \dot{u}_i = \ddot{u}_i \left(1 - \frac{\alpha}{2\beta} \right) \Delta t + \frac{\alpha}{\beta \Delta t} \Delta u_i - \frac{\alpha}{\beta} \dot{u}_i \tag{3.15}$$

From Eq. (3.14),

$$\Delta \ddot{u}_i \left(1 - \frac{\alpha}{2\beta} \right) \beta \, \Delta t^2 = \Delta u_i - \dot{u}_i \Delta t - \ddot{u}_i \left(1 - \frac{\alpha}{2\beta} \right) \frac{\Delta t^2}{2} - \frac{\alpha}{2\beta} \Delta u_i + \frac{\alpha}{2\beta} \Delta t \, \dot{u}_i$$

$$\Delta \ddot{u}_i \left(1 - \frac{\alpha}{2\beta} \right) \beta \, \Delta t^2 = \Delta u_i \left(1 - \frac{\alpha}{2\beta} \right) - \dot{u}_i \left(1 - \frac{\alpha}{2\beta} \right) \Delta t - \ddot{u}_i \left(1 - \frac{\alpha}{2\beta} \right) \frac{\Delta t^2}{2}$$

$$\Delta \ddot{u}_i = \frac{\Delta u_i}{\beta \, \Delta t^2} - \frac{\dot{u}_i}{\beta \, \Delta t} - \frac{\ddot{u}_i}{2\beta} \tag{3.16}$$

Similarly, For Pore Pressure terms (Zienkiewicz 1999)

$$\dot{p}_{i+1} = \dot{p}_i + \Delta \dot{p}_i \tag{3.17}$$

$$\Delta \dot{p}_i = \dot{p}_{i+1} - \dot{p}_i$$
$$p_{i+1} = p_i + \dot{p}_i \Delta t + \alpha \Delta \dot{p}_i \Delta t$$

$$\Delta p_i = \dot{p}_i \Delta t + \alpha \Delta \dot{p}_i \Delta t$$
$$\Delta \dot{p}_i = \frac{\Delta p_i - \dot{p}_i \Delta t}{\alpha \Delta t}$$

$$\Delta \dot{p}_i = \frac{\Delta p_i}{\alpha \Delta t} - \frac{1}{\alpha} \dot{p}_i \tag{3.18}$$

Dynamic coupled equations in incremental form are expressed as,

$$[M]\{\Delta \ddot{u}_i\} + [K]\{\Delta u_i\} - [Q]\{\Delta p_i\} = \{\Delta f_{ui}\} \tag{3.19}$$

$$[G]\{\Delta \ddot{u}_i\} + [Q]^T \{\Delta \dot{u}_i\} + [S]\{\Delta \dot{p}_i\} + [H]\{\Delta p_i\} = \{\Delta f_{pi}\} \tag{3.20}$$

Substituting Eqs. (3.16) in Eq. (3.19),

$$\left(\frac{1}{\beta \Delta t^2}[M] + [K]\right)\{\Delta u_i\} - [Q]\{\Delta p_i\} = \Delta F_u + \left(\frac{1}{\beta \Delta t}\dot{u}_i + \frac{1}{2\beta}\ddot{u}_i\right)[M] \tag{3.21}$$

Substituting Eqs. (3.15), Eqs. (3.16) and Eqs. (3.18) in Eq. (3.20),

$$\left(\frac{1}{\beta \Delta t^2}[G] + \frac{\alpha}{\beta \Delta t}[Q]^T\right)\{\Delta u_i\} + \left(\frac{1}{\alpha \Delta t}[S] + [H]\right)\{\Delta p_i\} =$$
$$\Delta F_p + \left(\frac{1}{\beta \Delta t}\dot{u}_i + \frac{1}{2\beta}\ddot{u}_i\right)[G] + \left(\frac{\alpha}{\beta}\dot{u}_i + \left(\frac{\alpha}{2\beta} - 1\right)\ddot{u}_i\right)[Q]^T + \frac{1}{\alpha}[S]\dot{p}_i \tag{3.22}$$

The stiffness matrix $[K]_e$, equivalent coupling matrix $[Q]_e$, dynamic coupling matrix $[G]_e$, compressibility matrix $[S]_e$ and permeability matrix $[H]_e$, are assembled in global stiffness vector $[A]$ in the dynamic analysis. Global force vector on right hand side is updated at every time step and system is solved for unknown incremental displacements and pore pressures. Then total displacement, velocity, acceleration, pore pressure and pore pressure rate vectors are updated which are used to calculate force vector for next time step.

3.4 FINITE ELEMENT DISCRETIZATION

For last five decades, finite element method (FEM) has been used into the analysis of geotechnical problems. It can assign different material property to each element for complicated soil layers. It is also possible to impose complex boundary conditions on the domain. Furthermore, the size of elements can be adjusted as per requirements. Similarly, interface elements can be introduced to model slip-frictional behaviour between two different materials. Zaman et al. (1984) discussed thin layer dynamic interface model for dynamic soil-structure interaction. For the present study, a 2-D finite element analysis program has been developed for the analysis of liquefaction phenomenon of the soil system assuming plane strain condition.

3.4.1 Mixed Displacement – Pore Pressure Element

In solid – fluid coupled analysis, the selection of interpolation functions for the solid phase and the fluid phase is the key to obtaining convergence and accuracy in the solution. Arbitrary combinations of displacements and pore pressure shape functions may cause spurious pore pressure, and/or poor convergence. The Babuska-Brezzi stability condition (Yu Bao, 2006) and the constraint count approach have been proven to be effective in solid – fluid coupled analysis. In the present study, an 8 – 4 – node mixed element which satisfies the Babuska-Brezzi stability condition and the constraint count is used. The mixed element (Fig. 3.1) has 8 displacement nodes and 4 pore pressure nodes. Hence, displacements are continuous biquadratic and pore pressures are continuous bilinear in the element.

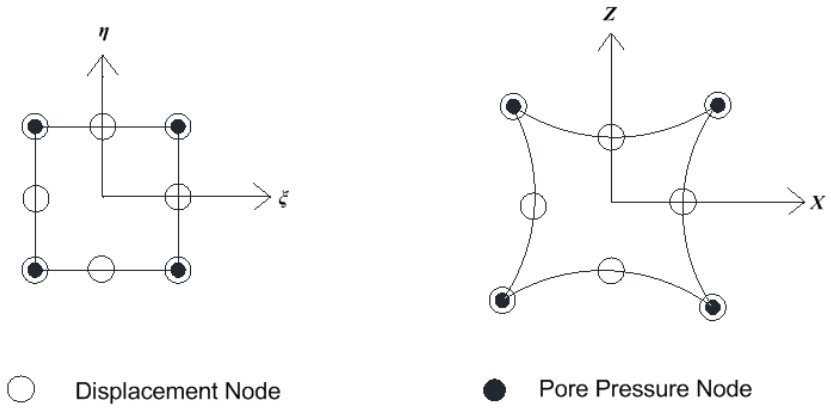

Fig. 3.1 Mixed Displacement-Pore Pressure Element

3.4.2 Eight Noded Quadrilateral Element

The scheme of node numbering followed for the elements has been shown in Fig. 3.2. The co-ordinates, x and z of any point within the element can be expressed in terms of the co-ordinates of its nodes and the shape functions associated with each of the nodes for the isoparametric element. These are given as,

$$x = \sum_{i=1}^{n} N_i x_i \quad ; \quad z = \sum_{i=1}^{n} N_i z_i \tag{3.23}$$

where, n is total number of nodes in element; x_i and z_i are the co-ordinates of node i and N_i are the shape function associated with node i.

Similarly, the displacements u and w at any point within the element can be expressed in terms of nodal displacements and the corresponding shape functions using the following relationships.

$$u = \sum_{i=1}^{n} N_i u_i \quad ; \quad w = \sum_{i=1}^{n} N_i w_i \tag{3.24}$$

where, u_i and w_i are nodal displacements along the cartesian coordinate axes.

The details of the eight node element is well documented in various literatures on finite element analysis (Krishnamoorthy, 2010), therefore the derivation of shape functions is not discussed. The shape functions associated with each of the element nodes in the natural co-ordinate system (ξ, η) for the node numbering as shown in Fig. 3.2 are given below.

$$N_i = 0.25\left(1+\xi_i\xi\right)\left(1+\eta_i\eta\right)\left(1+\xi_i\xi+\eta_i\eta\right) \qquad (i = 1, 3, 5, \text{and } 7) \tag{3.25a}$$

$$N_i = 0.5\left(1-\xi^2\right)\left(1+\eta_i\eta\right) \qquad (i = 2, 6) \tag{3.25b}$$

$$N_i = 0.5\left(1-\eta^2\right)\left(1+\xi_i\xi\right) \qquad (i = 4, 8) \tag{3.25c}$$

Further, ξ_i, η_i are the natural co-ordinates of node i and ξ, η are the natural coordinates of the point under consideration ($-1 \le \xi \le 1$ and $-1 \le \eta \le 1$).

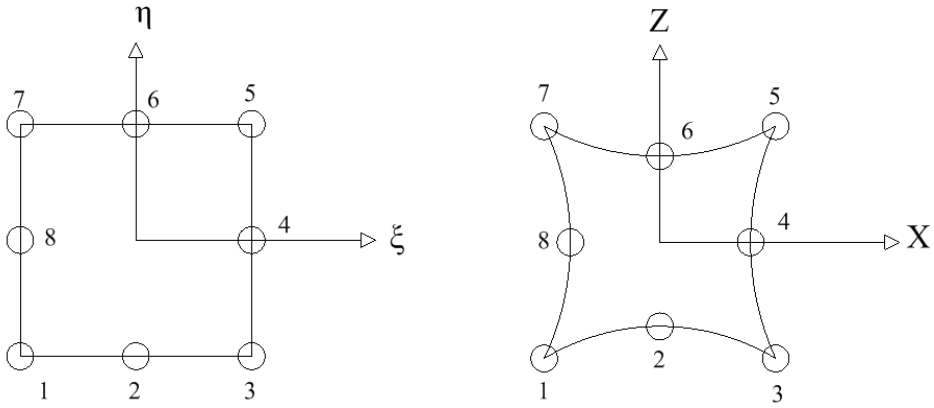

Fig. 3.2 Eight node continuum element

The shape function matrix for the solid phase is:

$$N_e(\xi,\eta)=\begin{bmatrix} N_1 & 0 & N_2 & 0 & \dots & \dots & N_8 & 0 \\ 0 & N_1 & 0 & N_2 & \dots & \dots & 0 & N_8 \end{bmatrix} \tag{3.26}$$

The three cartesian strain components ε_x, ε_z, and γ_{xz} at any point in the element are related to the displacements u and w at that point through the following expressions:

$$\varepsilon_x=\frac{\partial u}{\partial x} \quad ; \quad \varepsilon_z=\frac{\partial w}{\partial x} \quad ; \quad \gamma_{xz}=\frac{\partial w}{\partial x}+\frac{\partial u}{\partial z} \tag{3.27}$$

The relation between the derivatives in the natural (local) and cartesian (global) coordinate systems can be expressed by the chain rule of differentiation as:

If ϕ is function of $\{x, z\}$ then,

$$\begin{aligned} \frac{\partial \varphi}{\partial \xi} &= \frac{\partial \varphi}{\partial x}\frac{\partial x}{\partial \xi}+\frac{\partial \varphi}{\partial z}\frac{\partial z}{\partial \xi} \\ \frac{\partial \varphi}{\partial \eta} &= \frac{\partial \varphi}{\partial x}\frac{\partial x}{\partial \eta}+\frac{\partial \varphi}{\partial z}\frac{\partial z}{\partial \eta} \end{aligned} \tag{3.28}$$

In the matrix form,

$$\begin{Bmatrix} \frac{\partial \varphi}{\partial \xi} \\ \frac{\partial \varphi}{\partial \eta} \end{Bmatrix} = \begin{bmatrix} \frac{\partial x}{\partial \xi} & \frac{\partial z}{\partial \xi} \\ \frac{\partial x}{\partial \eta} & \frac{\partial z}{\partial \eta} \end{bmatrix} \begin{Bmatrix} \frac{\partial \varphi}{\partial x} \\ \frac{\partial \varphi}{\partial z} \end{Bmatrix} = [J] \begin{Bmatrix} \frac{\partial \varphi}{\partial x} \\ \frac{\partial \varphi}{\partial z} \end{Bmatrix} \tag{3.29}$$

The 2×2 matrix in the above equation is known as the Jacobian matrix (J) and derivatives in the global co-ordinate system can then be represented as,

$$\begin{Bmatrix} \frac{\partial \varphi}{\partial x} \\ \frac{\partial \varphi}{\partial z} \end{Bmatrix} = [J]^{-1} \begin{Bmatrix} \frac{\partial \varphi}{\partial \xi} \\ \frac{\partial \varphi}{\partial \eta} \end{Bmatrix} = \begin{bmatrix} \Gamma_{11} & \Gamma_{12} \\ \Gamma_{21} & \Gamma_{22} \end{bmatrix} \begin{Bmatrix} \frac{\partial \varphi}{\partial \xi} \\ \frac{\partial \varphi}{\partial \eta} \end{Bmatrix} \tag{3.30}$$

where, Γ_{ij} corresponds to the term in the i^{th} row and j^{th} column of inverse of the Jacobian matrix (J).

Using Eqs. (3.27) to (3.30) the relation between strains and nodal displacements is expressed as:

$$\{\varepsilon\} = \begin{Bmatrix} \varepsilon_x \\ \varepsilon_z \\ \gamma_{xz} \end{Bmatrix} = \begin{Bmatrix} \frac{\partial u}{\partial x} \\ \frac{\partial w}{\partial z} \\ \frac{\partial w}{\partial x} + \frac{\partial u}{\partial z} \end{Bmatrix} = \begin{bmatrix} \Gamma_{11} & \Gamma_{12} & 0 & 0 \\ 0 & 0 & \Gamma_{21} & \Gamma_{22} \\ \Gamma_{21} & \Gamma_{22} & \Gamma_{11} & \Gamma_{12} \end{bmatrix} \begin{Bmatrix} \frac{\partial u}{\partial \xi} \\ \frac{\partial u}{\partial \eta} \\ \frac{\partial w}{\partial \xi} \\ \frac{\partial w}{\partial \eta} \end{Bmatrix} \tag{3.31}$$

$$\begin{Bmatrix} \frac{\partial u}{\partial \xi} \\ \frac{\partial u}{\partial \eta} \\ \frac{\partial w}{\partial \xi} \\ \frac{\partial w}{\partial \eta} \end{Bmatrix} = \begin{bmatrix} \frac{\partial N_1}{\partial \xi} & 0 & . & . & . & . & \frac{\partial N_n}{\partial \xi} & 0 \\ \frac{\partial N_1}{\partial \eta} & 0 & . & . & . & . & \frac{\partial N_n}{\partial \eta} & 0 \\ 0 & \frac{\partial N_1}{\partial \xi} & . & . & . & . & 0 & \frac{\partial N_n}{\partial \xi} \\ 0 & \frac{\partial N_1}{\partial \eta} & . & . & . & . & 0 & \frac{\partial N_n}{\partial \eta} \end{bmatrix} \{\delta\}_e \tag{3.32}$$

Combining above two equations (Eqs. 3.31 and 3.32), we have,

$$\{\varepsilon\} = [B] \ \{\delta\}_e \tag{3.33}$$

where, [B] is strain-displacement transformation matrix, {ε} is strain vector and, {δ} is vector of unknown displacements.

Sub-matrix [B_i] for node i is given by following equation:

$$[B_i]=\begin{bmatrix} \Gamma_{11}\dfrac{\partial N_i}{\partial \xi}+\Gamma_{12}\dfrac{\partial N_i}{\partial \eta} & 0 \\ 0 & \Gamma_{21}\dfrac{\partial N_i}{\partial \xi}+\Gamma_{22}\dfrac{\partial N_i}{\partial \eta} \\ \Gamma_{21}\dfrac{\partial N_i}{\partial \xi}+\Gamma_{22}\dfrac{\partial N_i}{\partial \eta} & \Gamma_{11}\dfrac{\partial N_i}{\partial \xi}+\Gamma_{12}\dfrac{\partial N_i}{\partial \eta} \end{bmatrix} \tag{3.34}$$

For material which is isotropic, homogeneous and elastic, the three cartesian stress components σ_x, σ_z, and τ_{zx} are related to the corresponding strain components ε_x, ε_z, and γ_{xz} through the following expression:

$$\{\sigma\}=\begin{Bmatrix}\sigma_x\\ \sigma_z\\ \tau_{xz}\end{Bmatrix}=[D]\begin{Bmatrix}\varepsilon_x\\ \varepsilon_z\\ \gamma_{xz}\end{Bmatrix} \tag{3.35}$$

In which, [*D*] is the constitutive relation matrix relating the stresses and strains in 2-D space and it comprises of factors related to the material properties. For an isotropic, homogeneous elastic material, this matrix for plane strain condition is given as:

$$[D]=\frac{E}{(1-\mu)(1-2\mu)}\begin{bmatrix} 1-\mu & \mu & 0 \\ \mu & 1-\mu & 0 \\ 0 & 0 & \dfrac{1-2\mu}{2} \end{bmatrix} \tag{3.36}$$

Eq. (3.35) can be written in the abbreviated form as:

$$\{\sigma\}=[D]\{\varepsilon\}=[D][B]\{\delta\}_e \tag{3.37}$$

3.4.3 Four Noded Rectangular Elements

It is known that pressures are associated with strains, which are related to the first space derivatives of displacement. Therefore, it is natural to select the pressure element one order lower than the displacement element in order to obtain consistency. In the present study, a 4-node rectangular element (Fig. 3.3) is used to simulate pore pressures.

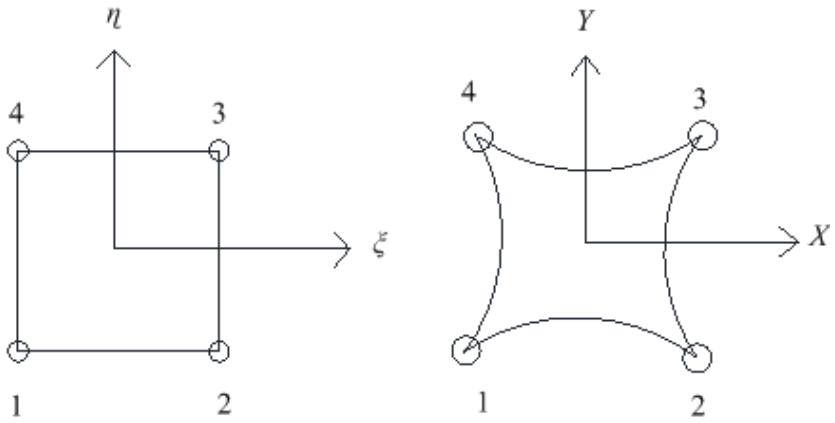

Fig. 3.3 Four node continuum element

For the node numbering shown in Fig. 3.3, shape functions are,

$$N_i^P = \frac{1}{4}(1+\xi_i\xi)(1+\eta_i\eta) \tag{3.38}$$

In which, the superscript '*p*' indicates pore pressures.

Pore pressure is a scalar, thus, the shape function matrix for pore pressure can be expressed in the vector form:

$$N^P(\xi,\eta) = \begin{bmatrix} N_1^P & N_2^P & N_3^P & N_4^P \end{bmatrix} \tag{3.39}$$

The nodal pore pressure vector is, $\{p\}^T$, given by,

$$\{p\}^T = \{p_1, p_2, p_3, p_4\}$$

The pore pressure within the element can be calculated by summation of multiplication of the shape function vector and the nodal pore pressures. The $[B^p]$ matrix has been derived in a similar way as $[B]$ matrix.

$$p = \sum_{i=1}^{4} N_i^p p_i \tag{3.40}$$

By combining the 8-node displacement element with the 4-node pore pressure element, a mixed displacement – pore pressure element is obtained for simulating the behavior of two phase saturated soil media. The modifications or the additional formulation required for nonlinear analysis, constitutive soil models will be discussed in the subsequent chapters.

CHAPTER - 4

LIQUEFACTION MODELING ON FINITE DOMAIN

4.1 CONSTITUTIVE RELATION

During the last few decades, a great effort has been devoted to (i) improving the knowledge of soil behaviour under complex loading paths, and (ii) developing suitable constitutive models able to reproduce most salient features of soil behavior found in experiments. Sand shows two type of extreme behavior under shear. It behaves as contractive in loose state whereas dilative in dense condition.

The strain hardening plasticity form of critical state model has been successfully predicting the behaviour of clays (Ling et al. 2002). The behaviour of sands are defined with the modified yield surface of critical state model but limited to monotonic loading only. However, since elastic behaviour is assumed within the yield locus, the prediction for repetitive loading and unloading behaviour imparted by seismic load or other dynamic load is not satisfactory.

Soil behaviour under cyclic loading is complex. Hence, the constitutive relation used for the numerical prediction should be able to model the soil behaviour during seismic loading considering permanent settlement, dilatancy and hysteresis loops to predict reasonable value of displacements and excess pore pressure. Hence, a generalized plasticity, bounding surface, non-associated type model known as Pastor–Zienkiewicz Mark III (Pastor et al. 1985, 1990; Zienkiewicz et al. 1999) has been used to model the soil domain. This model includes both volumetric and deviatoric plastic strains during loading and unloading in the hardening parameter of the bounding surface.

4.2 PASTOR–ZIENKIEWICZ MARK III MODEL

Pastor–Zienkiewicz Mark III Model is working on the concept of effective stress principle. In the elasto-plastic analysis, the total strain increment $\Delta\varepsilon$ is further separated into elastic strain $\Delta\varepsilon^{e}$ and plastic strain components $\Delta\varepsilon^{p}$.

$$\Delta\varepsilon = \Delta\varepsilon^{e} + \Delta\varepsilon^{p} \tag{4.1}$$

The relationships between incremental stress $\Delta\sigma$ and incremental strains $\Delta\varepsilon$ have been derived from the theory of generalized plasticity. This relationship is expressed as:

$$\Delta\sigma = D^{ep}\Delta\varepsilon \tag{4.2}$$

In which, D^{ep} is elastoplastic constitutive matrix respectively defined by following relation as given by Mroz and Zienkiewicz (1984).

$$D^{ep} = D^{e} - \frac{D^{e} n_{gL/U} n^{T} D^{e}}{H_{L/U} + n^{T} D^{e} n_{gL/U}} \tag{4.3}$$

In which, D^{e} signifies the elastic constitutive matrix, n is vector of normal in loading direction, $n_{gL/U}$ is flow direction vector during loading or unloading condition, and $H_{L/U}$ is defined as loading or unloading plastic modulus.

4.2.1 Elastic Behavior

The shear and bulk moduli (G and K) have been used to define the elastic behavior of the soil mass. These parameters are dependent on the stress condition. Hardin and Richart (1963) have given following expression for evaluating elastic shear modulus G.

$$G = G_0 \sqrt{\frac{p'}{p_a}} \tag{4.4}$$

where, G_0 is initial shear modulus of soil mass and p' is mean effective stress, p_a is atmospheric pressure Also, G_0 is dependent of initial void ratio (Ishihara 1996).

The Poisson's ratio is assumed constant throughout the numerical analysis. The bulk modulus can be evaluated as:

$$K = K_0 \sqrt{\frac{p'}{p_a}} \tag{4.5}$$

In which, K_0 is initial bulk modulus of soil.

4.2.2 Stress Dilatancy and Bounding Surface

P-Z Mark III model considers the linear distribution of the stress ratio $\eta = q/p$ for approximating dilatancy of the sand (Nova and Wood, 1982).

$$d_g = \frac{d\varepsilon_v^p}{d\varepsilon_s^p} = \left(1 + \alpha_g\right)\left(M_g - \eta\right) \tag{4.6}$$

In which, $d\varepsilon_v^p$ *and* $d\varepsilon_s^p$ are plastic volumetric and deviatoric strains increments, respectively.

M_g is correlated with the angle of friction ϕ of the Mohr-Coulomb relations

$$M_g = 6S \sin\phi / \left(3S - \sin\phi\right) \tag{4.7}$$

Value of S is ±1 based on compression or extension.

The plastic potential surface relationship has been evaluated from dilatancy relation (Eq. 4.6) as:

$$g = \left\{ q - M_g p \left(1 + \frac{1}{\alpha} \right) \left[1 - \left(\frac{p}{p_g} \right)^{\alpha} \right] \right\} \tag{4.8}$$

Also, the yield or bounding surface has been defined as:

$$f = \left\{ q - M_f p \left(1 + \frac{1}{\alpha} \right) \left[1 - \left(\frac{p}{p_c} \right)^{\alpha} \right] \right\} \tag{4.9}$$

In which, p and q are the mean effective and deviatoric stress respectively; M_g is defined as the slope of the critical state line; α and M_f are constants; and p_g and p_c are size parameters. The plastic potential and yield surface for the respective loose and dense sand are demonstrated in Fig. 4.1. The yield and plastic potential surfaces may not be explicitly described while considering generalized plasticity formulation proposed by Zienkiewicz and Mroz (1984) and modified by Zienkiewicz et al. (1985) and Pastor et al. (1985, 1990).

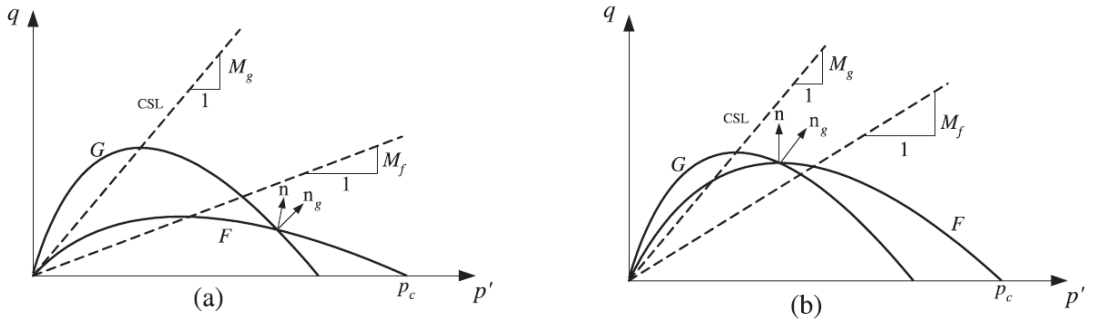

Fig.4.1. Plastic potential and yield surfaces for (a) loose sands and (b) dense sands (reproduced after Pastor et al. 1985). CSL (Critical state line)

4.2.3 Plastic Flow for Loading and Unloading

The direction vector $\boldsymbol{n}_{gL}$ can be evaluated from the dilatancy relationship given by Eq. (4.6),

$$\eta_{gL} = \frac{1}{\sqrt{1 + d_g}} \begin{Bmatrix} d_g \\ 1 \end{Bmatrix} \tag{4.10}$$

The unloading plastic flow vector is determined by following equation as irreversible strains are of a contractive (densifying) nature.

$$\eta_{gU} = \frac{1}{\sqrt{1+d_g}} \begin{Bmatrix} -|d_g| \\ 1 \end{Bmatrix} \tag{4.11}$$

The absolute sign is used so that constant densification occurs during unloading and this can model the behaviour of liquefaction and cyclic mobility of sand.

In the similar way, the direction cosine of the unit normal *n* to the corresponding bounding surface can be defined as: (Zienkiewicz and Pande 1977)

$$\eta = \frac{1}{\sqrt{1+d_f}} \begin{Bmatrix} d_f \\ 1 \end{Bmatrix} \tag{4.12}$$

In which, d_f is the dilatancy at yield given as

$$d_f = (1+\alpha_f)(M_f - \eta) \tag{4.13}$$

M_f maintains a constant ratio with M_g (Pastor et al. 1990) assumed this ratio to be dependent on relative density (R_D) suggesting relation for M_f as:

$$M_f = M_g \times R_D$$

4.2.4 Plastic Modulus for Loading and Unloading

In case of loading phase, the plastic modulus is evaluated from the relationship given by Pastor and Zienkiewicz (1986):

$$H_L = H_0 p H_f \{H_v + H_s\} H_{DM} \tag{4.14}$$

In which, H_0 is defined as the initial loading plastic modulus:

$$H_f = \left(1 - \frac{\eta}{\eta_f}\right)^4 \quad ; \quad H_v = 1 - \eta / M_g \tag{4.15}$$

$$H_s = \beta_0 \beta_1 \, \mathrm{e}^{-\beta_0 \xi} \quad ; \quad \xi = \int d\xi = \int \left| d\varepsilon_q^p \right| \tag{4.16}$$

where ε_q^p is the plastic shear strain.

In case of reloading, a discrete memory factor H_{DM} is defined for considering the previous loading history.

$$H_{DM} = \left(\zeta_{\max} / \zeta\right)^{\gamma_{DM}} \tag{4.17}$$

In which, γ_{DM} is suggested as parameter for considering reloading discrete memory factor whereas ζ is known as the mobilized stress function and given as:

$$\zeta = p\left[1-\left(\frac{1+\alpha}{\alpha}\right)\frac{\eta}{M}\right]^{1/\alpha} \tag{4.18}$$

The plastic strains are accumulated in successive loading and unloading phase in the present constitutive model. Ishihara and Okada (1982) used experimental results to observe that the amount of plastic strain generating during unloading phase depends upon the state of stress ratio at the starting point of unloading. Pastor et al. (1985) recommended the following relation for the unloading plastic modulus H_{U0} as follows:

$$H_u = H_{u0}\left(\frac{M_g}{\eta_u}\right)^{\gamma_u} \; for \left|\frac{M_g}{\eta_u}\right| > 1 \tag{4.19}$$

$$H_u = H_{u0} \, for \left|\frac{M_g}{\eta_u}\right| < 1 \tag{4.20}$$

In which, η_u is the unloading stress ratio $\eta_u = (q/p)_u$.

Chan et al. (1988) prescribed the detailed description of procedure to evaluate parameters in Pastor–Zienkiewicz Mark III model. The parameter evaluation procedure is dependent of the drained monotonic, undrained monotonic and cyclic triaxial experimental results.

4.3 NONLINEAR SOLUTION ALGORITHM

The total load is applied in the ten equal increments and the stiffness matrix, [*K*] is kept constant for all the load increments. Following algorithm is adopted for nonlinear analysis:

i) Apply incremental load ΔF and solve for incremental displacement, Δu

$$\{\Delta F\} = [K]\cdot\{\Delta u\} \tag{4.21}$$

ii) Update the total displacements by adding incremental displacement Δu in

$$u_i = u_{i-1} + \Delta u \tag{4.22}$$

u_i = displacement for *i* th increment

iii) Set $m_e=0$, where m_e indicates number of yielded elements.

iv) For each element, set $m_p=0$ (number of yielded points within the given element), obtain the element incremental displacement vector $\{\Delta u\}^e$ from global incremental

displacement vector, Δu .

v) For each Gauss point, compute the incremental stress $\{\Delta\sigma\}^e$ and total stress $\{\sigma_{Ti}\}^e$ for i^{th} increment from following relations,

$$\begin{aligned}\{\Delta\sigma\}^e &= [D]\cdot[B]\cdot\{\Delta u\}^e \\ \{\sigma_{Ti}\}^e &= \{\sigma_{Ti-1}\}^e + \{\Delta\sigma\}^e\end{aligned} \tag{4.24}$$

Check for yield, if the point have not yielded then go to next Gauss point, else, set $m_p = m_p + 1$, and calculate extra stress over yield stress, $\{\Delta\sigma\}_{\text{ext}}$

$$\{\Delta\sigma\}_{ext} = [D - D_{ep}]\cdot\{\Delta\varepsilon\}^e \tag{4.25}$$

Set total stress at yield level

$$\{\sigma_{Ti}\}^e = \{\sigma_{Ti}\}^e - \{\Delta\sigma\}_{ext} \tag{4.26}$$

Update the additional force vector to be applied in next iteration

$$\{\Delta F\}^e = \iiint_V [B]^T \cdot \{\Delta\sigma\}_{ext}\, dA \tag{4.27}$$

Complete loop over the Gauss points of the element

vi) If $m_p > 0$, then assemble load vector $\{\Delta F\}^e$ and set $m_e = m_e + 1$.

vii) Repeat step (iv) to (vi) for all the elements.

viii) If $m_e = 0$, then not a single element have yielded, go to next load level.

ix) If $m_e > 0$, then check for convergence using following displacement criteria,

$$e_d = \left(\sqrt{\sum (q_i)^2} - \sqrt{\sum (q_{i-1})^2}\right) \Big/ \sqrt{\sum (q_i)^2} \tag{4.28}$$

where, e_d = displacement norm, u_i = total displacement at the i^{th} iteration and

u_{i-1} = total displacement at the i-1th iteration.

If the convergence criterion is satisfied, then apply next load increment. If a convergence criterion is not satisfied then repeat the procedure from step (i) to step (ix), till the displacements are converged.

4.4 TRANSMITTING BOUNDARY

The wave propagation problem generally encountered in soil dynamics is basically different from the structural dynamics problem because of semi infinite nature of problem domain. Generally a finite domain of the foundation medium is analyzed in numerical calculations and attempts are directed to prevent the back-propagation of waves due to reflection at the boundary. Hence, a transmitting boundary is essential to model wave propagation in the domain of unbounded nature in any finite element analysis.

A huge number of transmitting boundaries are proposed in the last few decades. Lysmer and Kulhemeyer (1969) described the easiest and most commonly used transmitting boundary investigating the local boundaries to facilitate the finite dimension of unbounded soil mass. Various possibilities for analytically defining this boundary condition were analyzed. However total energy absorption at the viscous boundary was not guaranteed. Further, Kouroussis et al. (2011) proposed the modified version of viscous boundary efficiently, originally presented by Lysmer and Kuhlemeyer (1969). Novak (1974) established dimensionless parameters to obtain close-form formula for the pile stiffness and damping. All components of motion were considered in vertical plane including horizontal and vertical translation and rotation of pile head. Novak et al. (1978) described the plane strain boundary which can be placed directly to the body to account roughly for the soil reactions to body motion. This local boundary was reasonably accurate and easy in application for many practical problems (Novak and Aboul-Ella, 1978). Liao and Wong (1984) described the extrapolation algorithm to study wave propagation in an elastic half-space for plane strain condition. Novak and Mitwally (1988) presented an axi-symmetrical, volumetric deformation which is related to the radial propagation of P-waves. Homogeneous infinite medium and composite medium were considered for axis-symmetrical vibration. It contains an inner annular zone whose properties may be different from those of the outer infinite domain. AI-Hunaidi et al. (1990) developed a new specific method for simulating the radiation condition of infinite soil domain. This method was intended for semi-discretized finite models analyzed in the time domain assuming linear elastic nature of the exterior infinite domain and nonlinear behaviour of the inner periphery.

Zhao and Liu (2002) used the operator splitting method to re-evaluate the non-reflecting artificial boundary condition presented by Hagstrom and Hariharan (1998) as well as Thompson et al. (2001). This method deals with transient scalar wave propagation

problems in a 2-D homogeneous half space. Zhao and Liu (2002, 2003) presented an accurate non-reflecting boundary condition for defining transient scalar wave propagation problems for a 2-D infinite homogeneous layer. Two vertical artificial boundaries were inserted in the infinite layer so as to trim the infinite domain into a finite domain.

Du and Zhao (2010) presented a new local time-domain transmitting boundary for modeling cylindrical elastic wave radiation problem. This boundary had a mechanical model which consists of the spring, dashpot and mass elements. It comprised of the auxiliary degrees of freedom which was dynamically stable and easily applicable into the finite element analyses.

In the present study, an artificial transmitting boundary is applied to separate the whole unbounded soil domain into the finite near-field and the truncated far-field unbounded soil domain. These types of boundary are placed at a sufficient location from the source of vibration to absorb the wave energy of outgoing waves and prevent them from reflecting back towards the structure. The near field is approximated horizontally within the range of 10 m on each side from the centre of the soil domain and vertically 12 m in the downward direction. The far field is assumed to be outside this boundary. Kelvin elements (spring and dashpot) are connected in vertical and horizontal directions to the nodes of the transmitting boundary as shown in Fig. 4.2.

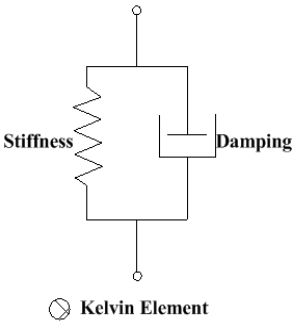

Fig. 4.2 Kelvin Element

The basic function of Kelvin element is to absorb the shear /surface energy of outward propagating waves and preventing backward reflection into the near field. The required mesh size with Kelvin elements is much smaller than that required with frequency independent viscous dampers. As the time-history analysis is performed in the present study, the stiffness and dashpot constants of the Kelvin element in horizontal and vertical direction are evaluated based on the predominant frequency of loading using the solution algorithm proposed by Novak (1974).

$$k_r^* = \frac{G}{2\pi R_o}\left[S_1 + i\,S_2\right] \tag{4.29}$$

In which, G is the shear modulus of soil mass, k_r^* is the complex stiffness and R_o is the radial distance of the Kelvin element from source. The stiffness and damping coefficients are represented by real and imaginary part of the above Eq. (4.29).

$$k_r = \frac{GS_1}{2\pi R_o} \qquad and \qquad c_r = \frac{GS_2}{2\pi R_o} \tag{4.30}$$

S_1 and S_2 are dimensionless parameters defined by following equations:

$$S_1 = 2\pi a_0 \frac{a_k c_k + b_k d_k}{c_k^2 + d_k^2} \quad and \quad S_2 = 2\pi a_0 \frac{a_k c_k - b_k d_k}{c_k^2 + d_k^2} \tag{4.31}$$

where

$$\begin{aligned}
a_k &= \frac{J_1(x_0)J_2(a_0)}{q_u} + J_1(a_0)J_2(x_0) - \frac{Y_1(x_0)Y_2(a_0)}{q_u} - Y_1(a_0)Y_2(x_0) \\
b_k &= \frac{J_1(x_0)Y_2(a_0)}{q_u} + J_1(a_0)Y_2(x_0) + \frac{J_2(a_0)Y_1(x_0)}{q_u} + J_2(x_0)Y_1(a_0) \\
c_k &= J_0(a_0)J_2(x_0) + J_0(x_0)J_2(a_0) - Y_0(a_0)Y_2(x_0) - Y_0(x_0)Y_2(a_0) \\
d_k &= J_0(a_0)Y_2(x_0) + J_0(x_0)Y_2(a_0) + J_2(a_0)Y_0(x_0) + J_2(x_0)Y_0(a_0) \\
a_0 &= \nu_m / \nu_s \quad and \quad x_0 = a_0\sqrt{2}
\end{aligned} \tag{4.32}$$

In the above equations (J_k, Y_k) presents the first and second kind of Bessel functions of k^{th} order respectively.

Similarly, the constants for vertical Kelvin element are evaluated by

$$k_V^* = \frac{G}{2\pi R_o}\left[S_{V1} + i\, S_{V2}\right] \tag{4.33}$$

The subscript v represents the vertical direction. Hence, the stiffness and damping constants for this particular case will be calculated by

$$k_v = \frac{GS_{v1}}{2\pi R_o} \qquad and \qquad c_v = \frac{GS_{v2}}{2\pi R_o} \tag{4.34}$$

$$where, \quad S_{V1} = 2\pi\, a_0 \frac{J_0(a_0)J_1(a_0) + Y_0(a_0)Y_1(a_0)}{J_0(a_0)^2 + Y_0(a_0)^2} \qquad and \qquad S_{V2} = \frac{8\pi\, R_0}{J_0(a_0)^2 + Y_0(a_0)^2} \tag{4.35}$$

In the same manner, the constants for the vertical Kelvin element connected to the horizontal transmitting boundary can be explained.

$$k_V^* = \frac{G}{2\pi\, Z_r}\left[S_{V1} + i\, S_{V2}\right] \tag{4.36}$$

In which, Z_r is the vertical distance of the Kelvin element from the source. The constants explained in Eqs. (4.30) and (4.34) are multiplied by respective surface area of the element perpendicular to the propagation direction to determine the stiffness and damping of the Kelvin elements.

4.5 SYSTEM DAMPING

The radiation damping and material damping are jointly considered to represent damping in the system adequately. Hence, the damping matrix [C] is comprised of two components, radiation damping [C_r] and material damping [C_m] as,

$$[C] = [C_r] + [C_m] \tag{4.37}$$

Radiation damping matrix, [C_r] is a diagonal matrix having nonzero terms only at the transmitting boundary nodes. For a particular node at which Kelvin elements are placed, stiffness and damping coefficients for the horizontal and vertical directions are calculated using Eqs. (4.30) and (4.34), respectively. Material damping [C_m] is modeled as Rayleigh damping and is explained in detail in subsequent section.

Rayleigh and Lindsay (1945) proposed the original damping formulation considering [C_m] matrix is proportional to the mass and stiffness matrices:

$$\left[C_m\right] = \alpha_1 \left[M\right] + \alpha_2 \left[K\right] \tag{4.38}$$

In which, α_1 and α_2 are mass and stiffness proportional scalar constants.

Rayleigh damping results in different damping ratios for different response frequencies according to the following equation:

$$\xi_r = \frac{\alpha_1}{2\omega_i} + \frac{\alpha_2 \omega_i}{2} \tag{4.39}$$

Where, ξ_r is damping ratio and ω_i is frequency corresponding to i th mode of system.

Park and Hashash, 2004 explained that if the damping ratio is constant throughout the soil domain, scalar values of α_1 and α_2 can be evaluated using two significant natural modes. In the present study, the values of ω_1 and ω_2 are considered as frequency corresponding to first and third peak of the frequency amplitude response (Ladhane et al. 2012).

For $\xi_{r1} = \xi_{r2}$ and $\omega_2 > \omega_1$, α_1 and α_2 are given by,

$$\alpha_1 = \frac{2\xi_r \omega_1 \omega_2 \left(\omega_2 - \omega_1\right)}{\left(\omega_2^2 - \omega_1^2\right)} \qquad \text{and} \qquad \alpha_2 = \frac{2\xi_r \left(\omega_2 - \omega_1\right)}{\left(\omega_2^2 - \omega_1^2\right)} \tag{4.40}$$

If the value of α_1 is set to zero then damping matrix becomes proportional to stiffness whereas for α_2 equal to zero it becomes mass proportional. Fig. 4.3 shows the typical variation of damping ratio with frequency for mass proportional, stiffness proportional and Rayleigh damping for ω_1 = 14 rad/sec and ω_2 = 24 rad/sec.

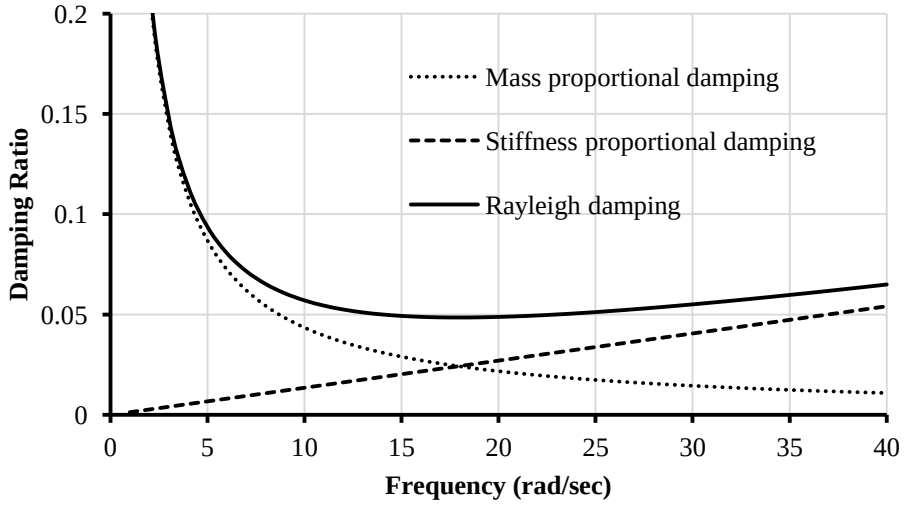

Fig. 4.3 Typical variation of damping ratio with frequency for ω_1 = 14 rad/sec and ω_2= 24 rad/sec

4.6 VALIDATION

Centrifuge modeling has been assumed among the best experimental methods for modeling and observing liquefaction behaviour. The stress conditions generated in the model approximately simulated in the full-scale prototype experimental setup. The suitability and precision of the proposed FEM algorithm are examined by comparison between numerical response with the centrifuge model test results conducted at the RPI centrifuge facility (Byrne et al. 2004). The centrifuge model used Nevada sand and simulates horizontal ground conditions subjected to a cyclic input motion. It is comprised of a uniform sand layer with a placed permeability $k = 8.2\times10^{-5}$ m/s and R_D = 55%. The frequency of the input motion was chosen in such a manner that it reduces the potential for amplification in the model. The centrifuge model was run at acceleration level of 120*g* with no surcharge. The viscosity of fluid in prototype model was 60 times higher than that of water. The fluid table was at the top surface of the prototype model. Maximum value of 380 kPa was observed for initial effective stress at the base level. A cross section view of centrifuge model which shows the locations of the pore pressure transducers and accelerometers are explained in Fig. 4.4. The input motion was 50 cycles of 0.2g at 1.5 Hz prototype scale.

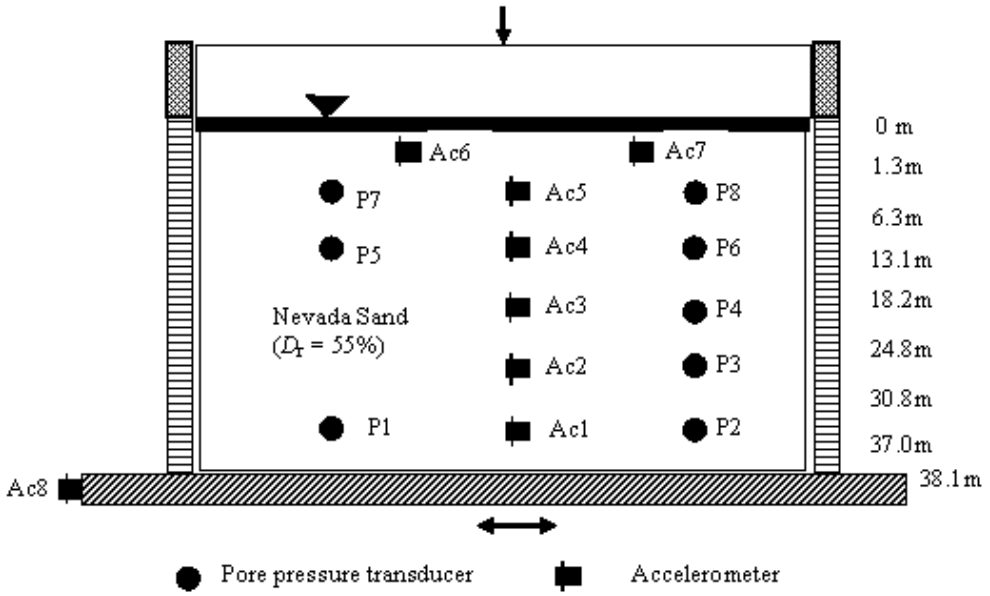

Fig.4.4 Cross-section of the centrifuge model and instrumentation layout (modified after Byrne et al. 2004)

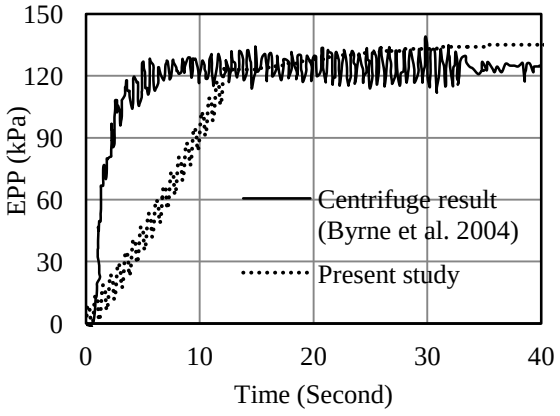

(a) 13.1m

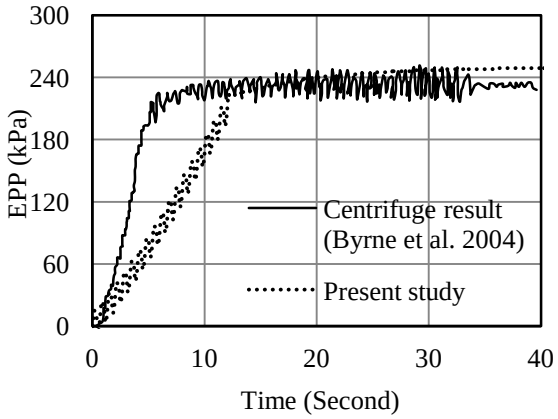

(b) 24.8m

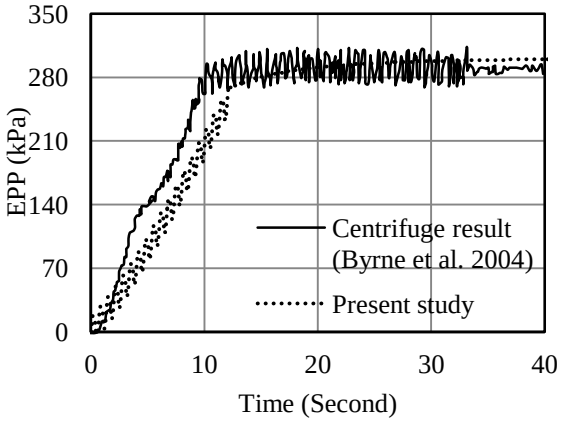

(c) 30.8m

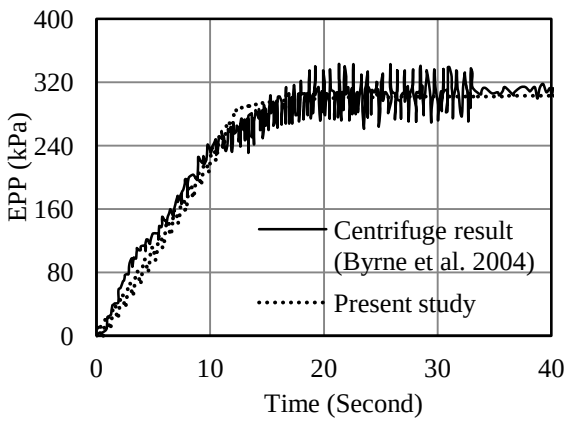

(d) 37m

Fig. 4.5 Excess Pore Pressure verses time at different depth

Variations in measured and computed values of EPP with time at prototype depths of 13.1, 24.8, 30.8, and 37.0 m are shown in Figs. 4.5a-d. At depth 30.8m and 37m, computed and measured values of EPP are in good agreement (Figs. 4.5c-d). But at 13.1m and 24.8m depth, the same value of EPP as measured value is attained at slower rate than measured value (Figs. 4.5a-b). At a depth of 13.1 m the EPP was built up to the value close to initial effective stress in 12s, indicative of liquefaction phenomenon. The time to build 100% pore pressure was increased with depth. So it is evident that, liquefaction initially triggers at shallow depth and advances in downward direction. At depth of 13.1m, the maximum computed EPP (133 kPa) is slightly lower than the experimental value (136 kPa), approximately by 2.2%. The discrepancy may be attributed to use of a constant coefficient of permeability throughout the analysis, which does not represent the real conditions, when liquefaction has initiated. Fig. 4.5 shows the trend of liquefaction at all the depth as EPP is slightly higher than the initial effective stresses. Results are in quietly good agreement with centrifuge results presented by (Byrne et al. 2004), with little deviation. The comparison explained that the proposed model can more or less simulate the real behavior of liquefaction phenomena.

4.7 NUMERICAL SIMULATION UNDER CYCLIC LOAD

The problem of saturated loose sand layer of thickness 10m, underlain by 3m depth of gravel had been considered for numerical simulation of liquefaction phenomena considering two-dimensional plane-strain conditions. The mesh under consideration is discretized into 156 elements as shown in Fig. 4.6. The 8-4 noded mixed element has been used for discretization of the soil domain. The transmitting boundary is approximated horizontally within the range of 10 m on each side from the centre of the soil domain and vertically 12 m in the downward direction. Kelvin elements are connected in vertical and horizontal directions to the nodes of the transmitting boundary.

The excess pore pressure was permitted to dissipate from the top surface of the sand layer. Material properties of the purposed model are reported in Table 4.1. The variation in displacement and excess pore pressure (EPP) with time had been calculated using finite element code written in FORTRAN-90. The variation of both parameters with time was considered for comparing the response. Numerical analysis was done in two steps: (1) static analysis and (2) Dynamic analysis.

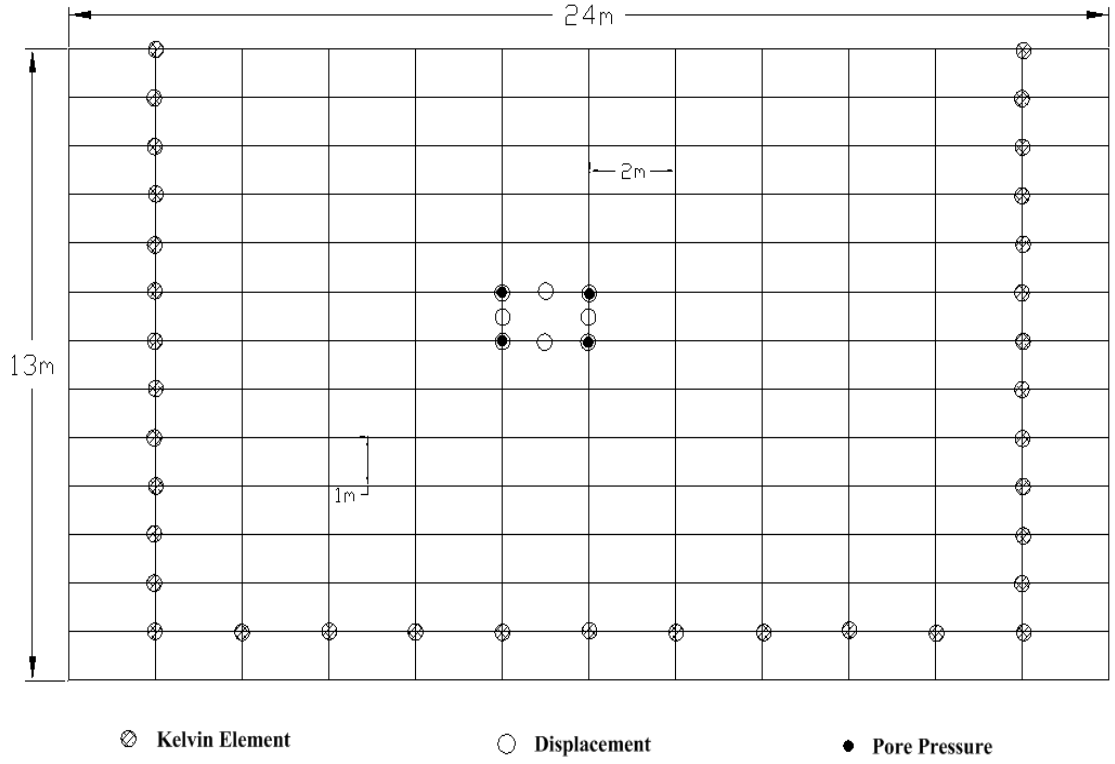

Fig. 4.6 Soil domain under Consideration

Table 4.1 Material properties and model parameters (Sadeghian and Manouchehr 2012)

Parameters	**Description**	**Value**
γ	Unit weight of soil	18 kN/m^3
μ	Poisson's ratio	0.31
M_g	Slope of the critical state line (CSL)	1.15
M_f	Yield surface parameter	1.03
D_R	Relative Density	0.4
β_0	Shear hardening parameter	4.2
β_1	Shear hardening parameter	0.2
α	Dilatancy parameters	0.45
H_0	Found by matching the shape of q–p plot	600
H_{u0}	Unloading plastic modulus	40000
γ_u	Unloading plastic deformation parameter	2

4.7.1 Static analysis

A static analysis was performed to consider the effect of self weight of the soil before applying dynamic loads. The predicted pore pressures and the stresses within the soil mass are retained and considered as initial conditions for the consequent dynamic analysis under cyclic or seismic load. The coupled equations considered for static analysis are as follows:

$$K \quad q_{e} - Q \quad p_{e} = f_{u} \tag{4.41}$$

$$Q^{T} \quad \dot{q}_{e} + H \quad p_{e} = f_{p} \tag{4.42}$$

4.7.2 Dynamic analysis

After attaining the equilibrium condition for initial stress condition, a nonlinear analysis was performed for the harmonic load with the supplied horizontal and vertical cyclic acceleration $a = a_0 \sin \omega t$. The dynamic analyses were performed using a Generalized Newmark scheme (Katona and Zienkiewicz, 1985) with nonlinear iterations using initial linear elastic tangential global matrix. The value of Newmark's integration constants were preferred to be as α = 0.60 and β = 0.3025 for the dynamic analysis.

The time step used is usually depends on time of cyclic loading and frequency of the input. Void ratio, permeability and other geometric properties were kept constant during the analysis. Rayleigh damping of 5% is applied at the dominant frequency in the earthquake-like motion input to enhance the energy dissipation characteristic of the constitutive model. The numerical analysis is performed for 15 cycles of loading in case of cyclic loading. The amplitude and frequency of the cyclic loading were given as a_0 = 0.15g and 1 Hz respectively. In the parametric study, parameters reported in Table 4.1 have been considered. Only a particular parameter has been varied to study its effect on the dynamic response while other parameters are kept same as reported in Table 4.1. Parameters considered for variation in the parametric study are shear modulus *G*, permeability *k* and cyclic frequency *f*.

Parametric Study

A fully coupled formulation is used to model the liquefaction behavior of saturated soil stratum. Fig. 4.7 displays the computed horizontal and vertical displacement at different depth (G = 10 MPa, k = 6.6×10^{-5} m/s). The maximum values of horizontal settlement of 3.38 cm are predicted at the top of soil layer whereas; maximum values of vertical

settlement of 4.45 cm are predicted at 8m depth. It has been observed that most part of the settlements occur during the cyclic excitation. Generally, the horizontal settlement is less than vertical settlement at different depths. Vertical displacement (4.45cm) at 8m depth is nearly equal to the top surface because higher confining stress at bottom. Similar trend of displacement with respect to time was reported by Dewoolar et al. (2009).

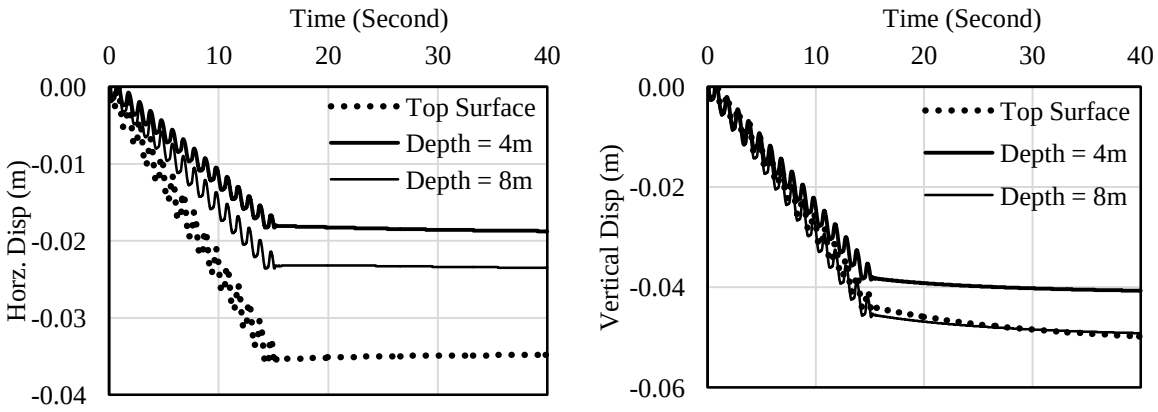

(a) Horizontal Displacement (b) Vertical Displacement

Fig.4.7 (a) Computed horizontal displacement and (b) Computed vertical displacement with respect to time at different depth

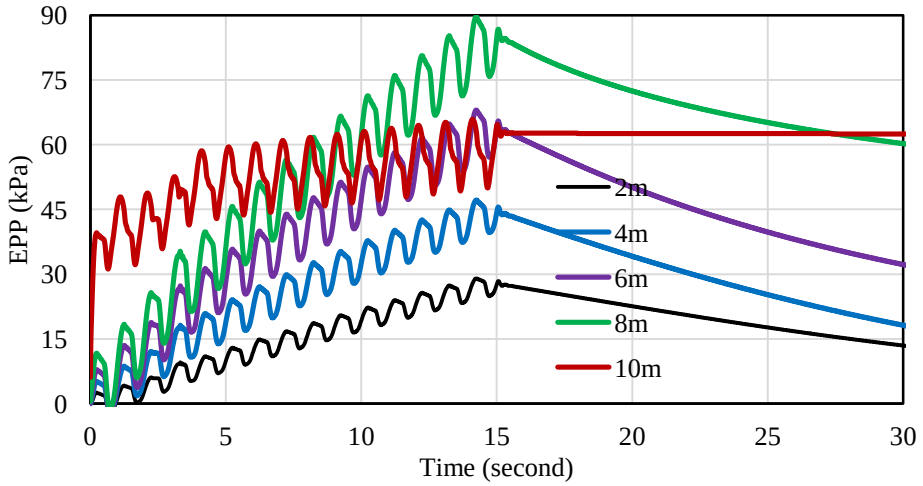

Fig.4.8 Computed EPP at depths 2m, 4m, 6m, 8m and 10m with respect to time

Fig. 4.8 displays the computed excess pore pressure at different depth. The computed excess pore pressure time histories point out that soil at the depth of 2m, 4m, 6m and 8m is liquefied because excess pore pressure (EPP) is higher than initial vertical stress. At 10m depth of soil domain, rise in excess pore water pressure is less due to gravel layer of higher permeability, hence no liquefaction occurs. It also seems that dissipation of EPP is

fast at shallow depth after completion of cyclic loading, which may be attributed to shorter drainage path for dissipation of excess pore pressure at shallow depth.

The stress paths noted in Fig. 4.9 shows the characteristic mechanism of cyclic decrease in effective stress due to generation of excess pore pressure, captured using the feature of the Pastor–Zienkiewicz Mark III model. It is also observed that maximum stress ratio q/p is 0.98 at the depth of 0.5 m, which decreases with depth mainly due to effect of overburden pressure.

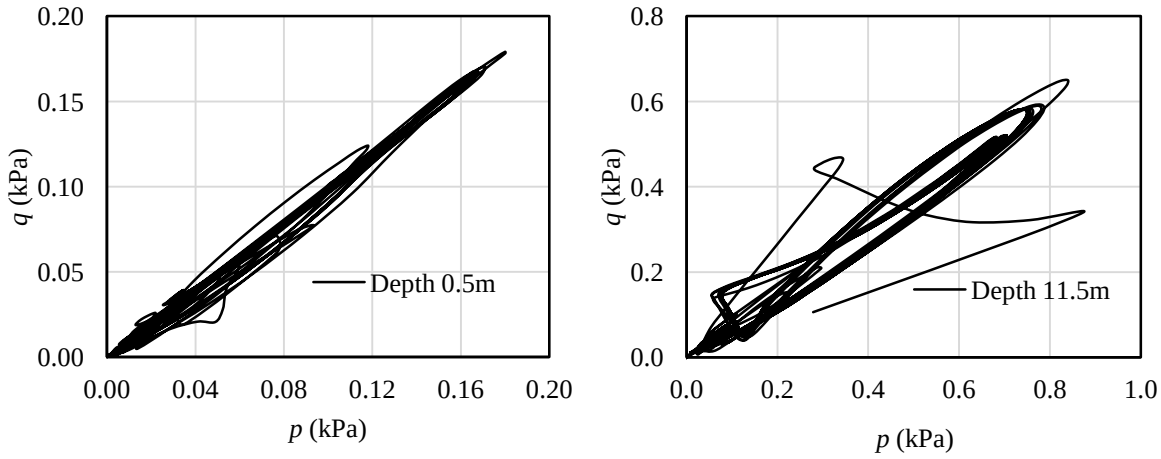

(a) 0.5m (b) 11.5m

Fig.4.9 Computed effective stress path at different depths (a) 0.5m (b) 11.5m

Figs. 4.10 and 4.11 show the computed horizontal and vertical acceleration time histories at different depths. It has been observed that the peak value of these parameters are found to be about 0.8 m/s^2 and 1.05 m/s^2 at top surface, resulting higher settlement. A relatively less value of accelerations are seen at 8m depth, corresponding to lesser excess pore pressure. A negligible acceleration is reported in both directions after the end of 15 cycle of loading. Results indicate amplification of earthquake input motion from base to the top surface showing maximum amplification at 4m depth.

4.7.3 Effect of Permeability

Soil stratum settles during dynamic shaking. The settlement increases with the increase in the amount of generated pore pressure and decrease or becomes stagnation corresponding to dissipation of excess pore pressure. Hence, the most significant factor which affects drainage is the permeability coefficient. A parametric study has been performed to outline the influence of permeability coefficient on liquefaction phenomena. The distributions of

displacement and EPP with time during the earthquake are presented in Figs. 4.12 and 4.13 respectively at three different value of permeability (k_1=1×10^{-4} m/sec, k_2=6.5×10^{-5} m/sec, k_3=1×10^{-7} m/sec**).**

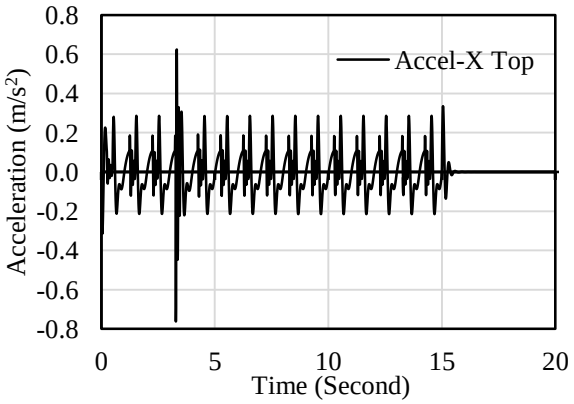

(a) Top surface

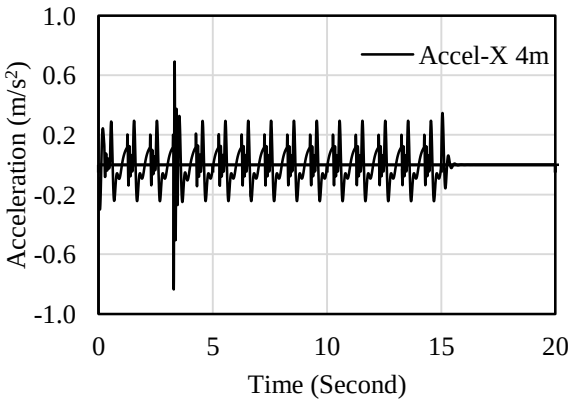

(b) 4m depth

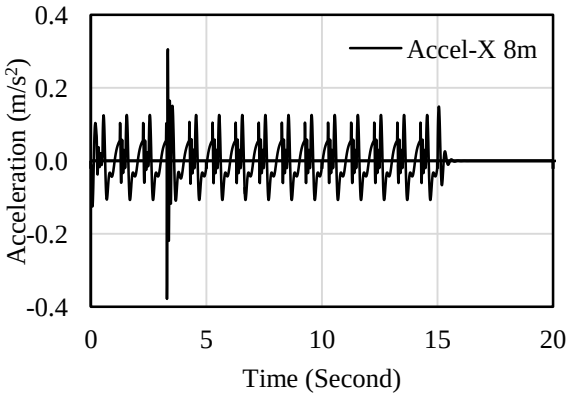

(c) 8m depth

Fig.4.10 Computed horizontal acceleration time histories at different depths

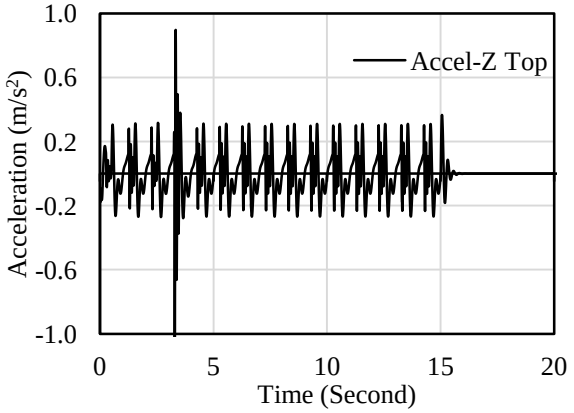

(a) Top surface

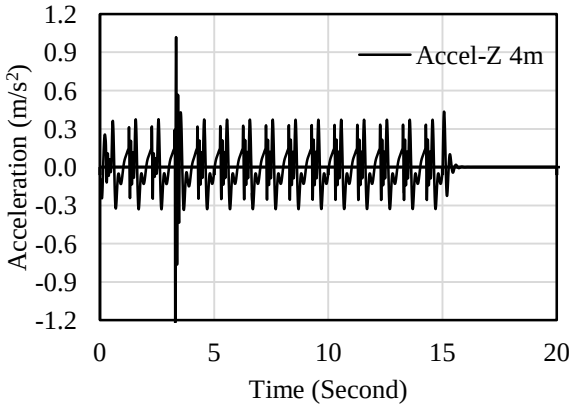

(b) 4m depth

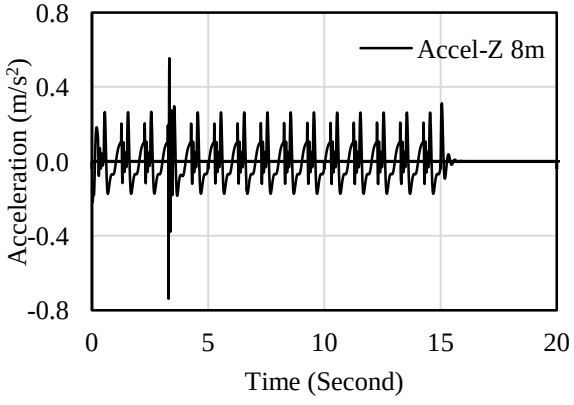

(c) 8m depth

Fig.4.11 Computed vertical acceleration time histories at different depths

From Fig.4.12, it has been observed that there is slight variation of about 1mm in maximum horizontal displacement (3.48cm) and 0.4mm in maximum vertical displacement (5.43cm) respectively with respect to permeability. It may be due to high

rise of pore water at the time of cyclic load and during this small duration a nearly undrained condition prevails irrespective of permeability.

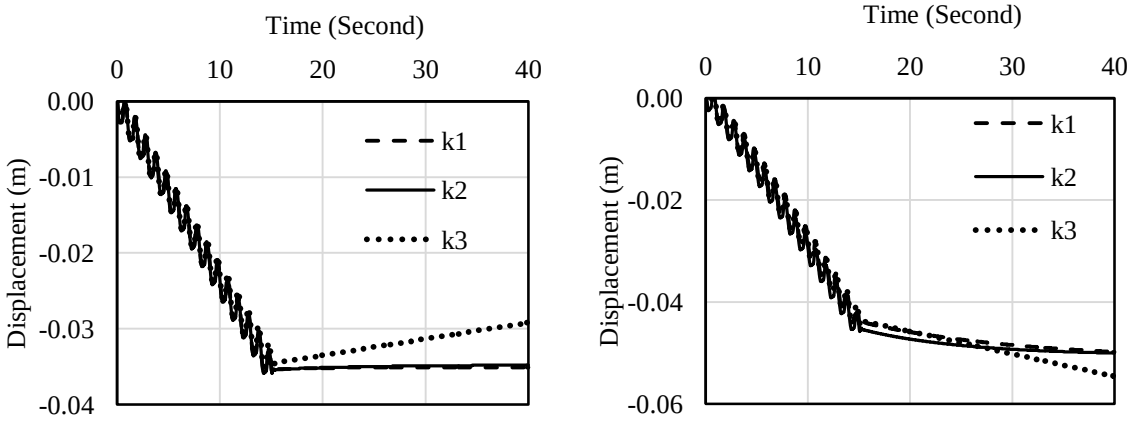

Horizontal Vertical

Fig. 4.12 Variation in displacement at top surface for different permeability

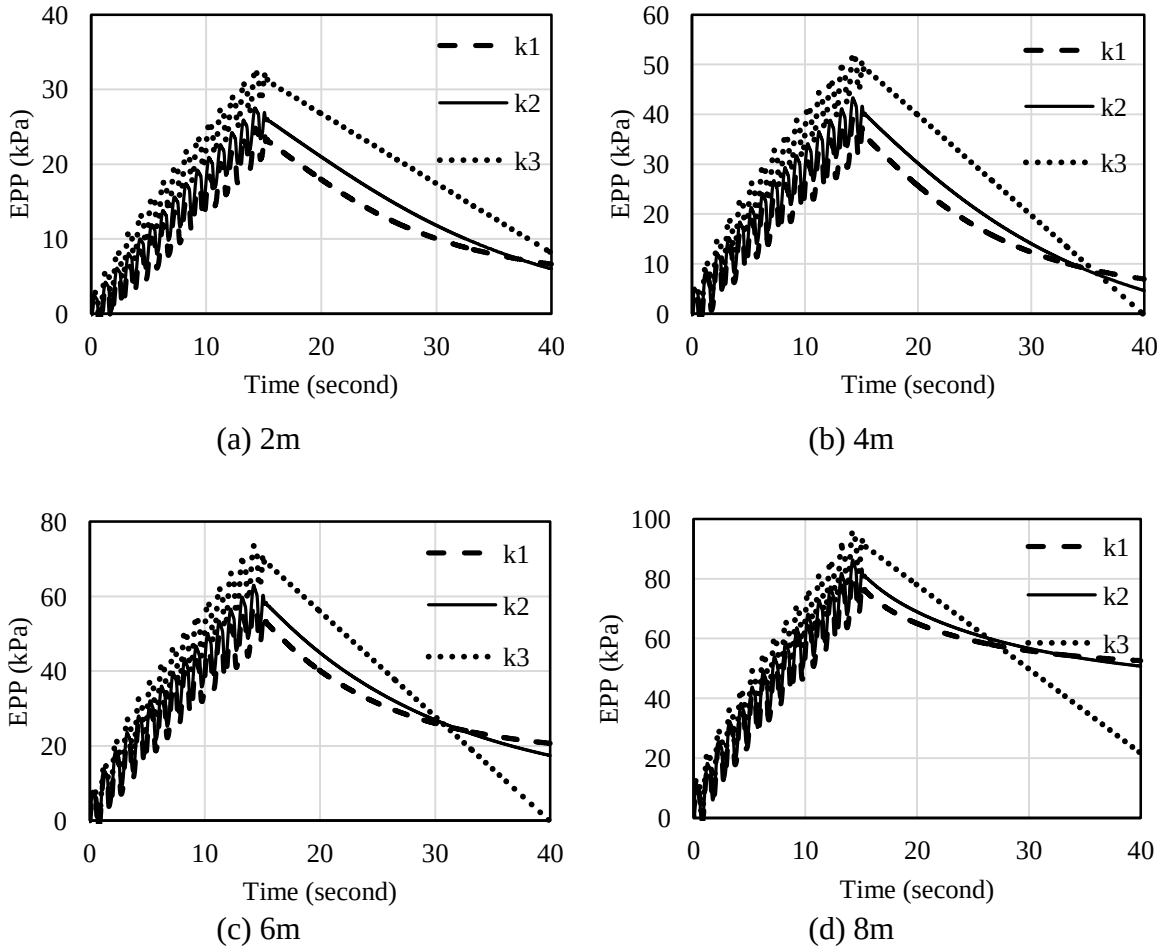

(a) 2m (b) 4m

(c) 6m (d) 8m

Fig.4.13 Computed EPP at different depths with respect to time at different permeability

Fig. 4.13 depicts a variation in generation of excess pore pressure (EPP) with respect to permeability at different depth. At depth of 2m, liquefaction occurs at 13.81 second for all three case of permeability because EPP is greater than initial effective stress. At depth of 4m liquefaction does not occur at higher permeability (k_1=1.0×10^{-4}m/sec), similar trend is observed at 8m also. Similarly at 6m depth, liquefaction is visible at k_2 and k_3 only. After end of the loading trend shows a clear indication of dissipation of excess pore pressure, thus the present model is able to capture generation and dissipation of excess pore pressure properly. The numerical results reveal that, a direct correlation exists in between the coefficient of permeability of soil mass and rate of generation and dissipation of excess pore pressure in liquefaction of soil.

4.7.4 Effect of Shear Modulus

To study the effect of shear modulus on sand liquefaction, shear modulus *G* has been varied as 10 MPa, 20 MPa and 30 MPa, while keeping other parameters constant. The present study is carried out at acceleration amplitude of 0.15 g with relative density of sand as 40%, permeability of 6.6×10^{-5} m/s. The variation of displacement and excess pore water pressure with at different shear modulus are shown Figs. 4.14 and 4.15 in respectively. A maximum value of horizontal displacement (3.56 cm) is noticed at *G* = 10 MPa whereas a minimum value of 0.43 cm at *G* = 30 MPa. A maximum value of vertical displacement (4.97 cm) is noticed at *G* = 20 MPa whereas a minimum value of 0.92 cm at *G* = 30 MPa. Displacements are decreasing with increase in soil modulus on the account of more stiffness.

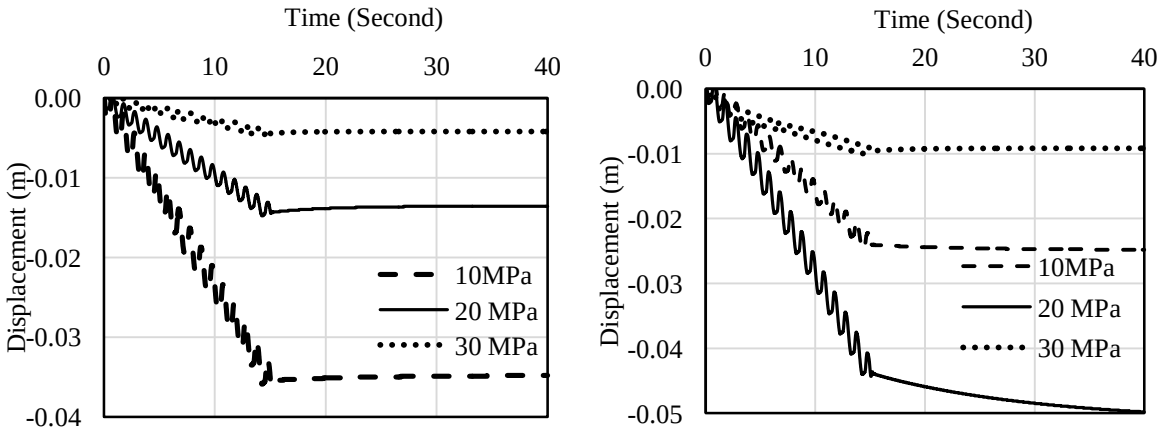

(a) Horizontal Displacement (b) Vertical Displacement

Fig. 4.14 Variation in top surface displacement with time for different shear modulus

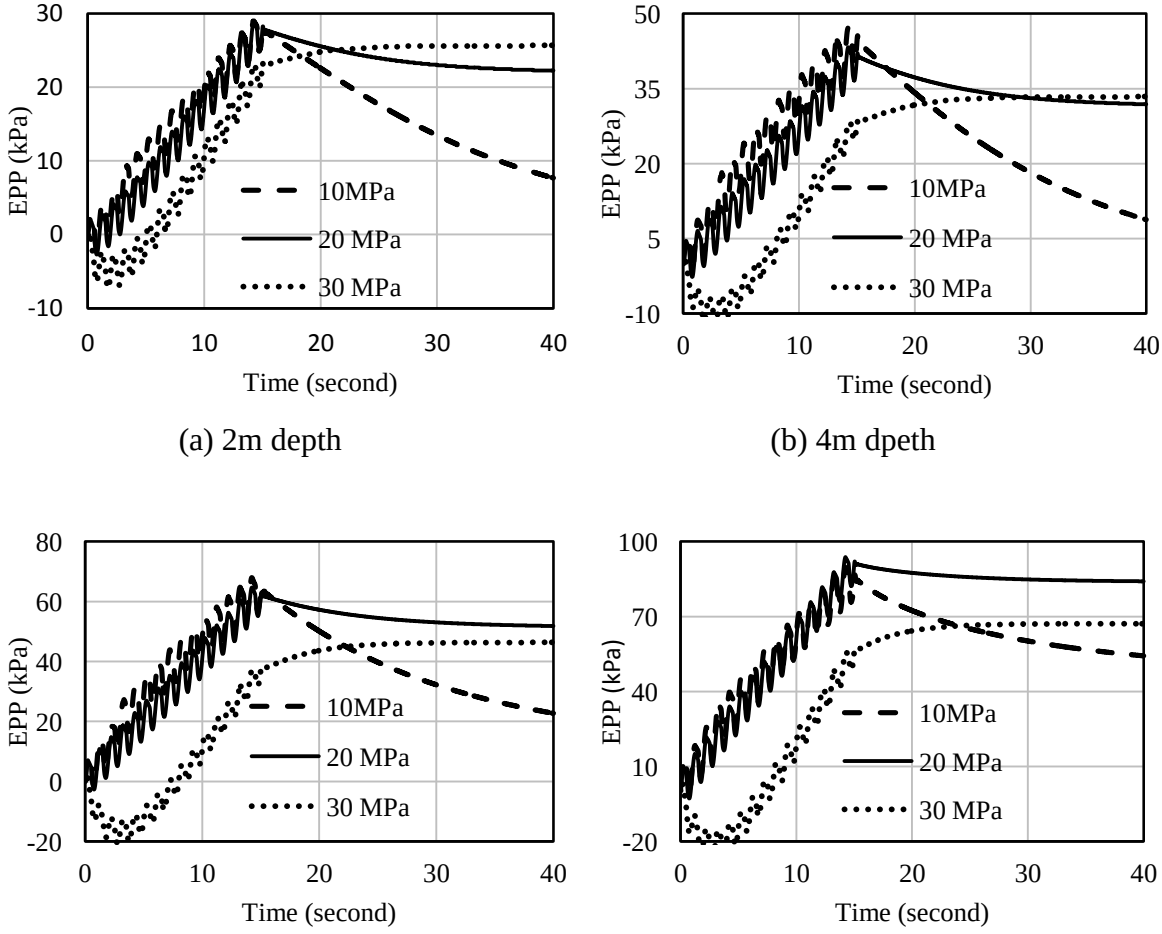

(a) 2m depth (b) 4m dpeth

(c) 6m depth (d) 8m depth

Fig.4.15 Variation in EPP with time at depths for different shear modulus

In general it is observed that EPP is building up with time. Similar trend of EPP with respect to time was reported by Dewoolar et al. (2009). From the variation of EPP with time (Fig. 4.15), it is observed that EPP are higher than initial effective stress for G = 10, and 20 MPa at all the depths upto 8m of suggesting initiation of liquefaction At higher value of shear modulus (G = 30MPa), liquefaction does not occur within the soil domain except at a depth of 2m. As the shear modulus is decreased, liquefaction phenomena is observed because of generation of higher displacement and pore pressure resulting in reducing the effective stress at shallow depth of soil mass. At higher soil modulus, more loads will be shared by skeleton. This in turn reduces the excess pore pressure at each step.

To examine the effect of permeability and shear modulus, a detailed study was considered in which as mentioned earlier three values of permeability were considered, but for each value of permeability, four different values of shear modulus (G = 10, 15,

20, 30 MPa) were assigned. To summarize the effect of these two key parameters, maximum values of displacement and EPP are reported in Table 4.2 to 4.4. From the reported values of maximum horizontal displacements (Table 4.2), the values are decreasing with increase in shear modulus. Reduction is of the order of 39 % to 92 % with higher values for higher shear modulus. They are also decreasing marginally with reduction in permeability. It is also observed that horizontal displacements are decreasing with depth. Similar trend was reported by Adalier et al. (2004). Similarly maximum vertical displacements (Table 4.3), the values are observed to be reducing with increase in shear modulus, but vertical displacements are slightly higher at lower permeability on account of higher EPP. Reduction is of the order of 34 % to 90 % for permeability k_1, 34 % to 65 % for permeability k_2, and 38 % to 70 % for permeability k_3. Higher percentage of reduction is corresponding to higher shear modulus. Effect of permeability is more pronounced in the values of EPP (Table 4.4). With reduction in permeability, considerable increase in EPP is observed. The change in permeability from k_1 to k_2 results in average 15 % increase in EPP, whereas 32 % increase in EPP is observed for change in permeability from k_1 to k_3. Similar trend for effect of permeability was reported by Finn et al. (1977), where dynamic analysis was performed using SHAKE program to consider liquefaction phenomenon. Marginal effect of shear modulus is observed on maximum EPP. There is slight reduction in EPP with increase in shear modulus.

Table 4.2 Comparison of maximum horizontal displacements

Permeability (m/sec)	G (MPa)	Disp (X-direction) at different depth in cm				
		Top	2m	4m	6m	8m
$k_1 = 1.0\times10^{-4}$	10	3.51	3.88	1.88	3.33	2.36
	15	2.08	2.35	1.18	2.02	1.43
	20	1.42	1.63	0.85	1.41	0.99
	30	0.26	0.30	0.15	0.26	0.17
$k_2 = 6.6\times10^{-5}$	10	3.48	3.86	1.88	3.31	2.35
	15	2.00	2.27	1.16	1.96	1.38
	20	1.36	1.58	0.83	1.36	0.96
	30	0.77	0.94	0.53	0.79	0.57
$k_3 = 1.0\times10^{-7}$	10	2.92	3.33	1.68	2.87	1.83
	15	1.32	1.63	0.92	1.44	0.85
	20	0.65	0.90	0.59	0.83	0.43
	30	0.24	0.29	0.29	0.30	0.16

Table 4.3 Comparison of maximum vertical displacements

Permeability (m/sec)	G (MPa)	Disp (Z-direction) at different depth in cm				
		Top	2m	4m	6m	8m
$k_1 = 1.0\times10^{-4}$	10	5.00	5.90	4.06	2.71	4.91
	15	3.28	3.90	2.69	1.73	3.28
	20	2.50	2.97	2.02	1.31	2.49
	30	0.50	0.59	0.40	0.26	0.49
$k_2 = 6.6\times10^{-5}$	10	4.98	5.89	4.07	2.68	4.92
	15	3.27	3.90	2.72	1.68	3.31
	20	2.48	2.96	2.04	1.27	2.51
	30	1.76	2.08	1.38	0.92	1.72
$k_3 = 1.0\times10^{-7}$	10	5.46	6.47	4.80	2.94	5.56
	15	3.32	4.09	3.25	1.51	3.69
	20	2.39	3.01	2.49	0.95	2.80
	30	1.57	2.03	1.74	0.53	1.94

Table 4.4 Comparison of maximum excess pore pressure

Permeability (m/sec)	G (MPa)	Maximum EPP at different depth in kPa				
		2m	4m	6m	8m	10m
$k_1 = 1.0\times10^{-4}$	10	24.8	39.1	58.1	81.9	56.2
	15	24.1	37.4	57.5	85.4	54.2
	20	25.3	38.0	58.6	89.0	52.7
	30	26.8	36.7	56.1	88.2	50.7
$k_2 = 6.6\times10^{-5}$	10	29.0	47.2	68.0	89.7	64.9
	15	27.3	42.2	63	90.1	54.5
	20	28.9	43.3	64.7	93.8	52.6
	30	31.5	43.3	64.0	94.5	51.0
$k_3 = 1.0\times10^{-7}$	10	32.6	52.2	73.5	96.0	56.9
	15	33.3	52.7	75.4	101.0	55.4
	20	27.2	35.2	56.4	97.6	52.6
	30	45.1	60.1	88.9	136	51.5

4.7.5 Effect of frequency of cyclic loading

To study the effect of dynamic loading frequency on sand liquefaction, sand beds are subjected to shaking at different frequencies, keeping other parameters constant except the shear modulus. The present study is carried out at acceleration amplitude of 0.15 g with R_D = 40 %, k = 6.6×10^{-5}m/s, G = 10-20 MPa, changing the frequency of shaking from 0.5 Hz to 2 Hz. Variation in displacement and EPP with time (k = 6.6×10^{-5}m/s, G = 10 MPa) are shown in Figs. 4.16 and 4.17, respectively. From the displacement response (Fig. 4.16), it is observed that the horizontal and vertical displacements are altered

significantly for frequency range 0.5–2 Hz. The maximum horizontal (1.72cm) and vertical displacement (2.22cm) are observed at frequency of 0.5 Hz whereas the lowest value of these values increased to horizontal (8.75cm) and vertical (14cm) at frequency of 2 Hz.

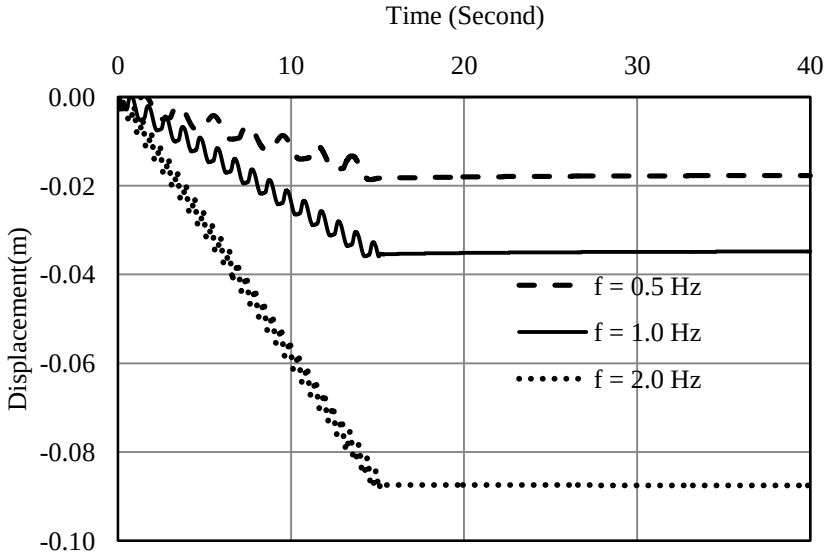

Fig. 4.16(a) Variation in horizontal displacement at top surface of sand bed subjected to different frequencies of shaking at 0.15 g

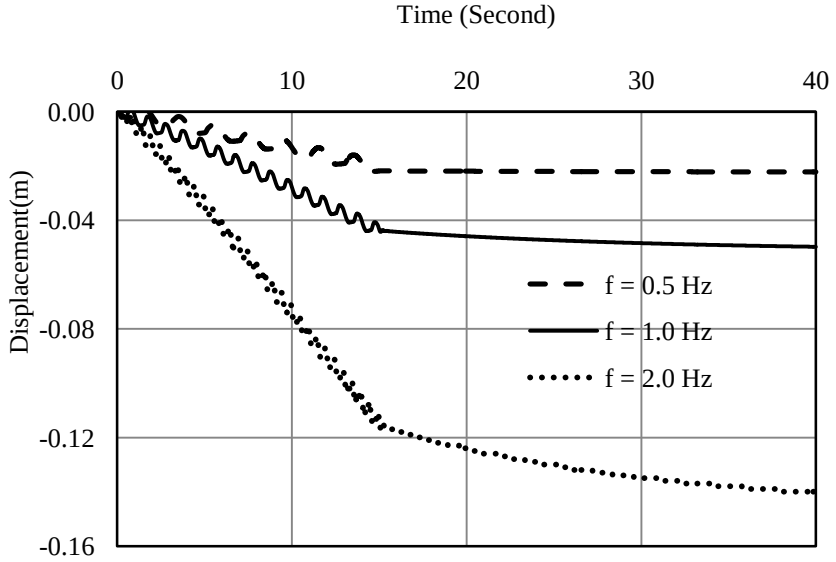

Fig. 4.16(b) Variation in vertical displacement at top surface of sand bed subjected to different frequencies of shaking at 0.15 g

From the variation in EPP (Fig. 4.17), EPP values are lower than initial effective stress at 0.5 Hz, so the effective stress does not drop down to zero, and hence, no liquefaction is visible at this particular frequency (0.5 Hz). It has been found from Fig.4.17 that the sand bed was subjected to liquefaction at 1.0 Hz and 2.0 Hz frequencies in 15 cycles of shaking, excess pore pressure increased drastically and reached a value higher than initial effective stress, and consequently the sand layers are liquefied. After completion of shaking period, dissipation of pore pressure is observed to be faster at frequency of 2 Hz, which can be attributed to higher effective stiffness at higher frequency. Figs.4.18 (a) and 4.18(b) demonstrate the effect frequency on computed horizontal and vertical acceleration at top surface. Horizontal acceleration is observed to increase with the frequency of loading (peak value 2.13 m/s^2) at 2 Hz frequency, whereas the peak value of vertical acceleration (1.08 m/s^2) is found to be at 1 Hz frequency.

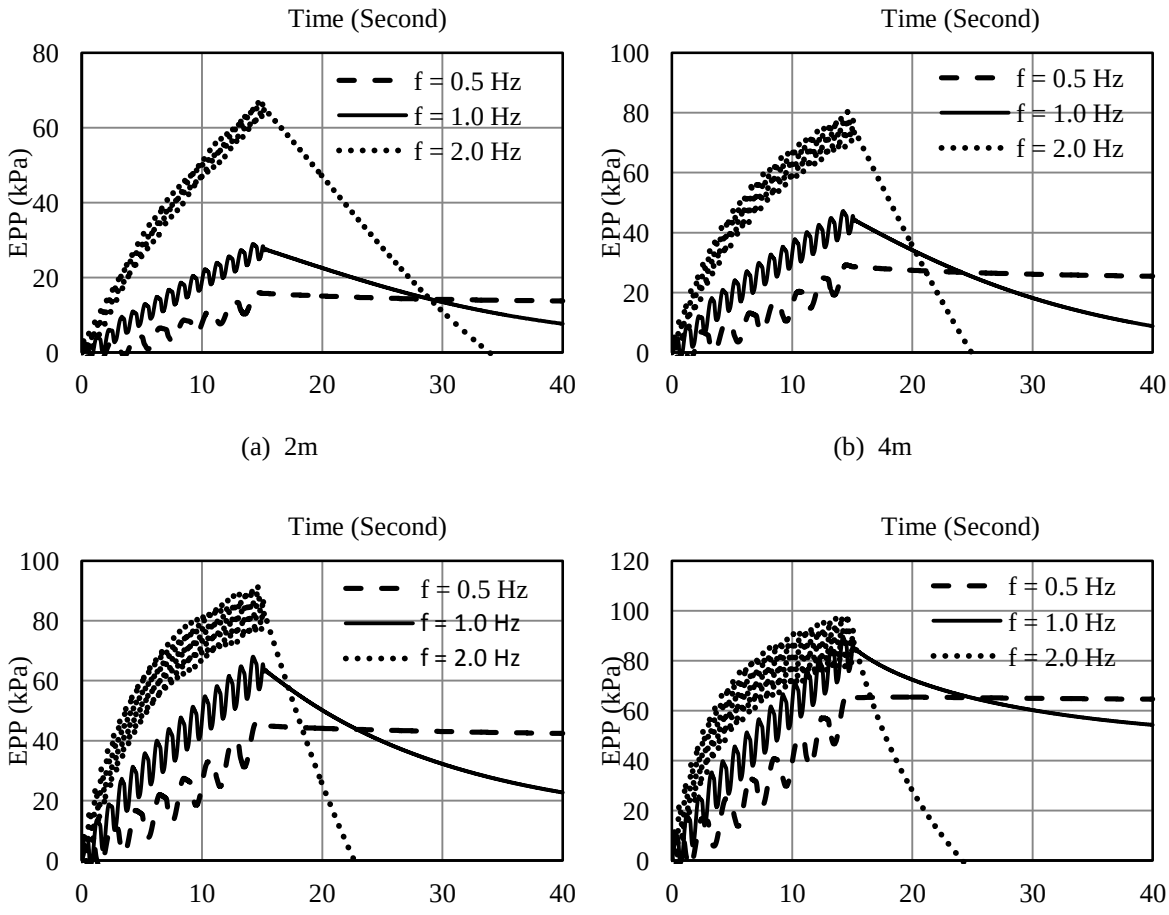

Fig. 4.17 Variation in EPP for sand bed subjected to different frequencies of shaking at 0.15 g at different depths

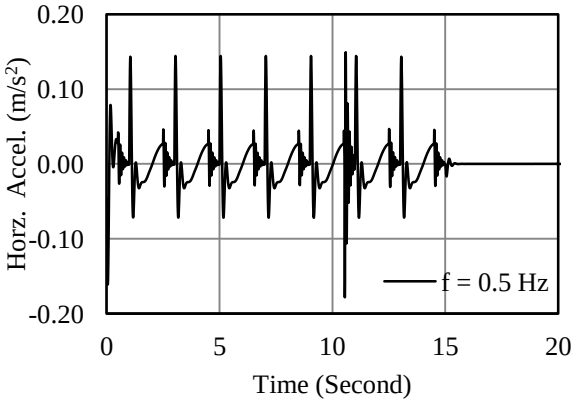

(a) 0.5 Hz

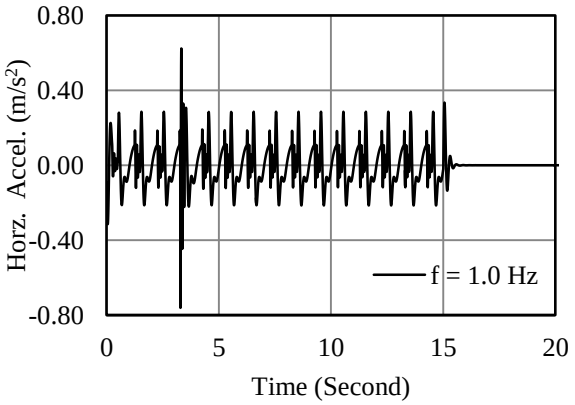

(b) 1.0 Hz

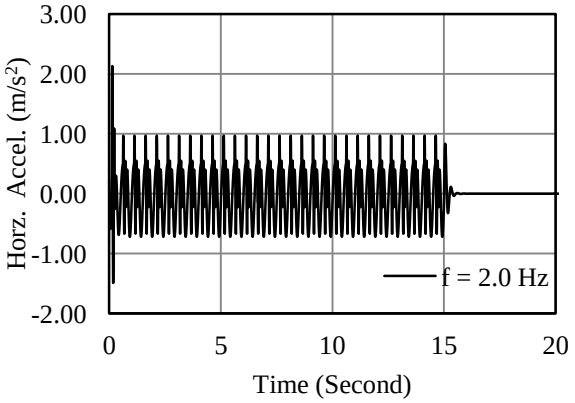

(c) 2.0 Hz

Fig. 4.18(a) Computed horizontal accel. time histories at different frequencies

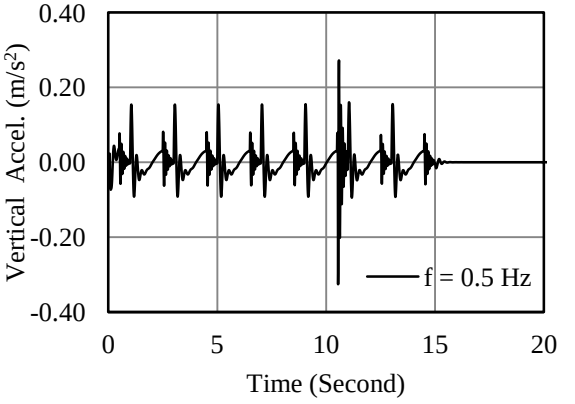

(a) 0.5 Hz

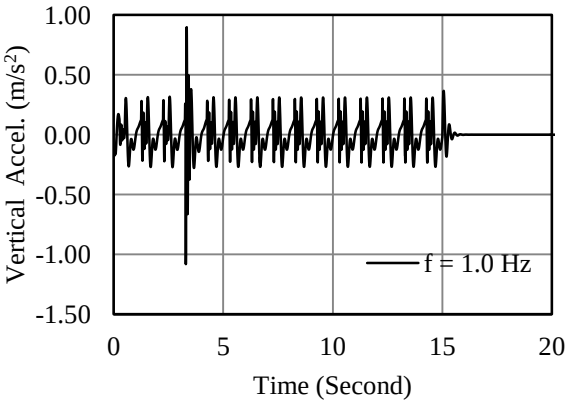

(b) 1.0 Hz

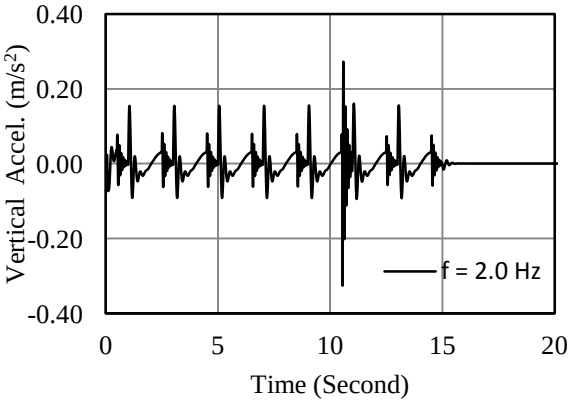

(c) 2.0 Hz

Fig.4.18(b) Computed vertical acceleration time histories at different frequencies

To summarize the effect of these frequencies and shear modulus, maximum values of displacement and EPP are reported in Table 4.5 to 4.6. From the reported values of maximum horizontal and vertical displacements (Table 4.5), the values are decreasing with increase in shear modulus. But effect of frequency is substantial. Values are

increasing with frequency. For example, maximum vertical displacement (G = 10 MPa) is 2.22cm at 0.5 Hz, 4.98cm at 1 Hz and 14cm at 2 Hz. With change in frequency from 0.5 Hz to 1 Hz, displacements are almost doubled, whereas changing frequency from 0.5 to 2 Hz displacements are increased 4 to 5 times.

Table 4.5 Comparison of displacements with variation in G and frequency

Frequency (Hz)	G (MPa)	Disp (X-direction) at different depth in cm				
		Top	2m	4m	6m	8m
0.5	10	1.72	1.93	0.92	1.73	1.16
	15	1.04	1.16	0.58	1.04	0.70
	20	0.71	0.81	0.42	0.72	0.49
	30	0.00	0.00	0.00	0.00	0.00
1.0	10	3.48	3.86	1.88	3.31	2.35
	15	2.00	2.27	1.16	1.96	1.38
	20	1.36	1.58	0.83	1.36	0.96
	30	0.77	0.94	0.53	0.79	0.57
2.0	10	8.75	10.00	4.90	8.36	6.08
	15	4.56	5.31	2.74	4.41	3.24
	20	2.92	3.47	1.86	2.87	2.11
	30	0.08	0	0	0	0
		Disp (Z-direction) at different depth in cm				
0.5	10	2.22	2.71	2.03	1.11	2.37
	15	1.56	1.90	1.40	0.76	1.66
	20	1.16	1.42	1.03	0.54	1.25
	30	0.00	0.00	0.00	0.00	0.00
1.0	10	4.98	5.89	4.07	2.68	4.92
	15	3.27	3.90	2.72	1.68	3.31
	20	2.48	2.96	2.04	1.27	2.51
	30	1.76	2.08	1.38	0.92	1.72
2.0	10	14.00	16.60	10.40	7.23	13.20
	15	8.30	9.77	6.27	4.39	7.89
	20	5.95	6.98	4.46	3.14	5.65
	30	0.21	0	0	0	0

Similar effects are observed on EPP. Predicted values of maximum are decreasing with increase in shear modulus. But with increase in the frequency, values are increasing drastically. For example, maximum EPP (G = 10 MPa) is 13.8 kPa cm at 0.5 Hz, 29 kPa at 1 Hz and 67.4 kPa at 2 Hz. Similar effect on EPP was reported by Renjitha and Latha (2014). Trend of increase in EPP is decreasing with increase in shear modulus. With increase in frequency, accelerations are increasing which results in increasing the values

of EPP and displacements. Similarly from the variation of maximum EPP with depth (Fig. 4.19), it is observed that values of EPP are increasing with depth up to 8 m, but at the 10 m depth significant reduction in EPP is observed due to presence of gravel layer of higher permeability below. This is also clear from the typical contour map of EPP presented in Fig 4.20. Here also it is observed that up to 9m (Z-coordinate 4 m) EPP is increasing with depth and after that reduction in EPP is observed.

Table 4.6 Comparison of EPP with variation in *G* and frequency

Frequency (Hz)	G (MPa)	Maximum EPP at different depth in kPa				
		2m	4m	6m	8m	10m
0.5 Hz	10	13.8	25.5	42.4	64.6	42.6
	15	14.9	26.5	44.1	69.4	40.6
	20	25.4	40.5	58.7	81.7	41.8
	30	1.9	11.2	21.6	29.0	41.2
1.0 Hz	10	29.0	47.2	68	89.7	64.9
	15	27.3	42.2	63	90.1	54.5
	20	28.9	43.3	64.7	93.8	52.6
	30	25.7	33.3	46.3	67.1	100
2.0 Hz	10	67.4	80.3	92	98.8	94.2
	15	52.3	52.8	56.6	61.3	90.1
	20	51.0	45.6	46.0	50.4	88.7
	30	-8.8	-8.9	-6.2	-0.8	19.4

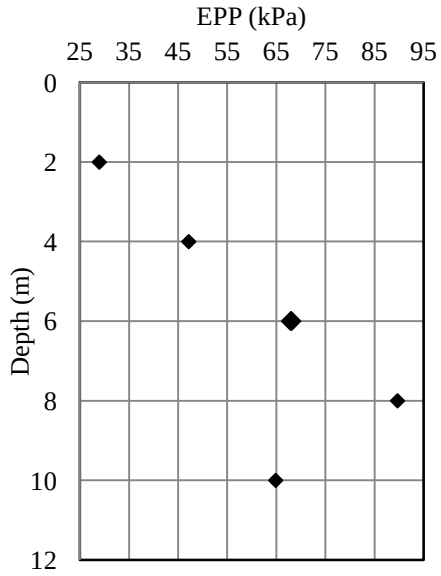

Fig.4.19 Variation of maximum EPP along depth

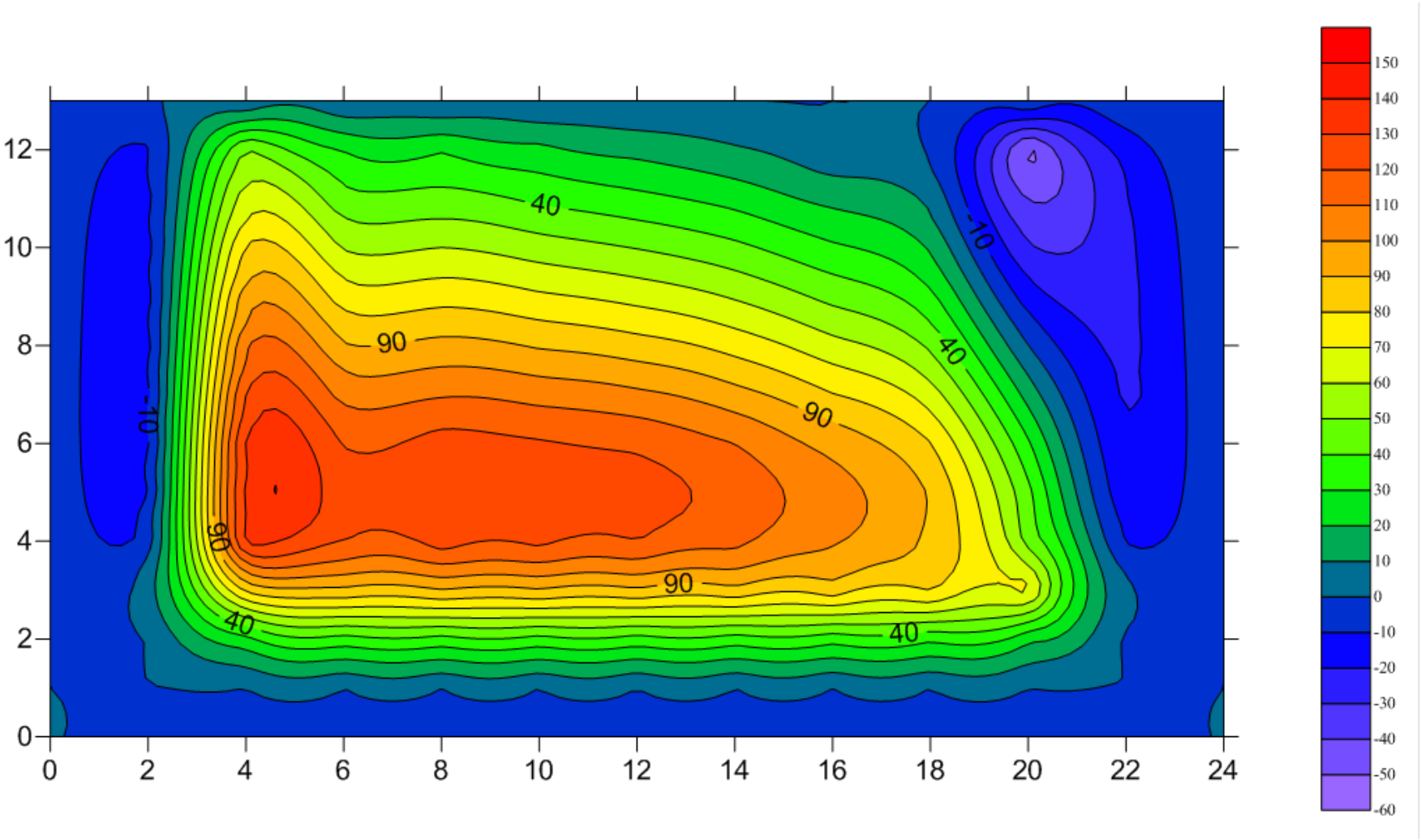

Fig.4.20 Contour map for EPP variation in cyclic loading

4.8 NUMERICAL SIMULATION UNDER SEISMIC LOAD

The model considered for cyclic case, is extended for seismic excitation with same material properties and boundary conditions. Mainly El-Centro ground motion (Fig. 4.21) is considered for seismic loading in the parametric study. Response in the form of resultant displacements, liquefaction tendencies, excess pore pressure and other parameter are studied. The time step used is same as time interval of input motion.

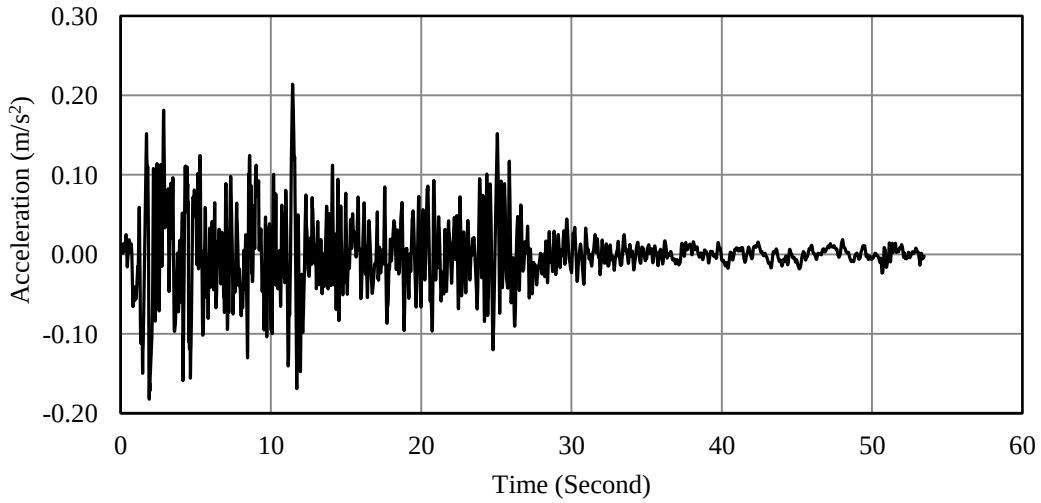

Fig.4.21 El-Centro earthquake ground motion

4.8.1 Results and discussion

Variation in predicted horizontal and vertical displacement at different depth with respect to time for El-Centro earthquake (k = 6.6×10^{-5} m/s and G = 8 MPa) has been shown in Fig. 4.22 and 4.23 respectively. The maximum values of horizontal settlement of 8.79 cm are predicted at the top of soil layer; whereas maximum values of vertical settlement of 9.64 cm are predicted at 8m depth because higher confining stress at bottom. It has been observed that the maximum settlements occur after 15 seconds of loading. After attaining maximum value, settlement again decreased and almost become constant during the rest of the shaking period. Similar trend in displacement was reported by Taiebat et al. (2007) under seismic loading. Generally, the horizontal settlement is less than vertical settlement at different depths.

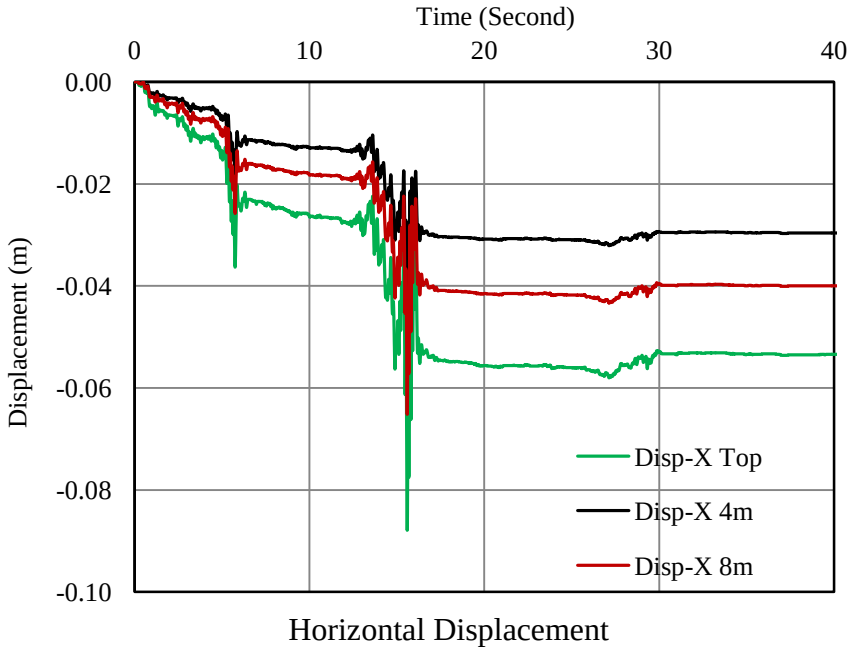

Fig.4.22 Variation in computed horizontal displacement at different depth

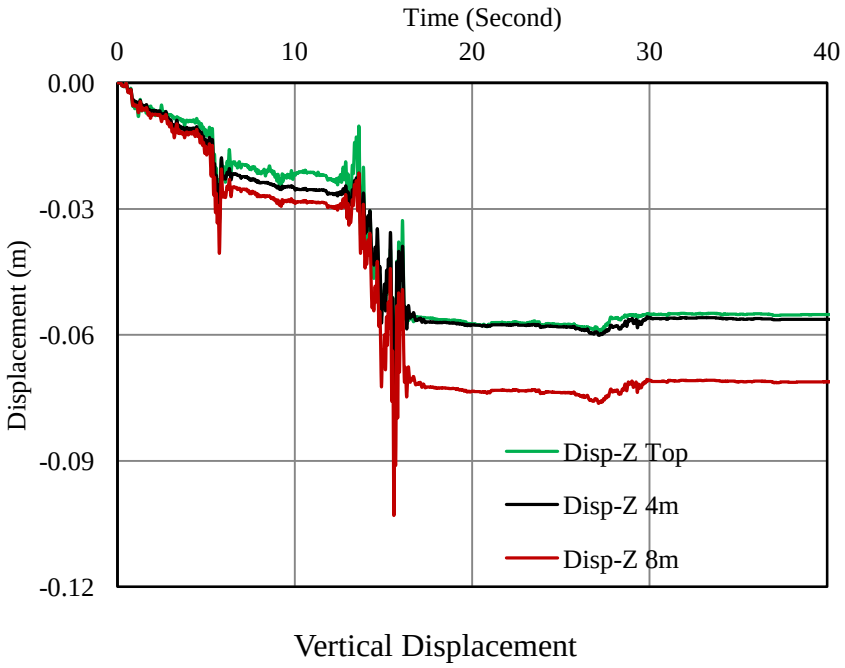

Fig.4.23 Variation in computed vertical displacement at different depth

Fig. 4.24 displays the computed excess pore pressure at different depth. The first maximum peak in EPP is attained at 5.73 seconds for a very small duration. At depth of 2m, 4m, 6m and 8m, EPP is higher than initial vertical stress at this particular time, resulting the phenomenon of liquefaction. At 10m depth of soil domain, increase in

excess pore pressure is less due to gravel layer of higher permeability, hence no liquefaction is visible. After this time a sudden decrease in EPP is noticed. Again after 8.38 second of loading a maximum peak in EPP is noticed. But this high value of EPP is retained for a longer duration of time, showing complete liquefaction. The numerical analysis is very much efficient in dissipating the energy. After attaining a maximum value of EPP, the model is efficient in dissipation the extra pore pressure. This trend is same at all the depth of the soil stratum. Similar trend of EPP was reported by Taiebat et al. (2007) under seismic loading.

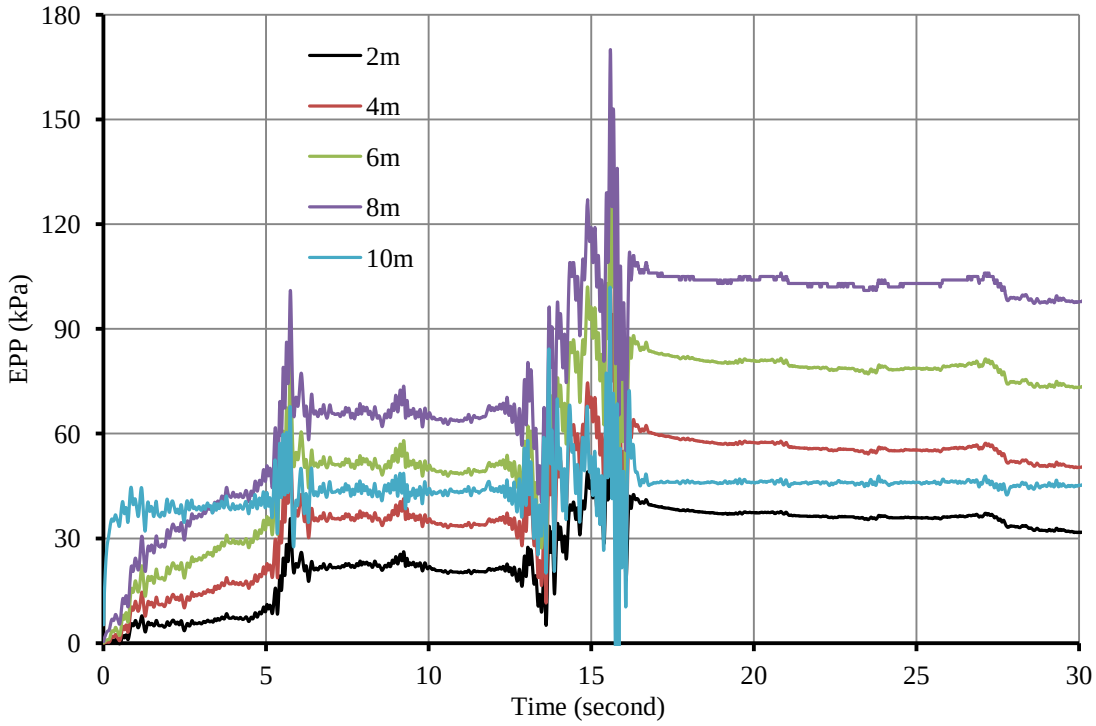

Fig.4.24 Computed EPP at depths 2m, 4m, 6m, 8m and 10m with respect to time

The stress paths presented in Fig. 4.25 shows the characteristic mechanism of cyclic decrease in effective stress due to excess pore pressure build-up, captured using the Pastor–Zienkiewicz Mark III model. It is observed that maximum stress ratio q/p is 1.05 at the depth of 0.5 m and 0.64 at 11.5m depth. The trend indicates a decreases value with depth mainly due to effect of overburden pressure.

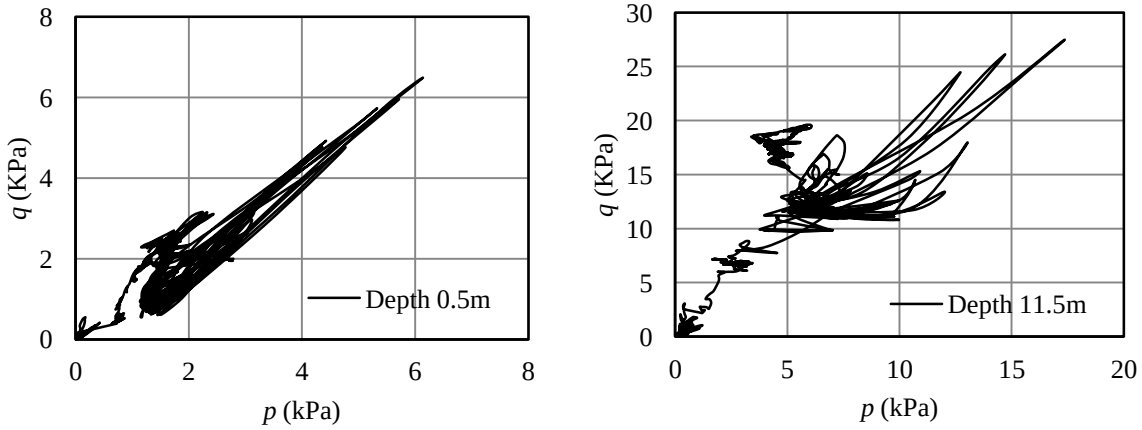

(a) 0.5m (b) 11.5m

Fig.4.25 Computed effective stress path at different depths (a) 0.5m (b) 11.5m

Figs. 4.26 and 4.27 show the computed horizontal and vertical acceleration time histories at different depths. It has been observed that the peak value of these parameters is found to be about 2.8 m/s^2 and 4.4 m/s^2 at top surface, resulting higher settlement. A relatively less value of accelerations are seen at 4m depth, corresponding to lesser excess pore pressure. A sudden peak in acceleration response is noticed at 5.73 second. At this particular time, sudden increase in displacement as well as EPP was also noticed because soil deposits show peak amplification in acceleration response at this point of time. This trend occurs only for very small span of time. A less value of acceleration is reported in both directions after 15.62 second of shaking. Results indicate amplification of earthquake input motion from base to the top surface showing maximum amplification at 4m depth. Sharp spikes are observed at 15 second of shaking at all the depth of soil stratum. The settlement and EPP are also very high at this particular time, marking the occurrence of liquefaction phenomena. In acceleration time history involving the soil densification, a significant decrease is observed in asymmetric spiky response after liquefaction. This can be explained by lesser lateral displacements after 15.62 seconds. The acceleration values are comparable in shape and magnitude to the input ground motion, showing an attenuation-spiky behavior. This behaviour may be defined as the gradual EPP-induced strength degradation, with stress-path excursions along the phase transformation line. Finally, full attenuation of ground motions occurs at the time when shear strength is almost lost due to liquefaction. It can be found (Figs. 4.26 and 4.27) that

the behaviour of liquefaction response progress from the surface downwards, in due course of time affecting the entire soil domain.

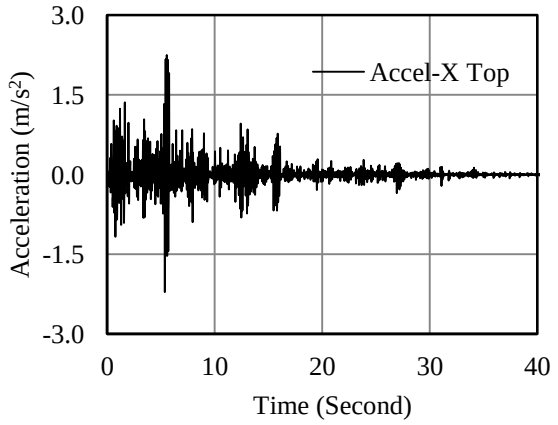

(a)

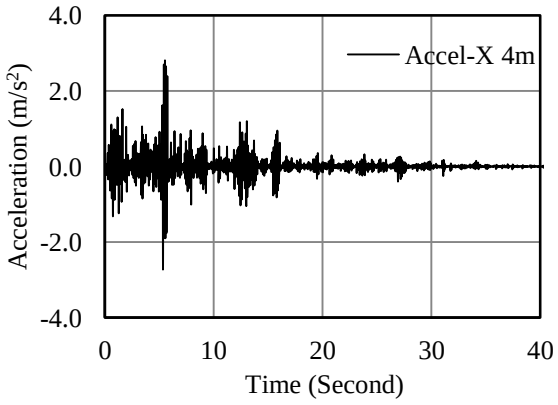

(b)

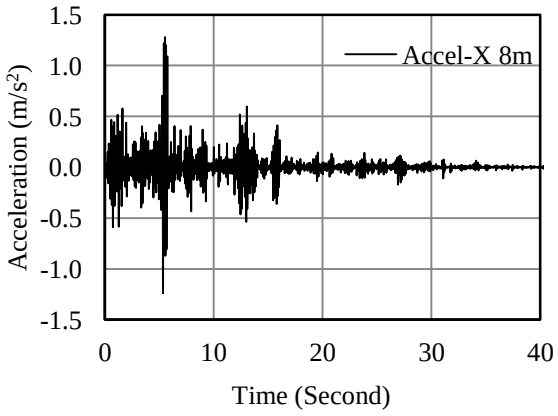

(c)

Fig.4.26 Computed horizontal acceleration time histories at different depths

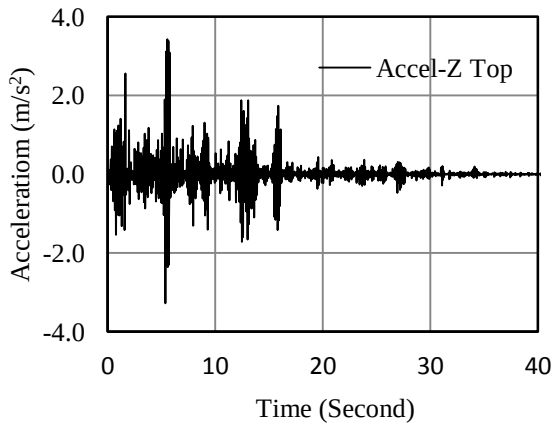

(a)

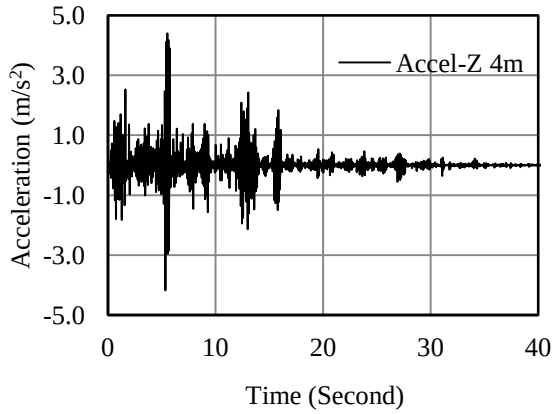

(b)

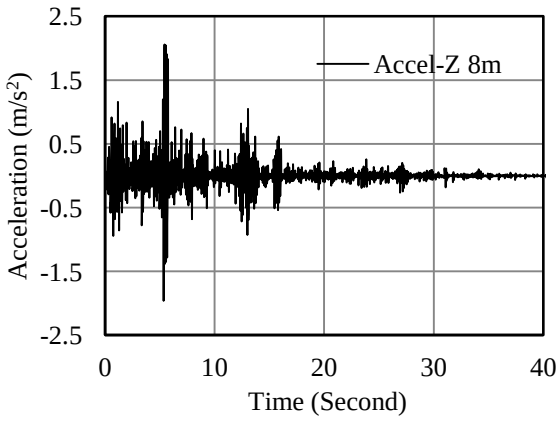

(c)

Fig.4.27 Computed vertical acceleration time histories at different depths

4.8.2 Effect of Permeability

A parametric study has been carried out to examine the effect of permeability coefficient on liquefaction phenomena during seismic loading. The distributions of displacement and pore pressure that developed at various times when drainage occurs during the earthquake are presented in Figs. 4.28 and 4.29 respectively at three different value of permeability (k_1=1×10^{-4} m/sec, k_2 = 6.5×10^{-5} m/sec, k_3 = 1×10^{-7} m/sec) at G = 8MPa.

From Fig.4.28, it has been observed that there is negligible variation in maximum horizontal displacement (2cm) and maximum vertical displacement (2.17cm) with respect to permeability. It may be due to high rise of pore water at the time of seismic load and during this small duration a nearly undrained condition prevails irrespective of permeability.

Fig. 4.29 depicts a variation in generation of excess pore pressure (EPP) with respect to permeability at different depth. At depth of 2m, liquefaction is noticed for k_3=1.0×10^{7}m/sec after 5.61 seconds because EPP is greater than initial effective stress, whereas at other permeability, liquefaction is not observed. Similar trend in EPP is also found at 4m and 6m depth for k_3=1.0×10^{-7}m/sec and encounter with nearly zero effective stress resulting liquefaction after 11.23 seconds and 12.39 seconds respectively. This suggests that liquefaction is triggered initially at a shallow depth (2m after 5.61s) and then progressed downward (4m after 11.23s and 6m after 12.39s). After liquefaction of top layer, load is transferred to next layer. But, for k_1=1.0×10^{-4} m/sec and k_2 = 6.5×10^{-5} m/sec, non zero effective stress is found at 2m, 4m and 6m due to rapid dissipation of excess pore pressure at higher value of permeability.

At 8m depth liquefaction does not occur at any value of permeability, due to presence of the gravel layer after 10m depth, indicating marginal effect of seismic loading due to higher permeability. The predicted results reveal that the existence of direct relationship in between permeability coefficient and rate generation and dissipation of EPP during liquefaction.

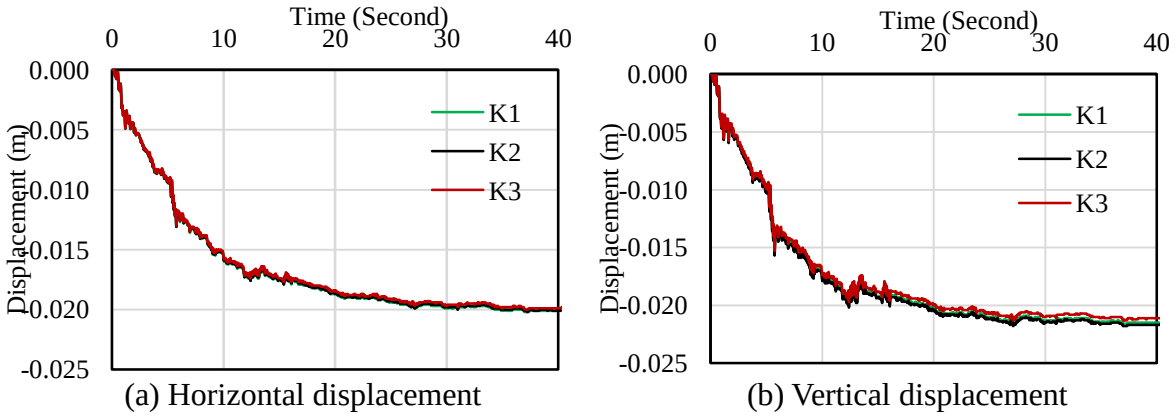

(a) Horizontal displacement (b) Vertical displacement

Fig. 4.28 Variation in displacement at top surface with different permeability

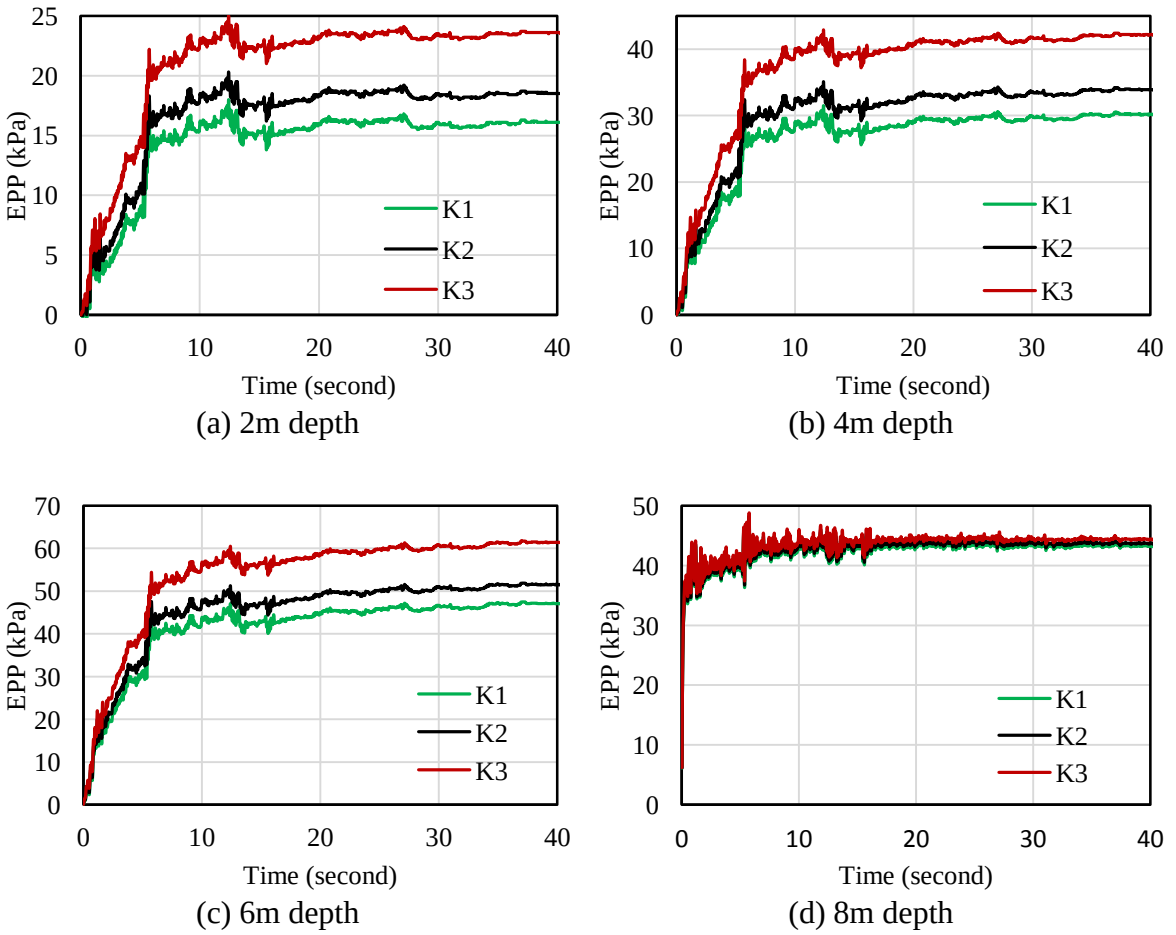

(a) 2m depth (b) 4m depth

(c) 6m depth (d) 8m depth

Fig.4.29 Variation in EPP with time at different permeability

4.8.3 Effect of Shear Modulus

To study the effect of shear modulus on sand liquefaction, shear modulus G has been varied as 8 MPa, 10 MPa and 15 MPa, while keeping other parameters constant. The variations in horizontal and vertical displacement with time for different value of shear modulus are shown Fig. 4.30. A maximum horizontal displacement 7.72 cm is noticed at G = 8 MPa which is reduced to of 1.24 cm at G = 15 MPa. A maximum value of vertical displacement (7.43 cm) is noticed at G = 8 MPa whereas a maximum value of 1.52 cm at G = 15 MPa. It is observed that vertical displacement at G = 10 MPa are higher than those at G = 8 MPa. This may be attributed to the fundamental frequency of the domain may be close to operating frequency.

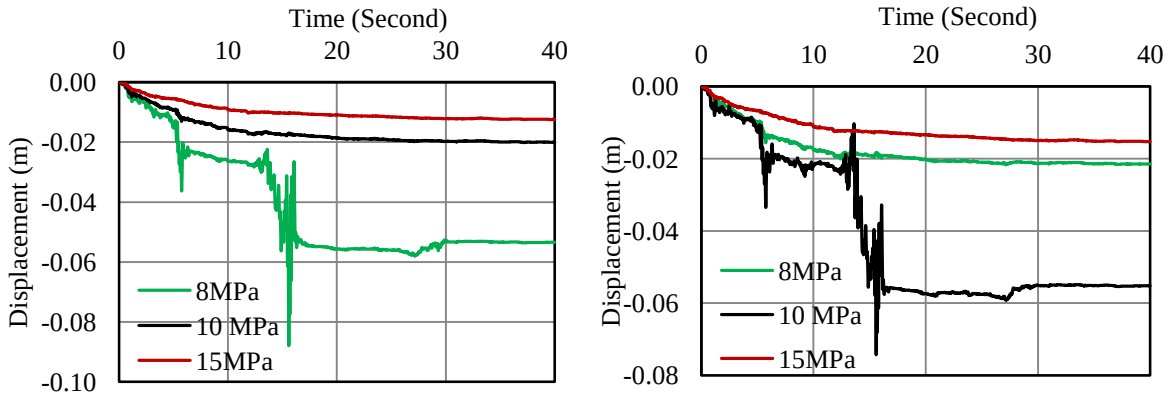

(a) Horizontal Displacement (b) Vertical Displacement

Fig.4.30 Variation in Displacement at top surface of sand bed subjected to different shear modulus

Fig. 4.31 shows variation of excess pore pressure for different value of shear modulus. For typical rise in EPP is visible at t = 5.73 second for G = 8 MPa along all the depth of soil mass. The evaluated EPP is higher than the initial vertical stress, indicating occurrence of liquefaction phenomenon. At shear modulus of G = 10 MPa liquefaction does not occur within the soil domain except at a depth of 2m whereas for G = 15 MPa liquefaction does not occur at any depth of soil mass. Hence, as the shear modulus is decreased, liquefaction phenomena is observed because of generation of higher displacement and pore pressure resulting in reducing the effective stress at shallow depth of soil mass. At higher soil modulus, more loads will be shared by skeleton. This in turn reduces the excess pore pressure at each step.

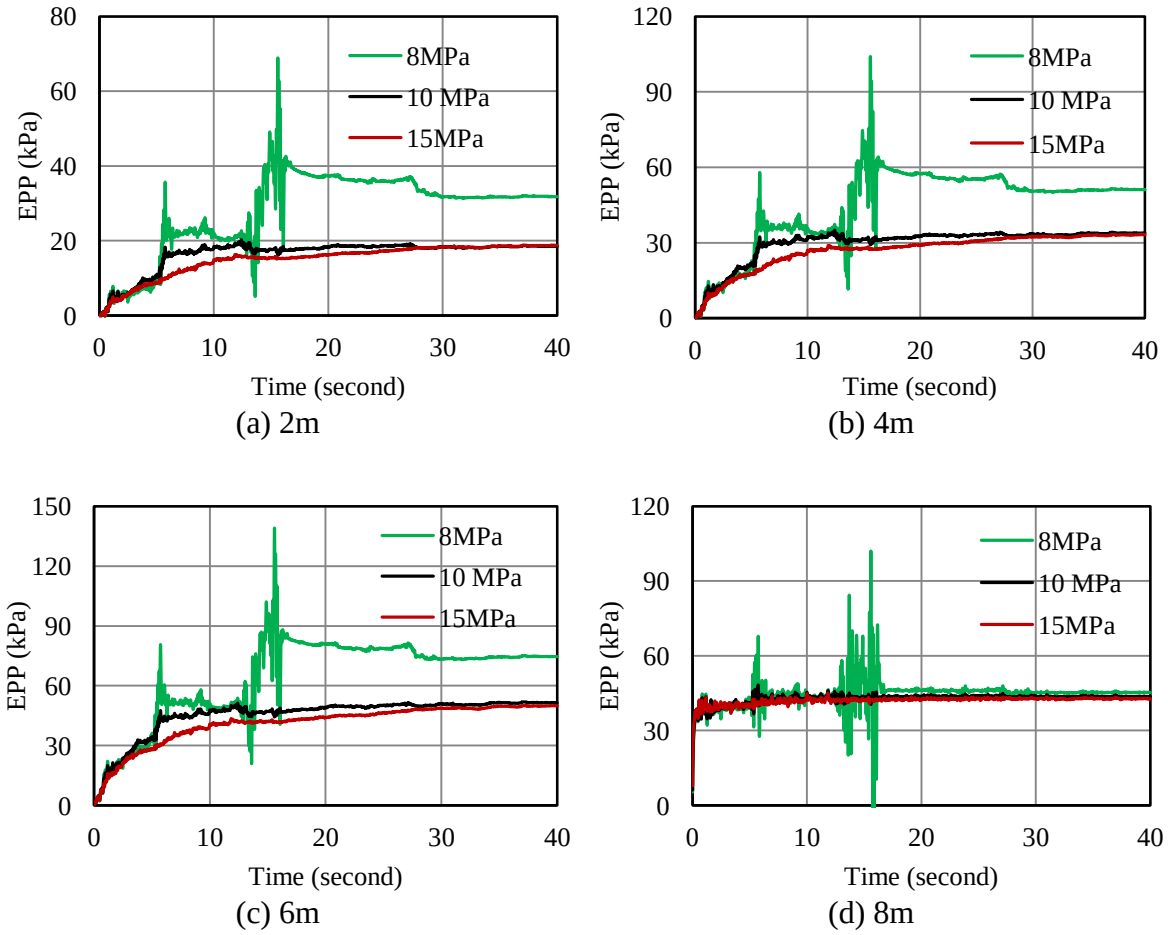

Fig. 4.31 Effect of shear modulus on variation in EPP with time

To examine the effect of permeability and shear modulus, a detailed study was considered in which as mentioned earlier three values of permeability were considered, but for each value of permeability, three different values of shear modulus (G = 8, 10, 15 MPa) were assigned. To summarize the effect of these two key parameters, maximum values of displacement and EPP are reported in Table 4.7 to 4.9. From the reported values of maximum horizontal displacements (Table 4.7), the values are decreasing with increase in shear modulus. Average reductions are in the order of 79.6% (G = 10 MPa) and 87% (G = 15 MPa). They are also decreasing marginally with reduction in permeability. Similarly maximum vertical displacements (Table 4.8), the values are observed to be reducing with increase in shear modulus. Average reductions are in the order of 75.5% (G = 10 MPa) and 83% (G = 15 MPa). Similar trend for displacements corresponding to shear modulus was reported by Adalier et al. (2004). Effect of permeability on displacements is marginal. Values are slightly reduced with decrease in permeability. Effect of permeability is more

pronounced in the values of EPP (Table 4.9). With change in permeability from k_1 to k_2, average increase in EPP is of the order 3.5 to 17% (higher value for higher modulus). Similarly, for change in permeability from k_1 to k_3, EPP are increased by 9.6 to 56% (again higher value for higher modulus). Drastic effect of shear modulus is observed on maximum EPP. A considerable reduction in EPP with increase in shear modulus is observed when shear modulus is increased from 8 MPa to 10 MPa or some higher value. Increase is of the order of 52 to 76%. Effect is more in significant in case of higher permeability. Similar trend for effect of permeability was reported by Finn et al. (1977).

Table 4.7 Comparison of maximum horizontal displacements

Permeability (m/sec)	*G* (MPa)	Disp (X-direction) at different depth in cm				
		Top	2m	4m	6m	8m
$k_1 = 1.0\times10^{-4}$	8	8.79	10.30	4.65	9.75	6.53
	10	2.02	2.06	0.96	1.79	1.30
	15	1.26	1.31	0.62	1.12	0.80
$k_2 = 6.6\times10^{-5}$	8	8.79	10.30	4.65	9.75	6.52
	10	2.02	2.05	0.96	1.79	1.30
	15	1.25	1.29	0.61	1.11	0.79
$k_3 = 1.0\times10^{-7}$	8	8.77	10.30	4.63	9.74	6.49
	10	2.00	2.04	0.95	1.78	1.28
	15	1.20	1.25	0.59	1.09	0.75

Table 4.8 Comparison of maximum vertical displacements

Permeability (m/sec)	*G* (MPa)	Disp (Z-direction) at different depth in cm				
		Top	2m	4m	6m	8m
$k_1 = 1.0\times10^{-4}$	8	7.44	11.70	8.14	-1.43	10.30
	10	2.18	2.48	2.04	1.65	2.30
	15	1.56	1.77	1.36	1.12	1.58
$k_2 = 6.6\times10^{-5}$	8	7.43	11.70	8.15	-1.44	10.30
	10	2.16	2.47	2.04	1.63	2.29
	15	1.53	1.75	1.36	1.10	1.57
$k_3 = 1.0\times10^{-7}$	8	7.39	11.70	8.18	-1.47	10.20
	10	2.13	2.44	2.05	1.59	2.28
	15	1.46	1.71	1.38	1.02	1.55

Fig. 4.32 depicts the variation of computed EPP along the depth for the case $k = 6.6\times10^{-5}$ m/sec and G = 8MPa. It has been observed that the value of EPP is increasing along the depth but at 10 m depth, a reducing trend has been predicted due presence of gravel deposit having higher permeability. The input value of are assigned as input parameter.

This is also clear from the typical contour map of EPP presented in Fig 4.33. Here also it is observed that up to 9 m (Z-coordinate 5 m) EPP is increasing with depth and after that reduction in EPP is observed.

Table 4.9 Comparison of maximum EPP

Permeability (m/sec)	G (MPa)	Maximum EPP at different depth in kPa				
		2m	4m	6m	8m	10m
$k_1 = 1.0\times10^{-4}$	8	66.7	99.9	134	165	102
	10	18	31.5	47.1	63.8	47.9
	15	15.7	29.1	45.4	63.5	42.5
$k_2 = 6.6\times10^{-5}$	8	68.9	104	139	170	102
	10	20.3	35.1	51.3	68	45.7
	15	19.5	34.6	51.8	70.6	42.9
$k_3 = 1.0\times10^{-7}$	8	72.5	112	149	176	103
	10	25	42.9	60.5	74.7	46.4
	15	28	47.9	67.7	83.5	43.6

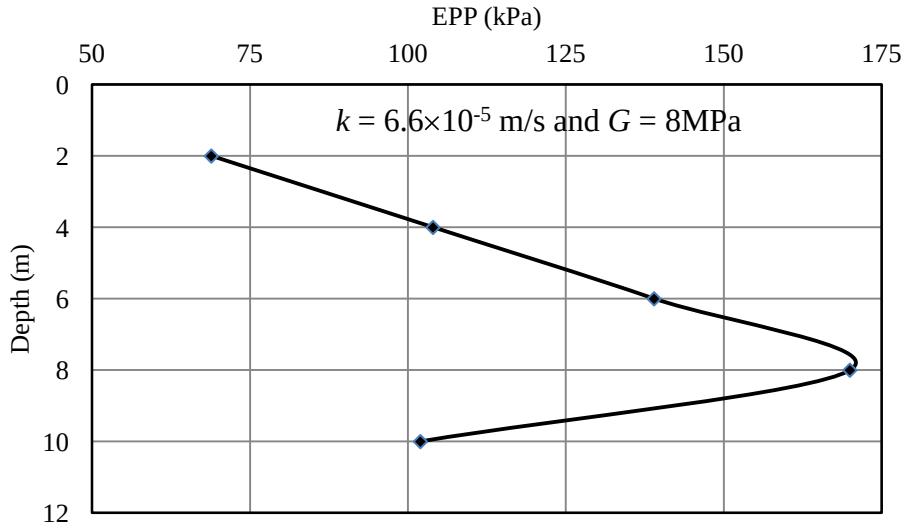

Fig.4.32 Variation of EPP along depth

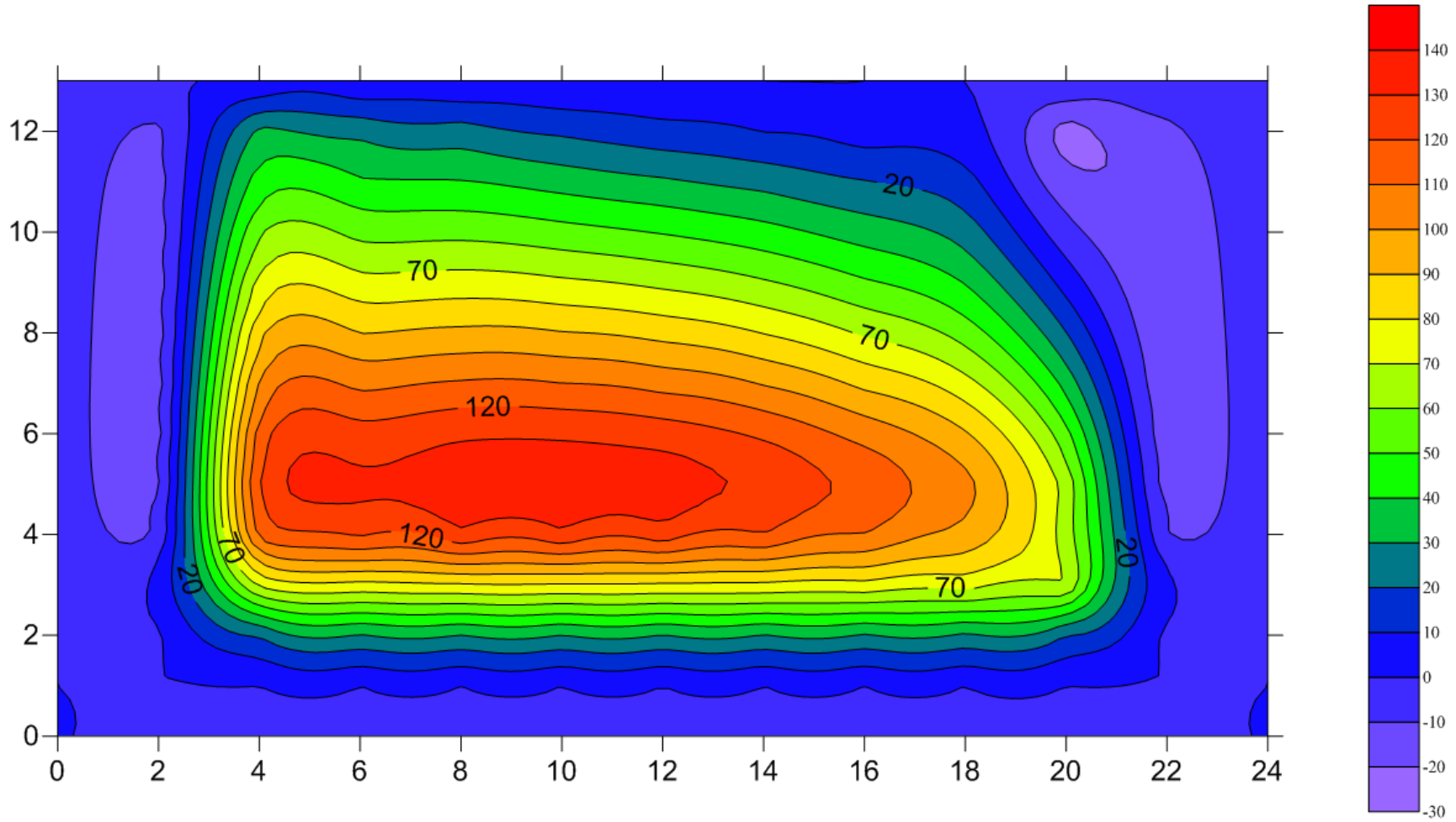

Fig.4.33 Contour map for EPP variation in cyclic loading

4.9 CONCLUDING REMARKS

The present model developed is able to predict reasonable changes in excess pore pressure occurring during cyclic loading which can be useful for analyzing earth structures situated in the regions of moderate to high seismic zone. It allows the distribution of pore pressure and the effects that drainage and internal flow have on the time of liquefaction to be determined quantitatively.

In case of cyclic excitation, a maximum vertical settlement of 4.45 cm at 8m depth and horizontal displacement of 3.38 cm at top surface are observed (G = 10 MPa). It is observed that maximum stress ratio q/p is 0.98 at the depth of 0.5 m, which decreases with depth mainly due to effect of overburden pressure. This results in development of higher excess pore pressure at shallow depth.

At higher value of shear modulus (G = 30 MPa), liquefaction occurs only at shallow depth of 2m, but does not progress at greater depths. As the shear modulus is decreased, liquefaction phenomenon is observed because of generation of higher pore pressure resulting in reduction of effective stress at shallow depths. Displacements are affected marginally with change in permeability. But EPP is affected significantly. Effect of permeability is more pronounced in the values of EPP. With decrease in permeability, considerable increase in EPP is observed. The change in permeability from k_1 to k_2 results in average 15 % increase in EPP, whereas 32 % increase in EPP is observed for change in permeability from k_1 to k_3. This also suggests that coupling matrix [Q] is working satisfactorily to transfer the load on soil-skeleton and pore - fluid. These observations are also evident from the seismic studies.

Effect of cyclic frequency is drastic for the range of frequencies considered in the analysis. It is noticed that the liquefaction occurs throughout all the depth of sand layer at frequency 1 Hz and 2 Hz of the cyclic loading, whereas no liquefaction is observed at 0.5 Hz. Horizontal acceleration is observed to increase with the frequency of loading, whereas the peak value of vertical acceleration is found to be at 1 Hz frequency.

Similar trends of displacements and EPP are observed for variation in shear modulus and permeability for El-Centro earthquake input motion. A maximum vertical settlement of 9.64 cm at 8m depth and horizontal displacement of 8.79 cm at top surface are observed. It is observed that maximum stress ratio q/p is 1.05 at the depth of 0.5 m, which is decreasing with depth as overburden pressure increases with depth. This results in development of higher excess pore pressure at shallow depth. Liquefaction occurs after 15 seconds at G = 8 MPa and $k = 6.6\times10^{-5}$ m/sec. At higher value of shear modulus (G = 15 MPa), liquefaction

occur only at shallow depth of 2m and does not advance at greater depths. As the shear modulus is decreased, liquefaction phenomenon is observed because of generation of higher pore pressure resulting in reduction of the effective stress at shallow depth of soil mass. It is noticed that liquefaction occurs throughout the depth of sand layer at lowest permeability.

From the summary of maximum displacements, the values are decreasing with increase in shear modulus. With change in permeability from k_1 to k_2, average increase in EPP is of the order 3.5 to 17% (higher value for higher modulus). Similarly, for change in permeability from k_1 to k_3, EPP are increased by 9.6 to 56% (again higher value for higher modulus).

CHAPTER - 5

LIQUEFACTION MODELING ON SEMI-INFINITE DOMAIN

5.1 INTRODUCTION

Liquefaction and spreading problems frequently relate to semi – infinite soil domain. However, in general the finite element method only satisfies the boundary displacement conditions of finite domains. For spatially unbounded seismic problems, the finite outer boundaries are problematic because undesired spurious reflections may be generated due to reflection of waves from boundary. Problem is more critical when material damping considered in the analysis is not significant. Undesired reflections affect the numerical simulation results and should be avoided from the formulation. In the case of strong ground motion this can be accomplished easily the material damping is usually substantial and relatively small amounts of energy are radiated away from the structure-soil system. Several techniques have been developed for modeling unbounded domains. For a geometrically complex continuum material, the finite element coupled with infinite element approach seems to be a rational way to deal with the unbounded region problems. Present formulation is based on a coupled finite element – infinite element numerical model for simulating semi – infinite two – phase soil media.

In this section, an infinite element formulation is described to model unbounded domain for computational efficiency. Infinite elements extending to infinity are placed at the boundary of the computational domain. A mapped 2-D infinite element is developed for simulating the response of unbounded domain. Infinite element shape functions are constructed for the infinite element. The unknown displacement in the infinite element varies in the infinite direction from the edge of the computational domain according to the selected decay function. The constructed element maintains compatibility between the finite domain and the infinite domain. The coupled 2-D finite element – infinite element model contains mixed 8-4 node displacement and pore pressure elements in the finite domain (as discussed in previous chapter) and mixed 5-4 node displacement and pore pressure infinite element for simulating the infinite boundary in vertical and horizontal direction. At the corner mixed 3-3 node displacement and pore pressure infinite element is used to model unbounded nature in both directions. The displacement and excess pore pressure (EPP) at the infinity are assumed zero.

5.2 DEVELOPMENT PROCEDURE FOR INFINITE ELEMENT

To model unbounded domain, 1-D infinite element is developed (Bettess 1977, Patil et al. 2010, Sawant et al. 2011, Sawant et al. 2012). Then this technique can be extended to developing 2-D (Patil et al. 2013a) and 3-D infinite elements (Patil et al. 2013b). Shape functions of this element should be derived to incorporate its unbounded nature at one end. The 1-D infinite element is shown in Fig. 5.1, where X_0 is the mapping origin, X_1 is at the end point of the boundary of the finite domain, X_2 is a selected point and X_3 extends to the infinity. X_2 is selected so that the distance between the mapping origin and the finite domain boundary is equal to the distance between the selected point X_2 and the finite domain boundary. Then the coordinate of the selected point can be calculated by the coordinates of the mapping origin and the finite domain boundary.

$$X_1 - X_0 = X_2 - X_1 \quad \Rightarrow \quad X_2 = 2X_1 - X_0 \tag{5.1}$$

The shape functions of 1-D infinite element are given by:

$$N_1^{\infty}(\xi) = -\frac{2\xi}{1-\xi} \qquad ; \qquad N_2^{\infty}(\xi) = \frac{1+\xi}{1-\xi} \tag{5.2}$$

The coordinate for an arbitrary point within the infinite element can be written as:

$$X = \sum_{i=1}^{2} N_i^{\infty}(\xi) X_i \tag{5.3}$$

In which, X_i represents the nodal coordinates. Apparently, from Eqs. (5.1) and (5.2), have $X = X_1$ at $\xi = -1$, $X = X_2$ at $\xi = 0$ and $X = \infty$ at $\xi = 1$.

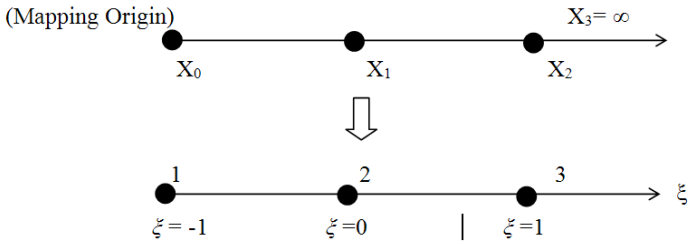

Fig.5.1 1-D Infinite Element

The unknown (displacement or stress) in the infinite element is assumed to decay from the boundary of the finite domain. Therefore, a decay function should be specified in the infinite direction. The most frequently used decay functions include exponential function, reciprocal function and so on. Now shape functions derived from 1-D element are included in normal 2-D finite element to model to model unbounded domain in specified direction. In the present study, mixed 5-4 node displacement and pore pressure infinite

elements are employed for simulating the infinite boundary in vertical and horizontal direction (Figs. 5.2 and 5.3). At the corner mixed 3-3 node displacement and pore pressure infinite element is used to model unbounded nature in both directions.

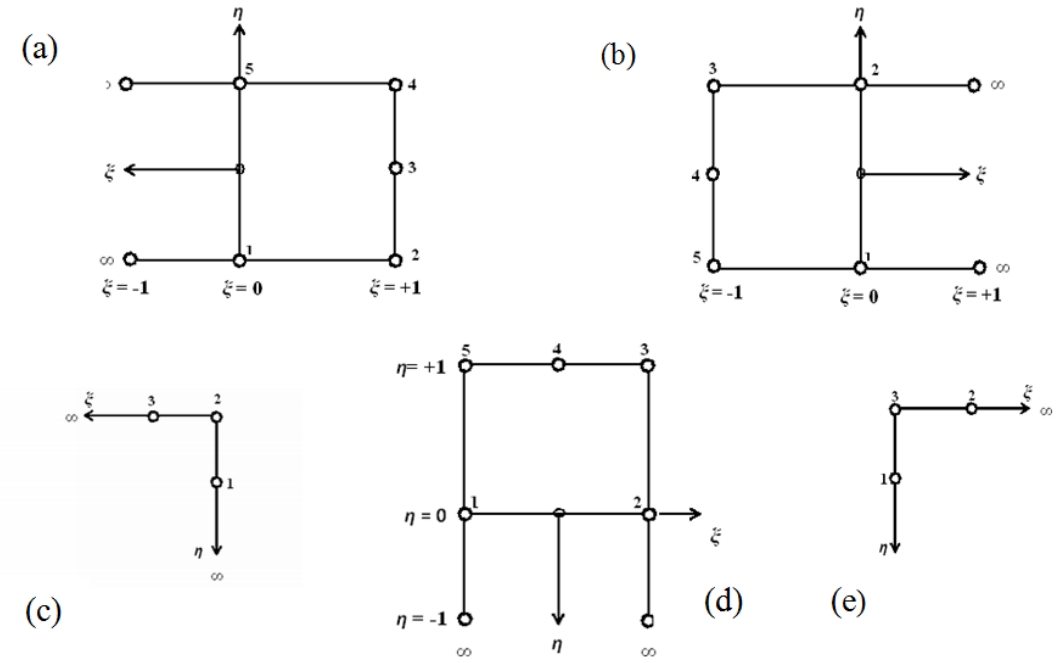

Fig. 5.2: 2-D Infinite elements showing displacement nodes (a) Horizontal LHS (b)Horizontal RHS (c)Left bottom Corner (d)Vertical (e)Right bottom corner

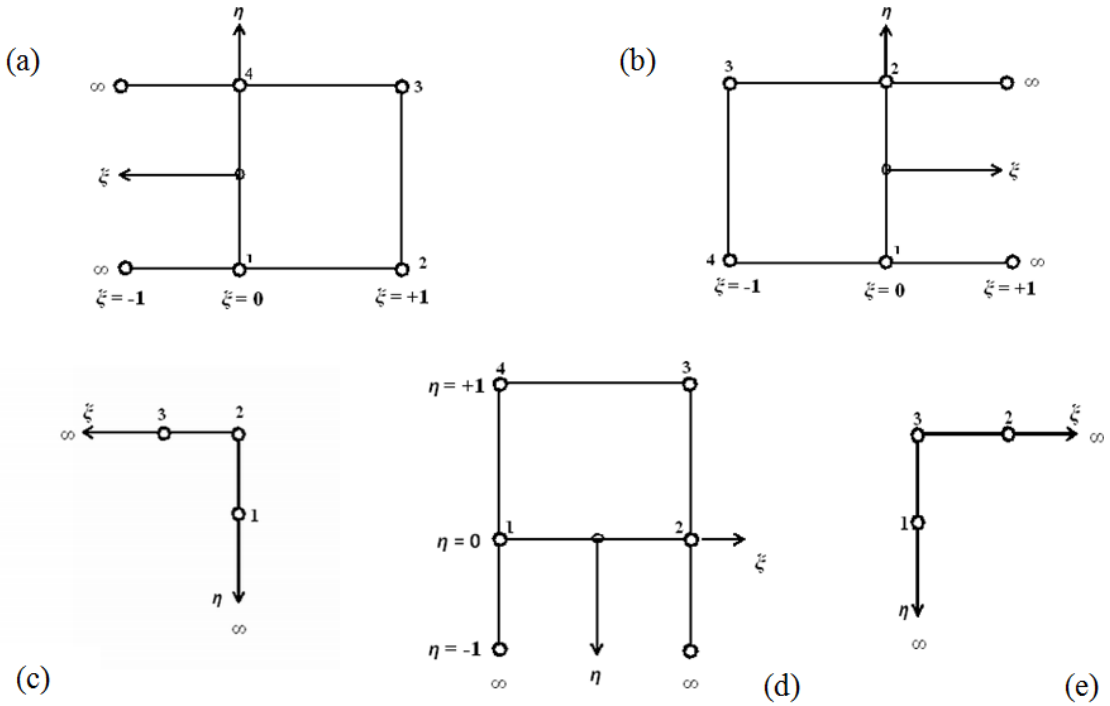

Fig. 5.3: 2-D Infinite elements showing pore pressure nodes (a) Horizontal LHS (b)Horizontal RHS (c)Left bottom Corner (d)Vertical (e)Right bottom corner

The shape functions for describing displacements and pore pressure within 2-D infinite elements at the LHS boundary, RHS boundary, vertical and both corner elements used in present study are presented in Table 5.1. For mixed 3-3 corner infinite elements shape functions for displacement and pore pressure are given by same expressions.

Table 5.1 Shape functions for displacement and pore pressure nodes of infinite elements

Horizontal LHS		**Horizontal RHS**	
Displacement	**Pore pressure**	**Displacement**	**Pore pressure**
$N_1 = \frac{1-\xi\ \ (1-\eta)}{2\ \ 1+\xi}$	$N_1^p = \frac{1-\xi\ \ 1-\eta}{2\ \ 1+\xi}$	$N_1 = \frac{\xi\eta(1-\eta)}{1-\xi}$	$N_1^p = -\frac{\xi(1-\eta)}{1-\xi}$
$N_2 = -\frac{\xi\ \eta\ \ 1-\eta}{1+\xi}$	$N_2^p = \frac{\xi(1-\eta)}{1+\xi}$	$N_2 = \frac{1+\xi\ \ 1-\eta}{2\ \ 1-\xi}$	$N_2^p = \frac{1+\xi\ \ 1-\eta}{2\ \ 1-\xi}$
$N_3 = \frac{2\xi\ \ 1-\eta^2}{1+\xi}$	$N_3^p = \frac{\xi(1+\eta)}{1+\xi}$	$N_3 = \frac{1+\xi\ \ 1+\eta}{2\ \ 1-\xi}$	$N_3^p = \frac{1+\xi\ \ 1+\eta}{2\ \ 1-\xi}$
$N_4 = \frac{\xi\eta(1+\eta)}{1+\xi}$	$N_4^p = \frac{1-\xi\ \ 1+\eta}{2\ \ 1+\xi}$	$N_4 = -\frac{\xi\eta(1+\eta)}{1-\xi}$	$N_4^p = -\frac{\xi(1+\eta)}{1-\xi}$
$N_5 = \frac{1-\xi\ \ (1+\eta)}{2\ \ 1+\xi}$		$N_5 = -\frac{2\xi(1-\eta^2)}{1-\xi}$	
Vertical Bottom		**Left Bottom Corner**	
Displacement	**Pore pressure**	**Displacement and pore pressure**	
$N_1 = \frac{1-\xi\ \ 1-\eta}{2\ \ 1+\eta}$	$N_1^p = \frac{1-\xi\ \ 1-\eta}{2\ \ 1+\eta}$	$N_1 = \frac{2\ \ 1-\eta}{1+\xi\ \ 1+\eta}$	
$N_2 = \frac{1+\xi\ \ (1-\eta)}{2\ \ 1+\eta}$	$N_2^p = \frac{1+\xi\ \ (1-\eta)}{2\ \ 1+\eta}$	$N_2 = \frac{\xi\eta+3\ \ \xi+\eta-1}{1+\xi\ \ 1+\eta}$	
$N_3 = \frac{\xi\eta(1+\xi)}{1+\eta}$	$N_3^p = \frac{\eta(1+\xi)}{1+\eta}$	$N_3 = \frac{2\ \ 1-\xi}{1+\xi\ \ 1+\eta}$	
$N_4 = \frac{2\ \ 1-\xi^2\ \ \eta}{1+\eta}$	$N_4^p = \frac{\eta\ \ 1-\xi}{1+\eta}$	**Right Bottom Corner** **Displacement and pore pressure**	
$N_5 = -\frac{\xi\eta\ \ 1-\xi}{1+\eta}$		$N_1 = \frac{2\ \ 1-\eta}{1-\xi\ \ 1+\eta}$	
		$N_2 = \frac{2\ \ 1+\xi}{1-\xi\ \ 1+\eta}$	
		$N_3 = \frac{-\xi\eta+3\ \ -\xi+\eta-1}{1-\xi\ \ 1+\eta}$	

5.3 VALIDATION

Centrifuge modeling has been assumed among the best experimental methods for modeling and observing liquefaction behaviour. The stress conditions generated in the model approximately simulated in the full-scale prototype experimental setup. For the purpose of validation, centrifuge experimental data reported by Bao and Sture (2010) is used. This experiment has been conducted in centrifuge at 40g level to test models of a Nevada sand layer of 10m thickness in a prototype with R_D = 30% and unit weight 19.7 kN/m^3, submerged unit weight 9.9 kN/m^3. To model semi-infinite sand layer, the laminar box was built of rectangular aluminum rings assembled on top of each other with roller bearings. Shock absorbers in the form of cork plates were devised in the shaking direction to model infinite boundary. A metolose solution was used to saturate sand which has viscosity 40 times higher than that of water. This provided proper scaling between dynamic and diffusion phenomena of the given *g*-level.

The pore pressure was measured from five pore pressure transducers at a depth of 2, 4, 6, 8 and 9.6 m. Accelerations at depth of 0, 2, 4, 6 and 8 m were recorded from accelerometers. Surface settlement was measured from LVDT. The input motion was 10 cycles of 0.2g at 1.0 Hz prototype scale. The cross-section of model and the layout of instrumentation are shown in Fig. 5.4.

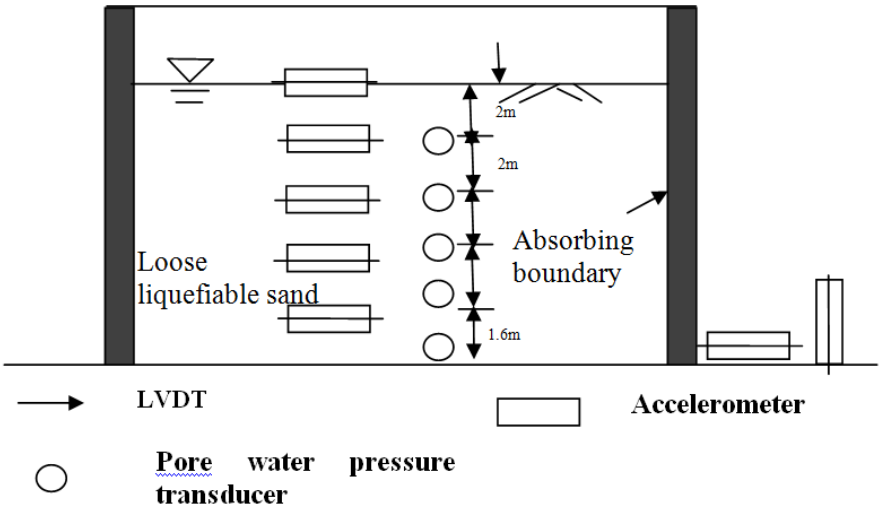

Fig. 5.4 Cross-section of the centrifuge model and instrumentation layout (modified after Bao and Sture, 2010)

Fig. 5(a) shows the comparison between the predicted and experimental excess pore pressure (EPP) results (Bao and Sture, 2010) at different depth. A fare agreement is observed between the predicted EPP values with centrifuge test result at different depth of the prototype model. It can be noticed from Fig. 5(a), that the maximum EPP computed at 2m depth, from centrifuge experiment (20.34 kPa) is slightly lower than the EPP (23 kPa) predicted from the present study. Similarly, at 4m depth the maximum experimental value is nearly equivalent (60 kPa) to the computed value. At 6m, the computed excess pore pressure (64.5 kPa) is slightly higher than experimental result (60 kPa). The present study shows similar trend in the EPP at 8m depth with experimental observation. But the values of predicted EPP are on higher side which may be attributed to poor drainage at bottom. The computed excess pore water pressures in Fig. 5.5(a) are generally consistent with the centrifuge experimental results. The computed pore pressure dissipation is a little bit slower than the experimental data. The possible reasons for this may be attributed to the possible reduction in the viscosity of the metolose solution used in the centrifuge test on account of rise in temperature during centrifuge spinning. In addition, the actual post-liquefaction permeability is higher than the constant value used in the simulation.

The computed maximum top displacement of 71.7 mm (Fig. 5.5-b) is lower than the experimental value of 80.63 mm by approximately 11%. The cause for this discrepancy may be the use of a constant coefficient of permeability, which does not represent the real conditions, when liquefaction has initiated. Another possible reason is that the LVDT sensing core was penetrated into the soil, which made the LVDT reading higher than the actually observed settlement. At all the depth, the soil shows the trend of liquefaction as EPP is almost higher than the initial effective stresses. Numerical predictions are in fair agreement with centrifuge results reported by Bao and Sture (2010), with little deviation. The comparison reveals that the present model can approximately simulate the real behavior of liquefaction phenomena.

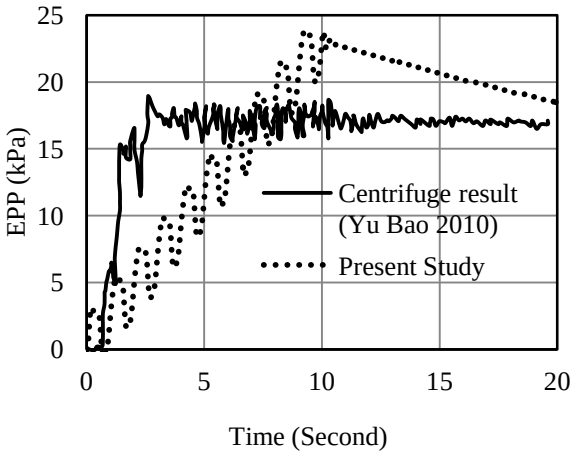

(a) 2 m depth

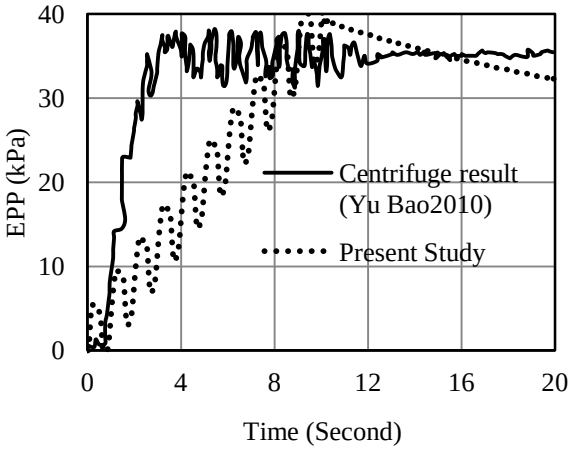

(b) 4 m depth

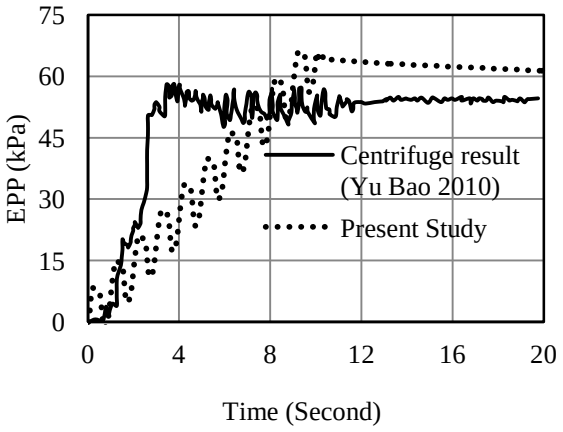

(c) 6 m depth

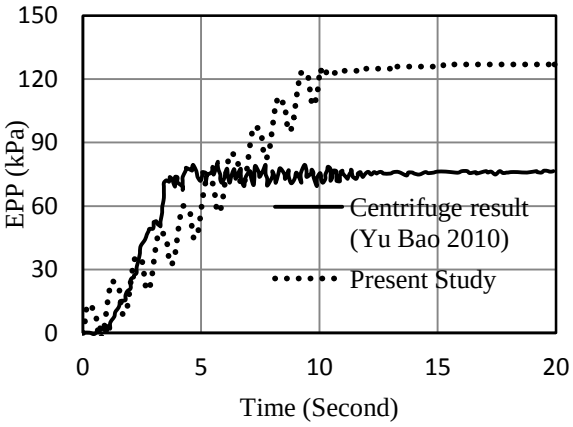

(d) 8 m depth

Fig. 5.5(a) Pore pressure verses time at different depths

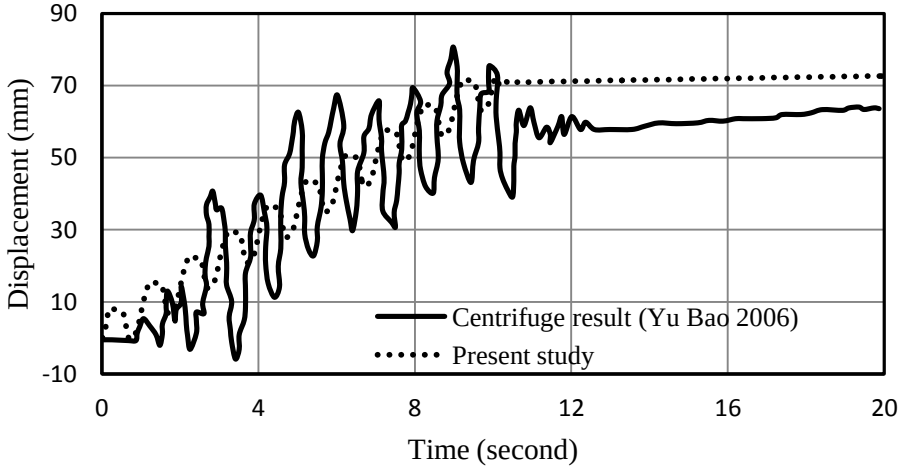

Fig. 5.5(b) Displacement verses time at top surface of soil domain

5.4 PROBLEM DEFINITION

In the present study, the saturated loose sand layer of thickness 10m, underlain by 4m depth of gravel had been considered for numerical simulation (Fig.5.6). Plane strain condition is assumed to reduce the computational efforts. The unbounded soil domain in *XZ* plane is discretized into 196 finite and infinite element mesh as shown in Fig. 5.6. Free drainage was assumed at the top surface only, while the lateral boundaries and the base were considered to be of infinite extent. The transmitting boundary is approximated horizontally within the range of 10m on each side from the centre of the soil domain and vertically 12m in the downward direction. Kelvin elements are connected in vertical and horizontal directions to the nodes of the transmitting boundary. The same material properties as proposed in Table. 4.2 have been considered for the purposed model. The variation of displacement and excess pore pressure with time at different nodes had been calculated using finite element code written in FORTRAN-90. The variation of both parameters with time was considered for comparing the response. Analyses were performed in two steps: (1) Static analysis and (2) Dynamic Analysis.

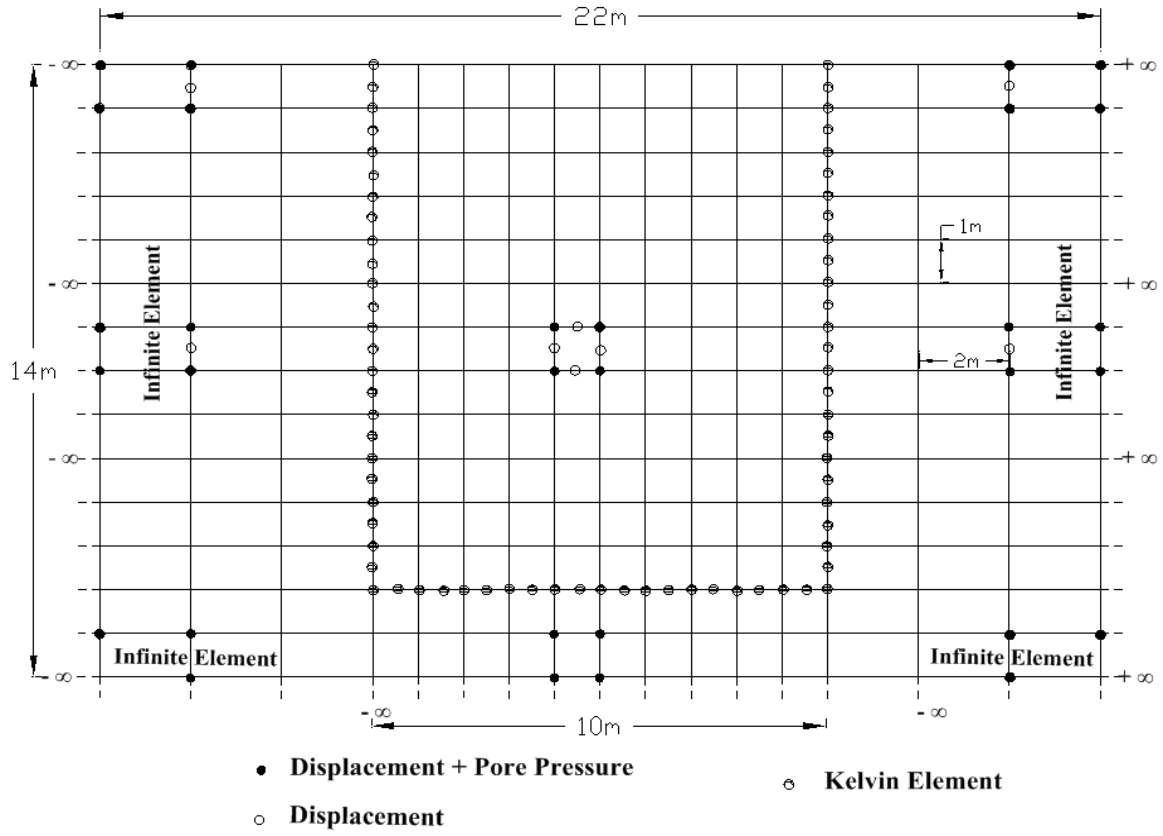

Fig. 5.6: Soil Domain under consideration

A static analysis was performed to apply the gravitational forces due to self weight of the soil before cyclic excitation. The resulted hydrostatic pressures of fluid and the stress state along a soil column were used as initial conditions for the subsequent dynamic analysis. The coupled equations for static analysis were considered. When equilibrium condition was achieved for initial stress condition, a nonlinear analysis was performed for the cyclic/seismic excitation. Cyclic shaking was applied in the form of horizontal and vertical cyclic acceleration $a = a_0 \sin \omega t$. Similarly, for seismic case El-Centro input motion was applied in the detailed parametric study. However, Bhuj earthquake was also considered for few cases to examine the response for different earthquake motions. The dynamic analyses were performed using a Generalized Newmark scheme (Katona and Zienkiewicz, 1985) with nonlinear iterations using initial linear elastic tangential global matrix. The numerical integration parameters of the generalized Newmark's method were selected as α = 0.60 and β = 0.3025 for the dynamic analysis. The time step used is usually depends on time of cyclic loading and frequency of the input. Void ratio, permeability and other geometric properties were kept constant during the analysis. Rayleigh damping of 5% is applied at the dominant frequency in the earthquake-like motion input to enhance the energy dissipation characteristic of the constitutive model.

5.5 PARAMETRIC STUDY FOR CYCLIC CASE

The numerical simulation has been performed for 24 cycles of the loading. The amplitude and frequency of the cyclic loading were a_0 = 0.22g and 1 Hz respectively. The typical results has been discussed for co-efficient of permeability, $k = 6.6\times10^{-5}$ m/sec, frequency, f =1.0 Hz and shear modulus, G = 8MPa. The effect of the soil properties like permeability, and shear modulus of the soil grain on liquefaction response is examined in the detailed parametric study. Fig. 5.7 displays the computed horizontal and vertical displacement at different depth of the soil domain (G = 8MPa, $k = 6.6\times10^{-5}$ m/sec, f =1.0 Hz). Observed trend of displacements is similar to the trend reported by Dewoolkar et al. (2009). The maximum values of horizontal settlement of 1.27 cm are predicted at 8 m depth of soil layer, whereas maximum values of vertical settlement of 10.5 cm are predicted at top surface. It has been observed that most part of the settlements occur during the seismic excitation. Generally, the horizontal settlement is less than vertical settlement at different depths. Vertical displacement is decreasing as the depth increases.

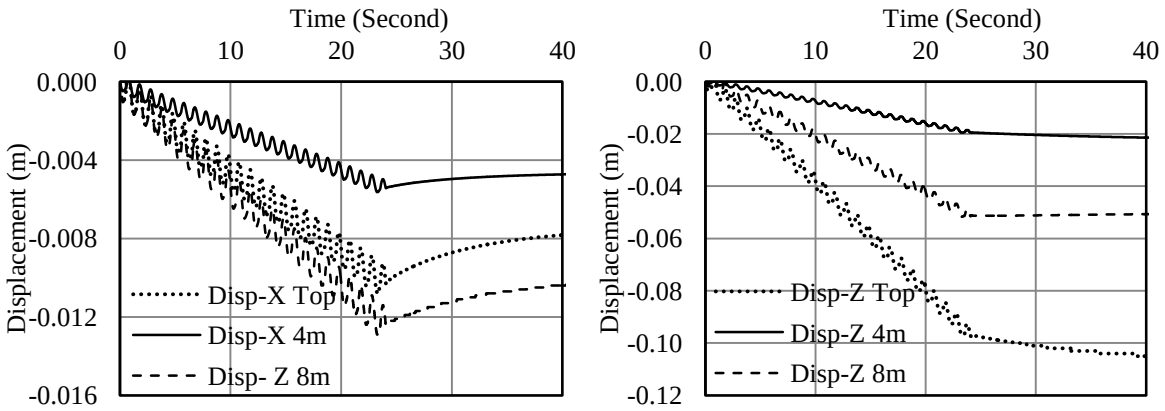

Fig.5.7 Computed horizontal and vertical displacement at different depth

Fig. 5.8 displays the computed excess pore pressure at different depth. Trend in EPP is matching with trend available in literature (Finn et al. 1977, Dewoolkar et al. 2009). The computed excess pore pressure time histories point out that soil at the depth of 2 m is liquefied because excess pore pressure (EPP) is higher than initial vertical stress. At 10 m depth of soil domain, rise in excess pore pressure is approximately equal to initial effective stress. It is observed that at 4m and 6m depth, less rise in EPP is visible that to for small time. Around after 9 seconds, reduction in EPP starts that lead to negative pore pressure. This directs the phenomena of dilatation occur at these depth. It also seems that dissipation of EPP is fast at shallow depth after completion of cyclic loading, which may be attributed to shorter drainage path for dissipation of excess pore pressure at shallow depth.

The stress paths presented in Fig. 5.9 show the typical mechanism of cyclic decrease in effective stress due to pore pressure build-up, captured using the Pastor–Zienkiewicz model. It is observed that maximum stress ratio q/p is 0.65 and 0.27 at the depth of 0.5 m and 11.5m respectively, which decreases with depth mainly due to effect of overburden pressure coming on soil mass. Figs. 5.10 and 5.11 shows the computed horizontal and vertical accelerations time histories at top and 8m respectively. It has been observed that the peak value of these parameters is found to be about 0.48m/s^2 and 0.25 m/s^2 at 8m depth, resulting higher horizontal settlement. A negligible acceleration is reported in both directions after the end of 24 cycle of loading.

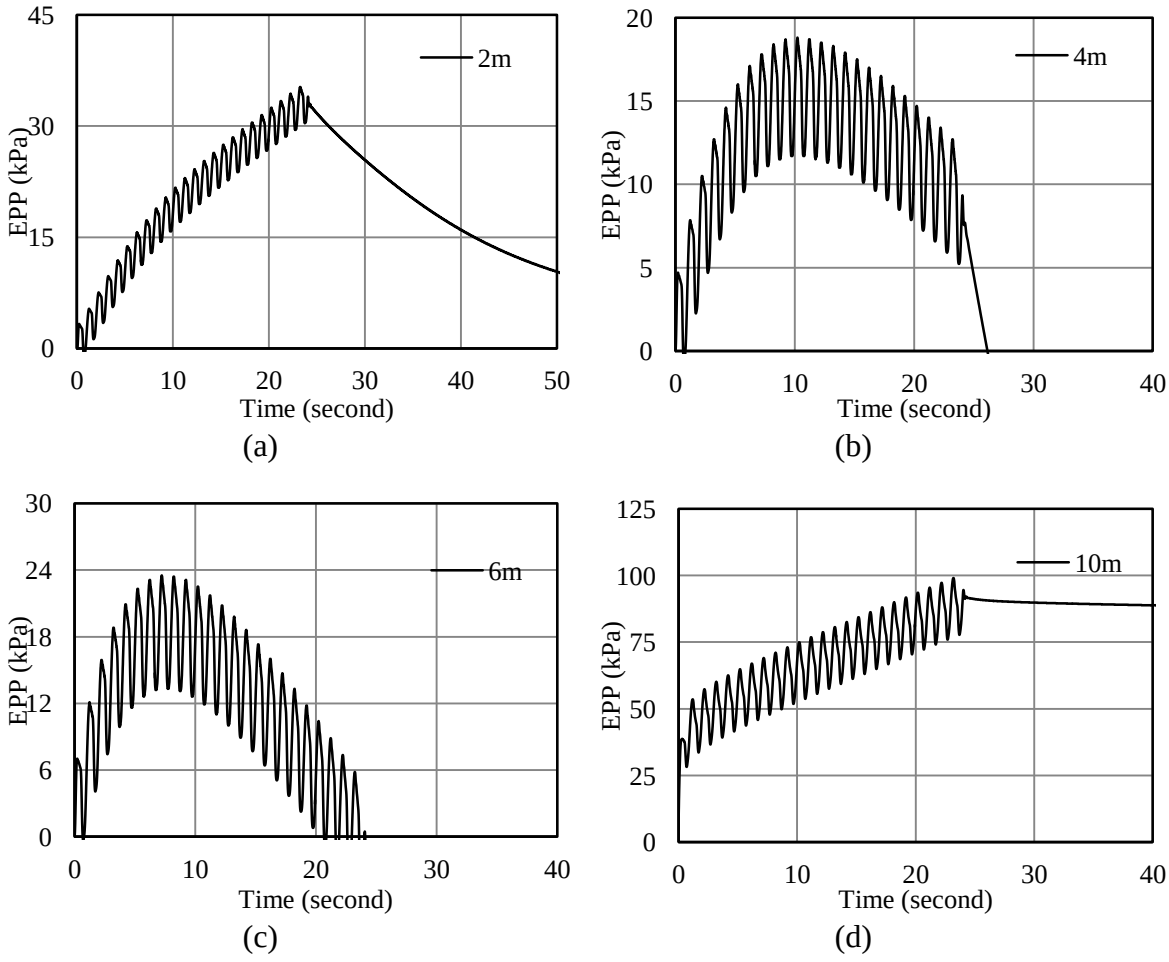

Fig. 5.8 Computed EPP at different depths (a) 2m (b) 4m (c) 6m (d) 10m

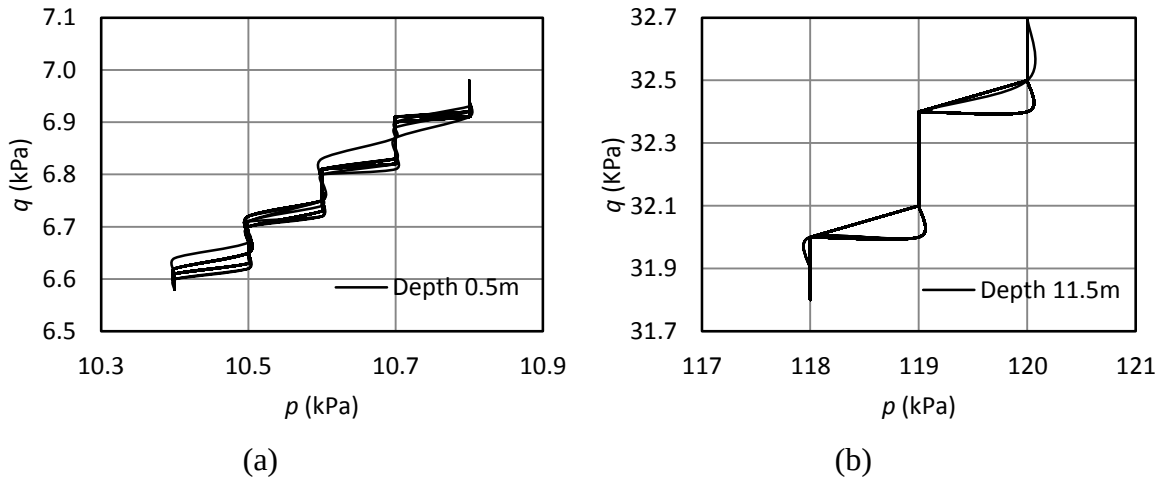

Fig. 5.9 Computed effective stress path at different depths (a) 0.5m (b) 11.5m

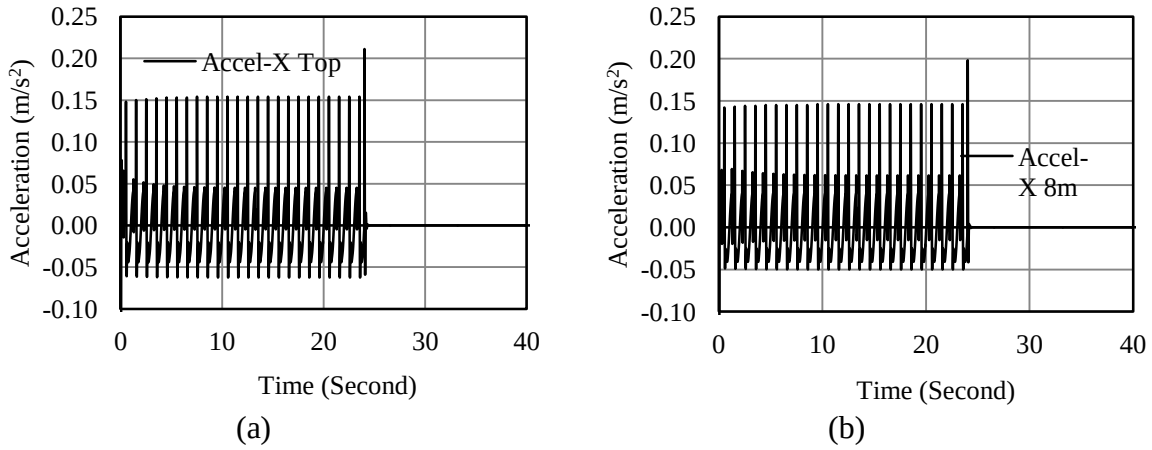

Fig. 5.10 Computed horizontal acceleration time histories at (a)Top surface (b) 8m depth

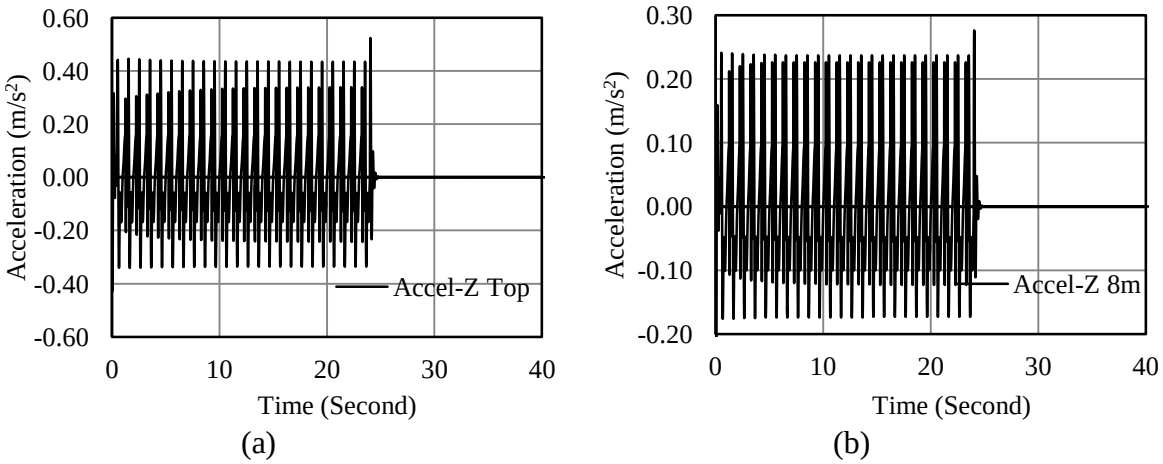

Fig. 5.11 Computed vertical acceleration time histories at (a)Top surface (b) 8m depth

5.5.1 Effect of Permeability

Settlement of saturated soil in the event of cyclic excitation is associated with the dissipation of pore pressure. It is proportional to the amount of generated pore pressure and also depends on drainage path. This implies the significance of permeability coefficient in liquefaction phenomenon. A parametric study has been carried out to outline the effect of permeability coefficient on liquefaction phenomena. Three different values of permeability ($k_1 = 1\times10^{-4}$ m/sec, $k_2 = 6.5\times10^{-5}$ m/sec, $k_3 = 1\times10^{-7}$ m/sec) are considered in the present study. The variations in displacement and excess pore pressure with respect to time when drainage occurs during the earthquake are presented in Figs. 5.12 and 5.13 respectively. From the displacement-time response (Fig.5.12), it has been observed that there is slight variation of about 1mm in maximum horizontal displacement

(2.39 cm) and 0.4 mm in maximum vertical displacement (17 cm) respectively with respect to permeability. It may be due to high rise of pore water pressure at the time of cyclic load and during this small duration a nearly undrained condition prevails irrespective of permeability.

Fig. 5.13 depicts a variation in generation of excess pore pressure (EPP) with respect to permeability at different depth. At 2 m depth, a dilation effect is noticed for k_3=1.0×10^{7}m/sec, resulting no liquefaction. But, for other two value of permeability, a clear indication of liquefaction is visible after 23 seconds because EPP is greater than initial effective stress. However, just opposite trend in EPP is found at 4m and 6m depth for k_3=1.0×10^{-7}m/sec and k_2 = 6.5×10^{-5}m/sec, encountering nearly zero effective stress resulting liquefaction after 22 seconds because of long drainage path or high frequency of loading, during the period of vibration. For k_1=1.0×10^{-4}m/sec, non zero effective stress is found at 4m and 6m due to rapid dissipation of excess pore pressure at higher value of permeability.

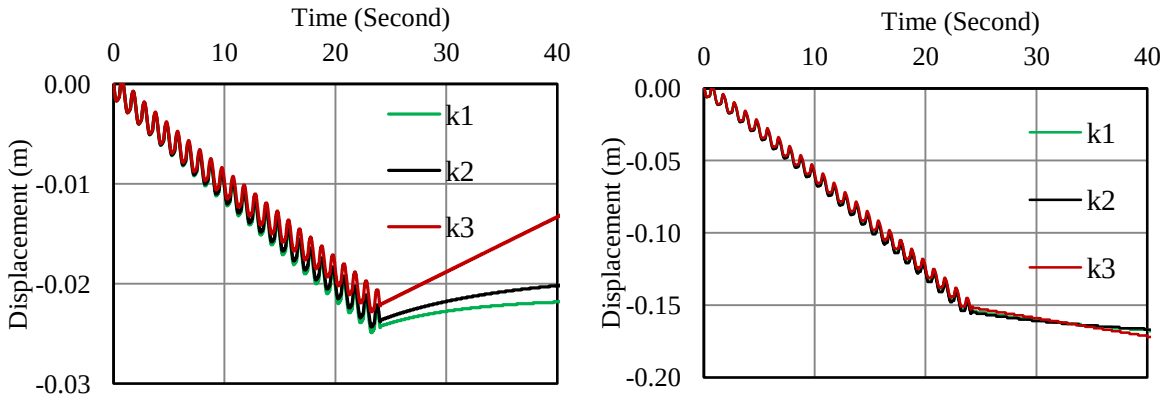

(a) (b)

Fig. 5.12 (a) Computed horizontal and vertical displacement with respect to time for different soil permeability at top surface of soil domain

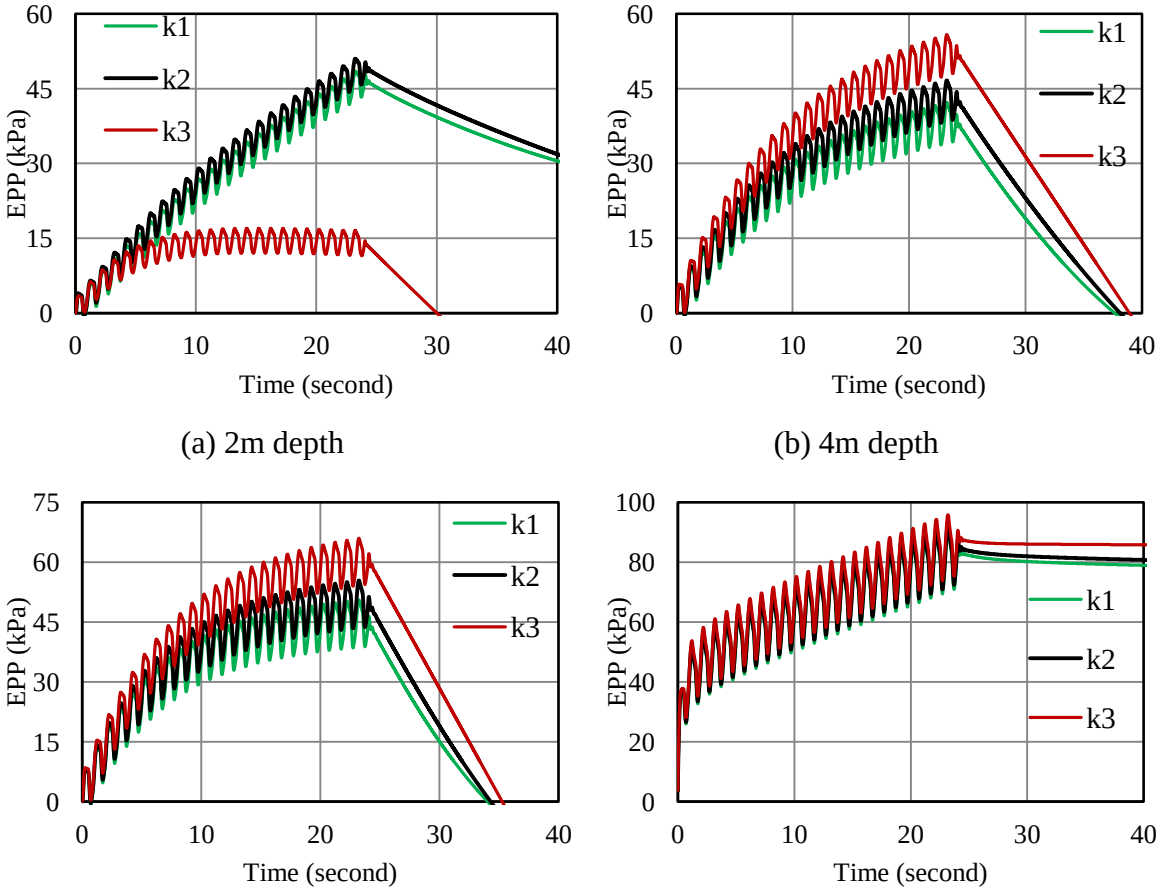

(a) 2m depth

(b) 4m depth

(c) 6 m depth

(d) 10 m depth

Fig. 5.13 Computed EPP at different depths with respect to time for different soil permeability

At 10 m depth liquefaction does not occur at any value of permeability co-efficient, due to presence of the gravel layer after 10m depth, indicating marginal effect of cyclic loading due to higher permeability. The numerical results reveal that there is a direct relationship between permeability coefficient and rate of excess pore pressure generation and dissipation in liquefying the soil profile.

5.5.2 Effect of Shear Modulus

Figs. 5.14 and 5.15 show the variation of displacement and excess pore pressure at three shear modulus (G = 5, 10 and 15 MPa). A maximum value of horizontal displacement (2.31cm) is noticed at G = 5 MPa whereas a minimum value of 2.26mm at G = 15 MPa indicating 90% reduction due to increase in shear modulus. Similarly, maximum value of 6.17mm is noticed at G = 5 MPa (73.3% reduction). A maximum value of vertical displacement (16.7cm) is noticed at G =10 MPa whereas a minimum value of 5.37cm at

G = 5 MPa. This may be attributed to the fundamental frequency of the domain may be close to operating frequency.

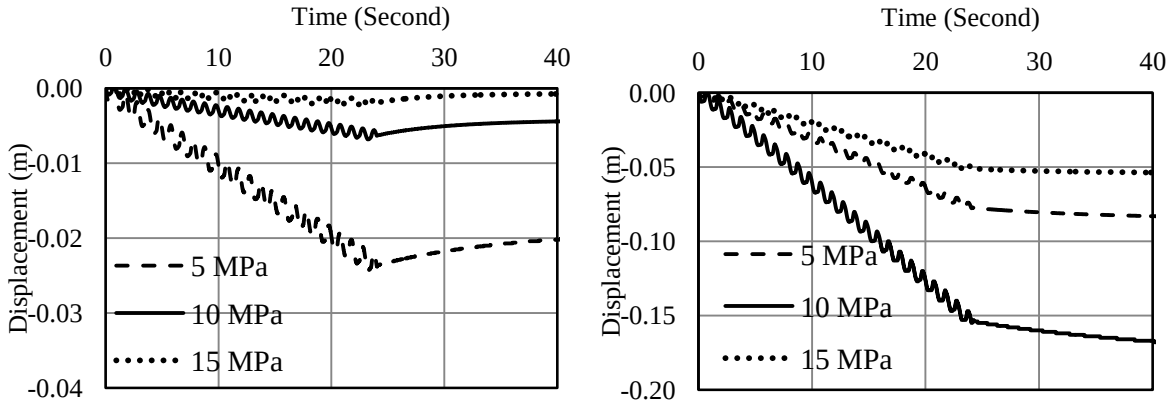

(a) (b)

Fig. 5.14 Computed horizontal and vertical displacement with respect to time for different Shear Modulus at top surface

From Fig. 5.15, it is predicted that at lower value of shear modulus (G = 5 MPa), liquefaction occurs within the soil domain at 2, 4 and 6m depth. At G =10 MPa and 15 MPa, liquefaction is noticed at 2m and 10m depth. Dilation is also noticed at 4m and 6m depth at the same value of shear modulus. Although there is a gravel boundary near 10m depth still significant rise in EPP as noticed, may be due to infinite boundary. As the shear modulus is increased, liquefaction phenomena is not observed because of less generation of excess pore pressure resulting in increasing the effective stress at shallow depth of soil mass. At higher soil modulus, more loads will be shared by skeleton. This in turn reduces the excess pore pressure at each step.

The effect of permeability and shear modulus has been examined for the present case. A detailed study was carried out for three values of permeability as mentioned earlier, but for each value of permeability, three different values of shear modulus (G = 5, 10, 15 MPa) were assigned. To summarize the effect of these two key parameters, maximum values of displacement and EPP are reported in Table 5.2 to 5.3. From the reported values of maximum horizontal displacements (Table 5.2), the values are decreasing with increase in shear modulus for the two permeability k_1 and k_2 where some discrepancies is noticed in this trend for k_3 may be due to occurrence of dilation at lower value of permeability. Reduction is of the order of 47 % to 96% with higher values for higher shear modulus. They are also decreasing slightly with reduction in permeability. Similarly maximum vertical displacements (Table 5.2) are observed to be reducing with

increase in shear modulus, but vertical displacements are slightly higher at lowest shear modulus (G = 5 MPa). Effect of shear modulus and permeability is more pronounced in the values of EPP (Table 5.2). With reduction in permeability, slight increase in EPP is observed (trend similar to Finn et al. 1977), whereas considerable effect of shear modulus is observed on maximum EPP. A considerable reduction in EPP with increase in shear modulus is observed when shear modulus is increased from 5 MPa to 10 MPa or some higher value. Reduction is of the order of 40 % to 90% with higher values for higher shear modulus.

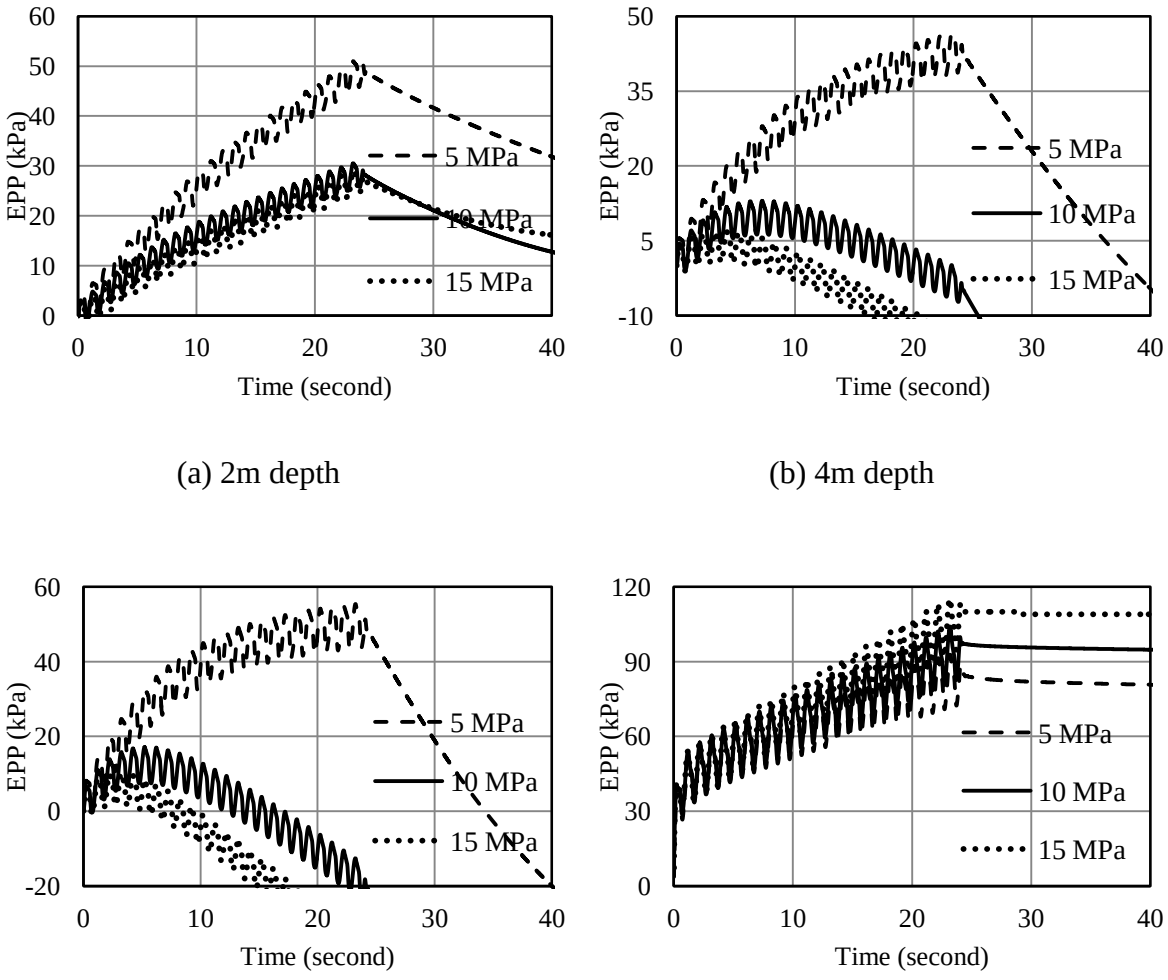

Fig. 5.15 Computed EPP with respect to time at different depths and soil modulus

Table 5.2 Comparison of maximum displacements

Permeability	G (MPa)	Disp (X-direction) at different depth in cm		
		Top	4m	8m
k_1	5	2.15	1.05	2.23
	10	1.13	0.23	0.47
	15	0.16	0.18	0.38
k_2	5	1.92	0.98	2.06
	10	0.42	0.31	0.68
	15	0.07	0.15	0.30
k_3	5	0.24	0.28	1.05
	10	1.13	0.23	0.47
	15	1.29	0.30	0.81
		Disp (Z-direction) at different depth in cm		
k_1	5	17.10	3.58	7.63
	10	10.40	2.03	4.49
	15	5.33	1.08	2.94
k_2	5	17.50	3.65	7.62
	10	8.47	1.73	4.14
	15	5.42	1.08	2.92
k_3	5	19.60	4.00	8.54
	10	10.40	2.03	4.49
	15	6.71	1.22	3.00

Table 5.2 Comparison of maximum EPP

Permeability	G (MPa)	Maximum EPP at different depth in kPa					
		2m	4m	6m	8m	10m	12m
k_1	5	48.5	42.2	50.5	65	91.1	28.7
	10	28.1	38.1	9.77	20.8	97.9	39.5
	15	27	4.07	7.35	12.5	111	55.3
k_2	5	51	46.6	55.4	69.6	92.8	29.7
	10	29.1	12.9	17	22.2	99.8	40.5
	15	27	6.77	10.2	14.7	110	55
k_3	5	52.2	51.6	59.4	72	88.1	26.3
	10	22.3	19.6	23.6	30.9	104	42.7
	15	14.5	13.3	15.8	21.8	117	58.7

5.6 PARAMETRIC STUDY FOR SEISMIC CASE

The same semi-infinite model discussed above is analysed under seismic condition. The boundary condition used here will be also same. This model is examined for El-Centro having parameter, $k = 6.6\times10^{-5}$ m/s and $G = 8$ MPa. Response in the form of resultant displacements, liquefaction tendencies, excess pore pressure and other parameters are studied. The time step used is same as time interval of input motion. A parametric study for parameter like coefficient of permeability and shear modulus is also conducted for the ground motion.

Variation in predicted horizontal and vertical displacement at different depth with respect to time has been shown in Fig. 5.16. Observed trend of displacements is in agreement with the trend reported by Taiebat et al. (2007). The maximum values of horizontal and vertical settlement of 0.918 cm and 1.89 cm are predicted at the top of soil layer; whereas minimum values 0.308 cm and 0.376 cm are predicted at 4m depth. It has been observed that the maximum settlements occur after 30.96 seconds of loading. After attaining approximately maximum value, settlement rate is decreased and settlement becomes constant during the rest of the shaking period. Generally, the horizontal settlement is less than vertical settlement at different depths.

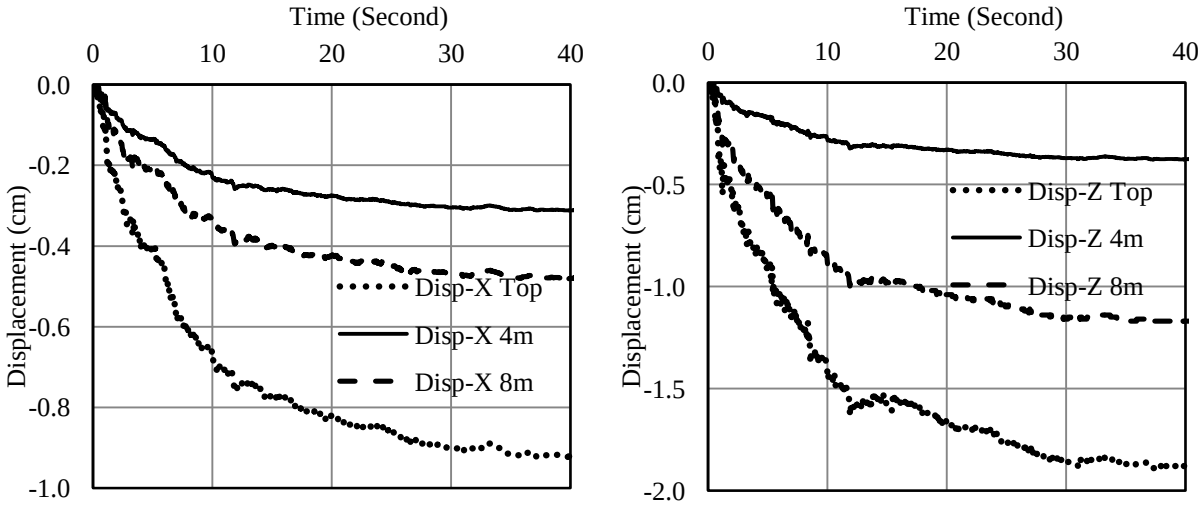

(a) Horizontal Displacement (b)Vertical Displacement

Fig. 5.16 Computed displacement at different depth

Fig. 5.17 displays the computed excess pore pressure at different depth. At depth of 2m, EPP is higher than initial vertical stress at 5.72 seconds of loading, showing liquefaction phenomenon. First maximum peak at 4m, 6m and 8m in EPP is attained at 12.17 seconds for a very small duration. After this time a slight decrease in EPP is noticed and liquefaction does not occur for these depths for the given parameter. Trend of EPP reported by Taiebat et al. (2007) is in confirmation with the observed trend.

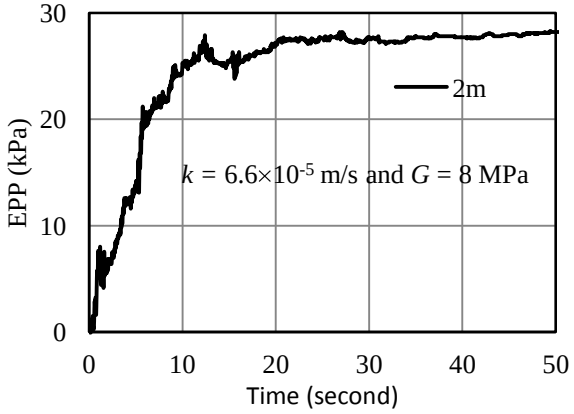

(a) 2m depth

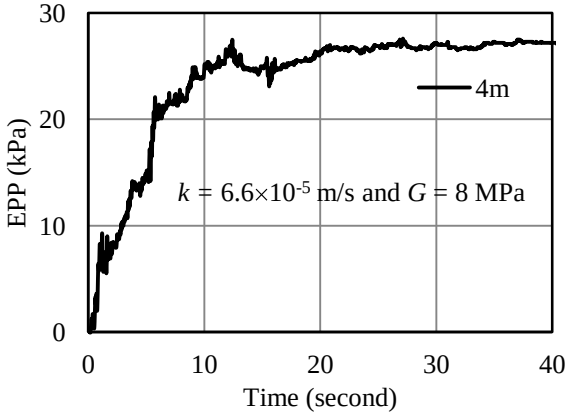

(b) 4m depth

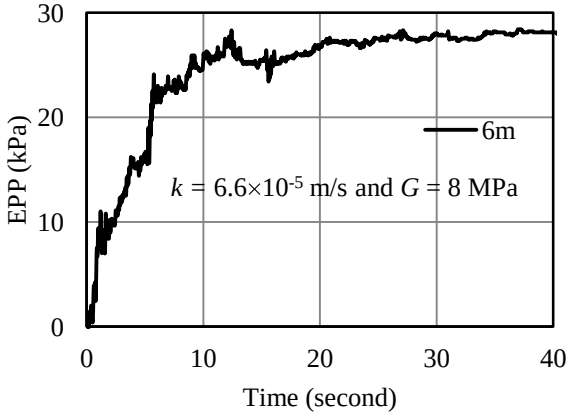

(c) 6m depth

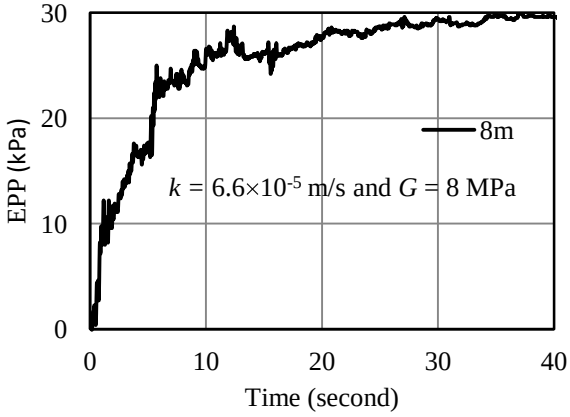

(d) 8m depth

Fig. 5.17 Computed EPP at different depths (a) 2m (b) 4m (c) 6m (d) 8m

The stress paths depicted in Fig. 5.18 show the typical mechanism of cyclic decrease in effective stress due to pore pressure build-up, captured using the present constitutive model.

It is observed that maximum stress ratio q/p is 0.398 at the depth of 0.5 m, which decreases with depth mainly due to effect of overburden pressure.

Figs. 5.19 and 5.20 shows the computed horizontal and vertical accelerations time histories at different depths. It has been observed that the peak value of these parameters is found to be about 0.86 m/s^2 and 2.56 m/s^2 at top surface, resulting higher settlement. A relatively less value of accelerations (0.59 and 1.06 m/s^2) are observed at 8 m depth, corresponding to lesser excess pore pressure. A negligible acceleration is reported in both directions after 16.32 second of shaking. Results indicate amplification of earthquake input motion from base to the top surface showing maximum amplification at top level. This peak of acceleration at about 3.4 seconds imparts a high displacement and EPP in the soil stratum. It initiates the liquefaction phenomenon.

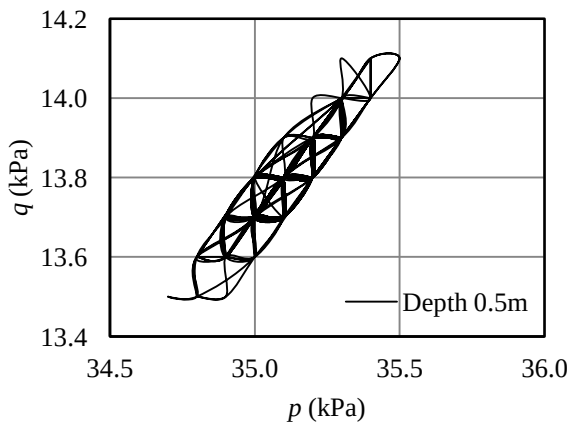

(a) 0.5 m depth

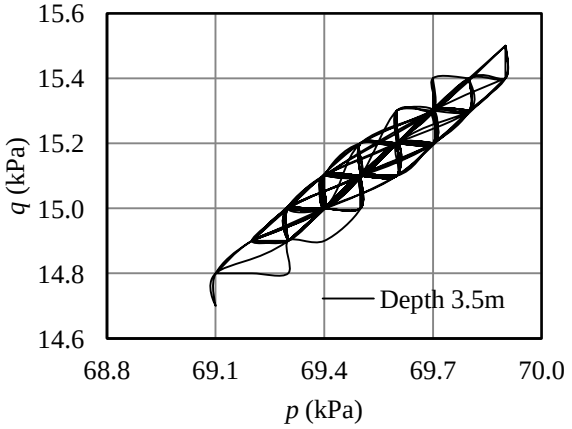

(b) 3.5 m depth

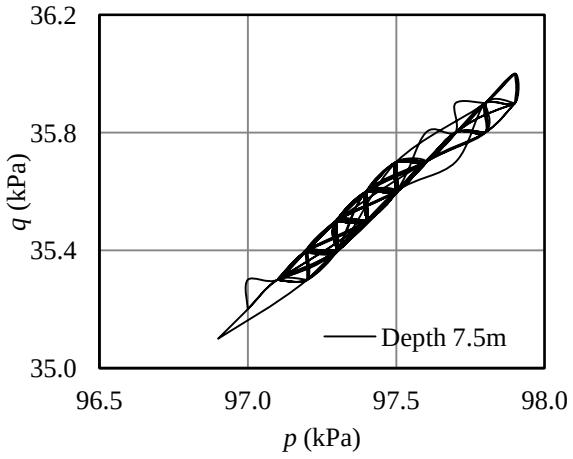

(c) 7.5 m depth

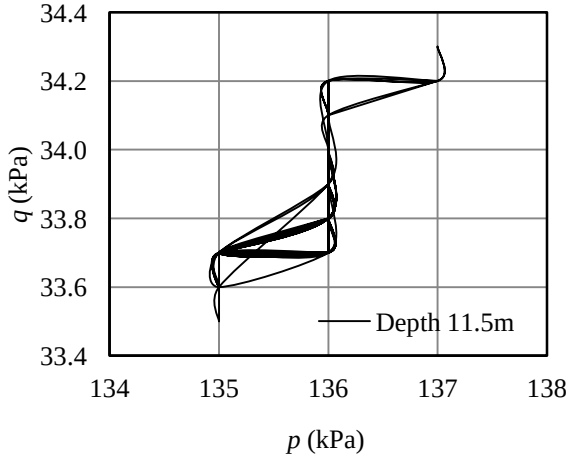

(d) 11.5 m depth

Fig. 5.18 Computed effective stress path at different depths

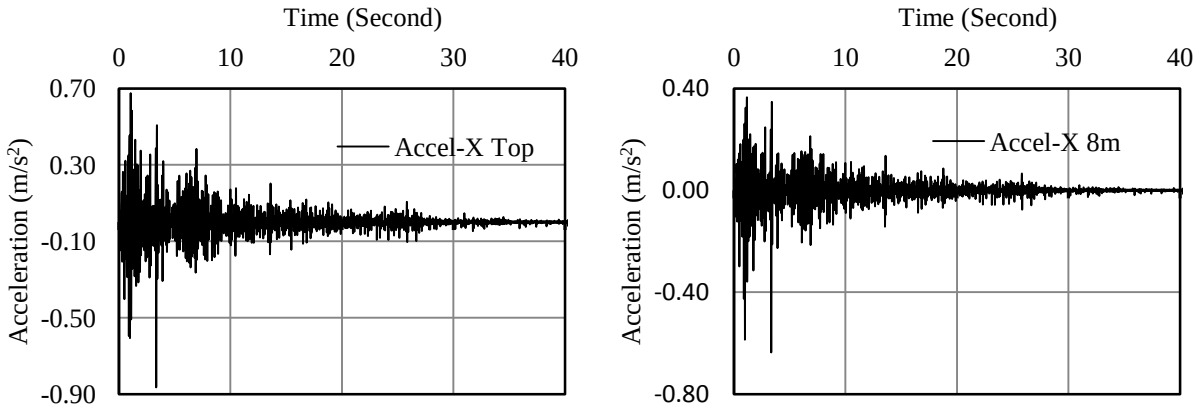

Fig. 5.19 Computed horizontal acceleration time histories at (a)Top surface (b) 8m depth

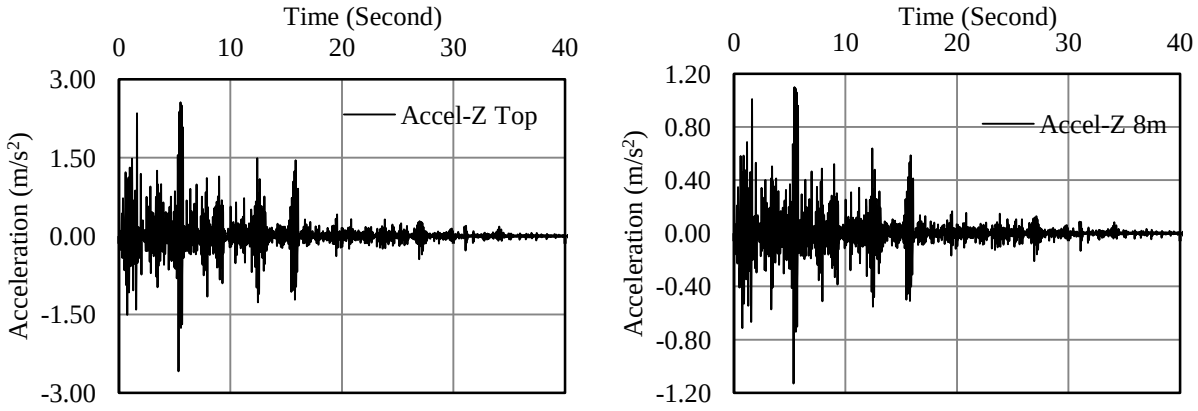

Fig. 5.20 Computed vertical acceleration time histories at (a)Top surface (b) 8m depth

5.6.1 Effect of Permeability

A parametric study has been carried out to outline the effect of permeability coefficient on liquefaction phenomena. The distributions of displacement and pore pressure that developed at various times when drainage occurs during the earthquake are presented in Figs. 5.21 and 5.22 respectively at three different value of permeability (k_1=1×10^{-4} m/sec, k_2=6.5×10^{-5} m/sec, k_3=1×10^{-7} m/sec) at G = 6MPa.

From Fig.5.21 (a) and (b), it has been observed that there is negligible variation seen in maximum horizontal displacement (1.4 cm) and in maximum vertical displacement (6.61cm) with respect to permeability. It may be due to high rise of pore water at the time of seismic load and during this small duration a nearly undrained condition prevails irrespective of permeability.

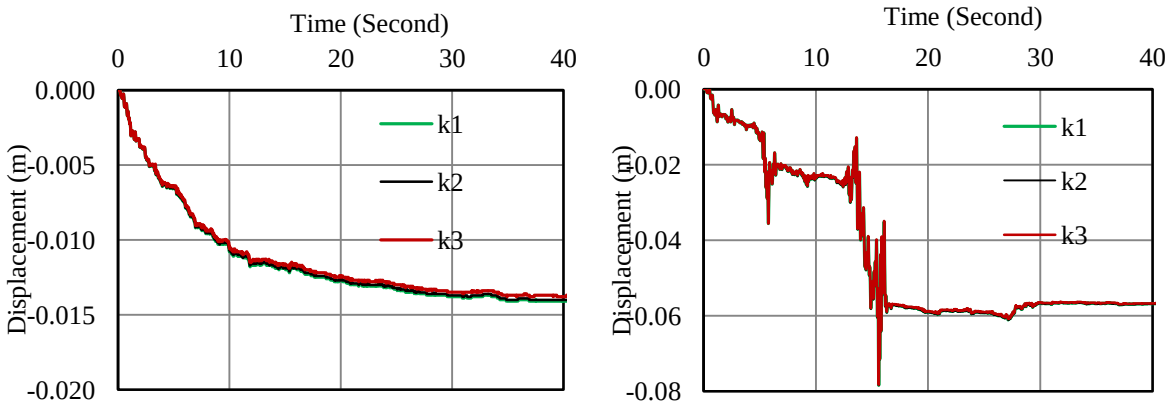

(a) horizontal displacement (b) vertical displacement

Fig. 5.21 Computed displacements with respect to time for different soil permeability at top surface of soil domain (G = 6MPa)

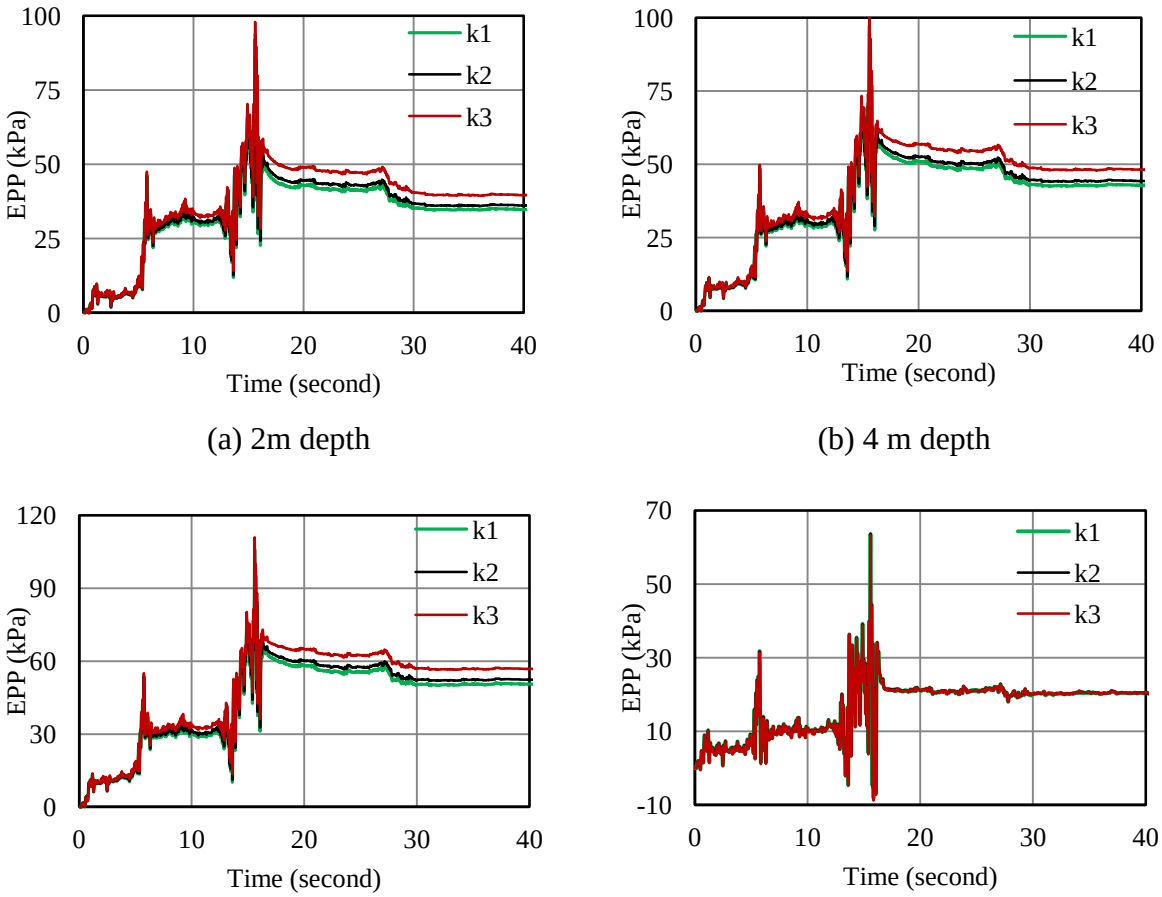

(a) 2m depth (b) 4 m depth

(c) 6m depth (d) 10 m depth

Fig. 5.22 Computed EPP with respect to time at different depths and permeability

Fig. 5.22 depicts a variation in generation of excess pore pressure (EPP) with respect to permeability at different depth. At depth of 2m, 4m and 6m, liquefaction is noticed for all permeability almost after 13.61 seconds because EPP is greater than initial effective stress having, whereas at depth of 10m, liquefaction is not seen (presence of gravel after 10m). This indicates a marginal effect of seismic loading due to higher permeability.

5.6.2 Effect of Shear Modulus

To study the effect of shear modulus on sand liquefaction, shear modulus *G* has been varied as 6 MPa, 10 MPa and 15 MPa, while keeping other parameters constant. The present study is carried out at relative density of sand as 40 %, permeability of 6.6×10^{-5} m/s. The variation of displacement and excess pore pressure for different value of shear modulus are shown Figs. 5.23 and 5.24 in respectively.

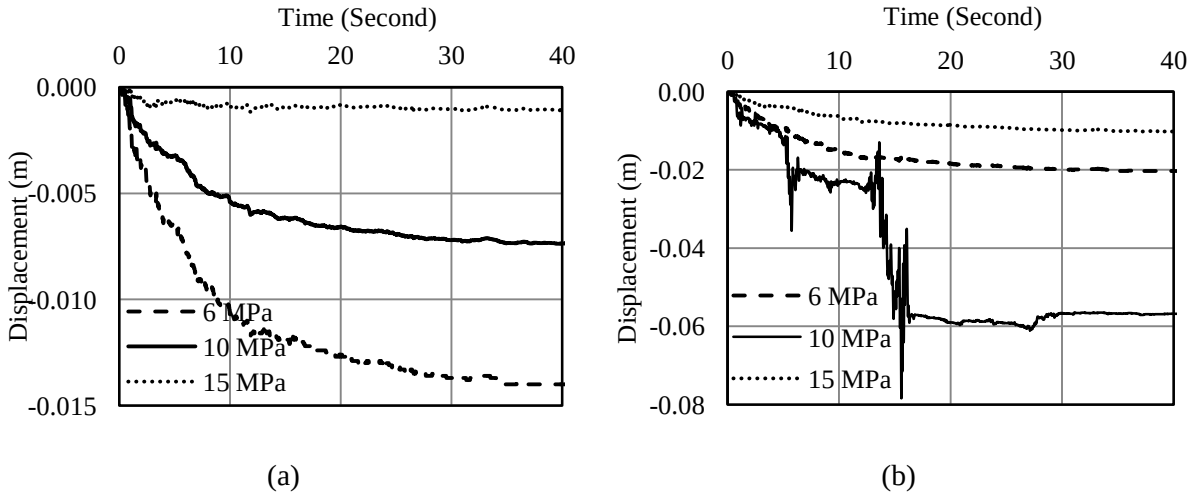

Fig. 5.23 Computed horizontal and vertical displacement with respect to time for different Shear Modulus at top.

A maximum value of horizontal displacement (1.4 cm) is noticed at *G* = 6 MPa whereas a maximum value of 1.07 mm at *G* = 15 MPa (92% reduction). A maximum value of vertical displacement (7.43 cm) is noticed at *G* = 10 MPa whereas a minimum value of 1.02 cm at *G* = 15 MPa. It is observed that vertical displacement at *G* = 10 MPa are higher than those at *G* = 6 MPa. This may be attributed to the fundamental frequency of the domain may be close to operating frequency.

At higher value of shear modulus (*G* = 15MPa), liquefaction does not occur within the soil domain except at a depth of 2m. As the shear modulus is decreased, liquefaction phenomena is observed because of generation of higher displacement and pore pressure resulting in

reducing the effective stress at shallow depth of soil mass excluding 10m. At higher soil modulus, more loads will be shared by skeleton. This in turn reduces the excess pore pressure at each step.

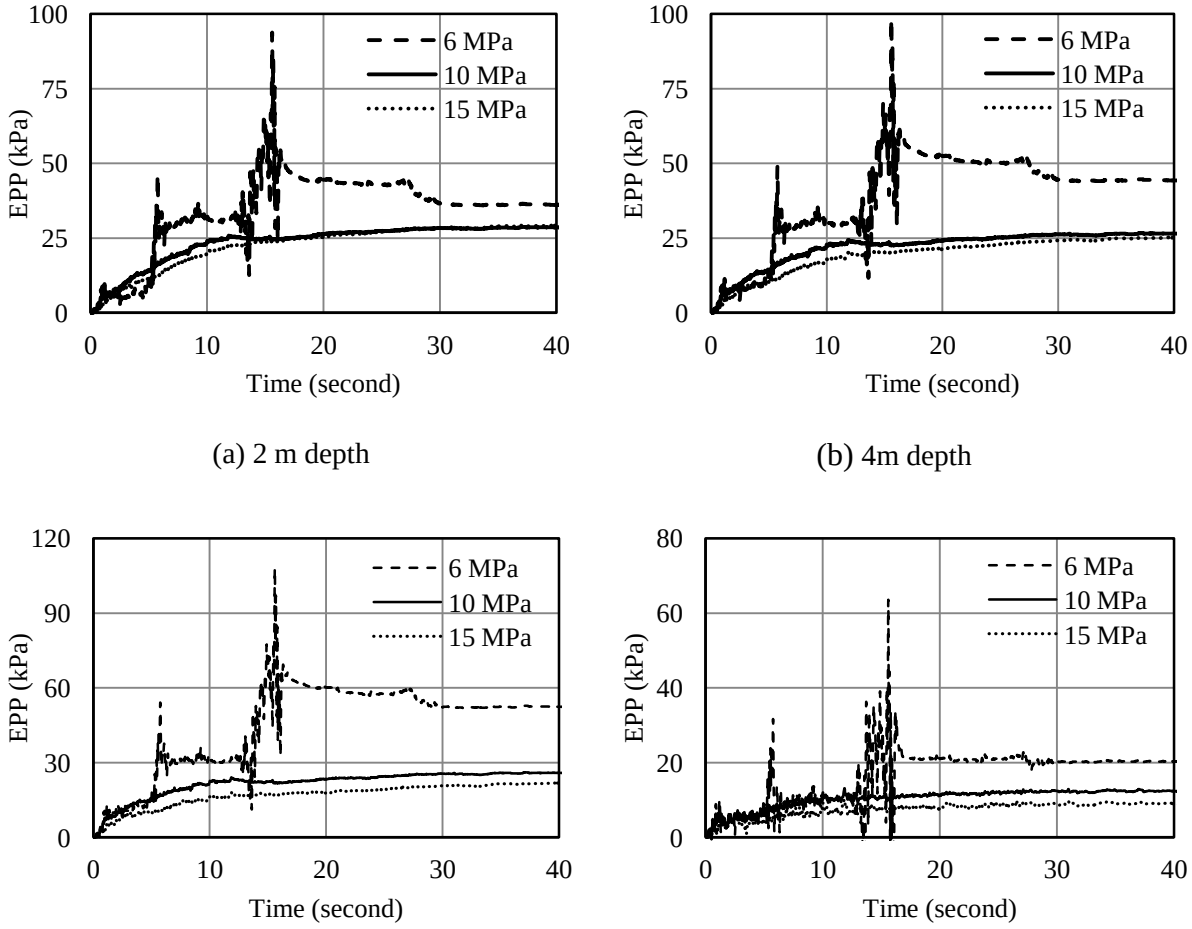

(a) 2 m depth

(b) 4m depth

(c) 6 m depth

(d) 10 m depth

Fig. 5.24 Computed EPP with respect to time at different depths and soil Modulus

The effect of permeability and shear modulus has been also carried out for the seismic excitation. A detailed study was carried out for three values of permeability as mentioned earlier, but for each value of permeability, three different values of shear modulus (G = 6, 10, 15 MPa) were assigned. To summarize the effect of these two key parameters, maximum values of displacement and EPP are reported in Table 5.4 to 5.5.

Table 5.4 Comparison of maximum horizontal and vertical displacements

Permeability	Disp (X-direction) at different depth in cm			
	G (MPa)	Top	4m	8m
k_1	6	1.41	1.22	2.88
	10	0.75	0.26	0.40
	15	0.13	0.08	0.09
k_2	6	1.40	0.49	0.76
	10	0.73	0.26	0.39
	15	0.11	0.08	0.07
k_3	6	1.38	0.48	0.73
	10	0.71	0.25	0.37
	15	0.01	0.04	0.00
	Disp (Z-direction) at different depth in cm			
k_1	6	5.69	1.22	2.88
	10	2.04	0.40	1.26
	15	1.04	0.16	0.72
k_2	6	5.68	1.21	2.88
	10	2.03	0.39	1.26
	15	1.02	0.15	0.73
k_3	6	5.67	1.17	2.88
	10	2.01	0.37	1.26
	15	0.97	0.11	0.73

From the reported values of maximum horizontal displacements (Table 5.4), the values are decreasing with increase in shear modulus for all the three permeability value. Reduction is of the order of 46 % to 96 % with higher values for higher shear modulus. Similarly maximum vertical displacements (Table 5.4), the values are observed to be reducing with increase in shear modulus. Reduction is of the order of 56 % to 88 % with higher values for higher shear modulus. Values are decreasing by small amount with decrease in permeability. But horizontal and vertical displacements are slightly higher at lowest shear modulus (G = 6 MPa). Effect of permeability is more pronounced in the values of EPP (Table 5.5). With reduction in permeability, slight increase in EPP is observed. This trend is in confirmation with the trend reported by Finn et al (1977). On the other hand, effect of shear modulus is significant on maximum EPP. A considerable reduction in EPP with increase in shear modulus is observed when shear modulus is increased from 6 MPa to 10 MPa or some higher value. Reduction is of the order of 53 % to 80 % with higher values for higher shear modulus.

Table 5.5 Comparison of maximum EPP

Permeability	G (MPa)	Maximum EPP at different depth in kPa					
		2m	4m	6m	8m	10m	12m
k_1	6	92.1	97.2	106	111	63.6	35.4
	10	31.6	29.6	28.9	27.9	14.6	10.1
	15	26.5	23.6	20.5	16.3	8.95	7.21
k_2	6	93.8	98.6	108	111	63.6	35.4
	10	28.6	26.5	25.9	25.6	12.3	8.7
	15	29.2	25.1	21.7	17.2	8.96	7.23
k_3	6	97.9	102	111	112	63.3	35.5
	10	35	33.2	32.9	30.5	15	10.5
	15	35.9	30.9	27.5	21.9	9.19	7.42

For comparison of responses with finite and semi-infinite domain, maximum displacements at top-surface and maximum EPP at 2m depth are compared (G = 10 MPa). It is observed that maximum horizontal displacements are reduced by average 63.7%, however vertical displacements have marginal effect and reduction is about average 6%. On the contrary, maximum EPP are observed to increase due to unbounded domain and increase is average 52%. Increase may be attributed to the log drainage path on account of unbounded domain.

5.6.3 Bhuj Earthquake

Bhuj earthquake (2001) produced a number of liquefaction associated ground failure phenomena including sand blows, lateral spreading, and waterspouts. The most prominent appearance of liquefaction was reported at Bharuch and Jambusar in south-eastern Gujarat in India. Raghunandan (2012) proposed 1D ground response analysis with variation in soil layer parameters for Bhuj Earthquake (M_w=7.7), India. Hence a brief analysis based on the proposed methodology has been also done for the Bhuj ground motion data (Fig. 5.25). The material properties used for the present analysis is same as mentioned for the El-Centro earthquake analysis. Fig. 5.26 shows variation in horizontal and vertical displacement at different depth of the considered soil domain (G = 50 MPa, $k = 1 \times 10^{-4}$ m/sec). It has been observed that a maximum horizontal displacement of 0.289 cm occurs at of soil stratum whereas this value is 2.17cm at top surface in case of vertical displacement. The vertical displacement at top surface is in vertical direction which indicates the occurrence of sand blows. Hazarika and Boominathan (2009) mentioned the occurrence of sand blows during Bhuj earthquake.

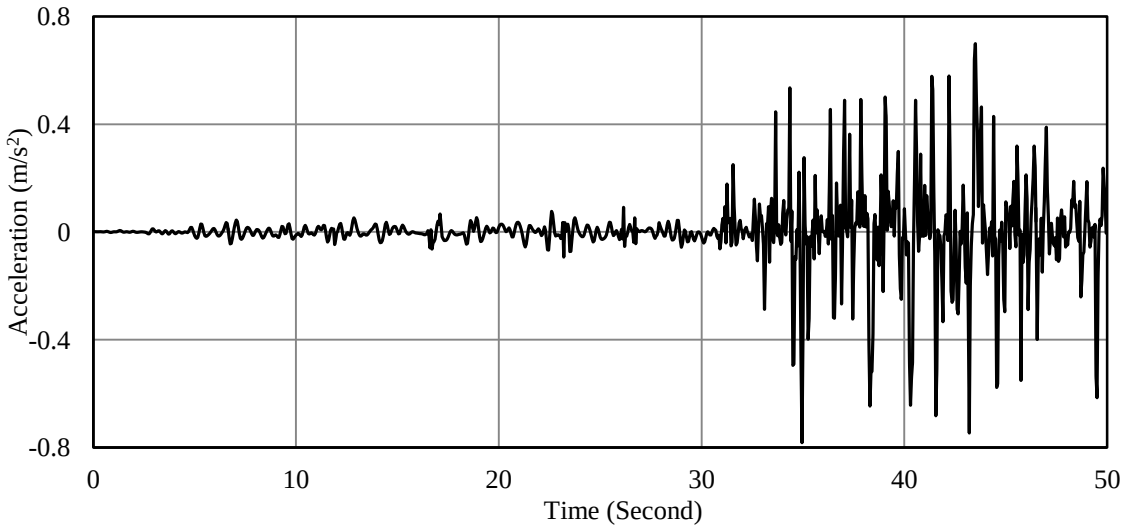

Fig. 5.25 Bhuj earthquake ground motion

Fig 5.27 shows the variation of excess pore pressure at different depth of the soil deposits. The EPP value predicted at 2m, 4m and 6m are higher than the initial vertical effective stress. This indicates the occurrence of liquefaction phenomenon. At 8m depth, The EPP value is very less as compared to initial effective stress, liquefaction does not occur at this depth, may be due to presence of gravel layer and infinite boundary after 10m. After shaking for 9.35 seconds, liquefaction first starts at 2m depth and reached at 4m after 38.44 second. It reaches at 6m after 46.2 seconds of seismic excitation. Hence, liquefaction spreads from top to bottom within a few seconds. This shows the maximum amplification at top surface of soil domain which reduced with depth.

Fig. 5.28 displays the horizontal and vertical acceleration at different depth with time. A maximum value of vertical acceleration of about -0.8m/s^2 is noted at top surface. Also a minimum horizontal acceleration (0.055 m/s^2) is noticed at 4m depth. These two values support the higher vertical displacement at top surface and minimum horizontal displacement at 4m. Fig. 5.29 depicts the typical stress paths mechanism of cyclic decrease in effective stress due to pore pressure build-up. It is observed that maximum stress ratio q/p is 0.826 at the depth of 11.5 m and 0.276 at 0.5m.

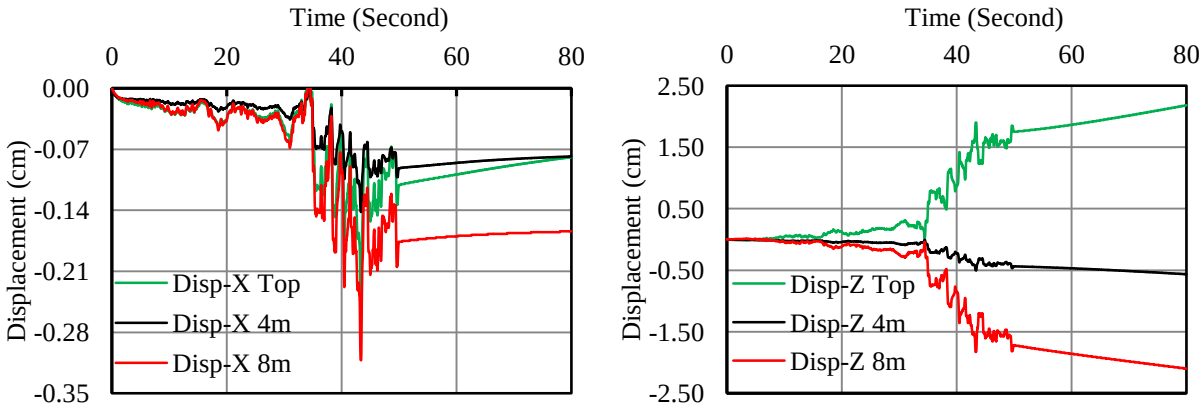

(a) Horizontal displacement (b) Vertical displacement

Fig.5.26 Computed horizontal and vertical displacement at different depth

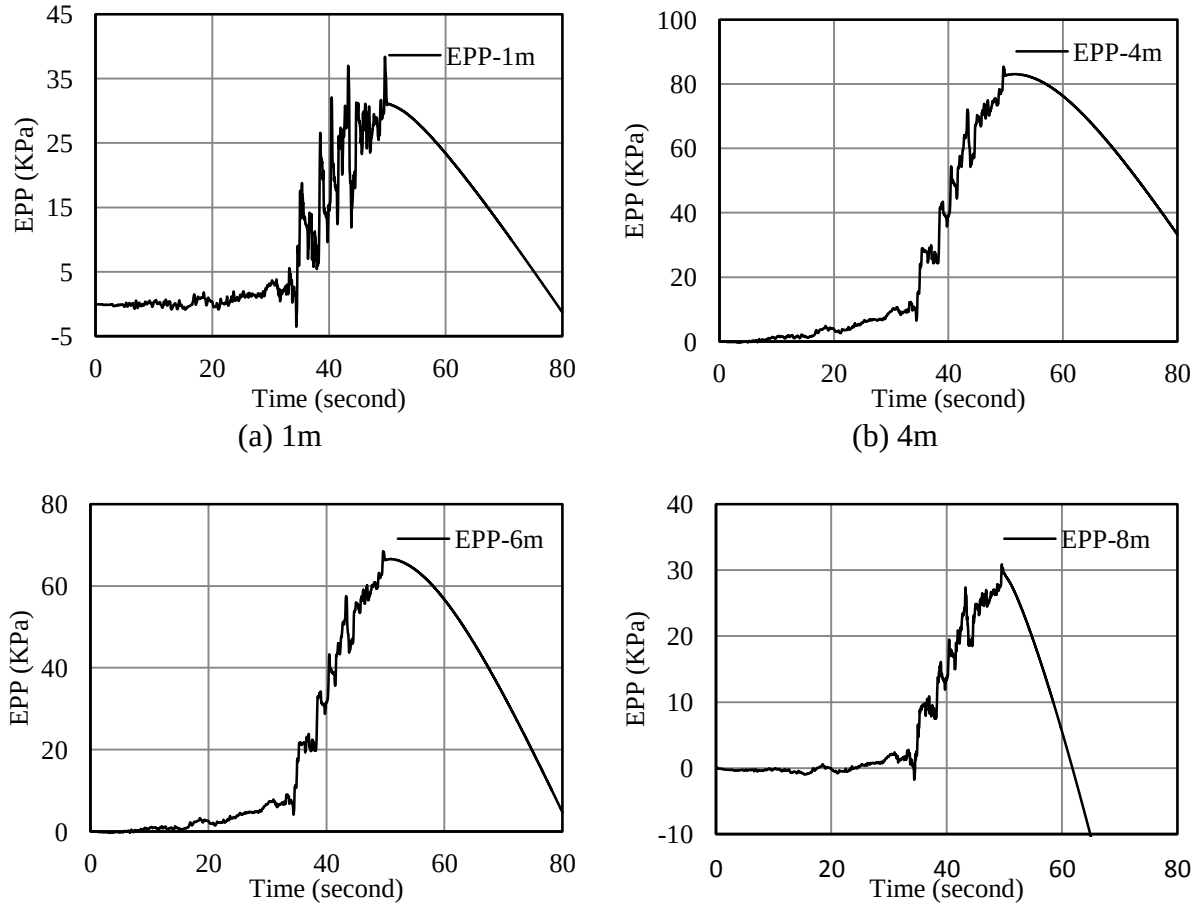

(a) 1m (b) 4m

(c) 6m (c) 8m

Fig.5.27 Computed EPP at different depth

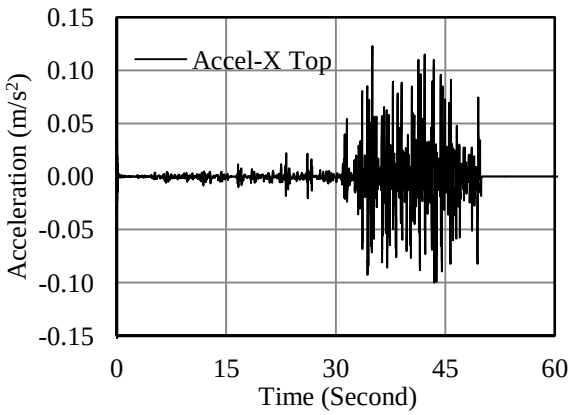

(a) Top

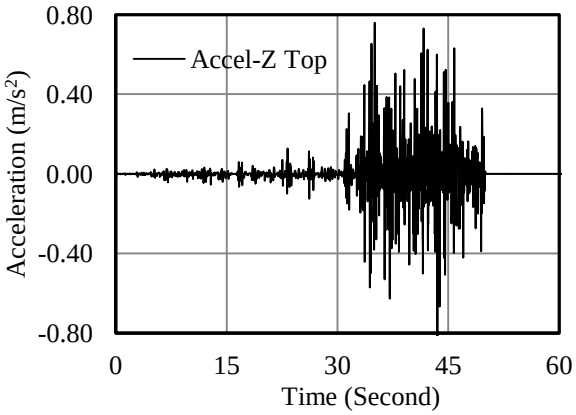

(a) Top

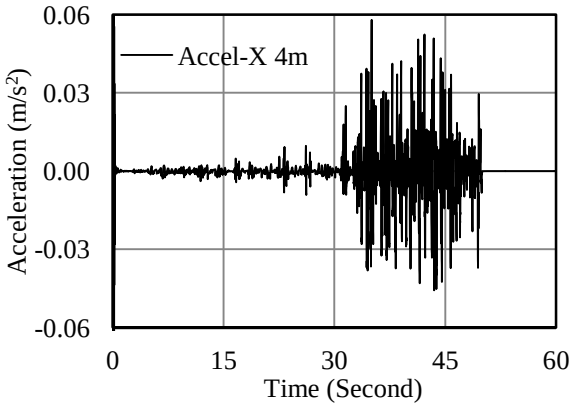

(b) 4m

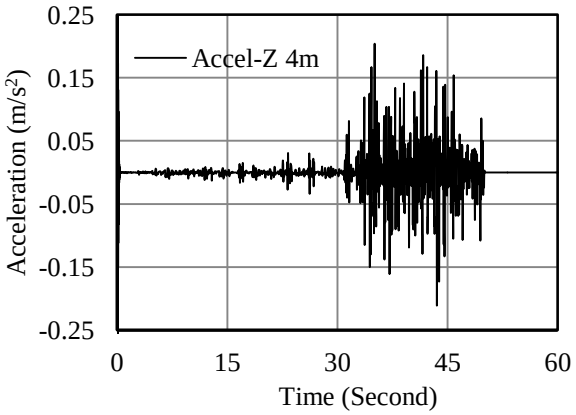

(b) 4m

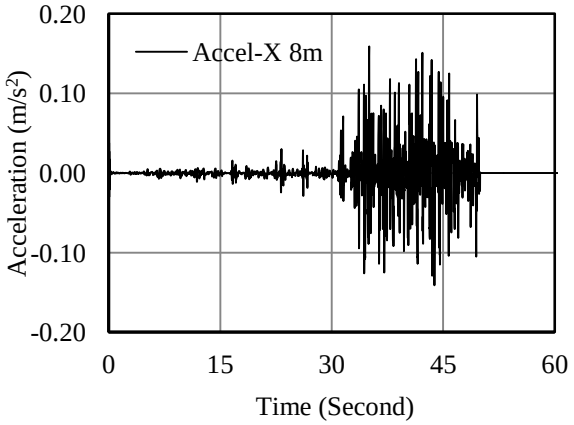

(c) 8m

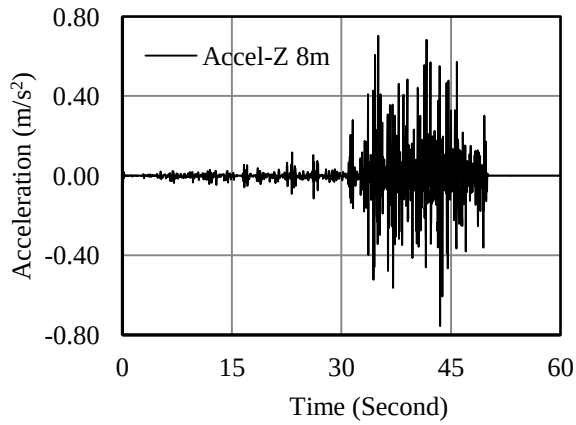

(c) 8m

Fig.5.28 Computed horizontal and vertical acceleration at different depth

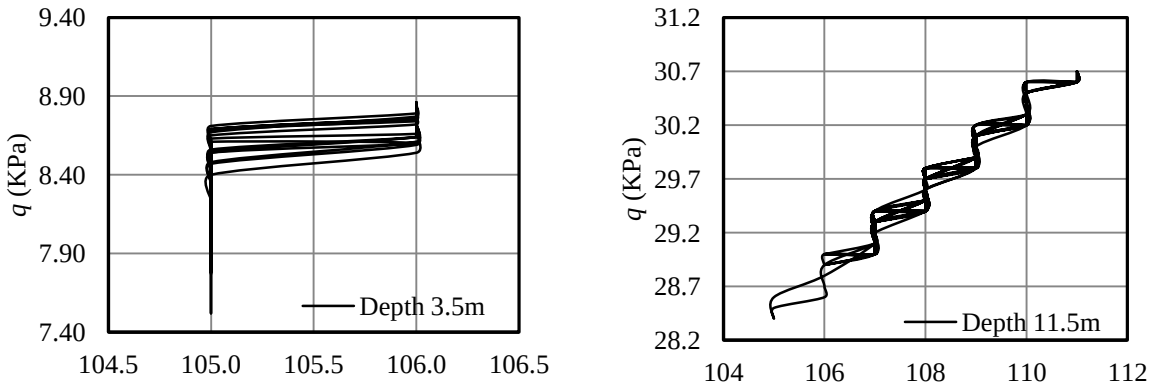

(a) 3.5m (b) 11.5m

Fig. 5.29 computed effective stress path at different depth

To examine the effect of shear modulus, two more values were attempted (G = 10 and 25 MPa). Variation in EPP with time at different depths is illustrated in Figs. 5.30-5.33. It can be noticed that liquefaction is triggered around 34 second when shear modulus is less than 50000 kPa due to higher input ground acceleration (peak value 0.78 m/s^2). Ground input motion after 30 second consists of high value of acceleration which results in high build up of pore pressure at smaller value of shear modulus. At higher value of G, part of the load is bared by soil skeleton (intergranular stress), which in turns reduces small increment of pore pressure.

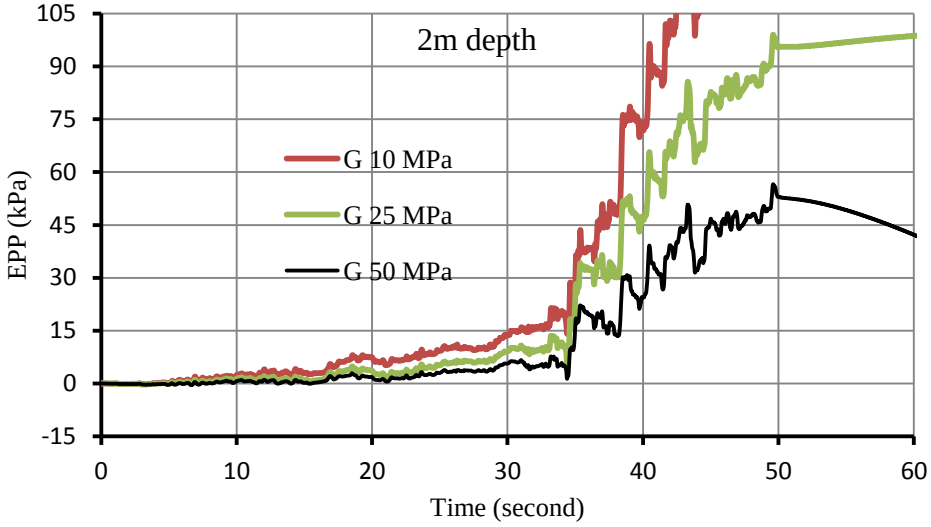

Fig. 5.30 Computed EPP at different shear modulus at 2m depth

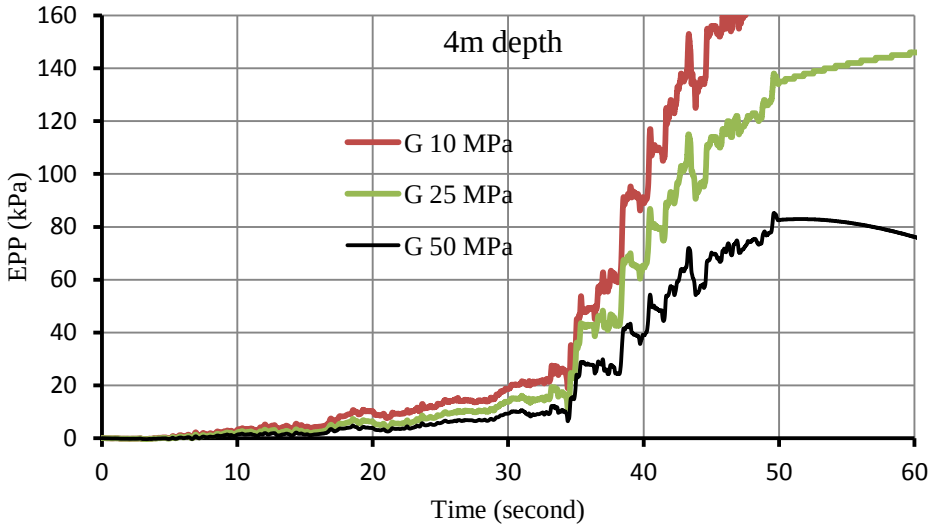

Fig.5.31 Computed EPP at different shear modulus 4m depth

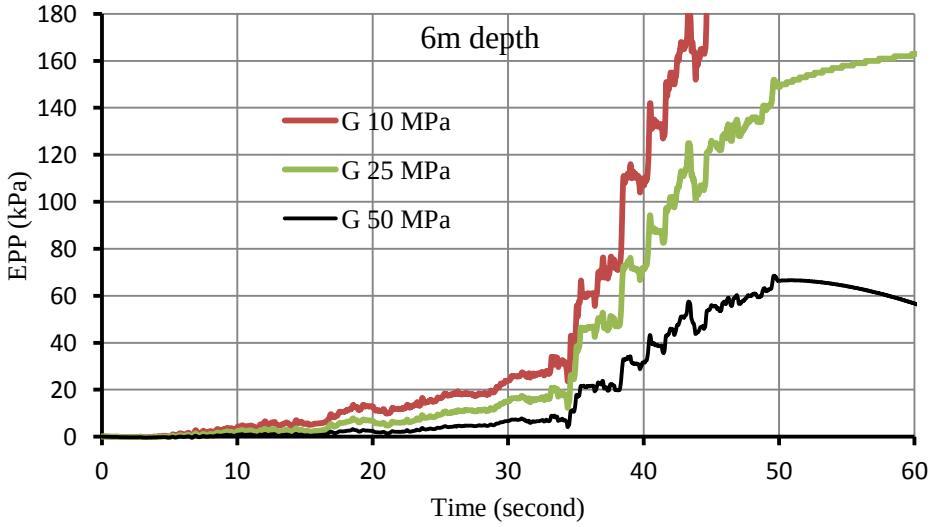

Fig.5.32 Computed EPP at different shear modulus 6m depth

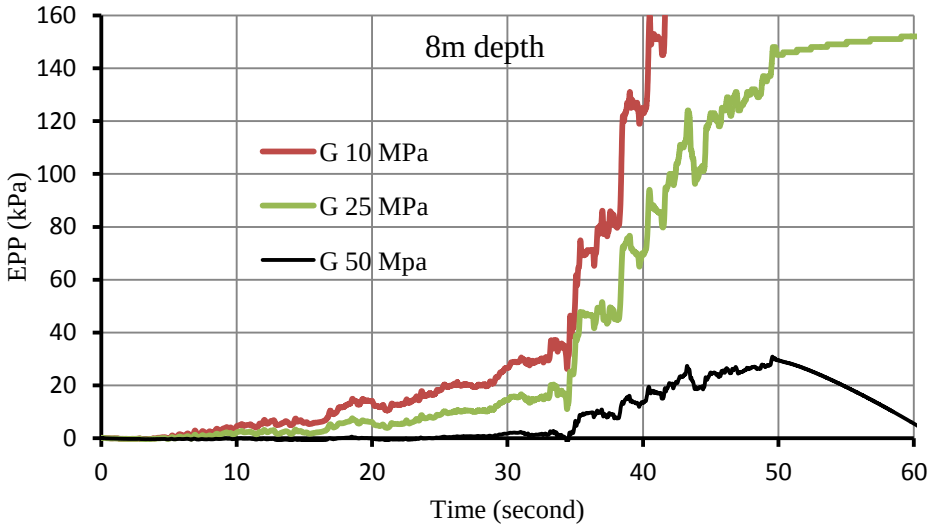

Fig.5.33 Computed EPP at different shear modulus 8m depth

5.6 CONCLUDING REMARKS

The present model developed is able to predict reasonable changes in pore pressure occurring during seismic loading which can be useful for earth structures located in regions of moderate to high seismicity. It allows the distribution of pore pressure and the effects that drainage and internal flow have on the time of liquefaction to be determined quantitatively.

For the cyclic ground motion, it is observed that values of maximum horizontal displacements are decreasing with increase in shear modulus. Reduction is of the order of 47 % to 96% with higher values for higher shear modulus. They are also decreasing slightly with reduction in permeability. Similarly maximum vertical displacements are observed to be reducing with increase in shear modulus, but vertical displacements are slightly higher at lowest shear modulus. Effect of shear modulus and permeability is more pronounced in the values of EPP. With reduction in permeability, slight increase in EPP is observed, whereas considerable effect of shear modulus is observed on maximum EPP. A considerable reduction in EPP with increase in shear modulus is observed when shear modulus is increased from 5 MPa to 10 MPa or some higher value. Reduction is of the order of 40 % to 90% with higher values for higher shear modulus.

For the El-Centro ground motion, it is observed that maximum horizontal and vertical displacements are decreasing with increase in shear modulus for all the three permeability value. Reduction is of the order of 46 % to 96 % for horizontal displacements with higher

values for higher shear modulus. Reduction is of the order of 56 % to 88 % for vertical displacements with higher values for higher shear modulus. Values are decreasing by small amount with decrease in permeability. But horizontal and vertical displacements are slightly higher at lowest shear modulus. Effect of permeability is more pronounced in the values of EPP. With reduction in permeability, slight increase in EPP is observed, whereas significant effect of shear modulus is observed on maximum EPP. A considerable reduction in EPP with increase in shear modulus is observed with increase in shear modulus. Reduction is of the order of 53 % to 80 % with higher values for higher shear modulus. Similar trend is observed for Bhuj earthquake ground motion also. Only soil domains with shear modulus more than 50000 kPa are sustainable. For smaller values of shear modulus, soil domain is liquefying at early stage of earthquake ground motion. It is observed that liquefaction is triggered around 34 second when shear modulus is less than 50000 kPa. Comparison of responses with finite and semi-infinite domain illustrated that maximum horizontal displacements are reduced by average 63.7%, however vertical displacements have marginal effect and reduction is about average 6%. On the contrary, maximum EPP are observed to increase due to unbounded domain and increase is average 52%. Increase may be attributed to the log drainage path on account of unbounded domain.

CHAPTER - 6

3D MODELLING OF LIQUEFACTION

6.1 INTRODUCTION

Liquefaction is defined as reduction in shear strength of loose saturated sand due to generation of excess pore pressures during seismic excitation. It generally occurs in areas of geographically young sediments of granular soil and silts under water table. Indication of liquefaction phenomenon has been found frequently in past earthquakes. Liquefaction occurs as ground failure as indicated from sand boiling, differential settlements, lateral spreading and loss of bearing strength beneath structures during past earthquakes (Ishihara and Yoshimine 1992). Such type of failures have caused significant loss damaged life and built environment.

Liquefaction mitigation measures generally consist of ground improvement, including removal and recompaction of low-density soils, removal of excess ground water, in situ ground densification, grouting, or surcharging. Use of stone column is a quite recent technique as compare to the traditional soil densification methods. If generation of high excess pore pressure takes place in the improved soil mass, the induced shear stresses during earthquake can be jointly distributed to dense gravel stone columns and the adjacent soil. This strength is proportional to the relative stiffness of the composite materials, improving the overall stability of the system. At present, this stress distribution mechanism in liquefied soils is not well properly understood (Adalier et al., 2003).

Adalier et al. (2003) carried out centrifuge model tests on a silty sand (with and without a surcharge) treated with the application of stone column as remedial measures at Rensselaer Polytechnic Institute, Troy, New York. The behaviour of all these treated models was predicted and quantified with respect to the benchmark models under same cyclic loading conditions.

Krishna et al. (2006) assessed liquefaction potential of soil with granular pile treatment. Seed and Booker's approach for pore pressure was modified to account for drainage and densification effect of granular pile. Permeability and coefficient of volume compressibility of soil surrounding the soil are altered. Effect of GP on liquefaction behaviour is quantified in the detailed study. Krishna, (2011) presented an overview of the use of granular piles as a liquefaction remedial measure for sand deposits. Suitability of different ground improvement techniques as liquefaction remedial measure was

discussed in light of the importance of granular piles. Various mechanisms of granular piles in controlling the liquefaction behaviour of loose sand were illustrated and quantified in detail proving their effectiveness in hazard mitigation.

Presently, reliable numerical prediction of earthquake-induced liquefaction and settlements in foundation is still a great task for the researcher and academician (Arulanandan and Scott 1993, Parra 1996, Marcuson et al. 1996, Elgamal et al. 2003).The available computer programs for predicting seismically induced deformations are sophisticated and difficult to use (Finn, 2000). It is the need of the hour to think about the further understanding about liquefaction potential and remedial measure to control the same. Full-scale testing and evaluation of remediated soil deposit under realistic earthquake conditions would be the most ideal method. However, it is highly expensive and in most cases too complex to put into practice. Numerical modeling is a reliable and very economical alternative which offers the opportunity to simulate full scale analysis with: (i) a wide variety of remediation geometries and input motions, (ii) well defined loading and boundary conditions, and (iii) soil with known properties. The choice of mitigation technique depends on the site conditions. In particular, the aim of the current research is to evaluate stone columns as a mitigation procedure to liquefaction-induced effects.

The present chapter describes the 3D numerical modeling of a loose sand stratum under earthquake loading. The benchmark model simulation was predicted first to obtain the dynamic behaviour of a loose sand deposit with and without a surface footing. The responses of this models treated with stone column improvement subjected to the same seismic loading has been predicted and compared with the response of benchmark models (BM), focusing on the evaluation of the strengthening effect of stone columns and its effect on the behaviour of the remediated soil deposits. Acceleration base input excitation of El Centro earthquake is applied to each model monitoring the displacements, liquefaction potential and excess pore pressures (EPP). Based on the response of the model, the relative effectiveness of stone columns as mitigation measure can be gauged. PLAXIS-3D finite element software is used for the analysis. The capabilities and limitations of the employed numerical procedure for modeling such type of complicated phenomena are also considered.

6.2 PROBLEM STATEMENT

A prototype soil stratum of 13 m height, 22 m width and 13m depth of loose sand having relative density (R_D) of 40% has been considered for the analysis in PLAXIS-3D. This model is examined for El-Centro earthquake motion. Response in the form of resultant displacements, liquefaction tendencies, excess pore pressure and other parameter are studied. Identical models comprising stone column having relative density (R_D) of 90% as remedial measures are considered for numerical analysis. A surface foundation is also applied to document the response of shallow foundation on liquefiable and remediated soil stratum. PLAXIS-3D uses the UBC3D-PLM model. This model is extended from UBCSAND model originally introduced by Peubla et al. (1997). Galavi et al. (2013) extended this formulation UBC3D-PLM model for liquefaction study. New features were introduced to obtain higher accuracy under seismic loading. The present analysis is effective stress analysis in which liquefaction occurs as a result of pore pressure generation. In this analysis all parameters are effective stress parameters and total stress is the summation of effective stress and pore pressure. Undrained conditions are stimulated and volumetric strain and bulk modulus of water in pores is considered. Parameter selection and use of numerical tool play a significant role in this type of analysis.

6.3 CONSTITUTIVE RELATION

A Drucker Prager criterion based modified non associative plastic potential function has been considered to maintain the coaxiality of stress strain behaviour in deviator plane for a stress path initiated from isotropic line. Soil densification mechanism is also included to obtain higher accuracy in predicted EPP during seismic excitation. This mechanism permits for the increase of EPP with decreasing rates when shearing takes place. This behaviour is also found in the experimental studies. Main characteristics of the model are presented as follows:

6.3.1 Yield Function

In the present analysis two types of yield surfaces has been incorporated, primary yield surface and secondary yield surface. Primary surface is based on isotropic hardening and becomes active when mobilized friction angle is equal to maximum mobilized friction angle that soil has ever reached. Here current stress ratio is the highest stress ratio in the loading history. Simplified Kinetic hardening rule is utilized for secondary yield surface. It becomes active when mobilized friction angle is less than maximum mobilized friction

angle. Here current stress ratio is lower than maximum stress ratio in the loading history. This distinction between yield surfaces is made to be able to have densification rule in secondary yield surfaces.

A stress state is considered on the isotropic axis and both yield surfaces are in the same position. From isotropic stress state, both primary and secondary yield surfaces expand according to the same hardening rule. When soil is unloaded, secondary yield surface shrinks and soil acts in an elastic behavior. Upon reloading secondary yield surface becomes active and behavior becomes elasto-plastic. When mobilized friction angle reaches maximum mobilized friction angle, the primary yield surface becomes active again and behavior becomes softer. Mohr-coulomb yield formulation is used to define both yield surfaces.

$$f_m = \frac{\sigma'_{\max} - \sigma'_{\min}}{2} - \left(\frac{\sigma'_{\max} + \sigma'_{\min}}{2} + c' \cot \phi'_p \right) \sin \phi'_{mob} \qquad (6.1)$$

In which, $\sigma'_{\max}$ *and* $\sigma'_{\min}$ are the maximum and minimum principal effective stress respectively. *c*' and ϕ'_p are defined as cohesion and peak effective friction angle. ϕ'_{mob} is the mobilized friction angle during hardening. It is assumed that intermediate principal stress is not affecting the yield surface in 3D yield space.

6.3.2 Elastic behavior

The secondary yield surface shows the elastic behaviour and it is governed by stress dependent nonlinear mechanism described by Peubla et al. (1997). Pure elastic behavior has been obtainable by the model in case of unloading phase.

$$K^e = K_B^e P_A \left(\frac{p'}{P_A} \right)^{n_k} \quad ; \quad G^e = K_G^e P_A \left(\frac{p'}{P_A} \right)^{n_g} \qquad (6.2)$$

In which, K^{e} is the elastic bulk modulus. G^{e} is the elastic shear modulus. K_B^e *and* K_G^e are bulk and shear moduli at reference stress condition. *p*' is mean effective stress n_{k} and n_{g} define the rate of stress dependency of stiffness. P_{A} is atmospheric pressure and defined as pressure at reference level.

6.3.3 Plastic potential function

Direction of plastic strain increment is specified by the gradient of plastic potential function. Non associated flow rule based on Drucker Prager model is expressed as follows:-

$$g = q - \frac{6\sin\psi_{mob}}{3-\sin\psi_{mob}}\, p \tag{6.3}$$

In which, g is the plastic potential function. ψ_{mob} is the mobilized dilation angle. p is mean effective stress. q is known as deviatoric stress.

Direction of plastic strain increment is perpendicular to Drucker Prager surface. Mobilized dilatancy angle is computed using flow rule as defined in Puebla et al. (1997) which results from stress dilatancy concept, linearized and simplified in accordance with energy considerations. It is defined as follows:

$$\sin\psi_{mob} = \sin\phi'_{mob} - \sin\phi'_{cv} \tag{6.4}$$

6.3.4 Hardening Rule

Hardening rule is described by Peubla et al. (1997) and given by the following expression:

$$d\sin\phi'_{mob} = 1.5K_G^p \left(\frac{p'}{P_A}\right)^{n_p} \left(\frac{P_A}{p'_m}\right)\left(1-\frac{\sin\phi'_{mob}}{\sin\phi'_{ult}}\right)^2 d\lambda \tag{6.5}$$

In which, K_G^p is the plastic shear modulus. n_{p} is a model parameter stands for stress dependency of the plastic shear modulus. p' is the mean effective stress. P_{A} is the effective stress. is defined as plastic strain increment multiplier. ϕ'_{ult} is the ultimate mobilized friction angle. It is obtained from the failure ratio (R_{f} <1) as

$$R_f = \frac{\sin\phi'_p}{\sin\phi'_{ult}} \tag{6.6}$$

6.3.5 Densification rule

Soil densification mechanism is considered to obtain higher accuracy in predicted excess pore pressure. (Beaty and Bryne, 1998). Secondary yield surface in the model ensures even transition into liquefied stage of soil mass. Plastic strains generated during this stage are lesser than the primary yield surface. Anisotropic hardening rule is employed during primary yield surface and Simplified kinematic hardening rule is considered during secondary yield surface.

$$K_G^P = K^p_{G,\mathrm{Primary}} \left(4+\frac{n_{ev}}{2}\right) k_{dens}\, f_{dens} \tag{6.7}$$

In which, n_{ev} is defined as the number of shear stress reversals in loading to unloading or vice versa. f_{dens} is a parameter input by user to calibrate densification rule. k_{dens} is a factor used to correct densification rule for loose and cohesionless soil having values 0.5 to 1.

$K^{p}_{G,Primary}$ is the initial value of K^{p}_{G} entered by user for primary yield surface. As per experimental validation, the rate of generation of pore pressure decreases with the increase of number of cycle.

6.3.6 Post liquefaction and cyclic mobility

Volumetric locking is vital in modeling cyclic liquefaction. Once stress path reaches the yield surface described by peak friction angles, volumetric strain approaches constant value due to formulation of flow rule ($\phi'_{mob} = \phi'_{p}$) and remains constant while ϕ'_{cv} is also constant. So, stiffness degradation of soil caused by post cyclic mobility of dense sands cannot be modeled. To solve this problem plastic shear modulus K^{P}_{G} is decreased gradually as a function of induced plastic deviatoric strain during dilation of soil element. This will result in stiffness degradation. Deconstruction of soil element occurs during dilative behavior hence soil stiffness decreases during contraction after unloading phase. Stiffness degradation is given as

$$K^{P}_{G} = K^{p}_{G,Primary} e^{E_{dil}} \tag{6.8}$$

$$E_{dil} = \min(110\varepsilon_{dil}, f_{post}) \tag{6.9}$$

ε_{dil} is the accumulated plastic deviatoric strain. f_{post} is used to limit the exponential multiplier term.

6.3.7 Undrained behavior

Increment of the pore pressure is computed by

$$dp_w = \frac{K_w}{n} d\varepsilon_v \tag{6.10}$$

In which, K_w is defined as the bulk modulus of the pore fluid, n signifies porosity and $d\varepsilon_v$ is the volumetric strain increment.

Bulk modulus when soil is fully saturated is derived from

$$\frac{K^{sat}_{w}}{n} = K_u - K' = \frac{2G^e}{3}\left(\frac{1+\mu_u}{1-2\mu_u} - \frac{1+\mu}{1-2\mu}\right) \tag{6.11}$$

In which, and K' denote the undrained and drained bulk moduli of the soil. μ and μ_u are the Poisson ratio in drained and undrained condition. μ_u is assumed equal to 0.495. Drained Poisson ratio can be derived from the elastic parameters of the model as

$$\mu = \left(3K^e - 2G^e\right) \Big/ \left(6K^e + 2G^e\right) \tag{6.12}$$

6.3.8 Dynamic Boundary Condition

In dynamic analysis it is required to absorb stresses at artificial boundaries to prevent reflection of waves. Selection of boundary conditions is made based on the problem, accuracy and stability of the boundary condition. Two types of boundary conditions are used in the proposed model.

1. Viscous boundaries:- Neumann type of boundary conditions where stresses at boundaries are updated to nullify the reflected stresses.
2. Free field boundaries:- Free field motion is given to boundaries by the means of free field elements. It can be assumed as one dimensional element with connected (one way) dashpots. To absorb the waves reflected from internal structures, viscous boundaries are considered at the boundary of main domain.

6.4 VALIDATION

Centrifuge experiment is one of the best experimental techniques for modeling and observing soil liquefaction. It simulates stress conditions in the model close to the full-scale prototype.

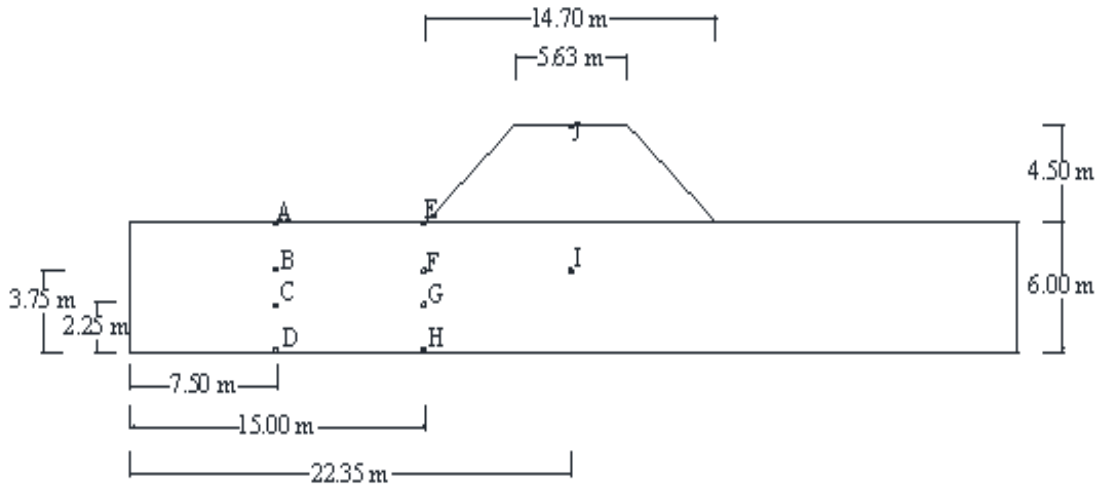

Fig. 6.1 Validation Model

The correctness and accuracy of the proposed numerical modeling in PLAXIS 3D is examined from comparison of numerical response with centrifuge data conducted at the RPI centrifuge facility (Adalier, 1996). Dynamic stability of a 4.5m clayey sand embankment (Fig.6.1) supported on 6m of medium saturated sand tested at 75*g* level in centrifuge (20m thick model) has been used for the validation of proposed model developed in Plaxis-3D. The embankment with 45° slope was composed of Kaolin clay

and Nevada sand mixtures (1:4 weight ratios) with density 1.9 t/m^3 and 14% moisture content of 14%. Foundation soil was saturated Nevada fine sand (R_D = 40%) was used as the liquefiable. The Nevada sand was having a prototype permeability coefficient of 5.5 × 10^{-4} m/sec, which is in the range of medium sands (Lambe and Whitman, 1969).

The input motion is comprised of 10 cycles of 0.18g at 1.6 Hz prototype scale. The measured and predicted displacement, acceleration and EPP time variation at different location are shown in Fig. 6.2.

It is clear from Fig. 6.2(a) that the predicted and measured values of displacements are in close agreement. At location E, the maximum vertical displacements are 1.03cm and 1.24cm for experimental and numerical study respectively, whereas these values are 20.6cm and 19.9cm at location J. A close agreement is observed between numerical and experimental results. Similar comparison of acceleration at location I and J is presented in Fig. 6.2(b). It is observed that predicted values of accelerations are slightly lower than the experimental values.

It is revealed from Fig. 6.2(c) that the predicted values of EPP are in good agreement with the measured values in centrifuge experiment. The maximum values of EPP at location F are 33.33 kPa and 30.07 kPa for experimental and numerical model respectively, whereas corresponding values at location I are 34.84 kPa and 37.8 kPa respectively.

At location F, the EPP has attained the value corresponding to 100% initial vertical effective stress at the time of 7 seconds, marking initial liquefaction. Numerical results are showing fairly good agreement with centrifuge results presented by Adalier (1996), with little deviation. The comparison reveals that the present model can approximately simulate the real behavior of liquefaction phenomena.

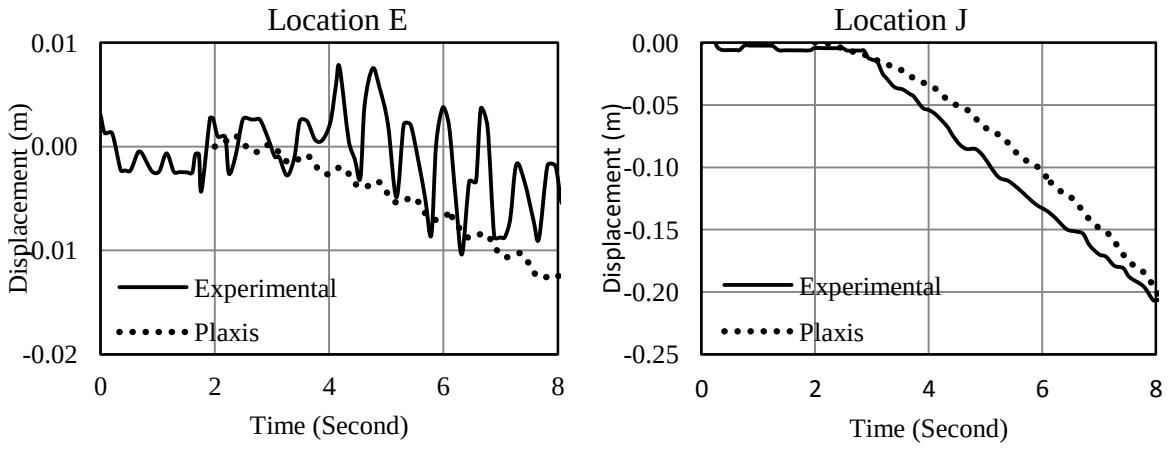

(a) Displacement

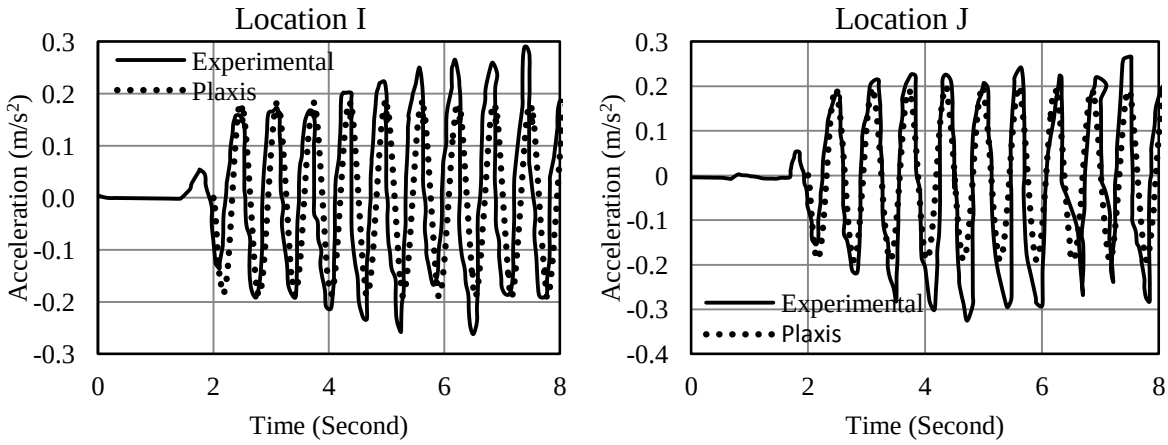

(b) Acceleration

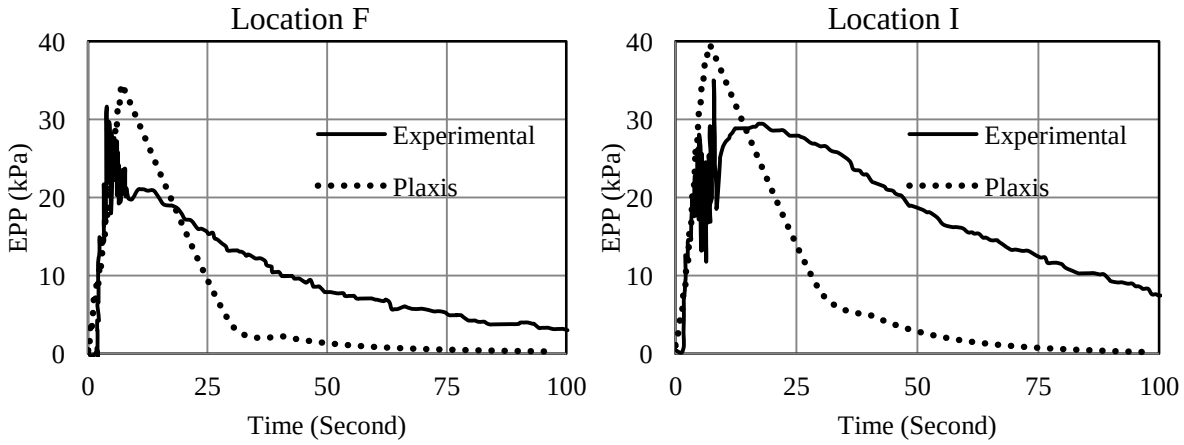

(c) Excess Pore Pressure

Fig. 6.2 Variation in displacement acceleration and EPP at different location

6.5 NUMERICAL STUDIES

The first numerical analysis (Model 1) is performed for the benchmark model to explore the response of a 13 m thick loose sand strata with R_D = 40% (Fig. 6.2-a). In the second analysis (Model 2), a total of 9 columns of 1.0 m diameter were placed with center-to center spacing of 4 m in x-direction and 2.5 m in y-direction in the benchmark model at predestined positions (Fig. 6.2-b and c.) The primary aim of Model 1 and 2 analyses is to examine the effect of stone columns on soil strengthening, and mitigation of liquefaction. In the third analysis (Model 3), the same stratum with surcharge applied through a rigid footing was considered (Fig. 6.2-d and e). The surcharge of 144 kPa is designed to simulate the vertical pressure of multistory reinforced concrete building. In the fourth analysis (Model 4), stone columns specified in Model 2 are introduced in Model 3 at predestined positions (Fig. 6.2-f and h). Ground water table is assumed to be at the soil surface in all analysis.

A 13m thick horizontal soil layer is modelled with the borehole option in PLAXIS 3D. Stone column are introduced in structure mode. Soil and Stone column are modeled using 10 noded tetrahedral elements in continuation of soil, with different properties. It is assumed that soil stratum is fully submerged in water. The numerical analysis is divided into different phases and specific type of analysis is done for that particular phase. Material properties of various parameters of soil stratum and stone column are reported in Table 6.1. Input model parameters for UBC3D-PLM are reported in Table 6.2. Input ground motions of El-Centro earthquake are described in Fig. 6.4. The SPT values are used as the input to find other values using formulae mentioned below. Relation between normalised SPT value and relative density are referred from Fig. 6.5. Permeability values and stone column properties were taken as suggested by (Adalier et al., 2003). The input parameters are evaluated based on Brinkgreve et al. (2012):

$$\begin{aligned} \gamma_{unsat} &= 15 + 4.0\, R_D/100 \quad (\text{kN/m}^3) \\ \gamma_{sat} &= 19 + 1.6\, R_D/100 \quad (\text{kN/m}^3) \\ E_{oed}^{ref} &= 60000\, R_D/100 \quad (\text{kN/m}^2) \end{aligned} \tag{6.13}$$

Galavi et al (2013) proposed equations for generic initial calibration as Follows:

$$\begin{aligned} K_G^e &= 21.7 \times 20 \times \left((N_1)_{60} \right)^{0.333} \quad ; \quad K_B^e = K_G^e \times 0.7 \\ K_G^p &= K_G^e \times \left((N_1)_{60} \right)^2 \times 0.003 + 100 \quad ; \quad R_f = 1.1 \times \left((N_1)_{60} \right)^{-0.15} \end{aligned} \tag{6.14}$$

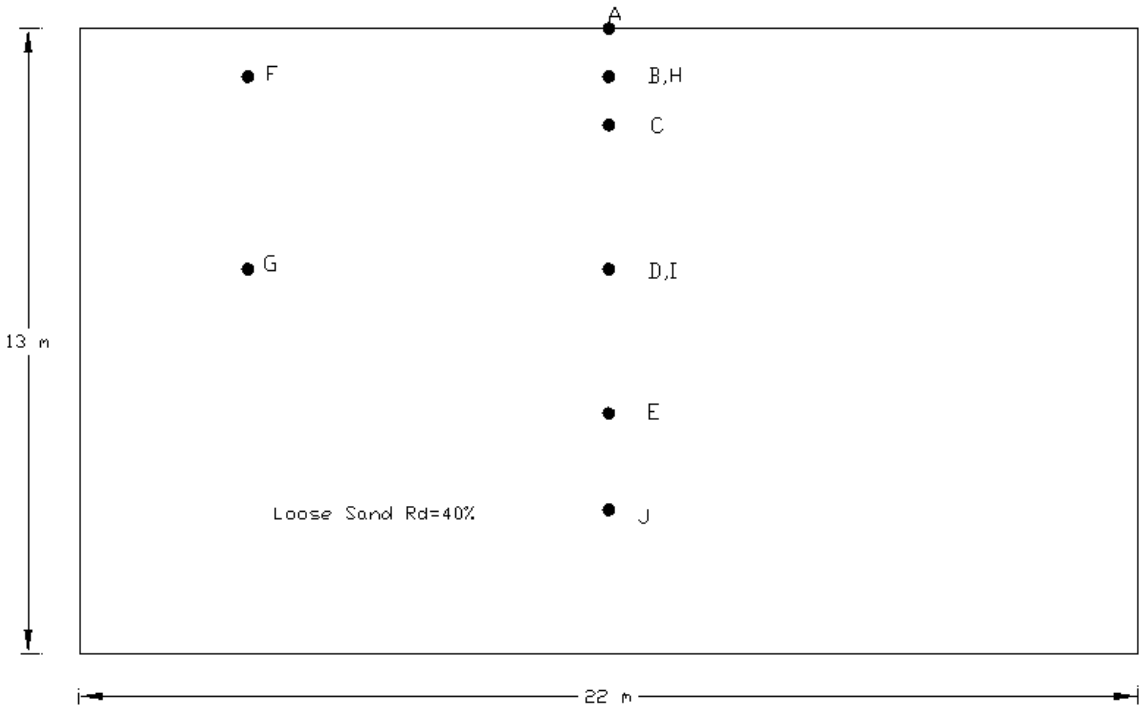

Fig. 6.3(a) Benchmark model

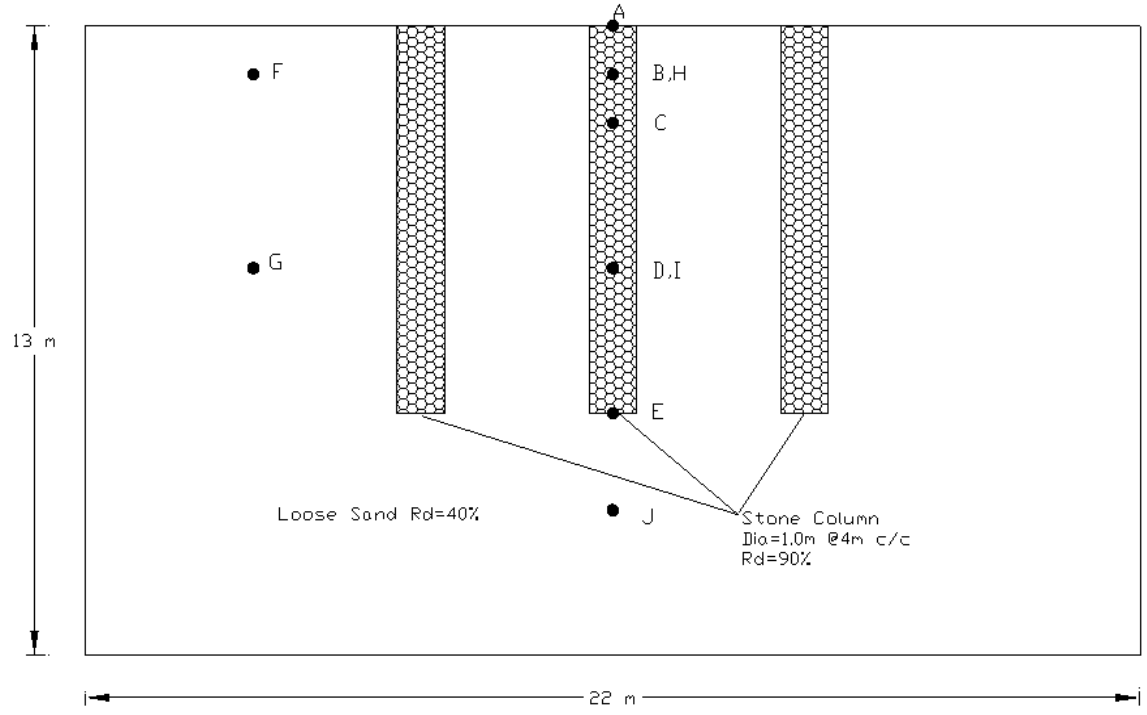

Fig. 6.3(b) Benchmark model with Soil Column (Cross-section)

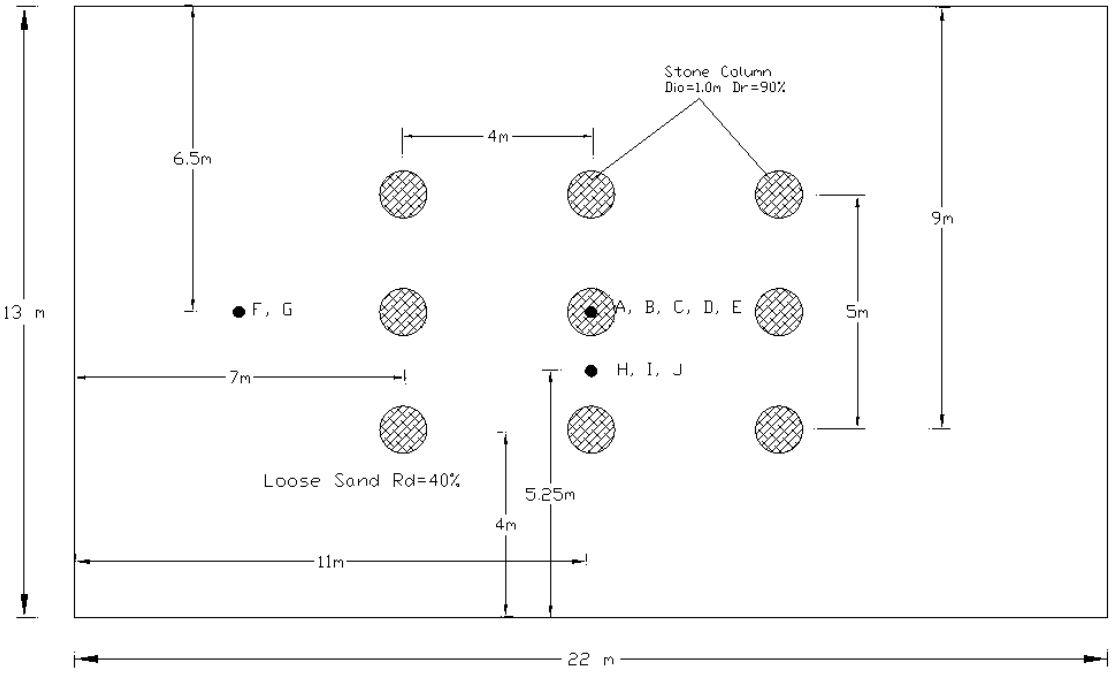

Fig. 6.3(c) Benchmark model with Stone Column (Plan)

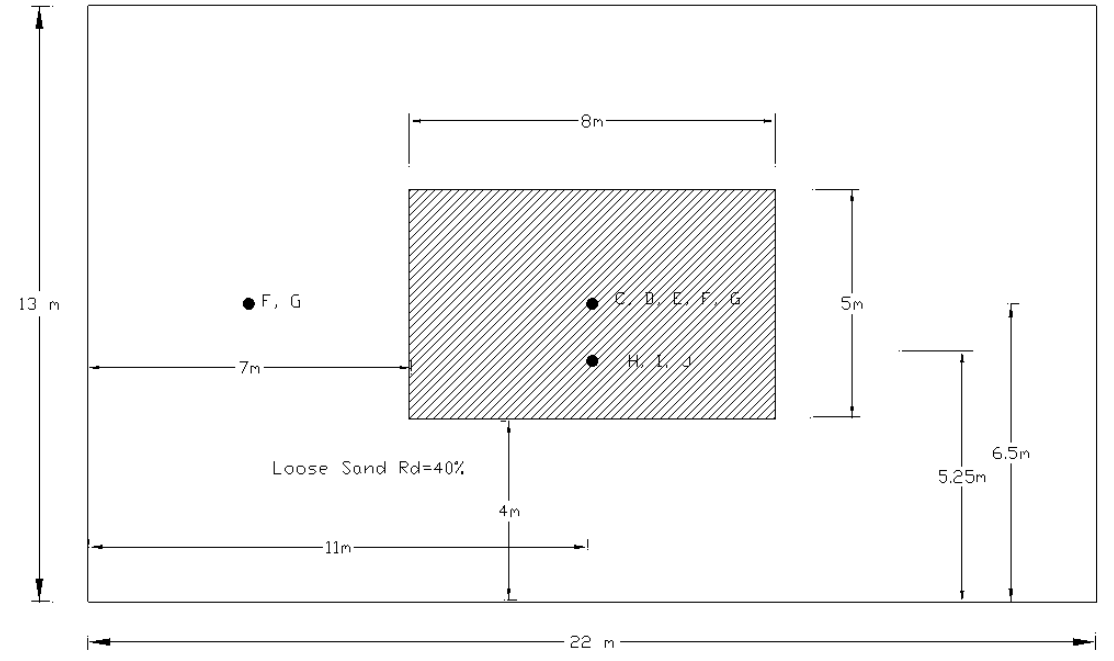

Fig. 6.3(d) Benchmark model with Footing (Plan)

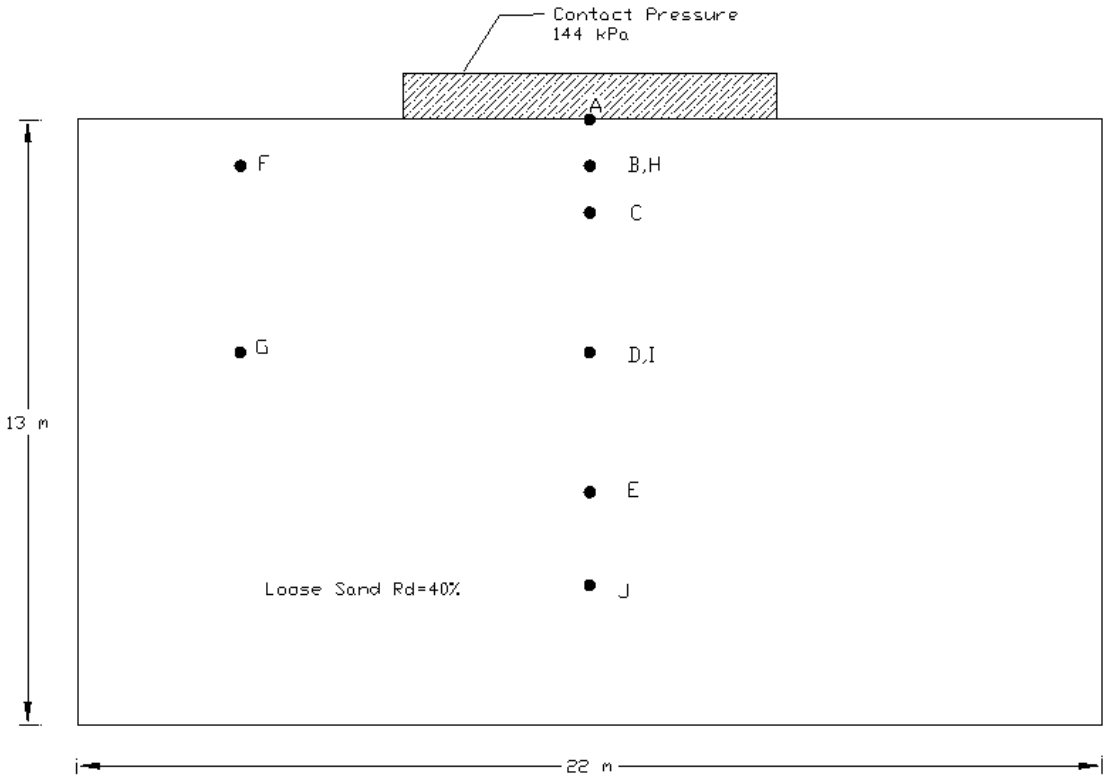

Fig. 6.3(e) Benchmark model with Footing (Cross-section)

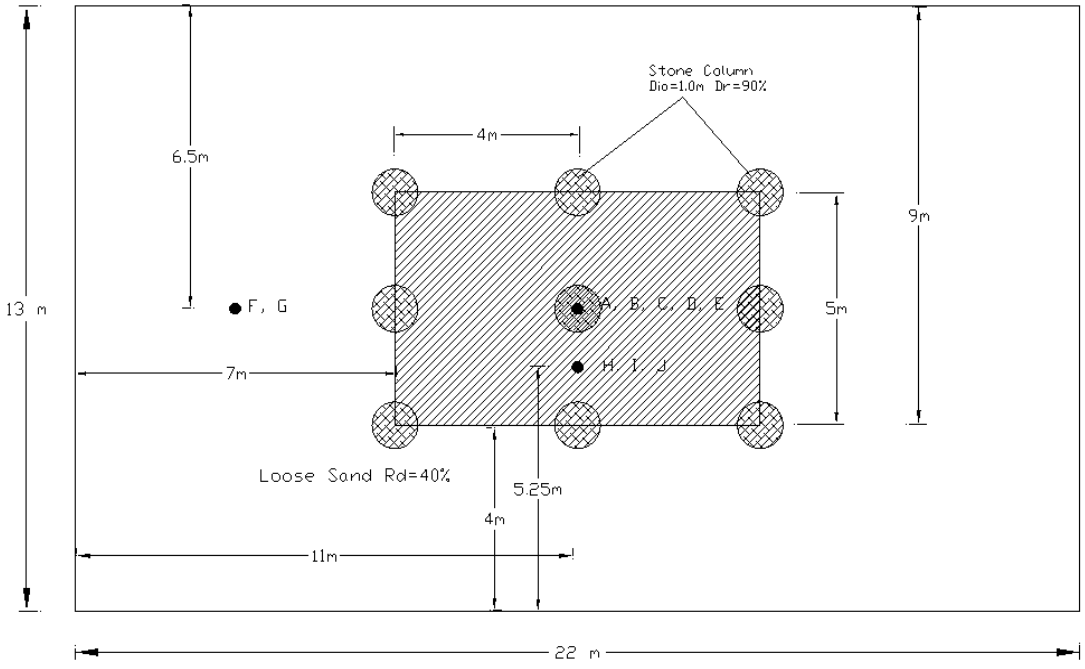

Fig. 6.3(f) Benchmark model with Footing and stone Column (Plan)

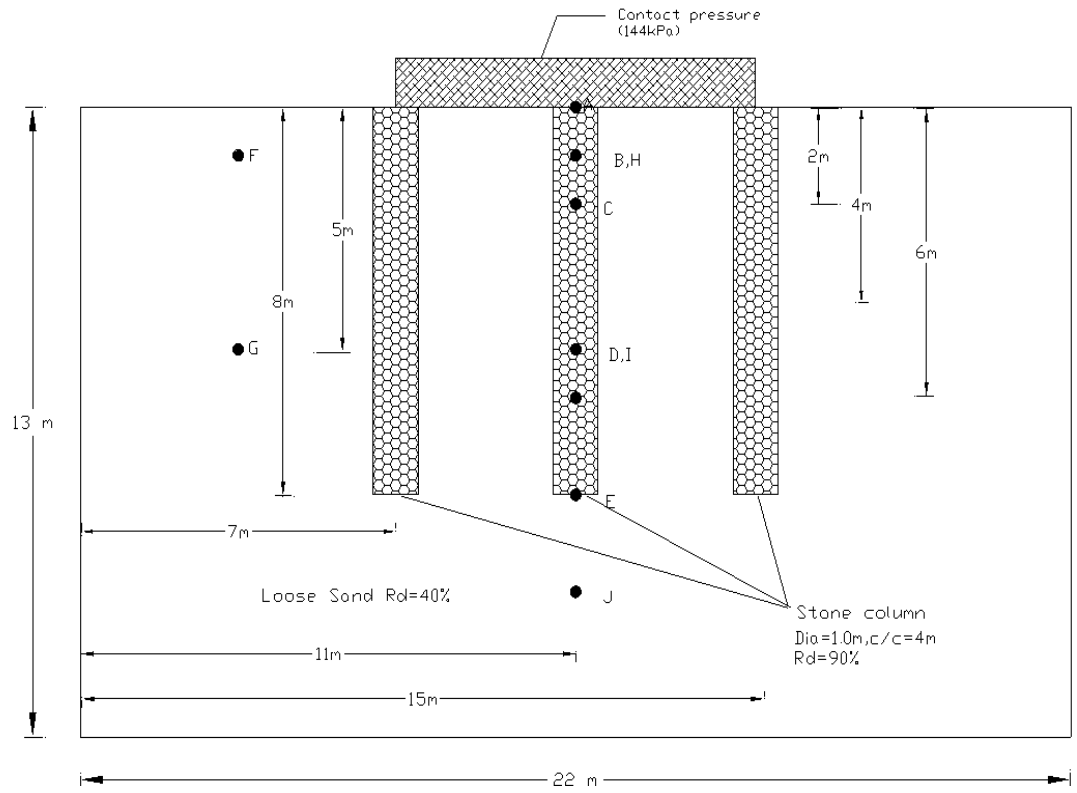

Fig. 6.3(g) Benchmark model with Footing and stone Column (Cross-section)

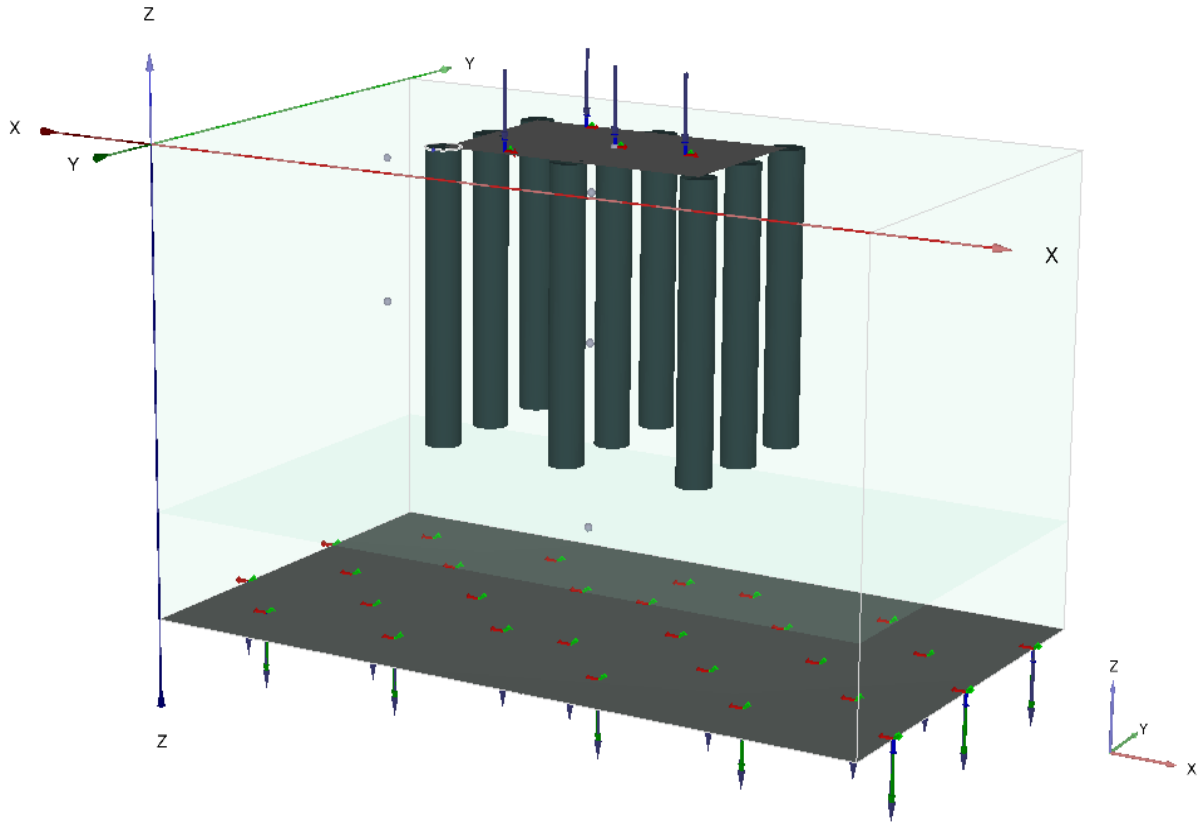

Fig. 6.3(h) Three dimensional Fig. of Model

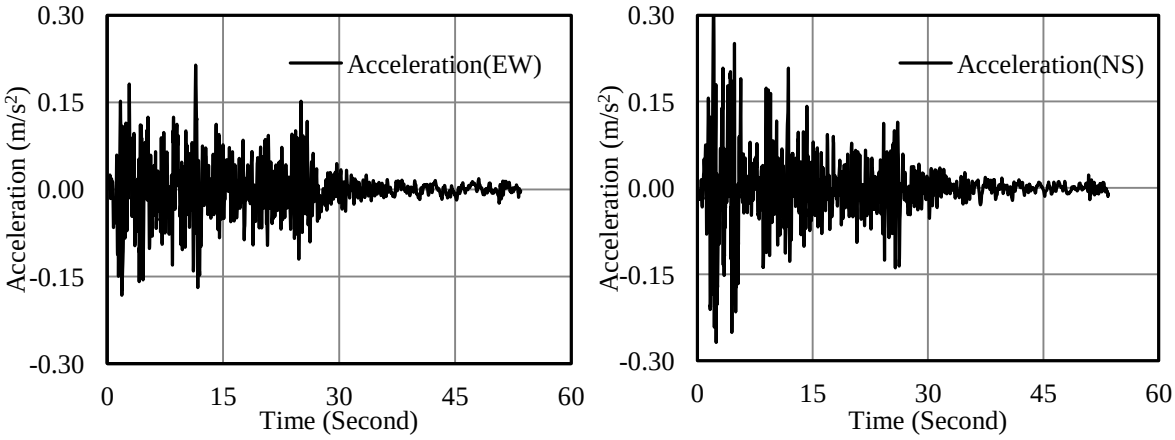

X-Direction Y-Direction

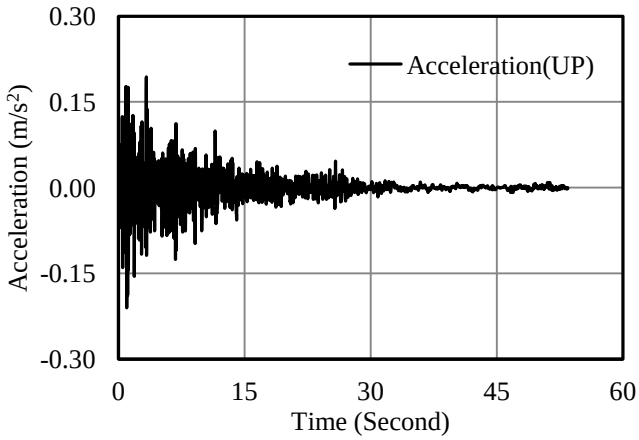

Z-direction

Fig. 6.4 Input El-Centro earthquake

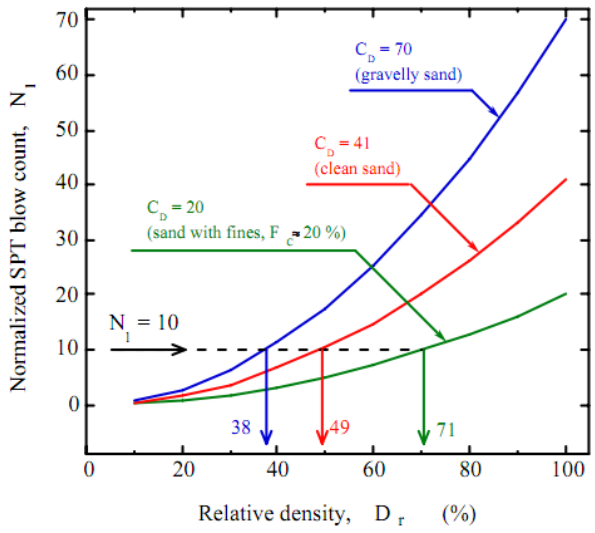

Fig. 6.5 Relation between normalised SPT value and relative density (After Cubrinovski et al., 1999)

Table 6.1 Material properties and boundary conditions

Properties of loose sand stratum			
γ_{dry} =16.6 kN/m^3	γ_{sat} =16.64 kN/m^3	$e_{initial}$ = 0.667	E'=25 MPa
C' = 0 kPa	$k_x = k_y = k_z = 6.6\times10^{-5} m/s$	μ = 0.3	ϕ'=31^o
Properties of stone column			
γ_{dry} =18.6 kN/m^3	γ_{sat} =20.4 kN/m^3	$e_{initial}$ = 0.546	E'=54 MPa
C' = 0 kPa	$k_x = k_y = k_z = 2.3\times10^{-5} m/s$	μ = 0.3	ϕ'=31^o
Boundary conditions	X min :- Viscous X max:- Viscous	Y min:- Viscous Y max:- Viscous	Z min:- None Z max:- None

Table 6.2 Input model parameters for UBC3D-PLM

Parameters with description	Loose sand	Stone Column
Peak friction angle (ϕ'_p)	33.65^0	40^0
Friction angle at constant volume (ϕ'_{cv})	33^0	37^0
Elastic shear modulus number (k_G^e)	809.4 kPa	890 kPa
Elastic bulk modulus number (k_B^e)	566.6 kPa	623 kPa
Plastic shear modulus number (k_G^p)	202.6 kPa	3755 kPa
Power for stress dependency elastic bulk modulus (n_k)	0.5	0.5
Power for stress dependency elastic shear modulus (n_g)	0.5	0.5
Power for stress dependency plastic shear modulus (n_p)	0.4	0.4
Failure ratio (R_f)	0.83	0.64
Reference stress (P_A)	100 kPa	100 kPa
Fitting parameter to adjust densification rule (f_{dens})	0.45	0.45
Fitting parameter to adjust post liquefaction behaviour(f_{post})	0.02	0.02
Corrected SPT blow counts ($(N_1)_{60}$)	6.5	37

A numerical study based on effective stress analysis is presented here to demonstrate the effect of liquefaction phenomena and its remedial measure for a case of soil stratum subjected to seismic loading. Extensive discussion of soil behaviors are not presented here with as main focus is given to computational modeling and prediction.

6.5.1 Model 1 and Model 2 (without surcharge)

Fig. 6.6 displays the computed vertical displacement with respect to time at different location of soil domain during the seismic event for Model 1 and Model 2. A maximum displacement of 28.2 cm and 24.6 cm are observed at location A (top most position of soil mass) for model 1 and model 2 respectively whereas these values are 25.4 cm and 22.9 cm at depth of 2m (Location C). Similar trend are visible at other depth also for the above said model. A relatively less is estimated at depth of 10m (Location H). In case of Model 2, lesser values of displacements are predicted in comparison with the benchmark Model 1, but the variation is marginal. In lack of surcharge at surface, stone-columns are apparently ineffective in controlling settlements. A summary of maximum values of displacements is reported in Table 6.3. The displacements at A, C, D, F, H, I and others points are roughly uniform in nature with maximum value ranging from 4.5 to 28 cm which is decreasing with depth. The values obtained in model 2 are about 13% less than those for Model 1. This reveals strengthening effect of stone column in Model 2. Similar effect of stone column was reported in the centrifuge study by Adalier (2003).

The variations in EPP with time at different locations in soil domain during the seismic loading for Model 1 and 2 are illustrated in Fig.6.7. The computed EPP at different location (B, E, G, H, I and J) are compared with remedial measures (stone column). The maximum value of EPP at point B is 6.27 kPa without remedial measure whereas with stone column, it is reduced to 5.13 kPa. At point E (depth 8m), a significant fall in EPP is observed in case of stone column. All EPP records (Fig. 6.7) display similar pattern. After an initial rise, a peak is achieved, and then the EPP remains more or less constant till the end of earthquake and even after for some time. Except at location I, a reduction of around 40% in EPP is visible in Model 2.

Table 6.3 Maximum Displacement of Benchmark Model and BM with stone column at different location

Location	**Bench Mark**				**Bench Mark + Stone Column**			
	U_x (cm)	*U*y (cm)	*U*z (cm)	*U*	U_x (cm)	*U*y (cm)	*U*z (cm)	*U*
A	2.14	-1.09	-30.59	30.69	2.17	-1.01	-27.05	27.16
B	2.00	-1.01	-29.58	29.67	2.02	-0.97	-26.43	26.52
C	1.83	-0.91	-28.31	28.39	1.83	-0.91	-25.50	25.58
D	1.22	-0.62	-21.71	21.76	1.26	-0.63	-20.55	20.60
E	0.31	-0.52	-11.53	11.55	0.36	-0.48	-12.70	12.71
F	2.05	-1.20	-29.39	29.49	2.03	-1.11	-26.56	26.66
G	1.09	-2.92	-21.89	22.11	1.12	-2.35	-20.92	21.09
H	-0.55	-3.42	-4.83	5.94	-0.56	-3.64	-5.43	6.56
I	-3.51	-0.44	-29.06	29.28	-3.28	-0.46	-27.93	28.13
J	-6.75	-0.39	-23.91	24.85	-5.76	-0.32	-23.13	23.84

Figs. 6.8(a-b) display contours of non-dimensional EPP R_u on a central vertical plane within the benchmark model and with stone column, The R_u lines define the status of build-up pore pressure with respect to initial effective stress. They are indicative of primary liquefaction state due to earthquake motion. Predicted pore-pressure time responses highlighted that soil is liquefied for a short period of time in Model 1and Model 2 having maximum R_u of 1.233 and 1.232, respectively. The soil is liquefied for very small location in case of Model 2 as compared to Model 1.

Comparisons of predicted accelerations for seismic excitation are shown in Fig. 6.9(a-b). In case of application of soil column, acceleration values have been reduced little as compared to the benchmark model. This is reflected in the reduced level of acceleration amplitudes. Similar trends are observed at different points of this model. A significant drop in magnitude of predicted acceleration is observed at all the locations after 30 seconds of loading.

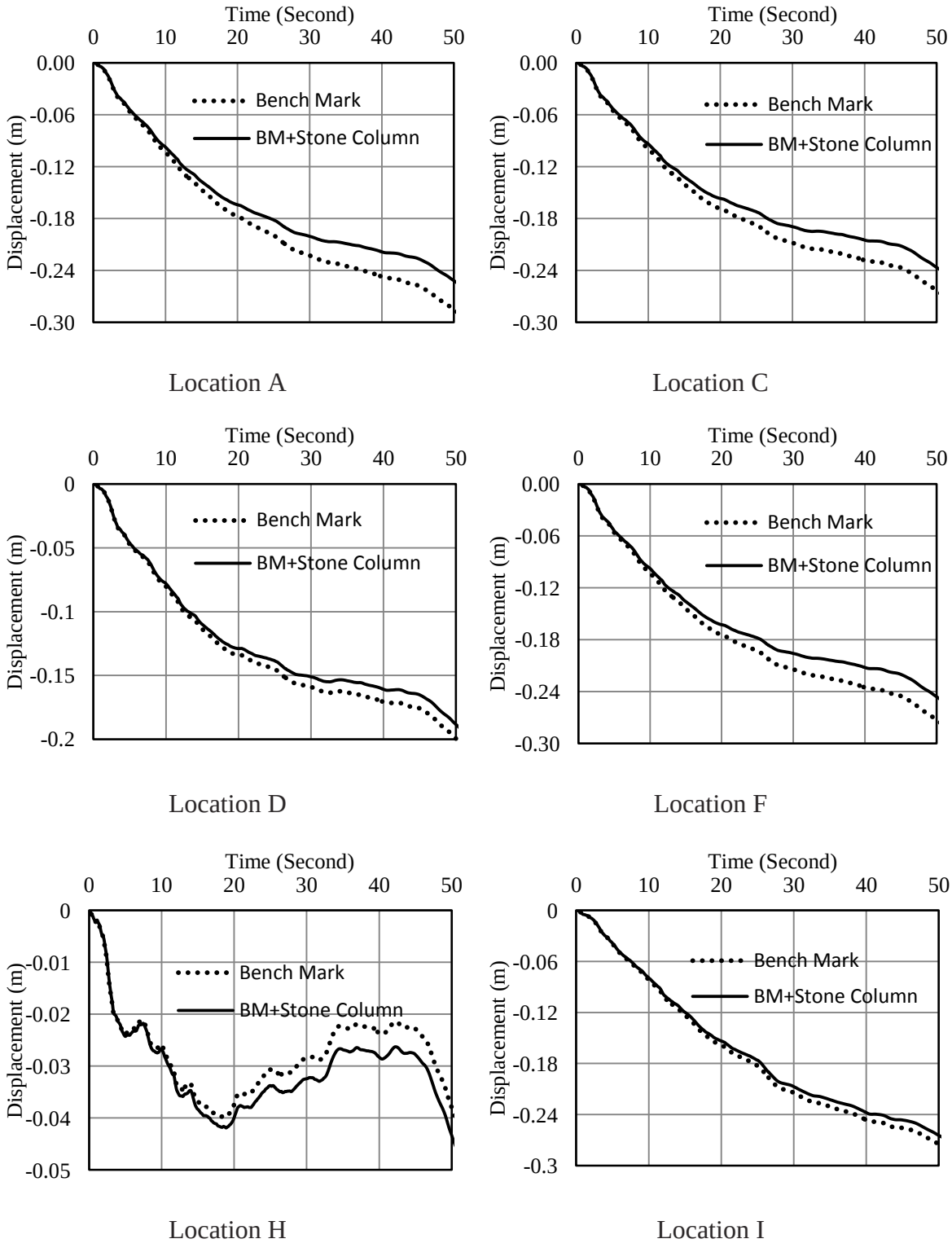

Fig. 6.6 Variation in vertical displacement with time at different location (Model 1 and 2)

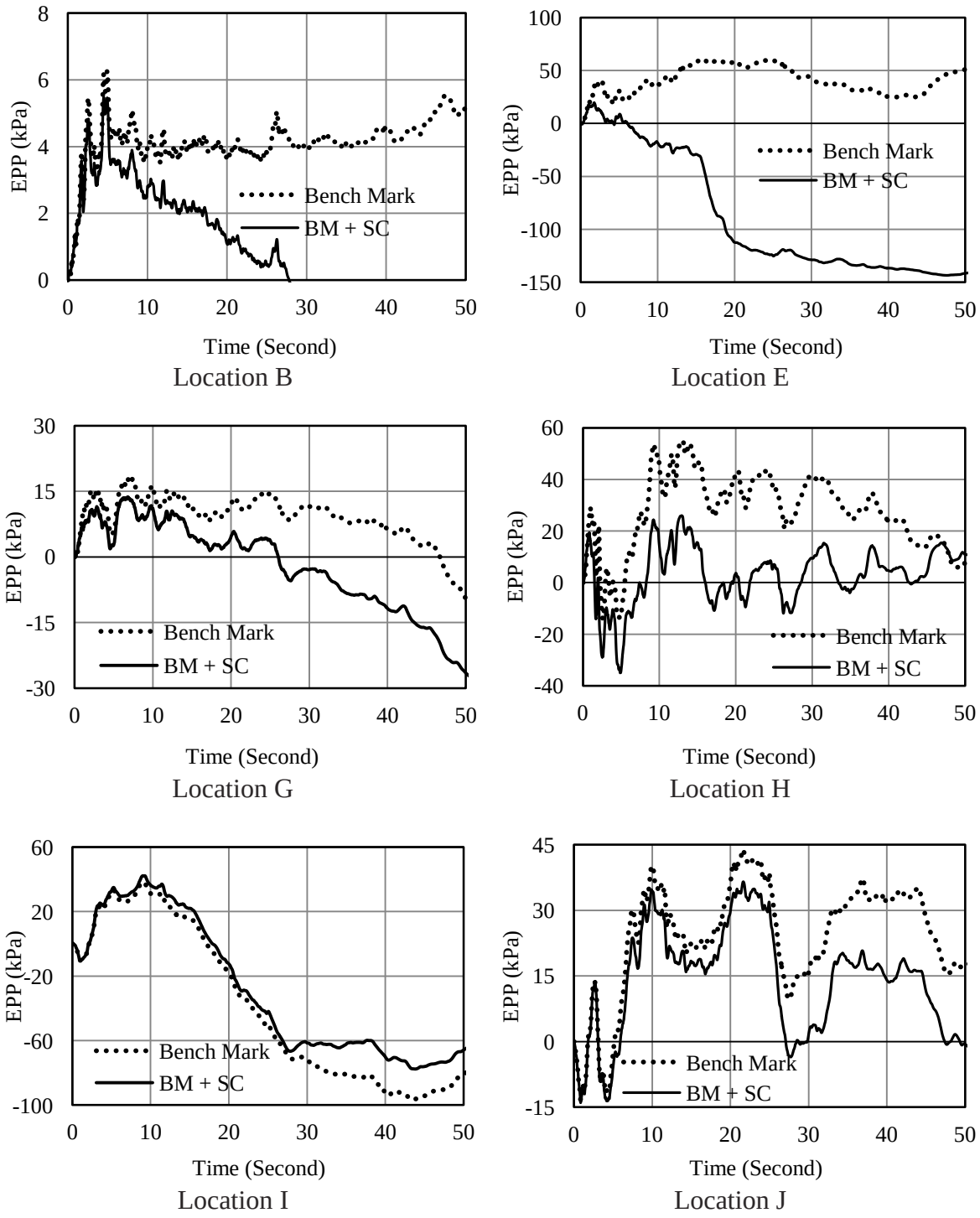

Fig. 6.7 Computed EPP with respect to time at different location for benchmark and benchmark with stone column (Model 1 and 2)

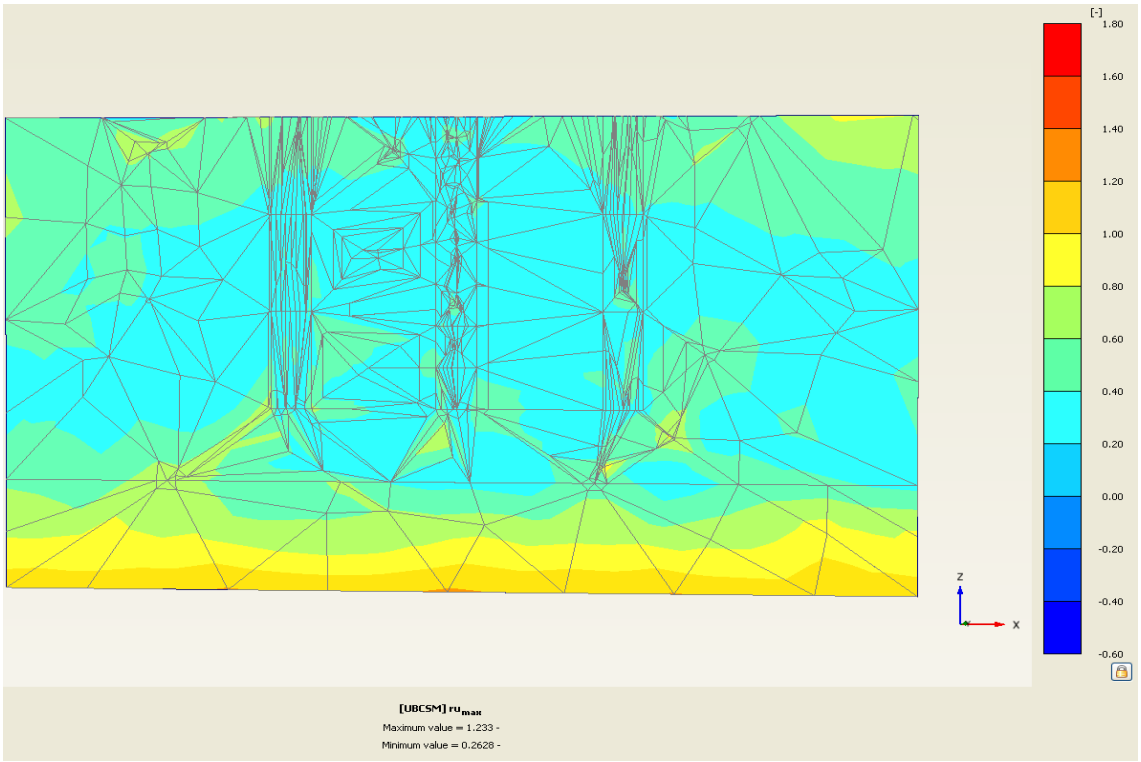

Fig. 6.8(a) R_u for Bench Mark Model

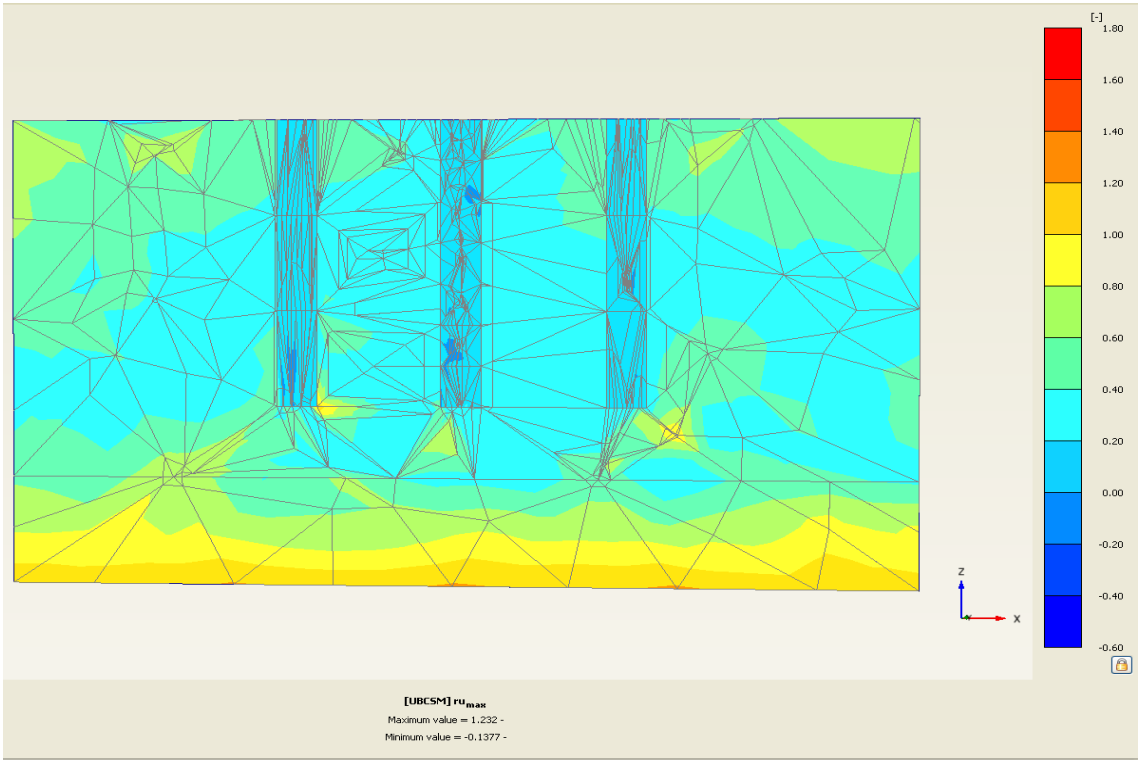

Fig. 6.8(b) R_u for Bench Mark Model with stone column

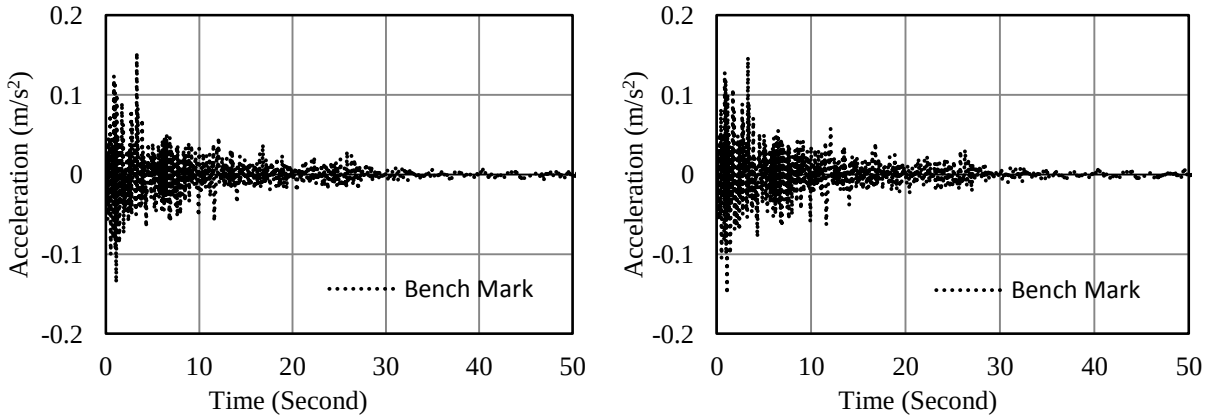

Fig. 6.9(a) Acceleration at location A and F for benchmark model (Model 1)

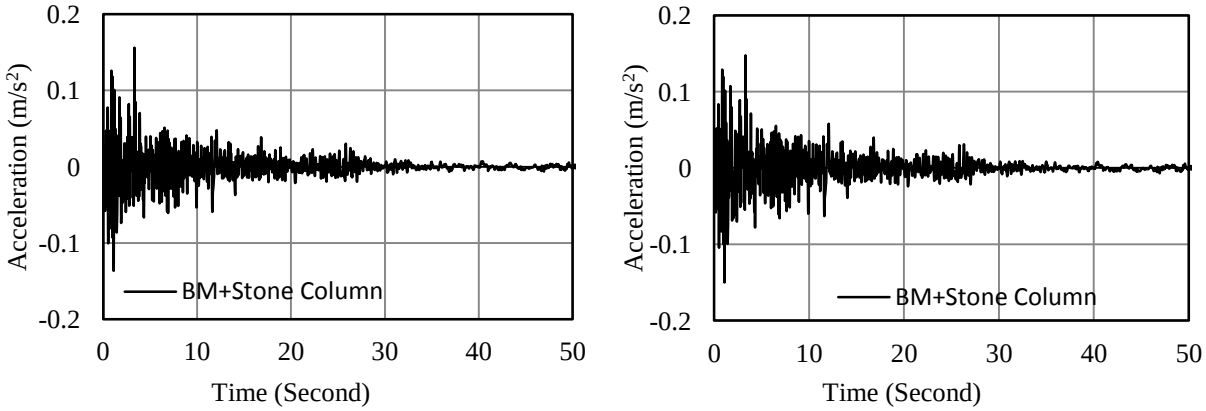

Fig. 6.9(b) Acceleration at location A and F for benchmark model with stone column (Model 2)

Based on reinforcement concepts proposed by Baez and Martin (1993), a system of stone columns would have been able to reduce displacement and factor of safety for the occurrence of liquefaction in the sand profile. But the said reduction is not so much appreciating. This implies necessity of considerable vertical or confining pressure to induce the reinforcing effect of the stone columns (Baez and Martin, 1993). In practice, surcharge in any form must be applied. Numerical analysis of Models 3 and 4 are presented in the light of this hypothesis.

6.5.2 Model 3 and 4 (model ground with surcharge)

Fig. 6.10 reports the computed vertical displacement with respect to time at different location of soil domain during the seismic event for Model 3 and Model 4. A maximum displacement of 99 cm and 54 cm are observed at location A(top most position of soil mass) for Model 3 and Model 4 respectively whereas these values are 47 cm and 24 cm at depth of 2m (Location C). Similar trend are visible at other depth also for the above said model. A relatively less value of displacement is estimated away from the surcharge load (Location I). Predicted values for Model 4 are less than those evaluated for the benchmark Model 3 and the variation is noteworthy. Due to presence of a surcharge, stone columns are very effective in settlement reduction. A summary of maximum values of displacements is reported in Table 6.4. The displacements at A, D, F, I and others points are roughly uniform in nature with maximum values ranging from 1m to 12 cm which is decreasing with depth. The values obtained in Model 4 are about 50% less than those in Model 3, signifying the competency of the Model 4 in controlling the displacement produced during seismic shaking showing stiffer composite-material behavior. Similar effect of stone column was reported in the centrifuge study by Adalier (2003).

Table 6.4 Maximum Displacement of Bench Mark Model with Footing and BM with footing and sand column at different location

Location	**BM with Footing**				**BM with Footing + SC**			
	Ux (cm)	Uy (cm)	Uz (cm)	U	Ux (cm)	Uy (cm)	Uz (cm)	U
A	1.45	-0.79	-102.31	102.32	-13.87	-8.90	-56.12	58.49
B	1.90	-0.89	-95.37	95.39	-12.97	-9.97	-52.71	55.19
C	2.00	-0.40	-83.87	83.90	-12.58	-10.61	-46.61	49.43
D	1.72	-0.75	-50.01	50.04	-11.56	-15.86	-26.55	33.02
E	1.02	-0.92	-24.24	24.28	-11.66	-21.40	-14.71	28.46
F	1.90	-9.22	-89.64	90.13	-12.88	-16.97	-52.00	56.19
G	1.69	-7.26	-48.22	48.79	-11.23	-19.12	-24.85	33.31
H	0.48	-7.14	-9.87	12.19	-10.04	-28.01	-8.04	30.82
I	-6.18	0.27	-30.30	30.93	-15.65	-9.77	-12.00	22.01
J	-13.40	-0.58	-28.32	31.34	-22.33	-15.85	-15.10	31.27

The variations in EPP with respect to time at different locations in soil domain during the seismic loading for Model 3 and 4 are shown in Fig.6.11. The computed EPP at different location (B, E, H and I) are compared with remedial measures (stone column). The maximum value of EPP at point B is 28.05 kPa without remedial measure whereas with stone column, it is reduced to 8.03 kPa. At point E (depth 8m), a significant fall in EPP is observed in case of stone column. All EPP plots (Fig. 6.11) show similar trend. After an initial rise, a peak is attained, and then the EPP remains more or less constant till the end of the earthquake. A significant reduction value of maximum EPP (104.81kPa) is visible in Model 4 as compared to maximum EPP (169.37 kPa) in Model 3.

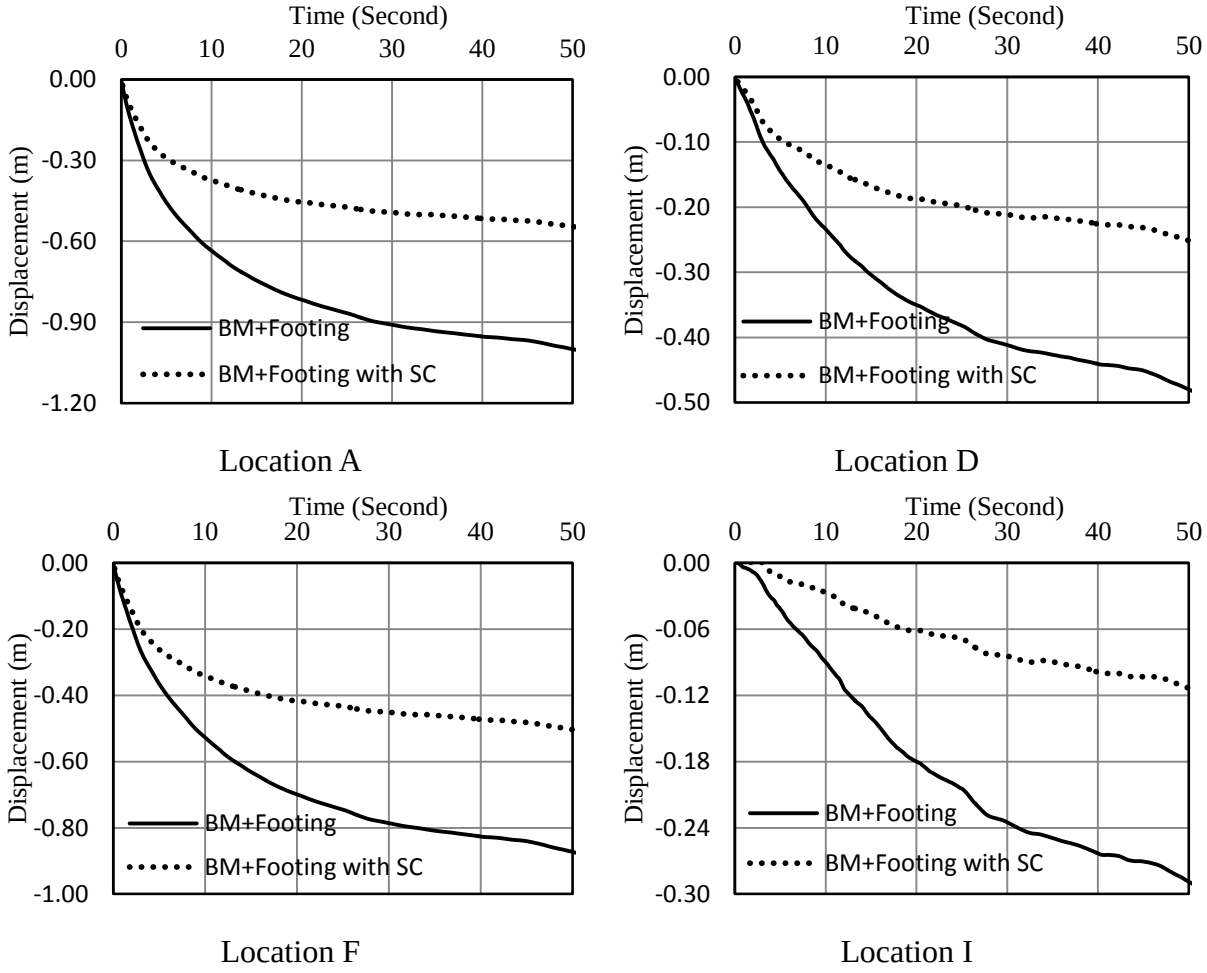

Fig. 6.10 Computed displacements with time at different location for BM with footing and BM with footing having stone column

Figs. 6.12(a-b) show contours of non-dimensional excess pore pressure R_u on a central vertical plane within the benchmark model and with stone column. The predicted pore pressure time variation reveals that soil is liquefied for a short period of time in Model 3 and

4 having maximum R_u of 1.275 and 1.166 respectively. The soil is liquefied for very small location in case of Model 4 as compared to Model 3.

Comparisons of predicted accelerations for seismic excitation are shown in Fig. 6.13(a-b). In case of application of soil column, acceleration values have been reduced little as compared to the benchmark model. This is reflected in the reduced level of acceleration amplitudes. Similar trends are observed at different points of this model. A significant drop in magnitude of predicted acceleration is observed at all the locations after 30 seconds of loading.

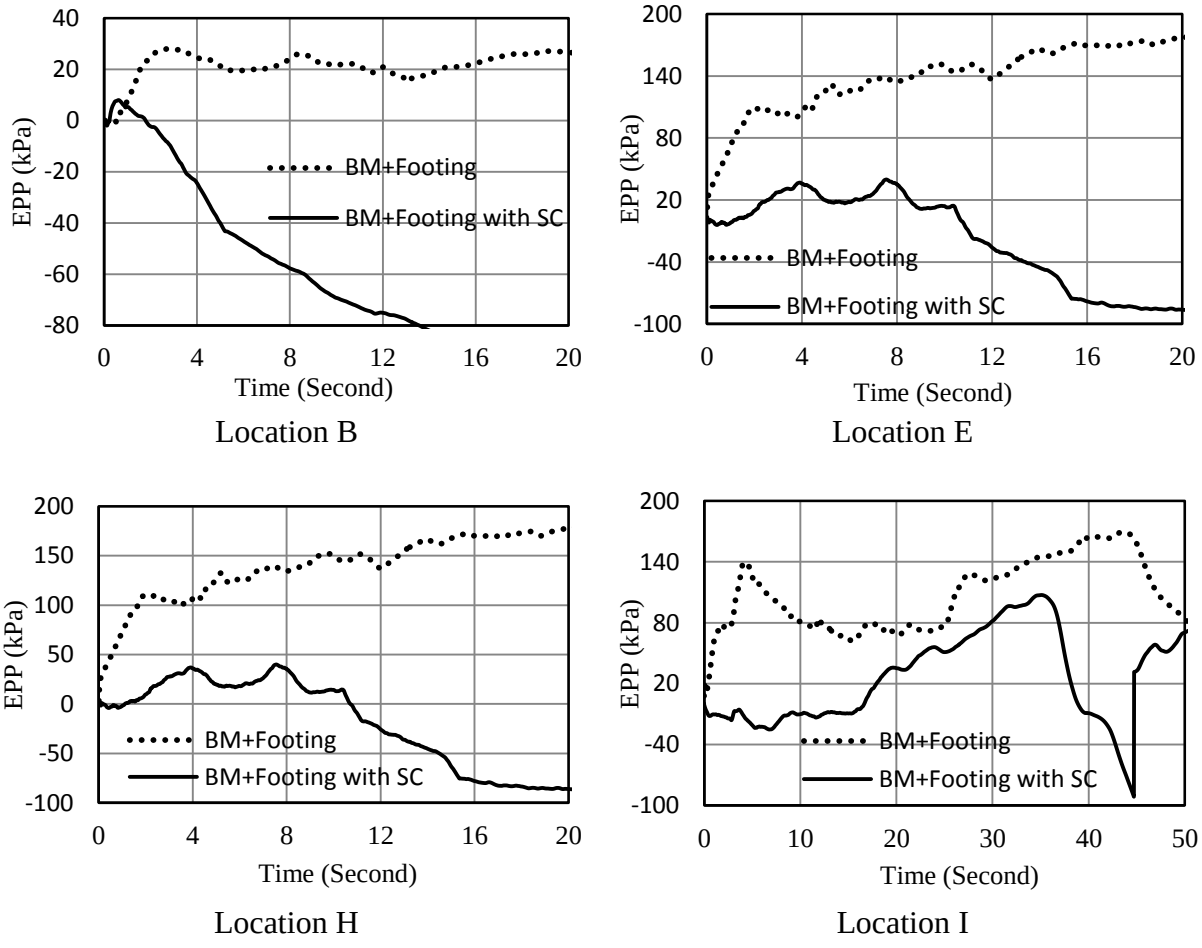

Fig. 6.11 Computed EPP with respect to time at different location for BM with footing and BM with footing having stone column

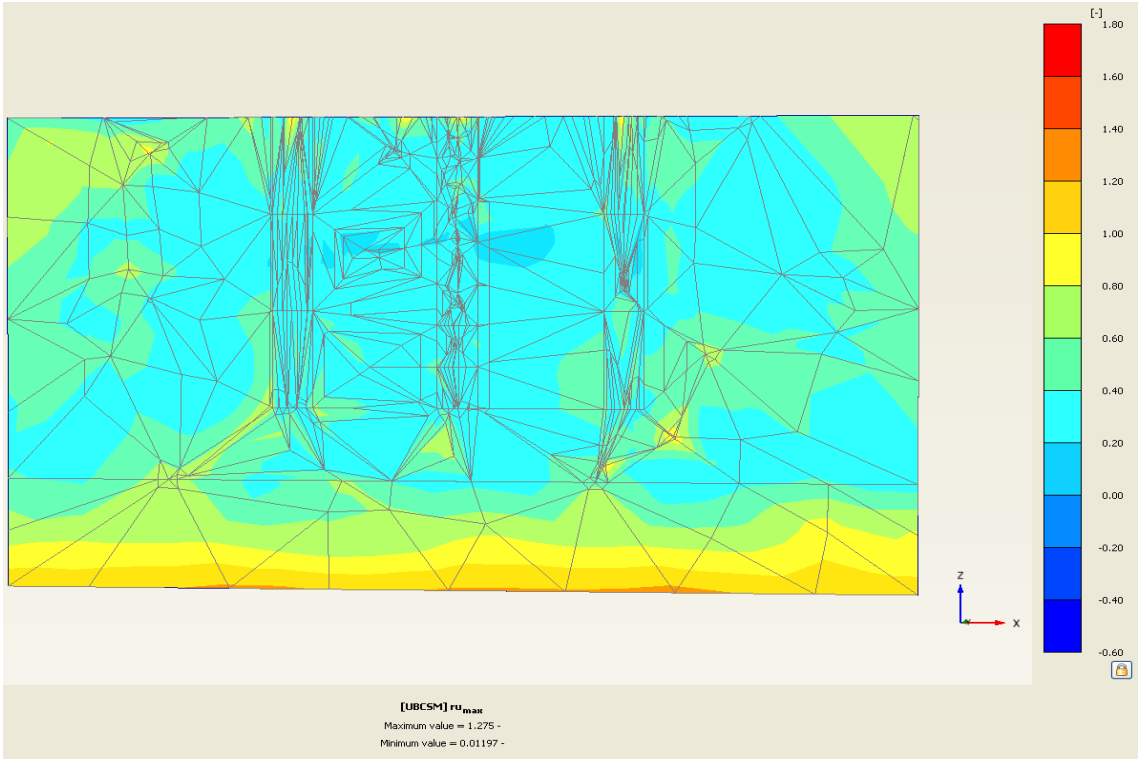

Fig. 6.12(a) R_u for Bench Mark Model with Footing

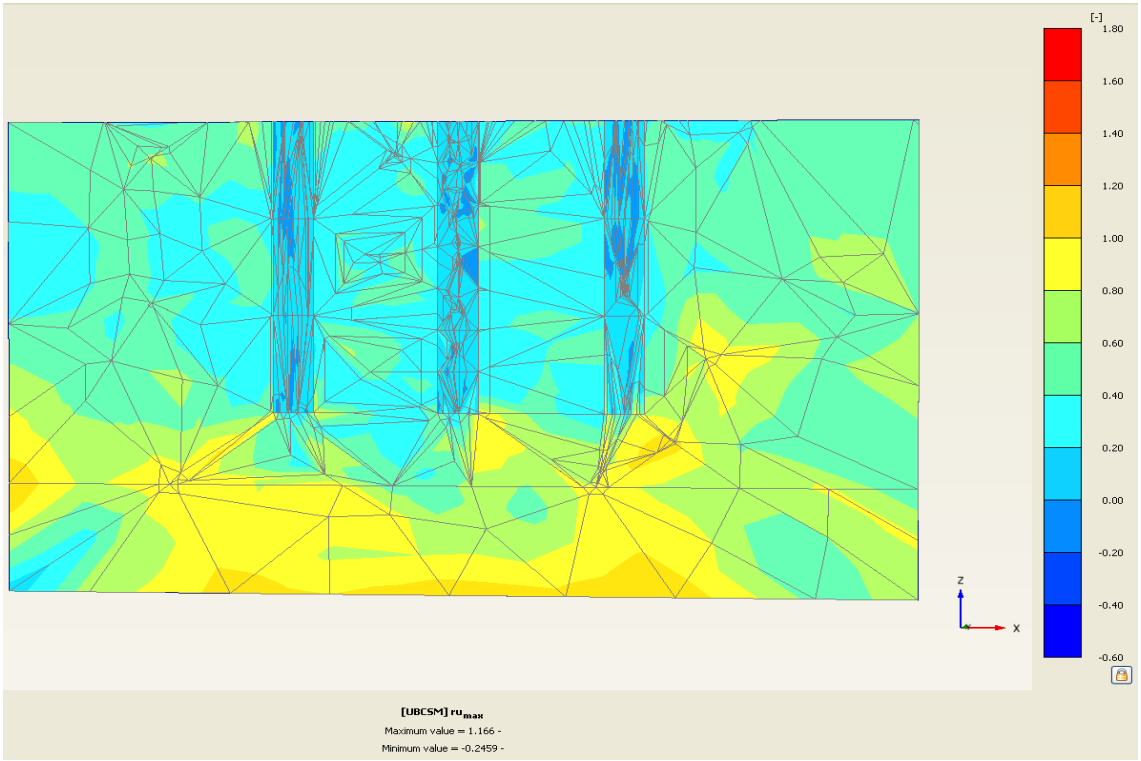

Fig. 6.12(b) R_u for Bench Mark Model with Footing having stone column

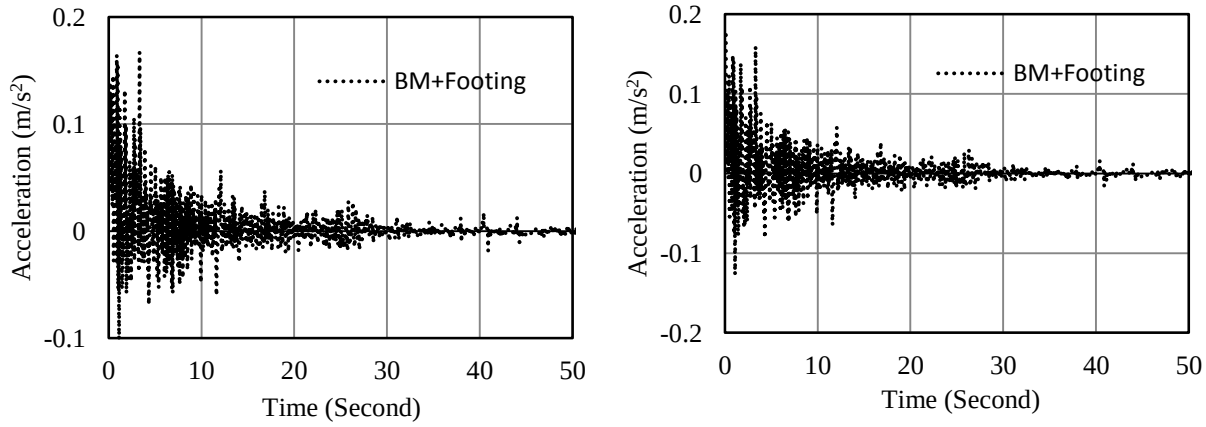

Location A Location F

Fig. 6.13(a) Acceleration at location A and F for benchmark model with footing

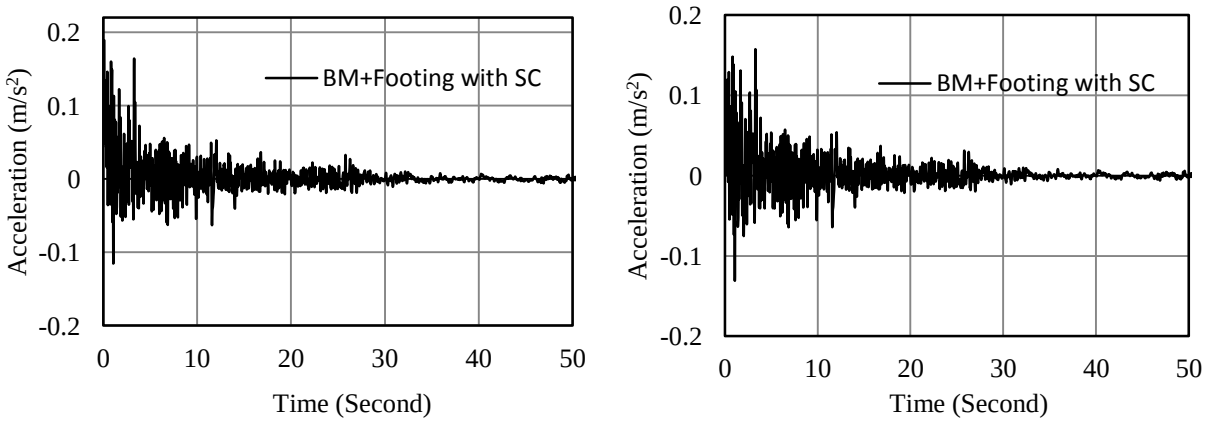

Location A Location F

Fig. 6.13(b) Acceleration at location A and F for BM with footing having stone column

6.6 CONCLUDING REMARKS

The present study was directed to examine the effectiveness of remedial measures for liquefaction. The models with and without remedial countermeasures were analyzed. A comparative study was performed to highlight the effect of countermeasure on liquefaction. The stone column resulted in the smaller strains and cyclic mobility of the soil stratum. Maximum lateral strains and highest EPP in soil domain were observed in the no-remediation case with surcharge.

In case of Model 2, lesser values of displacements are predicted in comparison with the benchmark Model 1, but the variation is marginal. In lack of surcharge at surface, stone-

columns are apparently ineffective in controlling settlements. As compared to Model 1, a reduction of around 40% in EPP is visible in Model 2. In case of application of soil column, acceleration values have been reduced little as compared to the benchmark model.

Predicted values for Model 4 are less than those evaluated for the benchmark Model 3 and the variation is noteworthy. Due to presence of a surcharge, stone columns are very effective in settlement reduction. The values obtained in Model 4 are about 50% less than those in Model 3, signifying the competency of the Model 4 in controlling the displacement produced during seismic shaking showing stiffer composite-material behavior. A significant reduction value of maximum EPP (104.81kPa) is visible in Model 4 as compared to maximum EPP (169.37 kPa) in Model 3.

The results of this study show that numerical modeling of earthquake effects on liquefiable soil strata with and without remedial measures is feasible using the common laboratory test results and a well-defined numerical approach. Reasonable evaluations similar to the present study can develop confidence to implement UBC sand model in the dynamic analysis of geotechnical structures with cost-effective countermeasures.

CHAPTER - 7

CONCLUSIONS AND FUTURE SCOPE

7.1 GENERAL

Using coupled formulation based on Biot's theory, a mathematical framework has been established to describe the liquefaction phenomenon. A fully coupled formulation is developed to predict the liquefaction potential of a finite and semi-infinite saturated sandy layer assuming plane strain condition. The soil behaviour is modeled by Pastor–Zienkiewicz Mark III to describe the inelastic behaviours under dynamic loadings. Cyclic and Seismic analysis was performed considering finite and infinite domain. PLAXIS 3D software based on UBC3D-PLM model has been used to analyze 3-D modeling of liquefaction and mitigation. A parametric study is conducted, highlighting the significance of permeability, shear modulus and frequency on the response of liquefaction phenomena. The conclusions are presented in three parts as per the type of analysis performed.

7.2. 2-D Analysis Considering Finite Domain

The present model developed is able to predict reasonable changes in excess pore pressure occurring during cyclic loading which can be useful for analyzing earth structures situated in the regions of moderate to high seismic zone. It allows the distribution of pore pressure and the effects that drainage and internal flow have on the time of liquefaction to be determined quantitatively.

7.2.1 Cyclic excitation

1. A maximum vertical settlement of 4.45 cm at 8m depth and horizontal displacement of 3.38 cm at top surface are observed (G = 10 MPa). It is observed that maximum stress ratio q/p is 0.98 at the depth of 0.5 m, which decreases with depth mainly due to effect of overburden pressure. This results in development of higher excess pore pressure at shallow depth.
2. At higher value of shear modulus (G = 30 MPa), liquefaction occurs only at shallow depth of 2m, but does not progress at greater depths. As the shear modulus is

decreased, liquefaction phenomenon is observed because of generation of higher pore pressure resulting in reduction of effective stress at shallow depths.

3. From the reported values of maximum horizontal and vertical displacements, the values are decreasing with increase in shear modulus. For horizontal displacements, reduction is of the order of 39 % to 92 % with higher values for higher shear modulus. It is also observed that horizontal displacements are decreasing with depth. Similarly for maximum vertical displacements, reduction is of the order of 34 % to 90 % for permeability k_1, 34 % to 65 % for permeability k_2, and 38 % to 70 % for permeability k_3. Higher percentage of reduction is corresponding to higher shear modulus.
4. Displacements are affected marginally with change in permeability. But EPP is affected significantly. Effect of permeability is more pronounced in the values of EPP. With decrease in permeability, considerable increase in EPP is observed. The change in permeability from k_1 to k_2 results in average 15 % increase in EPP, whereas 32 % increase in EPP is observed for change in permeability from k_1 to k_3.
5. Effect of cyclic frequency is drastic for the range of frequencies considered in the analysis. It is noticed that the liquefaction occurs throughout all the depth of sand layer at frequency 1 Hz and 2 Hz of the cyclic loading, whereas no liquefaction is observed at 0.5 Hz. Horizontal acceleration is observed to increase with the frequency of loading, whereas the peak value of vertical acceleration is found to be at 1 Hz frequency.

7.2.2 Seismic excitation

1. Similar trends of displacements and EPP are observed for variation in shear modulus and permeability for El-Centro earthquake input motion. A maximum vertical settlement of 9.64 cm at 8m depth and horizontal displacement of 8.79 cm at top surface are observed. It is observed that maximum stress ratio q/p is 1.05 at the depth of 0.5 m, which is decreasing with depth as overburden pressure increases with depth. This results in development of higher excess pore pressure at shallow depth. Liquefaction occurs after 15 seconds at G = 8 MPa and $k = 6.6\times10^{-5}$ m/s.
2. At higher value of shear modulus (G = 15 MPa), liquefaction occur only at shallow depth of 2m and does not advance at greater depths. As the shear modulus is decreased, liquefaction phenomenon is observed because of generation of higher pore pressure

resulting in reduction of the effective stress at shallow depth of soil mass. It is noticed that liquefaction occurs throughout the depth of sand layer at lowest permeability.

3. From the summary of maximum displacements, the values are decreasing with increase in shear modulus. Average reductions in maximum horizontal displacements are in the order of 79.6% (G = 10 MPa) and 87% (G = 15 MPa). Average reductions in maximum vertical displacements are in the order of 75.5% (G = 10 MPa) and 83% (G = 15 MPa). They are also decreasing marginally with reduction in permeability.
4. With change in permeability from k_1 to k_2, average increase in EPP is of the order 3.5 to 17% (higher value for higher modulus). Similarly, for change in permeability from k_1 to k_3, EPP are increased by 9.6 to 56% (again higher value for higher modulus).

7.3 2-D Analysis Considering Infinite Domain

The present model developed for unbounded soil domain is able to predict reasonable changes in pore pressure occurring during seismic loading which can be useful for earth structures located in regions of moderate to high seismicity.

7.3.1 Cyclic excitation

1. The maximum values of horizontal settlement of 1.27 cm are predicted at 8 m depth of soil layer (G = 8MPa, k = 6.6×10^{-5} m/sec, f =1.0 Hz), whereas maximum values of vertical settlement of 10.5 cm are predicted at top surface. It has been observed that most part of the settlements occur during the seismic excitation. Generally, the horizontal settlement is less than vertical settlement at different depths. Vertical displacement is decreasing as the depth increases. It is observed that maximum stress ratio q/p is 0.65 and 0.27 at the depth of 0.5 m and 11.5m respectively, which decreases with depth mainly due to effect of overburden pressure coming on soil mass.
2. From the computed horizontal and vertical accelerations time histories at top surface and 8m (G = 8MPa, k = 6.6×10^{-5} m/sec, f =1.0 Hz), the peak value of these parameters is found to be about 0.48m/s^2 (horizontal) and 0.25 m/s^2 (vertical) at 8m depth, resulting higher horizontal settlement. A negligible acceleration is reported in both directions after the end of 24 cycle of loading.
3. It is observed that values of maximum horizontal displacements are decreasing with increase in shear modulus. Reduction is of the order of 47 % to 96% with higher

values for higher shear modulus. Similarly maximum vertical displacements are observed to be reducing with increase in shear modulus, but vertical displacements are slightly higher at lowest shear modulus.

4. They are also decreasing slightly with reduction in permeability.
5. Effect of shear modulus and permeability is more pronounced in the values of EPP. With reduction in permeability, slight increase in EPP is observed, whereas considerable effect of shear modulus is observed on maximum EPP. A considerable reduction in EPP with increase in shear modulus is observed when shear modulus is increased from 5 MPa to 10 MPa or some higher value. Reduction is of the order of 40 % to 90% with higher values for higher shear modulus.

7.3.2 Seismic excitation

1. For the El-Centro ground motion, the maximum values of horizontal and vertical settlement ($k = 6.6\times10^{-5}$ m/s and $G = 8$ MPa) of 0.918 cm and 1.89 cm are predicted at the top of soil layer; whereas minimum values 0.308 cm and 0.376 cm are predicted at 4m depth. It is observed that maximum stress ratio q/p is 0.398 at the depth of 0.5 m, which decreases with depth mainly due to effect of overburden pressure. the computed time histories at different depths. It has been observed that the peak values of horizontal acceleration (0.86 m/s^2) and vertical acceleration (2.56 m/s^2) are found at top surface resulting higher settlement. A relatively less value of accelerations (0.59 and 1.06 m/s^2) are observed at 8 m depth, corresponding to lesser excess pore pressure. A negligible acceleration is reported in both directions after 16.32 second of shaking.
2. It is observed that maximum horizontal and vertical displacements are decreasing with increase in shear modulus for all the three permeability value. Reduction is of the order of 46 % to 96 % for horizontal displacements with higher values for higher shear modulus. Reduction is of the order of 56 % to 88 % for vertical displacements with higher values for higher shear modulus.
3. Values are decreasing by small amount with decrease in permeability. But horizontal and vertical displacements are slightly higher at lowest shear modulus.
4. Effect of permeability is more pronounced in the values of EPP. With reduction in permeability, slight increase in EPP is observed, whereas significant effect of shear

modulus is observed on maximum EPP. A considerable reduction in EPP with increase in shear modulus is observed with increase in shear modulus. Reduction is of the order of 53 % to 80 % with higher values for higher shear modulus.

5. Similar trend is observed for Bhuj earthquake ground motion also. It has been observed that a maximum horizontal displacement (G = 50 MPa, $k = 1 \times 10^{-4}$ m/sec) of 0.289 cm occurs at of soil stratum whereas this value is 2.17cm at top surface in case of vertical displacement. After shaking for 9.35 seconds, liquefaction first starts at 2m depth and reached at 4m after 38.44 second. It reaches at 6m after 46.2 seconds of seismic excitation. Only soil domains with shear modulus more than 50000 kPa are sustainable. For smaller values of shear modulus, soil domain is liquefying at early stage of earthquake ground motion due to high value of input acceleration (peak value 0.782 m/s^2).
6. From the study on effect of shear modulus, it is observed that liquefaction is triggered around 34 second when shear modulus is less than 50000 kPa.
7. For comparison of responses with finite and semi-infinite domain, maximum displacements at top-surface and maximum EPP at 2m depth are compared. It is observed that maximum horizontal displacements are reduced by average 63.7%, however vertical displacements have marginal effect and reduction is about average 6%. On the contrary, maximum EPP are observed to increase due to unbounded domain and increase is average 52%.

7.4 3-D Analysis using PLAXIS

The present study was directed to examine the effectiveness of remedial measures for liquefaction. The models with and without remedial countermeasures were analyzed. A comparative study was performed to highlight the effect of countermeasure on liquefaction. The stone column resulted in the smaller strains and cyclic mobility of the soil stratum. Maximum lateral strains and highest EPP in soil domain were observed in the no-remediation case with surcharge.

1. In case of Model 2, smaller values of displacements are predicted in comparison with the benchmark Model 1, but the variation is marginal. In lack of surcharge at surface, stone-columns are apparently ineffective in controlling settlements. As compared to Model 1, a

reduction of around 40% in EPP is visible in Model 2. In case of application of soil column, acceleration values have been reduced little as compared to the benchmark model.

2. Predicted values for Model 4 are less than those evaluated for the benchmark Model 3 and the variation is noteworthy. Due to presence of a surcharge, stone columns are very effective in settlement reduction. The values obtained in Model 4 are about 50% less than those in Model 3, signifying the competency of the Model 4 in controlling the displacement produced during seismic shaking showing stiffer composite-material behavior. A significant reduction value of maximum EPP (104.81kPa) is visible in Model 4 as compared to maximum EPP (169.37 kPa) in Model 3.
3. The results of this study show that numerical modeling of earthquake effects on liquefiable soil strata with and without remedial measures is feasible using the common laboratory test results and a well-defined numerical approach. Reasonable evaluations similar to the present study can develop confidence to implement UBC Sand Model in the dynamic analysis of geotechnical structures with cost-effective countermeasures.

7.4 LIMITATIONS AND FUTURE SCOPE

Present study was devoted to numerical modeling of liquefaction phenomenon using coupled formulation on finite and infinite domain. Pastor–Zienkiewicz Mark III model is used to capture the inelastic behaviours under dynamic loadings. Dynamic load was applied in the form of harmonic loading and seismic load.

7.4.1 Limitations of present study

Although efforts were made to consider most of the aspects, all aspects were not considered due to time limit and computational difficulties. Some of the limitations can be listed as follows:

1. Present study is based on small strain analysis. However, after the initiation of liquefaction large displacement and strains may be developed.
2. Transmitting boundary is developed with assembly of Kelvin elements. However, large accumulation of plastic strains at the Kelvin element may give erratic response. Present study assumes that accumulation of plastic strains is marginal and not significant.

3. Present study assumes that far field behaviour is linear. Infinite elements are modelled to simulate unbounded domain. Present infinite element works well if they are in linear range.
4. It is assumed that soil is fully saturated.
5. Effect of relative density was tried by varying its value. But the response was nearly same. In the lack of proper correlation between relative density and strength parameter, response was insensitive to relative density.

7.4.2 Future Scope

Based on the above limitations future scope can be suggested as follows:

1. The plasticity model should be further simplified and enhanced for the applicability of the model by reducing the number of the model parameters as much as possible.
2. Present Biot formulation can be extended to partially saturated soil by incorporating the third phase (gas) into the analysis.
3. The 2-D coupled finite element – infinite element numerical model can be extended to 3-D.
4. Dynamic infinite elements can be incorporated to model the infinite nature of soil domain without back-propagation of reflected waves. Similarly more appropriate viscous elements can be used to absorb the wave energy at transmitting boundary.
5. The presented code is unable to cope with large strain increments. Further effort should be directed towards considering large strain analysis. If possible experimental simulation should be developed.
6. More numerical simulations and predictions of dynamic centrifuge experiments and prototype situations, such as shallow foundations, piled foundations and dams subjected to earthquake loading, should be performed to assess the capabilities of the developed Biot formulation.

REFERENCES

1. Abifadel, N. R. (1991). "On the modelling of two-phase media by the finite element method."*University of Colorado, Composite materials.*
2. Adalier, K. (1996). "Mitigation of earthquake induced liquefaction hazards" *Ph.D. thesis, Rensselaer Polytechnic Institute* (RPI), Troy, N.Y, 659.
3. Adalier, K. and Aydingum, O. (2003). "Numerical Analysis of seismically induced liquefaction in earth embankment foundations Part 2. Application of remedial measures." *Canadian Geotechnical Journal*, 40, 766-779.
4. Adalier, K., Pamuk, A. and Zimmie, T. F. (2004). "Earthquake retrofit of highway/railway embankments by sheet-pile walls." *Geotechnical and Geological Engineering*, 22:73–88.
5. AI-Hunaidi, M. O., Towhata, I. and Ishihara, K. (1990). "Silent boundary for time domain wave motion analyses based on direct energy deletion." *Soil Dynamics and Earthquake Engineering*, 9(2), 85-95.
6. Alam, M. J. (2005). "Model tests on mitigation measures of ground distortions induced by seismic liquefaction." *PhD. thesis, Tokyo Univ., Tokyo*.
7. Alam, M. J., Towhata, I. and Wassan, T. H., (2005). "Seismic behavior of a quay wall without and with a damage mitigation measure*". GSP 133 Earthquake Engineering and Soil Dynamics.* Geo-Frontiers 2005
8. Andrianopoulos, K. I., Papadimitriou, A. G. and Bouckovalas, G. D. (2010). "Explicit integration of bounding surface model for the analysis of earthquake soil liquefaction." *Int. J. Numer. Anal. Meth. Geomech*, 34, 1586–1614.
9. Andrus, R. D. and Stokoe, K. H. (1997). "Liquefaction resistance based on shear wave velocity." *In Proc. NCEER Workshop on Evaluation of Liquefaction Resistance of Soils, National Centre for Earthquake Eng. Res.,* State Univ. of New York at Buffalo,89-128.
10. Andrus, R. D. and Stokoe, K. H. (2000). "Liquefaction resistance of soils from shear wave velocity." *Journal of Geotechnical and Geo-environmental Engineering*, ASCE, 126(11), 1015-25.

11. Arduino, P., Kramer S. L. and Baska, D. (2001). "Applications of a simple constitutive model for liquefiable soils." *Proceedings of the 2001 ASCE-ASME-SES Joint Applied Mechanics & Materials Summer Conference*, La Jolla, San Diego, June 27-29.
12. Arulanandan, K. and Scott, R. F. (Eds.) (1993). "Verification of numerical procedures for the analysis of soil liquefaction problems."*Conference Proceedings, Balkema, Rotterdam*, Vol. 1.
13. Arulanandan, K., Muraleetharan, K. K. and Yogachandran, C. (1997). "Seismic response of soil deposits in San Francisco marina district." *Journal of Geotechnical and Geo-environmental Engineering*, ASCE, 123(10), 965-974.
14. Arya, A.S., Nandakumaran, P., Puri, V. K. and Mukerjee, S. (1978). "Verification of liquefaction potential by field blast tests." *In Proc. 2nd International Conference on Microzonation*, Seattle, USA.
15. Baez, J. I. and Martin, G. R. (1993). "Advances in the design of vibro systems for the improvement of liquefaction resistance." *Symposium of ground improvement*, Vancouver, BC: Vancouver Geotechnical Society.
16. Bao, Y. (2006). "A biot formulation for geotechnical earthquake engineering applications." *PhD Thesis, University of Colorado*.
17. Bao, Y. and Sture, S. (2011). "Application of a kinematic-cyclic plasticity model in simulating sand liquefaction." *International Journal of Advances in Engineering Sciences and Applied Mathematics*, 2(3), 119–124.
18. Beaty, M. and Byrne, P. M. (1998). "An effective stress model for predicting liquefaction behaviour of sand."*Geotechnical Earthquake Engineering and Soil Dynamics* III *ASCE Geotechnical Special Publication*, 75(1), 766-777.
19. Bettess, P. (1977). "Infinite element." *Int. J. for Numerical Methods in Engg*., 11, 53–64.
20. Biot, M. A. (1941). "General Theory of Three-Dimensional Consolidation." *Journal of Applied Physics*, 12(2), 155-164.
21. Biot, M. A. (1956). "Theory of propagation of elastic waves in a fluid-saturated porous solid."*J. Acoustical Society of America*, 28(2), 168-178.

22. Boulanger, R. W., Wilson, D. W. and Idriss, I. M. (2012). "Examination and Re-evalaution of SPT-Based Liquefaction Triggering Case Histories." *Journal of geotechnical and geo-environmental engineering*, 138(8), 898–909.
23. Bowen, R. M. (1982)."Compressible porous media models by use of the theory of mixtures."*Int J Eng Sci*, 20(6), 697–735.
24. Brinkgreve, R. B. J., Engin, E. and Swolfs, W. M. (2012). PLAXIS, Finite Element code for soil and rock analysis, user's manual. Website: www.plaxis.nl
25. Byrne, P. M., Park, S., Beaty, M., Sharp, M., Gonzalez, L. and Abdoun, T. (2004). "Numerical modeling of liquefaction and comparison with centrifuge tests."*Can. Geotech. J.* 41, 193–211.
26. Casagrande, A. (1936). "Characteristics of cohesionless soils affecting the stability of earth fills."*Journal of Boston Society of Civil Engineers*, 23(1), 13-32.
27. Castro, G. and Poulos, S.J. (1977). "Factors affecting liquefaction and cyclic mobility."*J. Geotech. Engg.* ASCE, 103(6), 501–516.
28. Chan A. H. C., Zienkiewicz, O. C. and Pastor, M. (1988). "Transformation of incremental plasticity relation from defining space to general Cartesian stress space." *Int. J. Numer. Analyt. in Biomedical Engineering*., 14(3), 577–580.
29. Chang, M., Kuo, C., Shau, S. and Hsu, R. (2011). "Comparison of SPT-N-based analysis methods in evaluation of liquefaction potential during the 1999 Chi-chi earthquake in Taiwan."*Computers and Geotechnics*, 38,393-406.
30. Chern, S. and Chang, T. (1995). "Simplified procedure for evaluating soil liquefaction characteristics."*Journal of Marine Science and Technology*, 3(1), 35-42.
31. Cooke, H. G. (2000). "Ground improvement for liquefaction mitigation at existing highway bridges." *PhD Thesis, Virginia Polytechnic Institute and State University*.
32. Cubrinovski, M. and Ishihara, K. (1999). "Empirical correlation between SPT N-value and relative density for sandy soils." *Soils and Foundations*, Elsevier, 39(5), 61-71.
33. Das, B. M. and Ramana, G. V. (2011). "Principles of Soil Dynamics." Second Edition, *Cengage Learning*.
34. Dashti, S. and Bray, J. (2013). "Numerical Simulation of Building Response on Liquefiable Sand." *J. Geotech. Geoenviron. Eng.*, 139(8), 1235–1249.

35. Deresiewicz, H. (1960). “The effect of boundaries on wave propagation in a liquid-filled porous solid-I: Reflection of plane waves at a free plane boundary (non-dissipative case).” *Bull.seism. SOC.Am.,* 50, 599-607.

36. Deresiewicz, H. and Rice, J. T. (1962). “The effect of boundaries on wave propagation in a liquid-filled porous solid-III: Reflection of plane waves at a free plane boundary.”*Bull seism. SOC. Am.,* 52, 595-626.

37. Derski, W. (1978). “Equations of motions for a fluid- saturated porous solids.”*Bull. Acad. Pol. Sc. Ser. Tech.*26, 1, 11-16.

38. Dewaikar, D. M. and Halkude, S. A. (2002). “Seismic passive/active thrust on retaining wall- point of application.” *Soils and Foundations,* 42(1), 9-15.

39. Dewoolkar, M. M., Ko, H. Y. and Pak, R. Y. S. (2000). “Experimental developments for studying static and seismic behavior of retaining walls with liquefiable backfills.” *Soil Dynamics and Earthquake Engineering*, 19(8), 583-594.

40. Dewoolkar, M. M., Ko, H. Y. and Pak, R. Y. S. (2001). “Seismic behavior of cantilever retaining walls with liquefiable backfills.” *Journal of Geotechnical and Geoenvironmental Engineering*, 127(5), 424-435.

41. Dewoolkar, M. M., Santichaianant, K. and Ko, H. Y. (2007). “Centrifuge modeling of granular soil response over active circular trapdoors.” *Soils and Foundations,* 47(5), 931-945.

42. Dewoolkar, M. M., Chan, A. H. C., Ko, H. and Pak R. Y. S. (2009). “Finite element simulations of seismic effects on retaining walls with liquefiable backfills.”*Int. J. Numer. Anal. Meth. Geomech,* 33, 791–816.

43. Dixit, J., Dewaikar, D. M. and Jangid, R. S. (2012). “Soil liquefaction studies at Mumbai city.” *Natural Hazards, Springer,* 63, 375–390.

44. Dixit, J., Dewaikar, D. M. and Jangid, R. S. (2012). “Assessment of liquefaction potential index for Mumbai city.” *Natural Hazards and Earth System Sciences,* 12(9), 2759-2768.

45. Dixit, J., Dewaikar, D. M., and Jangid, R. S. (2012), “Free field surface motion at different site types due to near-fault ground motions.”*ISRN Geophysics,* Vol. 2012, Article ID 821051 doi:10.5402/2012/821051, 2012.

46. Du, X. and Zhao, M. (2010). "A local time-domain transmitting boundary for simulating cylindrical elastic wave propagation in infinite media." *Soil Dynamics and Earthquake Engineering*, 30(10), 937–946
47. Elgamal, A.W., Yang, Z., Parra, E. and Ragheb, A. (2003). "Modeling of cyclic mobility in saturated cohesionless soils."*International Journal of Plasticity*, 19, 883–905.
48. Finn, W. D. L., Emery, J. J. and Gupta, Y. P. (1971). "A shaking table study of the liquefaction of saturated sands during earthquake." *Third European Symposium on Earthquake Engineering*, Bulgaria, 253-62.
49. Finn, W. D. L., Lee, K. W. and Martin, G. R. (1977). "An effective stress model for liquefaction," *J. Geotech. Engrg. Div. ASCE*, 103, 513–533.
50. Finn, W. D. L. (1988). "Dynamic analysis in geotechnical engineering." *In Proc. Earthquake Engineering and Soil Dynamics II - Recent Advances in Ground Motion Evaluation*, ASCE *Geotechnical Engineering Division*, Park City, Utah, June, 523-91.
51. Finn, W. D. L. (1991). "Estimating how embankment dams behave during earthquakes." *Water Power and Dam Construction*, London, April, 17-22.
52. Finn, W. D. L. (2000). "State-of-the-art of geotechnical earthquake engineering practice.*"Soil Dynamics and Earthquake Engineering*, 20, 1–15.
53. Galavi, V., Petalas, A. and Brinkgreve, R. B. J. (2013). "Finite element modelling of seismic liquefaction in soils." *Geotechnical Engineering Journal of the SEAGS & AGSSEA*, 44(3) 55-64.
54. Ganesalingam, D., Read, W. W. and Sivakugan, N. (2013). "Consolidation behaviour of a cylindrical soil layer subjected to non-uniform pore-water pressure distribution." *International Journal of Geomechanics*, 13 (5), 665-671.
55. Garg, S. K. (1971). "Wave propagation effects in a fluid-saturated porous solid." *Journal of Geophysical Research*, 76(32), 7947-7962.
56. Garg, S. K., Adnan, H., Nayfeh, A. H. and Good, A. J. (1974). "Compressional waves in fluid-saturated elastic porous media." *Journal of Applied Phys*ics, 45, 1968 -1974.
57. Ghaboussi, J. and Wilson, E. L. (1972). "Variational formulation of formulation of dynamics of fluid-saturated porous elastic solids."*Journal of the Engineering*

Mechanics Division, Proceedings of the American Society of Civil Engineers 98(4), 947-963.

58. Ghaboussi, J. and Wilson, E. L. (1973). "Flow of compressible fluid in porous elastic media." *International Journal for Numerical Methods in Engineering*, 5(3), 419–442.
59. Green, A. E. and Naghdi, P. M. (1965). "A dynamical theory of interacting continua."*Int J Eng Sci*, 3, 231–41.
60. Hagstrom, T. and Hariharan, S. I. (1998). "A formulation of asymptotic and exact boundary conditions using local operators." *Applied Numerical Mathematics*, 27, 403-416.
61. Halpern, M. R. and Christiano, P. (1986). "Steady-state harmonic response of a rigid plate bearing on a liquid-saturated poroelastic half space."*Earthquake Engineering and Structure Dynamics* 14, 439-454.
62. Harder, L. F. and Seed, H. B. (1986). "Determination of penetration resistance for coarse-grained soils using the Becker hammer drill." *Earthquake Engineering Research Centre*, Rep. UCB/EERC- 86/06, *University of California at Berkeley*.
63. Hardin, B. O. and Richard, F. E. (1963). "Elastic wave velocities in granular soils." *Journal of the Soil Mechanics and Foundations Division*, ASCE, 89(1), 33-65.
64. Hausler, E. A. (2002). "Influence of ground improvement on settlement and liquefaction: a study based on field case history evidence and dynamic geotechnical centrifuge tests." *PhD thesis, University of California, Barkeley*.
65. Hazarika, H. and Boominathan, A. (2009). "Liquefaction and ground failures during the 2001 Bhuj earthquake." *Earthquake geotechnical case histories for performance-based design – Kokusho (ed), Taylor & Francis Group, London, ISBN 978-0-415-80484-4*
66. Hwang, J. H., Yang, C. W. and Juang, D. S. (2004). "A practical reliability-based method for assessing soil liquefaction potential."*Soil Dynamics and Earthquake Engineering*, 24, 761–770.
67. Idriss, I. M. and Boulanger, R. W. (2006). "Semi-empirical procedures for evaluating liquefaction potential during earthquakes." *Soil Dynamics and Earthquake Engineerin*g 26, 115–130.

68. Iwasaki, T., Arakawa, T. and Tokida, K. (1984). "Simplified procedures for assessing soil liquefaction during earthquakes." *Soil Dynamics and Earthquake Engineering*, 3(1), 49-59.

69. Ishihara, K. and Yoshimine, M. (1992). "Evaluation of settlements in sand deposits following liquefaction during earthquakes."*Journal of Soils and Foundations* 32(1), 173–188.

70. Ishihara, K. and Okada, S. (1982). "Effects of large pre shearing on cyclic behaviour of sand." *Soils and Foundations*, 22, 109–125.

71. Ishihara, K. (1996). "Soil Behaviour in Earthquake Geotechnics." Vol. 46, *Oxford University Press*.

72. Jafari-Mehrabadi, A. (2006). "Seismic liquefaction countermeasures for waterfront slopes", *PhD thesis, Memorial University of Newfoundland*.

73. Jakka, R. S., Datta, M. and Ramana, G. V. (2010a). "Liquefaction behavior of loose and compacted pond ash."*Soil Dynamics and Earthquake Engineering*, 30(7), 580-590.

74. Jakka, R. S., Ramana, G. V. and Datta, M. (2010b). "Shear strength characteristics of loose and compacted pond ash."*Geotechnical and Geological Engineering*, 28, 763-778.

75. Jakka, R. S., Ramaiah, B. J. and Ramana, G. V. (2011). "Dynamic characterization of settled pond ash: Correlation between SPT-N value and measured shear wave velocity." *International Journal of Geotechnical Earthquake Engineering*,2(1), 83-97.

76. Jaya, V., Dodagoudar, G. R. and Boominathan, A. (2008). "Seismic Soil Structure interaction of tall slender structures." *Int. J. of Geotechnical Engineering*, 2(4), 381-393.

77. Jaya, V., Dodagoudar, G. R. and Boominathan, A. (2011). "Seismic response analysis of nuclear island building: A case study." *Journal of Structural Engineering, SERC*, 38,217-229.

78. Jaya, V., Dodagoudar, G. R. and Boominathan, A. (2012). "Seismic soil-foundation-structure interaction analysis of deeply embedded ventilation Stack." *Journal of Earthquake and Tsunami*, 6(1), (doi: 10.1142/S1793431112500030).

79. Jeremic, B., Cheng, Z., Taiebat, M. and Dafalias, Y. (2008). "Numerical simulation of fully saturated porous materials." *Int. J. Numer. Anal. Meth. Geomech.*, 32, 1635–1660.

80. Kamatchi, P., Rajasankar, J., Iyer, N. R., Lakshmanan, N., Ramana, G. V. and Nagpal, A. K. (2010). "Effect of depth of soil stratum on performance of buildings for site-specific earthquakes." *Soil Dynamics and Earthquake Engineering*, 30, 647-661.

81. Katona, M. G. and Zienkiewicz, O. C. (1985). "A unified set of single step algorithms Part 3: the Beta-m method, a generalization of the Newmark scheme."*International Journal for Numerical Methods in Engineering*, 21(7), 1345–1359.

82. Kouroussis, G., Verlinden, O. and Conti, C. (2011). "Finite-dynamic model for infinite media: corrected solution of viscous boundary efficiency." *Journal of Engineering Mechanics*, 137(7), 509-511.

83. Kramer, S. L. and Seed, B. H. (1988). "Initiation of static liquefaction under static loading conditions."*Journal of Geotechnical Engineering*, ASCE, 114(4), 412-430.

84. Krishna, A. M. , Madhav, M. R. and Latha, G. M (2006). "Liquefaction mitigation of ground treated with granular piles: densification effect." *ISET Journal of Earthquake Technology*, 43(4), 105-120.

85. Krishna, A. M. and Latha, G. M. (2007). "Seismic response of wrap-faced reinforced soil-retaining wall models using shaking table tests."*Geosynthetics International*, 14(6), 355 –364.

86. Krishna, A. M. (2011). "Mitigation of liquefaction hazard using granular piles."*International Journal of Geotechnical Earthquake Engineering* (IJGEE), DOI: 10.4018/jgee.2011010104.

87. Krishnamoorthy, C. S. (2010). *Finite element analysis: Theory and programming.* Tata McGraw Hill Pub., New Delhi. 2nd edition, 25th reprint.

88. Ladhane, K., Sawant, V. A. and Shukla, S. (2013). "Effect of damping on response of pile group." *Research, Development and Practice in Structural Engineering and Construction*, 577-582, Perth, DOI: 10.3850/9789810879204_GFE150380.

89. Lambe, T. M., and Whitman, R. V. (1969). *Soil Mechanics*. John Wiley & Sons, Inc., New York.

90. Liao, S. S. C. and Whitman, R. V. (1986). "Overburden correction factors for SPT in sand." ASCE, *Journal of Geotechnical Engineering*, 112 (3), 373-377

91. Liao, S. S. C., Veneziano, D. and Whitman, R. V. (1988). "Regression models for evaluating liquefaction probability."*J Geotech Eng* ASCE, 114(4), 389 – 411.

92. Liao, Z. P. and Wong, H. L. (1984). "A transmitting boundary for numerical simulation of elastic wave propagation." *Soil Dyn. Earthquake Engng,* 3, 174-183.

93. Li, H., White, L and Zaman, M. (2000). "A model for fluid accumulation and flow in a three-dimensional porous medium." *Applied Mathematics and Computation,* 108, 177-196.

94. Ling, H. I., Yue, D., Kaliakin, V. and Themelis, N. J. (2002). "Anisotropic elasto plastic bounding surface model for cohesive soils." *J. Eng. Mech.*, 128(7), 748–758.

95. Liyanapathirana, D. S. and Poulos, H. G. (2002). "Numerical simulation of soil liquefaction due to earthquake loading." *Soil Dynamics and Earthquake Engineering,* 22, 511–523.

96. Liyanapathirana, D. S. and H. G. Poulos. (2004). "Assessment of soil liquefaction incorporating earthquake characteristics." *Soil Dynamics and Earthquake Engineering,* 24, 867–875.

97. Lo'pez-Querol, S. and Bla´zquez, R. (2007). "Validation of a new endochronic liquefaction model for granular soil by using centrifuge test data." *Soil Dynamics and Earthquake Engineering*, 27, 920–937

98. Lysmer, J. and Kuhlemeyer, R. L. (1969). "Finite-dynamic model for infinite media." *J. Eng. Mech. Div.*, 95(4), 859–877.

99. Madabhushi, S. P. G. and Schofield, A. N. (1993). "Centrifuge modeling of tower structure on saturated sands subjected to earthquake perturbations." *Geotechnique*, 43(4), 555-65.

100. Madabhushi, S. P. G. and Zeng, X. (1998). "Seismic response of gravity quay walls II: numerical modeling." *Journal of Geotechnical and Geo-environmental Engineering*, ASCE, 124(5), 418-27.

101. Maheshwari B. K., Singh, H. P. and Saran, S. (2012). "Effects of reinforcement on liquefaction resistance of Solani sand."*Journal of Geotechnical and Geoenvironmental Engineering*, 138(7), 831–840.

102. Marcuson, W. F. III. (1978). "Definition of terms related to liquefaction." *Journal of Geotechnical Engineering Division, ASCE,* 104(9), 1197-1200

103. Marcuson, W.F., Hadala, P.F. and Ledbetter, R.H. (1996). "Seismic rehabilitation of earth dams."*Journal of Geotechnical Engineering*, ASCE, 122(1), 7–20.

104. Martin, G. R., Finn, W. D. L. and Seed, H. B. (1975). "Fundamentals of liquefaction under cyclic loading."*J. Geotech. Engg. Div.*, ASCE, 101(5), 423-438.
105. Morland, L. W. (1972). "A simple constitutive theory for a fluid-saturated porous solid." *Journal of Geophysical Research*, 77(5), 890-900.
106. Nair, R., Abousleiman, Y. and Zaman, M. (2005). "Modeling fully coupled oil-gas flow in dual-porosity medium." *International Journal of Geomechanics*, ASCE, 5(4), 326-338.
107. Newmark, N. M. (1959). "A method of computation for structural dynamics." *Journal of Engineering Mechanics*, ASCE, 85(EM3), 67-94.
108. Nova, R. and Wood, D. M. (1982). "A constitutive model for soil under monotonic and cyclic loading, Soil Mechanics-Transient and Cyclic loads, edited by G. N. Pande and O. C. Zienkiewicz."*John Wiley & Sons Ltd*., New York, 343-373.
109. Novak, M. (1974). "Dynamic stiffness and damping of pile." *Canadian Geotechnical Journal*, 11, 574-598.
110. Novak, M. and Mitwally, H. (1988). "Transmitting boundary for axisymmetrical dilation problems." *J. Eng. Mech.*, 114(1), 181–187.
111. Novak, M., Nogami, T. and Aboul-Ella, F. (1978). "Dynamic soil reactions for plane strain case." *J. Engrg. Mech. Div.*, ASCE, 104(4), 953-959.
112. Novak, M. and Mitwally, H. (1988). "Transmitting boundary for axisymmetrical dilation problems." *Journal of Engineering Mechanics*, 114, No. 1, 181-187.
113. Novak, M., Nogami, T. and Aboul-Ella, F. (1978). "Dynamic soil reactions for plane strain case." *J. Engrg. Mech. Div., ASCE*, 104(4), 953-959.
114. Oka, F., Yashima, A., Shibata, T., Kato, M. and Uzuoka, R. (1994). "FEM-FDM coupled liquefaction analysis of a porous soil using an Elasto-Plastic Model."*Applied Scientific Research*, 52, 209-245.
115. Oka, F., Kodaka, T., Moromoto, R. and Kita, N. (2002). "An elasto-plastic liquefaction analysis method based on finite deformation theory." *Proc. 15th KKCNN 2002, NUS*, Dec. 19-20, G81-88.
116. Oka, L. G., Dewoolkar, M. M. and Olson, S. (2012). "Liquefaction assessment of cohesionless soils in the vicinity of large embankments." *Soil Dynamics and Earthquake Engineering*, 43, 33-44.

117. Park, K. C. (1983). “Stabilization of partitioned solution procedures for pore fluid interaction analysis.” *Int J Numer Methods Eng*, 19, 1669–73.

118. Park, D. and Hashash, Y. M. A. (2004). “Soil damping formulation in nonlinear time domain site response analysis.” *Journal of Earthquake Engineering*, 8(2), 249-274.

119. Parra, E. (1996). “Numerical modeling of liquefaction and lateral ground deformation including cyclic mobility and dilation response in soil systems.” *Ph.D. thesis, Rensselaer Polytechnic Institute, Troy, N.Y.*

120. Parra, E., Adalier, K., Elgamal, A. W., Zeghal M. and Ragheb, A. (1996). “Analyses and modeling of site liquefaction using centrifuge tests.” *Eleventh World Conference on Earthquake Engineering, Acapulco, Mexico,* June 23-28.

121. Pastor, M., Zienkiewicz, O. C. and Leung, K. H. (1985). “Simple model for transient soil loading in earthquake analysis. II: Non-associative models for sands.” *Int. J. Numer. Analyt. Meth. Geomech*., 9(5), 477–498.

122. Pastor, M. and Zienkiewicz, O. C. (1986). “A generalized plasticity hierarchical model for sand under monotonic and cyclic loading.” Proc. 2nd Int. Symp. on *Numerical Models in Geomechanics*, 5(1), 141-150.

123. Pastor, M., Zienkiewicz, O. C. and Chan, A. H. C. (1990). “Generalized plasticity and the modeling of soil behavior.” *Int. J. Numer. Analyt. Meth. Geomech*., 14(3), 151–190.

124. Pastor, M., Chan, A. H. C. and Zienkiewicz, O. C. (2000). “Constitutive and numerical modelling of liquefaction.” *In: Zaman M, Gioda G, Booker J, editors. Modelling in geomechanics. Chichester: Wiley*, 91–128.

125. Patil, V. A., Sawant, V. A. and Deb, K. (2010). “Use of finite and infinite elements in static analysis of pavements.” *Interaction and Multiscale Mech. an Int. J,* 3 (1), 95-110.

126. Patil, V. A., Sawant, V. A. and Deb, K. (2013a). “2-D finite element analysis of rigid pavement considering dynamic vehicle pavement interaction effects.” *Applied Mathematical Modelling*, 37, 1282-1294.

127. Patil, V. A., Sawant, V. A. and Deb, K. (2013b). “3-D finite element dynamic analysis of rigid pavement using infinite elements.” *International Journal of Geomechanics,* ASCE, 13(5), 533-544.

128. Paul, S. (1976). “On the displacements produced in a porous elastic half-space by an impulsive line load (non-dissipative case).” *Pure and Applied Geophysics*, 114, 605-614.
129. Peacock, W. H. and Seed, H. B. (1968). “Sand Liquefaction under Cyclic Loading Simple Shear Conditions.” Proc. *ASCE*, 94(SM3), 689-703.
130. Popescu, R. and Prevost, H. (1993). “Centrifuge validation of a numerical model for dynamic soil liquefaction.” *Soil Dynamics and Earthquake Engineering*, 12, 73-90.
131. Popescu, R., Prevost, J. H. and Decodatis, G. (1997). “Effects of spatial variability on soil liquefaction: some design recommendations.” *Geotechnique*, 47, 1019-1036.
132. Popescu, R., Prevost, J. H., Deodatis, G. and Chakrabortty, P. (2006). “Dynamics of nonlinear porous media with applications to soil liquefaction.” *Journal of Soil Dynamics and Earthquake Engineering*, 26(6-7), 648–665.
133. Prakash, S. and Gupta, M. K. (1970). “Blast Tests at Tenughat Dam Site.” *Journal of the Southeast Asian Society of Soil Engineering*, 1(1), 41-50.
134. Prakash, S. (1981). *Soil dynamics*, McGraw-Hill Book Company.
135. Prevost, J. H. (1980). “Mechanics of continuous porous media.”*Int J Eng Sci*, 18(5), 787–800.
136. Prevost, J. H. (1982). “Nonlinear transient phenomena in saturated porous media.” *Computer Methods in Applied Mechanics and Engineering*, 20, 3-18.
137. Prevost, J. H. and Popescu, R. (1996). “Constitutive relations for soil materials.” *The Electrical journal of Geotechnical Engineering*, 1.
138. Puebla, H., Byrne, P. M. and Phillips, P. (1997). “Analysis of canlex liquefaction embankments prototype and centrifuge models.”*Canadian Geotechnical Journal*, 34,641-657.
139. Ragheb, A. M. (1994). “Numerical analysis of seismically induced deformations in saturated granular soil strata.”*PhD Thesis, Dept. of Civil Engineering, Rensselaer Polytechnic Institute*, Troy, NY.
140. Raghunandan, M. E. (2012). “Effect of soil layering on the ground response parameters – A parametric study.” *Natural Hazards*, 63(2), 1115-1128.
141. Rayleigh, J. W. S. and Lindsay, R. B. (1945). The theory of sound. *Dover Publications, North Chelmsford, MA, New York, 2nd edition.*

142. Riemer, M. F. and Seed, R. B. (1997). "Factors Affecting Apparent Position of Steady-State Line." *Journal of Geotechnical and Geoenvironmental Engineering*, 123(3), 281–288.
143. Robertson, P. K. and Companella, R. G. (1985). "Liquefaction potential of sand using CPT." *Journal of Geotechnical Engineering Division*, ASCE, 111(3), 384-403.
144. Robertson, P. K. and Wride, C. E. (1998). "Evaluating cyclic liquefaction potential using the cone penetration test." *Canadian Geotechnical Journal*, 35(3), 442-52.
145. Sadeghian, S. and Manouchehr, L. N. (2012). "Using state parameter to improve numerical prediction of a generalized plasticity constitutive model." *J. Computers & Geosciences*, 51, 255–268.
146. Sandhu, R. S. (1968). "Fluid Flow in Saturated Porous Elastic Media." *Ph.D. Dissertation*, University of California, Berkeley, CA.
147. Sandhu, R. S. and Wilson, E. L. (1969). "Finite element analysis of seepage in elastic media." *J. Engng. Mech.* ASCE, 95, 641-652.
148. Sawant, V. A., Patil, V. A. and Deb, K. (2011). "Effect of vehicle-pavement interaction on Dynamic Response of Rigid Pavements." *Geomechanics and Geoengineering*, 6(1), 31-39.
149. Sawant, V. A., Patil, V. A. and Deb, K. (2012). "Finite element analysis of rigid pavement on a nonlinear two parameter foundation model." *International Journal of Geotechnical Engineering*, J. Ross Publication, U.S.A, 6(3), 275-286.
150. Sawant, V., Shukla, S., Sivakugan, N., Das, B., (2013), "Insight into pile setup and load carrying capacity of driven piles." *International Journal of Geotechnical Engineering*, 7(1), 71-83.
151. Seed, H. B. and Lee, K. L. (1966). "Liquefaction of saturated sands during cyclic loading." *J. Geotechnical Engineering*, ASCE, 92(6), 105-134.
152. Seed, H. B. and Idriss, I. M. (1967). "Analysis of Soil Liquefaction: Niigata Earthquake." *J. of the Soil Mechanics and Foundations Div.*, ASCE, 93(SM3), 83-108.
153. Seed, H. B. and Idriss, I. M., (1971). "Simplified Procedure for Evaluating Soil Liquefaction Potential."*J. of soil Mechanics and Foundations Division, ASCE* 92(6), 1249-1273.

154. Seed, H.B., Martin, P.P. and Lysmer, J. (1976). "Pore-Water Pressure Changes during Soil Liquefaction", *Journal of the Geotechnical Engineering Division*, Proceedings of ASCE, Vol. 102, No. GT4, pp. 323–346.
155. Seed, H. B. (1979). "Soil liquefaction and cyclic mobility evaluation for level ground during earthquakes." *J. Geotechnical Engineering Division*, ASCE, 105(2), 201-255.
156. Seed, H. B., Idriss, I. M. and Arango, I. (1983). "Evaluation of liquefaction potential using field performance data." *Journal of Geotechnical Engineering Division*, ASCE, 109(3), 458-482.
157. Seed, H. B., Tokimatsu, K., Harder, L. F. and Chung, R. M. (1985). "Influence of SPT procedures in soil liquefaction resistance evaluations." *Journal of the Geotechnical Engineering Division*, ASCE, 111(12), 1425-1445.
158. Seed, H. B. and De-Alba, P. (1986). "Use of SPT and CPT tests for evaluating the liquefaction resistance of sands." *In Proc. Use of In-situ Tests in Geotechnical engineering*, ASCE, *New York*, 281-302.
159. Seed, H. B., Romo, M. P., Sun, J. I., Jaime, A. and Lysmer, J. (1988). "The Mexico Earthquake of September 19, 1985--relationships between soil conditions and earthquake ground motions, *Earthquake Spectra*, 4, 687-729.
160. Shahir, H. and Pak, A. (2010). "Estimating liquefaction-induced settlement of shallow foundations by numerical approach." *Journal of Computers and Geotechnics*, 37(3), 267–279.
161. Shan, Z., Ling, D. and Ding, H. (2012). "Exact solutions to one-dimensional transient response of incompressible fluid-saturated single-layer porous media." *Applied Mathematics and Mechanics*, 34(1), 75–84.
162. Shukla, S., (2013), "Generalized analytical expression for dynamic passive earth pressure from c-phi soil backfills." *International Journal of Geotechnical Engineering*, 7(4), 443-446.
163. Shukla, S., Sivakugan, N., Das, B. M. (2011), "An analytical expression for dynamic passive pressure from c-phi soil backfill with surcharge." *International Journal of Geotechnical Engineering*, 5(3), 357-362.

164. Silver, M. L. and Seed, H. B. (1971). “Deformation Characteristics of Sands under Cyclic Loading.” *J. of the Soil Mechanics and Foundations Div.*, ASCE, 97(SM8), 1081-1098.

165. Simon, B. R., Wu. J. S. S., Zienkiewicz, O. C. and Paul, D. K. (1986). “Evaluation of *u–w* and *u–p* finite element methods for the dynamic response of saturated porous media using one-dimensional models.” *Journal for Numerical and Analytical Methods in Geomechanics*, 10, 461–82.

166. Sitharam, T. G., Ravishankar, B. V. and Patil, S. M. (2012). “Liquefaction and pore water pressure generation in sand: Cyclic Strain Controlled Triaxial Tests.” *International Journal of Geotechnical Earthquake Engineering*, 3(1), 57-85.

167. Sivakugan, N., Lovisa, J. P., Ameratunga, J. and Das, B. M. (2014). “Consolidation settlement due to ramp loading.” *International Journal of Geotechnical Engineering*, 8(2), 191-196.

168. Snieder, R. and Beukel, A. V. D. (2004). “The liquefaction cycle and the role of drainage in liquefaction.” *Granular Matter*, 6(1), 1–9.

169. Taiebat, M., Shahir, H. and Pak, A. (2007). “Study of pore pressure variation during liquefaction using two constitutive models for sand.” *Soil Dynamics Earthquake Engineering*, 27, 60–72

170. Taiebat, M., Jeremic, B., Dafalias, Y. F., Kaynia, A. M. and Cheng, Z. (2010). “Propagation of seismic waves through liquified soils.” *Soil Dynamics and Earthquake Engineering*, 30(4), 236-257.

171. Taiyab, M. A., Alam, M. J. and Abedin, M. Z. (2010). “Numerical simulation of level ground loose sand deposit subjected to cyclic loading.” *Proc., Bangladesh Geotechnical Conf., Bangladesh Society for Geotechnical Engineering in Association with ISSMFE*, Dhaka, Bangladesh, 346–352.

172. Taiyab, M. A. (2012). "Modeling of quay wall systems subjected to seismic liquefaction." *PhD. thesis, Bangladesh University of Engineering And Technology.*

173. Taiyab, M. A., Alam, M. J. and Abedin, M. Z. (2014). “Dynamic soil-structure interaction of a gravity quay wall and the effect of densification in liquefiable Sites.” *International Journal of Geomechanics*, ASCE, 14(1), 20-33.

174. Tatsouka, F., Zhou, S., Sato, T. and Shibuya, S. (1990). "Evaluation method of liquefaction potential and its application." *Report on seismic hazards on the ground in urban areas*, Ministry of Education of Japan, Tokyo, 75-109 (In Japanese).
175. Terzaghi, K. (1943). *Theoretical soil mechanics*. New York: Wiley;
176. Thompson, L. L., Huan, R. N. and He, D. T. (2001). "Accurate radiation boundary conditions for the two-dimensional wave equation on unbounded domains." *Comput. Meth. Appl. Mech. Engrg.*, 191, 331–351.
177. Tsai, P.H., Lee, D-H., Kung, G. T.C. and Juang, C. H. (2009). "Simplified DMT-based methods for evaluating liquefaction resistance of soils." *Engineering Geology,* Elsevier, 103(1-2), 13–22.
178. Vaid, Y. P. and Sivathayalan, S. (1996). "Static and cyclic liquefaction potential of Fraser Delta sand in simple shear and triaxial tests." *Canadian Geotechnical Journal,* 33(2), 281-89.
179. Vaid, Y. P. and Sivathayalan, S. (2000). "Fundamental factors affecting liquefaction susceptibility of sands." *Canadian Geotechnical Journal,* Vol. 37(3), 592-606.
180. Varghese, R. M. and Latha, G. M. (2014). "Shaking table tests to investigate the influence of various factors on the liquefaction resistance of sands." *Natural Hazards, Springer,* published online DOI 10.1007/s11069-014-1142-3.
181. White, L. W. and Zaman, M. (1998). "A simple model for fluid accumulation and flow in a porous medium." *Applied Mathematics and Computation* , 90, 181-203.
182. Wijewickreme, D., Somasundaram, S. and Byrne, P. (2005). "Cyclic loading response of loose air-pluviated Fraser River sand for validation of numerical models simulating centrifuge tests." *Canadian Geotechnical Journal*, 42(2), 550-61.
183. Yang, Z. (2000). "Numerical Modeling of Earthquake Site Response Including Dilation and Liquefaction." *PhD Thesis*, Dept. of Civil Engineering and Engineering Mechanics, *Columbia University*, NY, New York.
184. Yoshimine, M., Robertson, P. K. and Wride, C. E. (1999). "Undrained shear strength of clean sands to trigger flow liquefaction." *Canadian Geotechnical Journal,* 36(5), 891-906.

185. Youd, T. L. and Perkins, D. M. (1978). “Mapping of liquefaction induced ground failure potential.” *Journal of Geotechnical Engineering Division,* ASCE, 104(4), 433-46.

186. Youd, T. L. and Idriss, I. M. (2001). “Liquefaction resistance of soils: Summary report from the 1996 NCEER and 1998 NCEER/NSF workshops on evaluation of liquefaction resistance of soils.”*J. Geotech. And Geoenvir. Engg. Div.*, ASCE, 127(10), 817-833.

187. Zaman, M. M., Desai, C. S. and Drumm, E. C. (1984). “Interface model for dynamic soil-structure interaction.” *J. Geotechnical Engineering*, 110(9), 1257–1273.

188. Zhao, C. and Liu, T. (2002). “Non-reflecting artificial boundaries for modelling scalar wave propagation problems in two-dimensional half space.”*Computer Methods in Applied Mechanics and Engineering*, 191(41–42), 4569-4585.

189. Zhao, C. and Liu, T. (2003). “Non-reflecting artificial boundaries for transient scalar wave propagation in a two-dimensional infinite homogeneous layer.” *Int. J. Numer. Meth. Engng.* 58, 1435–1456.

190. Zhang, Y. (2003). “Treatment of seismic input and boundary conditions in nonlinear seismic analysis of a bridge ground system.” *16th ASCE Engineering Mechanics Conference*, (July 16-18, Seattle), 1–11.

191. Zheng, W. and Luna, R. (2011). “Nonlinear site response and liquefaction analysis in the New Madrid seismic zone.” *Geotechnical and Geological Engineering*, 29(4), 463–475.

192. Zienkiewicz, O.C., Bettess, P. and Kelly, D.W. (1978). “The Finite Element Method for determining fluid loadings on rigid structures, Two-and Three-Dimensional Formulations.” *Numerical Methods in Offshore Engineering*, O.C. Zienkiewicz et al. *(eds.), Wiley, Chichester*.

193. Zienkiewicz, O. C., Chan, A. H. C., Pastor, M, Schrefler, B. A. and Shiomi, T. (1999). *Computational geomechanic: with special reference to earthquake engineering*, Wiley New York.

194. Zienkiewicz, O. C. and Mroz, Z. (1984). “Generalized plasticity formulation and applications to geomechanics.”*Mechanics of engineering materials*, C. S. Desai, and R. H. Gallagher, eds., *Wiley*, New York, 655–679.

195. Zienkiewicz, O. C. and Shiomi, T. (1984). “Dynamic behaviour of saturated porous media; the generalized Biot formulation and its numerical solution.”*International Journal for Numerical Methods in Engineering*, 8, 71–96.
196. Zienkiewicz, O. C. and Pande, G. N. (1977). “Some useful forms of isotropic yield surfaces for soil and rock mechanics. *In Finite elements in geomechanics*.”*G. Gudehus, eds.,Wiley, Newyork*, 179–190.
197. Zienkiewicz, O. C., Leung, K. H. and Pastor, M. (1985). “Simple model for transient soil loading in earthquake analysis I — Basic model and its application.”*International Journal of Numerical and Analytical Methods Geomechanics*, 9, 453–476.

LIST OF PUBLICATIONS

- Sunita Kumari and V. A. Sawant (2013) "Use of Infinite elements in simulating liquefaction phenomenon using coupled approach", *Coupled Systems Mechanics (CSM), Techno Press*, Volume 2, Number 4, 375-387.
- Sunita Kumari and V. A. Sawant (2013) "Modelling of Liquefaction Phenomena in Semi-Infinite Soil Domain" *International Journal of Civil Engineering and Applications*, Volume 3, Special Issue,143-147, ISSN No 2249-426X.
- Sunita Kumari and V. A. Sawant (2014) "Simulation of Liquefaction Phenomenon in Semi-infinite Domain under Harmonic Loading", *International Journal of geotechnical Engineering, Maney Publication*, DOI 10.1179/1939787914Y.0000000059.
- Sunita Kumari and V. A. Sawant (2014) "Assessment of Liquefaction Hazard using Coupled Finite Element Analysis", *Natural Hazard, Springer* (Communicated).
- Sunita Kumari and V. A. Sawant (2012) "Finite Element Formulation of One Dimensional Consolidation", *SEC-2012, NIT Surat*, 591-594, ISBN No: 978-93-82062-40-0.
- Sunita Kumari and V. A. Sawant (2013) "Numerical Modeling of Liquefaction considering two-dimensional plane strain conditions", *4IYGEC-2013, IIT Chennai*, 217-220, *Indian Geotechnical Society, Chennai Chapter*.
- Sunita Kumari and V. A. Sawant (2013) "Modelling of Liquefaction using coupled Finite Element Method", *AGE-2013, NIT Surat*, 53-57, ISBN No: 978-93-82062-40-0.
- Sunita Kumari and V. A. Sawant (2013) "Modeling of Liquefaction Phenomenon Using Coupled Approach", *Indian Geotechnical conference, IGC-2013, IIT Roorkee*.